Sede Amministrativa: Università degli Studi di Padova

Dipartimento di Ingegneria Industriale

SCUOLA DI DOTTORATO DI RICERCA IN: INGEGNERIA INDUSTRIALE
INDIRIZZO: INGEGNERIA DELL’ENERGIA
CICLO XXVI

Analysis and Design of a Linear Tubular Electric Machine for Free-piston Stirling Micro-cogeneration Systems

Direttore della Scuola: Ch.mo Prof. Paolo Colombo

Coordinatore d’indirizzo: Ch.ma Prof.ssa Luisa Rossetto

Supervisore: Ch.mo Prof. Giovanni Attilio Martinelli

Co-supervisori: Ch.mo Prof. Mauro Andriollo
Ch.mo Prof. Andrea Tortella

Dottorando: Luca Dall’Ora

31 gennaio 2014

Abstract

The UE investments for the renewable source development, in order to achieve the set goals (Kyoto protocol and "20-20-20" targets), push to investigate in new technologies and to develop the existing. In this context, the cogeneration (CHP) plays a fundamental role, and in particular, the micro-CHP has wide development margins.

Among the different cogeneration process, the systems driven by a free-piston Stirling engine are one of the most significant challenges in the research area. In such systems, the thermal energy, coming from primary energy source (for example renewable energy), is converted into mechanical energy through a Stirling engine, and then a linear generator converts the mechanical energy into electrical energy, finally, the generator is connected to the electric grid or to the load by means of an electric converter. The use of the linear generator, instead of the traditional systems of linear to alternating motion conversion (rod-crank system), allows achieving several advantages, including: improving the system reliability, noise and cost reduction. Finally, this kind of system, if well-designed, allows improving the system efficiency.

In this thesis a linear generator, directly coupled to a free-piston Stirling engine in a CHP system, was developed and analysed. It was found, after a first phase of the study and literature review, that the most convenient choice, from the technical and economic point of view, is a single-phase tubular permanent magnet linear generator. In particular, the magnets are made of plasto-neodymium, while, for the realization of the stator magnetic circuit, due to the geometrical complexity, soft magnetic composites (SMC) materials have been considered.

In order to determine the generator performance, an analysis method based on FEAs was developed. This simplified method (HFEA) allows the study and the comparison of different magnetization patterns and current supply strategies. The proposed methodology exploits the representation of the magnetization spatial harmonics through an analytical processing that allows taking into account different magnetization profile of the permanent magnets. Thus, it was possible to reconstruct the most important quantities, such as the flux density and the flux linkage, superposing the effect of each harmonic obtained through the Fourier analysis. Furthermore, a procedure, able to reproduce the effects of magnetic saturation of the mover, generally not negligible in such kind of machines, was developed. For this purpose, an appropriate surface current distribution on the yoke of the mover was introduced, in order to reproduce the demagnetizing effect due to the saturation.

By means of the air gap flux density, the force provided by linear generator was calculated, while, by means of the flux density sampled on suitable points on the stator and mover yokes, the iron losses were estimated and then the machine efficiency. By means of the flux linkage the emf provided by linear generator was determined.

The results show a very good agreement with corresponding FEAs. The proposed analysis method allows carrying out a parametric analysis with a lower computational effort. Thanks to this feature, different magnetization patterns, supply strategies and SMC materials can be compared in order to optimize the machine design.

A prototype based on the design guidelines was built; then, a procedure based on experimental measurement was developed to characterize the electromagnetic parameters. To determine the magnetization profile of the magnets, the flux density on the mover surface was carried out by means of a Gaussmeter. As regards the SMC materials that compose the stator core, a calculation method was developed from suitable experimental elaborations, in order to determine the most important magnetic properties, such as the BH curve and core loss coefficients.

From experimental results, it can be noted that the actual characteristics are poorer than those provided by the manufactured datasheets, likely due to the manufacturing processes and spurious air gaps between the SMC modules. The update electromagnetic parameters are used to determine the actual performance of the machine, particularly to estimate the efficiency, the emf and the force.

Finally, a simplified model of the cogeneration system was developed in order to predict the dynamic behaviour and particularly, the actual values of the speed, output power and efficiency. This model allows developing the control strategy of the linear generator acting on the electric converter.

Sommario

Gli investimenti da parte dei paesi della UE per lo sviluppo delle fonti rinnovabili, al fine di raggiungere gli obiettivi preposti (Protocollo di Kioto e Piano "20-20-20"), spingono a ricercare nuove tecnologie e a sviluppare quelle già esistenti. In questo ambito, la cogenerazione ricopre un ruolo fondamentale, ed in particolare, la micro-cogenerazione, anche in ambito domestico, presenta ancora ampi margini di sviluppo.

Tra le diverse modalità di cogenerazione, i sistemi *free-piston* azionati da motori Stirling rappresentano una tra le sfide più importanti nell'ambito della ricerca. In tali sistemi l'energia termica, proveniente da una fonte di energia primaria (ad esempio di tipo rinnovabile), è convertita in energia meccanica attraverso un motore Stirling; successivamente un generatore lineare converte l'energia meccanica in elettrica; ed infine, un convertitore elettrico interfaccia il generatore con un carico o con la rete elettrica. L'utilizzo del generatore lineare, al posto dei tradizionali sistemi di conversione del moto da lineare ad alternato (sistema biella-manovella), consente di ottenere diversi benefici, tra cui: migliorare l'affidabilità del sistema, limitare il rumore e ridurre i costi. Infine, questo sistema, se ben progettato, permette di aumentare il rendimento dell'impianto di cogenerazione.

In questo lavoro di tesi è stato progettato ed analizzato un generatore lineare da accoppiare direttamente ad un motore Stirling *free-piston* in un sistema di cogenerazione domestico. Dopo una prima fase di studio e ricerca bibliografica, è stato riscontrato che la scelta più conveniente dal punto di vista tecnico-economico, risulta essere quella di un generatore monofase tubolare a magneti permanenti. In particolare, i magneti sono a base di plasto-neodimio, mentre, per la realizzazione del circuito magnetico di statore, data la complessità geometrica, si sono considerati materiali magnetici compositi (SMC).

Al fine di determinare le prestazioni del generatore, è stata sviluppata una metodologia di analisi, basata su analisi FEM, che permettesse lo studio ed il confronto di diverse tipologie di magnetizzazione, in particolare radiale e Halbach, e considerare diverse strategie di alimentazione. Tale metodologia (HFEA) sfrutta la rappresentazione delle armoniche spaziali di magnetizzazione attraverso un'elaborazione di tipo analitico che permette di riprodurre diverse funzioni di magnetizzazione dei magneti permanenti. In tal modo, è stato possibile ricostruire le principali grandezze di interesse (induzione e

flusso concatenato) sovrapponendo l'effetto di ciascuna armonica ricavata attraverso l'analisi di Fourier. Inoltre, è stata sviluppata una procedura in grado di riprodurre gli effetti della saturazione magnetica del traslatore, generalmente non trascurabile in questo tipo di macchine. A questo proposito sono state introdotte opportune distribuzioni superficiali di corrente sul giogo del traslatore che riproducono l'effetto smagnetizzante dovuto alla saturazione.

Dai valori dell'induzione al traferro, è possibile risalire al valore della forza esplicata dal generatore; mentre, dai valori dell'induzione, campionati in opportuni punti all'interno dei nuclei magnetici dello statore e del traslatore, è stato possibile stimare le perdite nel ferro e quindi il rendimento della macchina. Dal profilo del flusso concatenato è stato possibile stimare l'andamento della forza elettromotrice generata.

I risultati hanno evidenziato un ottimo accordo con le corrispondenti analisi agli elementi finiti, con il vantaggio rispetto a queste di poter effettuare analisi parametriche che coinvolgono diverse grandezze progettuali con tempi di calcolo inferiori. Grazie a questa caratteristica, è stato possibile confrontare le prestazioni con varie tipologie di magnetizzazioni, strategie di alimentazione e caratteristiche di materiali SMC, effettuando una prima ottimizzazione del progetto della macchina.

Dopo aver realizzato un prototipo sulla base delle indicazioni progettuali, è stata sviluppata una procedura sperimentale atta a determinare i parametri elettromagnetici del generatore, per verificarne la congruenza con le ipotesi progettuali e mettere a punto quindi i modelli per le analisi successive. Per determinare il profilo di magnetizzazione dei magneti sono state effettuate delle misure di induzione sulla superficie del materiale magnetico mediante l'uso di un Gaussmetro. Invece, per i materiali SCM che costituiscono lo statore della macchina, a partire da opportune elaborazioni sperimentali, è stato sviluppato un metodo di calcolo in grado di determinare le principali proprietà magnetiche (permeabilità, caratteristica BH e coefficienti delle perdite nel ferro per isteresi, correnti parassite ed eccesso).

Dai risultati sperimentali si nota che le caratteristiche reali sono meno performanti rispetto a quelle fornite dai datasheet dei costruttori, molto probabilmente a causa dei processi di lavorazione e dei traferri spuri presenti tra i moduli di SMC. I valori delle grandezze magnetiche aggiornate sono stati utilizzati per stimare le reali condizioni di esercizio della macchina, in particolare per determinare il valore del rendimento, della tensione e della forza sviluppata dalla macchina.

È poi stato sviluppato un modello semplificato che consente di riprodurre il comportamento dinamico del sistema di cogenerazione completo e di ricavare il profilo effettivo di velocità, la potenza erogata e il rendimento complessivo del sistema. Considerando l'interazione tra i singoli componenti, l'applicazione di questo modello risulta di estrema importanza per eseguire l’analisi e permette di mettere a punto la strategia di controllo del generatore agendo sul convertitore di interfacciamento con il carico.

Contents

Chapter 1

Introduction

The depletion of fossil energy resources and the global warming involve searching alternative solutions to develop clean renewable energy resource. The rapid development of renewable energies represents a challenge for the scientific community to develop new technology or improve the old ones. Among the many technologies, permanent magnet linear generators (PMLG) represent, of course, an important case of study. PMLGs convert mechanical energy into electric energy. They find application in all the fields that involves linear motion, such as: cogeneration systems that use free-piston combustion engine (FPCE), wave energy converters and hybrid automotive field.

The choice of a linear motion generator overcomes a possible mechanical linkage system (crankshaft), which is source of losses, noise and failures.

In this chapter some linear generator applications will be presented, in order to identify the technical specifications for the machine design. Then, main linear generator features and layouts will be discussed. Finally, the research scope and the adopted methodology will be described in order to pointing out the original contribution to actual knowledge.

1.1 Stirling engine applications

Applications of the Stirling engine range from mechanical propulsion to heating and cooling to electrical generation systems. Particularly, Stirling engines can find application in cogeneration systems, as solar and wave energy converters and in the hybrid electric vehicles.

1.1.1 Cogeneration systems

The domestic sector accounts for a considerable portion of the final energy consumption of most developed countries. Within the European Union (EU), approximately 25% of the total annual final energy consumption is used in dwellings [1]. A precise breakdown of how this energy is consumed on a country by country basis is difficult to ascertain, especially considering that such a breakdown is highly dependent on factors such as climate, technology used and other conditions which are variable from country to country [2]. However, an approximate breakdown is given by the European Environmental Agency (EEA) in [3], which indicates that a substantial amount of this energy, about 69%, goes into space heating with the remaining balance accounted for by water heating (15%), providing electricity for appliances and lighting equipment (11%) and cooking activities (5%). In warm climates such as that present in southern European countries, space cooling is the predominant load [4]. Ensuring the efficient provision and use of energy in dwellings is therefore an essential aspect in attaining the overall 20% improvement in energy efficiency target set out by the Presidency Conclusions of the European Council [5] for 2020.

In order to reach the energy-efficiency improvement targets set by the EU, a concrete and perhaps active approach is therefore required [6]. Most of the energy efficiency measures which have been implemented so far are considered to be a first step towards decreasing energy demand in the domestic sector; a step in the right direction but still far away from achieving the desired target. One way in which the individual targets can be achieved is through policy measures specifically aimed at achieving higher penetrations of renewable energy technologies or efficient micro-generation technologies in dwellings [48].

The term “cogeneration”, often called combined heat and power (CHP), means the simultaneous production of two type of energy from the only one primary energy source. The most common cogeneration system produces both heat and electricity at the same time.

Unlike conventional heat and power supplies to buildings in which each is satisfied separately by two distinct energy flow processes, cogeneration systems, as shown in Figure 1.1, make use of a single process whereby the ‘waste heat’ from electricity generation is recovered and re-utilised to satisfy a heating demand [8], hence improving the fuel usage efficiency. As shown in Figure 1.1, the efficiency to produce electrical energy and heat separately is less than 50%, instead the (global) efficiency of a CHP system is around 80 %.

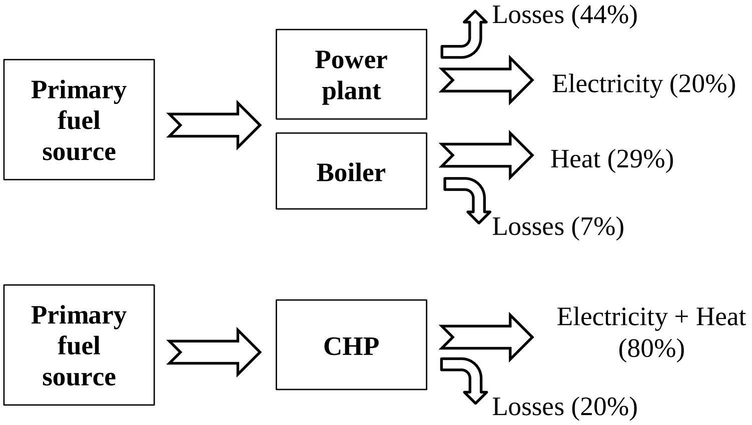

Figure 1.1. *Separate generation vs. cogeneration (efficiency values are indicative).*

Cogeneration can make use of the ‘waste heat’ exhausted from practically any energy conversion system including the traditional internal combustion engines (ICE), Stirling engines, to the more advanced technologies such as micro-gas turbines and fuel cells.

The idea of re-utilising waste heat from an electricity producing process is not a new concept. In 1882, Thomas Edison’s first commercial power station in Pearl Street used to supply both power and heat [9] to a neighbouring block in Manhattan. Similarly, district heating in northern and central Europe has been successfully implemented for many years, with the result that an average 13% of the gross electricity generation in the EU is currently produced by cogeneration as shown in

Figure 1.2.

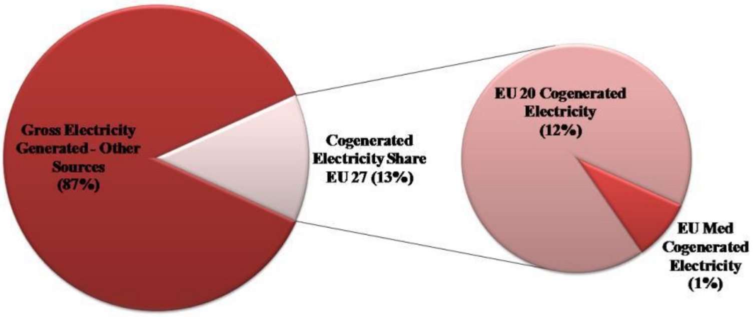

Figure 1.2. *Share of electricity produced by cogeneration in the EU (data published by Eurostat for 2009 [10]).*

From Figure 1.2 it can be observed how the average share of electricity produced from cogeneration, in the 7 countries which border the Mediterranean Sea and which have a predominant warm climate with short mild winters, is still a small part of the overall cogenerated electricity produced in the EU. Like any other technology, the feasibility and market interest in cogeneration depends on the payback period. When assessing the payback period an important role is played by the operational or usage time, as this has a direct effect on the ability of a system to offer reasonable and adequate return on investments. Although plant configuration schemes such as additional storage can be used to introduce a degree of flexibility in micro-cogeneration operation [11], the operational or usage time is still a function of the electrical and thermal demand. In warm climates with the exception of the provision of hot water, the thermal demand is very low due to the low number of heating days. Consequently, the investment required for the installation of a micro-cogeneration system is difficult to justify [12].

A solution to this problem is discuss in [13], that suggest to extend the concept of cogeneration to tri-generation by including a thermally driven cooling load. Unlike cogeneration, tri-generation also known as Combined Cooling, Heat and Power (CCHP), is the process whereby the ‘waste heat’ recovered from an energy conversion process is used either to supply a heating demand such as in a normal cogeneration system or to supply a thermally activated cooling (TAC) device [14] capable of satisfying a cooling demand.

There are various types of TAC devices which can be used in a tri-generation system, single-effect absorption chillers are the preferred type, due to low temperature heat source at which ‘waste heat’ is exhausted from CHP units used in micro-cogeneration systems.

In warm climates this provides a more consistent requirement for heat, thus increasing the system utilisation time. This makes the tri-generation process particularly suitable for use in warm climates given that it can be used both during the summer and the winter period [12]. Tri-generation offers an interesting avenue for efficiently delivering power, heating and cooling to residential buildings in warmer climates.

Further increase in the use of cogeneration in such countries or indeed introducing large scale cogeneration in countries with no prior experience of district heating is however hindered by the fact that district heating requires huge investments costs and implementing such a scheme requires appropriate location conditions (e.g. dense population) and extensive infrastructural work.

One way how these limitations can be overcome is by extending cogeneration to include micro-scale cogeneration. The idea of micro-scale cogeneration or micro-cogeneration differs from district heating or centralised cogeneration, in that, micro-scale cogeneration typically refers to single systems capable of supplying heat and power to individual buildings such as households, small commercial premises, hotels etc. which may or may not be connected to the centralised grid network. Sizes for micro-cogeneration are considerably smaller than typical cogeneration or district heating systems, running into only few kW_{el}. Although the official definition given in Directive

2004/8/EC on the promotion of cogeneration based on a useful heat demand in the internal energy market, the relevant EU directive on cogeneration, qualifies micro-cogeneration as systems with an electrical power output of less than 50 kW_{el}.

One of the most promising systems for cogeneration is powered by free-piston Stirling engine (FPSE), shown in Figure 1.3.

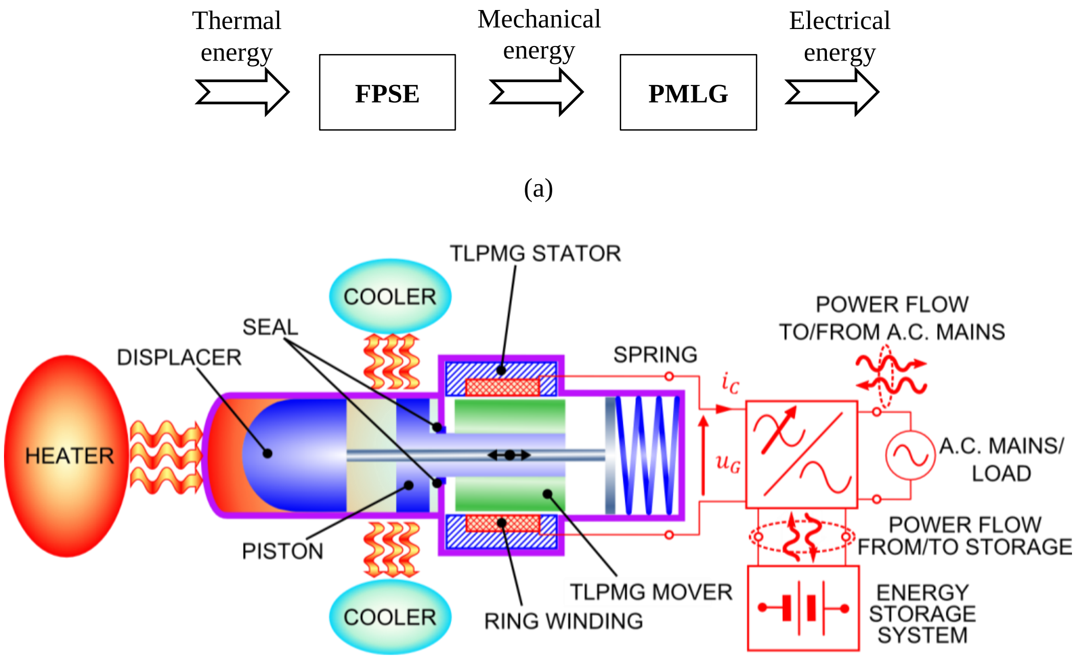

(a)

(b)

Figure 1.3. *Energies transformation process of a free-piston Stirling engine cogeneration system* (a), *cross-section showing major components* (b).

Despite its relatively low efficiency, it has a lot advantages. The Stirling engine is an internal combustion engine, for this reason the working fluid is enclosed, thus guarantee no pollution, reliability and overall, the possibility to use different kind of primary energy sources, such as fossil fuels (oil, coal, gas, etc.) or renewable source (biomass, biogas, solar energy, etc.).

In response to the short-comings of the conventional kinematic Stirling engine, William Beale invented the free-piston Stirling engine (FPSE) in 1964 [15]. All kinematic Stirling machines, no matter what the arrangement, face a number of very significant engineering design challenges which may be so great as to prevent any commercial success. These challenges include the requirement for long-lived non-contact bearings and seals, the difficulty of sealing and pressurizing the machine, the need for lubrication and to separate the lubricant from the heat exchangers, modulation and control. The promise of the free piston machine has been a hermetically sealed, near fixed-frequency device operating in a non-contact mode providing very long life, with no need for lubricants, and direct alternating current output from an integral linear alternator. Figure 1.4 describes the road map to commercialization for some of Sunpower's technology [16].

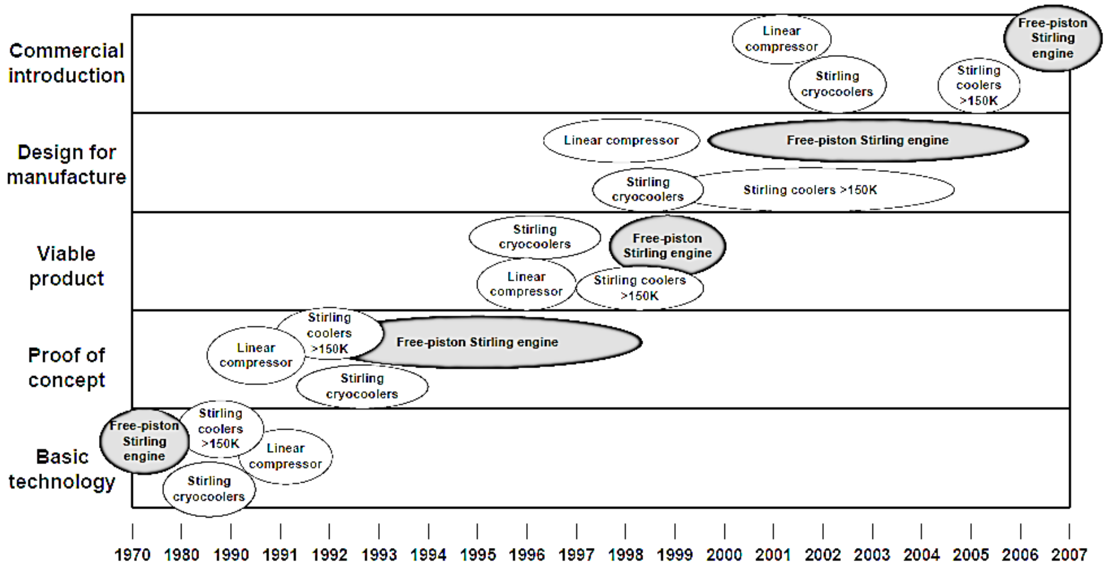

Figure 1.4. *Free-piston Machine Commercialization Roadmap (Sunpower).*

In the idealised form of Stirling engine, heat is supplied to as well as rejected from the engine during isothermal expansion and compression processes, respectively. The cycle is completed by two constant volume processes, during which the heat transported by working fluid is stored and released by a regenerative heat exchanger. Theoretically, the Stirling cycle is the unique that is able to reach the maximum efficiency achieved by the Carnot cycle. Practically, the Stirling engine can attain around 60 – 70 % of the Carnot efficiency, in the case it operates at high wall temperature (600 – 700 °C) [17].

As suggested in [18], one of the critical tasks in the linear machines operation is the initial process of engine starting. A linear engine cannot be started by an ordinary starting motor because it has not a flywheel, crankshaft or any other mechanical coupling which can accept the rotating push of the starter engine. This problem could be solved running linear generator as a linear motor to produce the required reciprocating motion, supplying the linear machine with a suitable current supply strategy (Rectangular Current Commutation).

Paper [19] describe different topologies of linear generator for Stirling cogeneration systems.

1.1.2 Solar energy converters

Solar energy is one of the most important renewable energy sources. The yearly solar fluxes is estimated around 3.85 10^{24} J. Insolation in most countries is from 150 to 300 W/m^2 that means from 1.3 to 2.5 MWh/m^2/year [20]. In 2012, the word's human primary energy consumption was 539 10^{18} J [21], more than 7000 times less of the yearly word's solar energy.

Solar cogeneration systems convert the thermal energy of solar radiation to mechanical energy (by means of Stirling engine) and then to electrical energy (by means of linear generator). The conversion principle is the same utilized in the conventional power plants (oil, coal, gas, etc.).

There are different typologies of solar cogeneration systems, the main are: parabolic trough, linear Fresnel reflectors, solar tower and dish Stirling; the main features of these systems are reported in Table 1.1 [22]. The solar irradiance has enough potential to produce the hot fluid with temperatures up to 165 °C using solar evacuated collectors and up to 400 °C using a concentrating mirror system (usually parabolic troughs).

Table 1.1. *Main features of concentrated solar-thermal-electric technologies.*

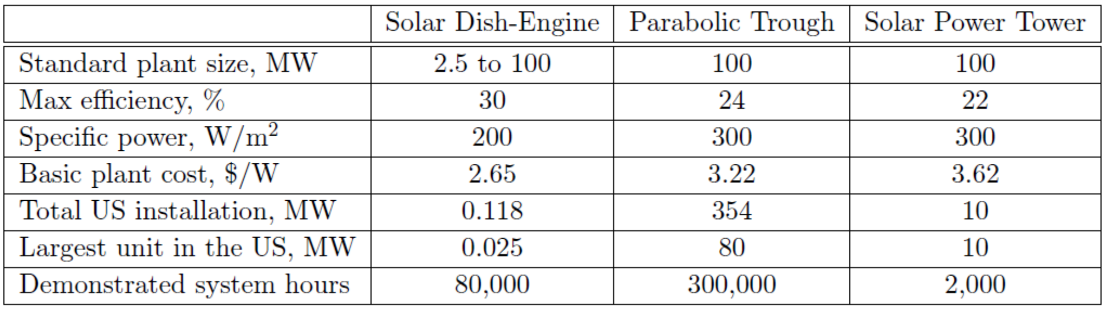

	Solar Dish-Engine	Parabolic Trough	Solar Power Tower
Standard plant size, MW	2.5 to 100	100	100
Max efficiency, %	30	24	22
Specific power, W/m^2	200	300	300
Basic plant cost, \$/W	2.65	3.22	3.62
Total US installation, MW	0.118	354	10
Largest unit in the US, MW	0.025	80	10
Demonstrated system hours	80,000	300,000	2,000

The most promising system is dish Stirling (shown in Figure 1.5), thanks its higher efficiency. The dish Stirling systems use a mirror array to reflect and concentrate solar insolation to a receiver, in order to achieve the temperature required efficiency convert heat to work.

The ideal concentrator shape is a paraboloid of revolution which concentrates sunlight on the focus of paraboloid. Concentration ratio is typically over 2000 and, hence, the concentrator must track the sun in two axes. At the focus is a receiver which is heated up to over 700 °C [22].

Figure 1.5. *Solar dash Stirling cogeneration system.*

The solar-to-electric conversion efficiency of Dish Stirling systems can achieve 30% [23], which represent the highest value of all solar energy converters.

The advantages of dish Stirling technology are [24]:

i. small land requirement (2.5 Ha/MW), due to high efficiency;
ii. short construction times (10 months for a 20 MW plant);
iii. low maintenance and operating costs,
iv. more stable output than photovoltaic systems.

Paper [24] reports the study of a low-cost solar cogeneration system. This system, cheaper than dish Stirling, is conceived to operate with collector temperature in the range of 120° C to 150° C, which is consistent with the use of stationary solar thermal collectors employing low-concentration nonimaging reflectors [25]. A non-tracking system avoids the cost and maintenance issues associated with tracking collectors with high concentration ratios. A Stirling engine converts the delivery heat provided by solar collector into mechanical power. Even if the efficiency (around 10% [18]) is less than dish Stirling systems, due to low-temperature operating conditions, the lower costs and reduced maintenance make this solution interesting in the micro-cogeneration systems. The complete system cost (collector and Stirling engine) is around 0.8 $/W [24].

Since during two-thirds of the day, solar energy is not available, solar/fuel hybrids are needed in case of continuative energy production. Improving the solar system with an external fuel source is not a problem for Stirling engine, as it is able to use all kinds of fuel with any quality.

The efficiency of a solar-thermal collector η_c, as measured experimentally, is given by:

$$\eta_c = \eta_0 - \frac{U_1}{G}(T_m - T_a) - \frac{U_2}{G}(T_m - T_a)^2 \tag{1.1}$$

where η_0 is the maximum collector efficiency, U_1 and U_2 are the thermal loss coefficients [W/m^{2}K] and [W/m^{2}K^2] respectively, G is the power density of incident sunlight [W/m^2], T_m is the mean temperature of the collector [K] and T_a is the ambient temperature [K], respectively.

As regards the engine, the efficiency η_e is given by:

$$\eta_e = \eta_{Carnot}\left(1 - \frac{T_c}{T_m}\right) \tag{1.2}$$

where η_{Carnot} is the fraction of the theoretical Carnot efficiency that the engine can achieves and T_c is the cold side working temperature of the Stirling [K], respectively.

The total conversion system efficiency η, is then given by:

$$\eta = \eta_c\, \eta_e \tag{1.3}$$

For a representative system, the efficiencies of the collector, engine, and system are plotted as a function of temperature in Figure 1.6 [20].

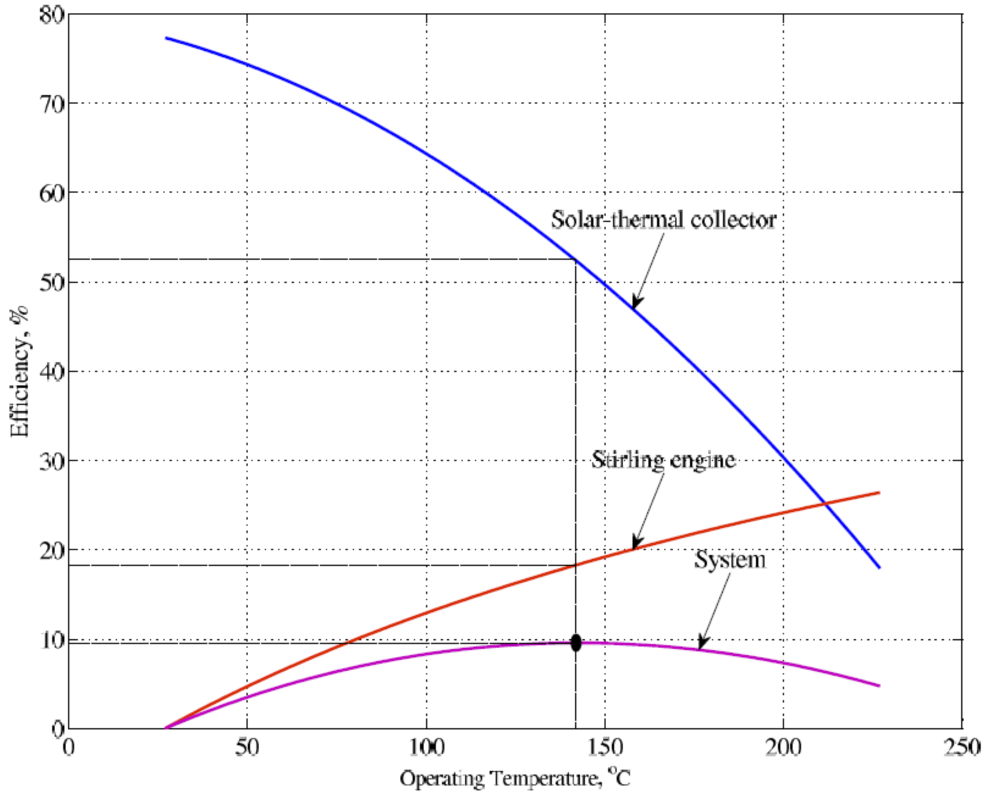

Figure 1.6. *Efficiency as a function of temperature for a representative system. The parameters used are:* G *= 1000 W/m*^{2}, η_0 *= 77.3%,* U_1 *= 1.09 W/m*^{2}*K,* U_2 *= 0.0094 W/m*^{2}*K*^{2}, T_a *= 27 °C,* T_c *= 27 °C, and* η_{Carnot} *= 66%. The dot indicates the point of optimal system efficiency.*

To minimize cost per watt of output electricity, it is desirable to operate a system of given cost at the temperature corresponding to peak system efficiency. This temperature is a function of collector properties as well as ambient temperature and intensity of sunlight. The heat engine can be designed to regulate its loading to maintain optimum collector temperature and system efficiency. Figure 1.6 shows that the system efficiency is rather flat over a range of temperatures near the extremes.

An operating temperature of 142 °C permits a maximum thermodynamic (Carnot) efficiency of 31.6%, assuming the sink temperature is 27 °C. We might reasonably expect the Stirling engine and generator to achieve a thermal-electric efficiency of about 18.3%, roughly 66% of the Carnot efficiency, while the collector operates at a thermal efficiency of about 52.3%. Thus, the estimated overall efficiency of the system would be about 9.6%.

1.1.3 Automotive applications

Linear generator finds application as well as in the hybrid electric vehicles, particularly in the series topology. The topology of these vehicles is reported in Figure 1.7.

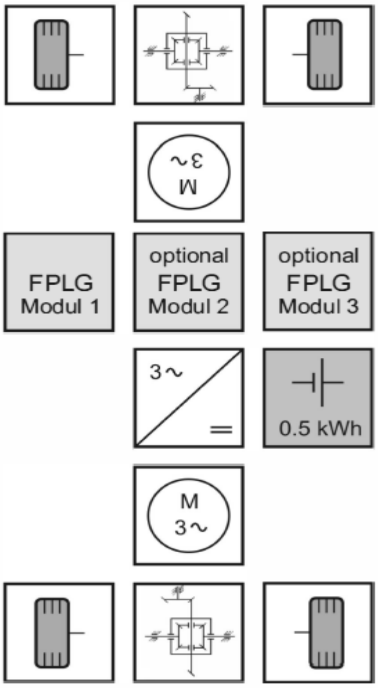

Figure 1.7. *Series hybrid electric vehicle topology.*

One of the main disadvantages of Stirling engines is the very low dynamic speed: they take a lot of time (several tens of seconds) to achieve the steady state condition. This is the reason whereby they cannot use in traditional vehicles, whereas they represent a very interesting choice in series hybrid electric vehicles. In facts, in this kind of hybrid electric vehicles, free-piston Stirling can be used to provide the mean value of power amount, while the ripple of power can be supply by batteries and/or ultracapacitors. The Stirling engine is designed in order to working at its maximum efficiency value. As explained in [26], the high degree of efficiency of free-piston linear generators at all load levels is inherent in their design. It is achieved by keeping the system frequency constant and adapting to the power demanded by varying stroke and compression. One of the main advantages of this system is the possibility to operate with different fuel typologies, such as conventional fuels (petro, diesel and gas) as well as alternative fuel (sun fuel, natural fuel, hydrogen, etc.).

An innovative construction technology, called linear generator of second generation, is reported in [27]. This construction is implemented as a double chamber set-up and an iron-less mover configuration. This is a set-up that uses two stators arranged around one mover (Figure 1.8). This set-up allows for an optimal usage of the whole installation space available and, therefore, for reaching the highest power density possible.

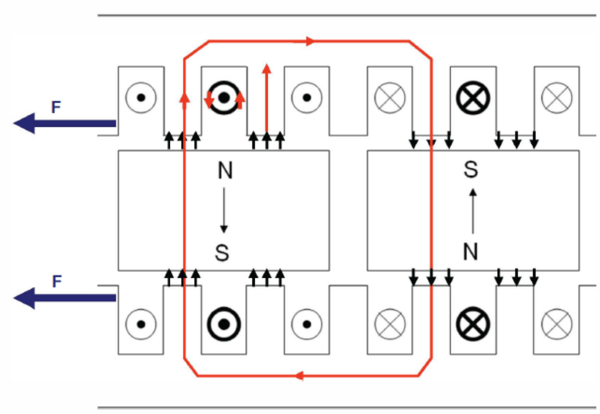

Figure 1.8. *Linear generator of second generation topology.*

The frequency-dependent losses that usually occur in the mover's core no longer occur in this configuration, due to the fact that the mover no longer contains iron. Thus, the mover losses can be reduced considerably, resulting in an efficiency improving and in a reduction of cooling efforts. Another advantage of this configuration is the mover mass reduction, a nice feature to reach a high dynamic performance.

1.1.4 Wave energy converters

The wave energy is generally provided by ocean tides. Oceanic waves could be considered as concentrated form of solar energy. Waves are produced by wind that is created by pressure difference in the Earth's atmosphere, which is created by different solar heating. The energy transferred from wind to water is in the form of potential energy and kinetic energy. The amount of see wave energy is related to wind speed, the amount of time that the wind blowing and the distance over which the waves travel [28].

The World Energy Council has estimated the global ocean wave energy over 2 TW., which means 17,500 TWh/year. From this, it has been estimated that practical amount of see energy that could be converted is around 2,000 TWh/year, similar to current installed nuclear power. Most of this energy (around 95%) is offshore.

The power potential for waves can be described as units of power per meter of wave crest length. The greatest power achievable is about 100 kW/m in the Atlantic Ocean, Southern Ocean and Cape Horm [29].

There are several compelling arguments for using the wave energy technology: first, it is one of the lowest cost renewable energy sources, thanks to its high power density; second, the wave energy is more predictable than other renewable energy source, such as solar and wind energy; then, the it is one of the most environmentally ways to generate electricity, hence it does not produce any waste; finally, the wave energy conversion devices can be located far enough away from the shore (offshore) in order they are generally not visible.

The fundamental principle behind absorbing energy from a water wave is that energy must be removed from that wave. It therefore follows that the resultant wave, after passing the wave energy device, is either reduced or cancelled altogether. For the device to remove energy from the wave, it is necessary for the resultant wave to be smaller than the incoming wave, and hence the two waves interfere destructively. If a device is to be a good wave absorber it must therefore inherently be a good wave maker.

A symmetrical body constrained such that it may only oscillate in one plane, either perpendicular or parallel to the water surface, is only able to absorb a maximum of 50% of the energy contained in an incident wave [30]. It hence shows the effect of a wave energy converter (WEC) being allowed to move in two degrees of freedom. The wave approaching the device is unaltered from the original wave, as the effects of the body corresponding to its degrees of freedom cancel each other out. After passing the WEC, however, these effects are summated and equal in magnitude to the original wave. Thus, in order to absorb from the approaching wave the theoretical ideal of 100 % energy, a device with two degrees of freedom is required.

Different topologies for wave energy converter are reported in Figure 1.9. The simplest way to convert the wave energy is through a floating buoy lifted-dropped by the waves connected directly to the linear generator fixed on a concrete foundation, which stands on the bottom of the sea (as shown in Figure 1.9a) [31].

The power generation is provided by linear oscillating of buoy between wave top and wave bottom. By optimizing the shape and operation of the buoy, up to 90% efficiency can be achieved with such devices.

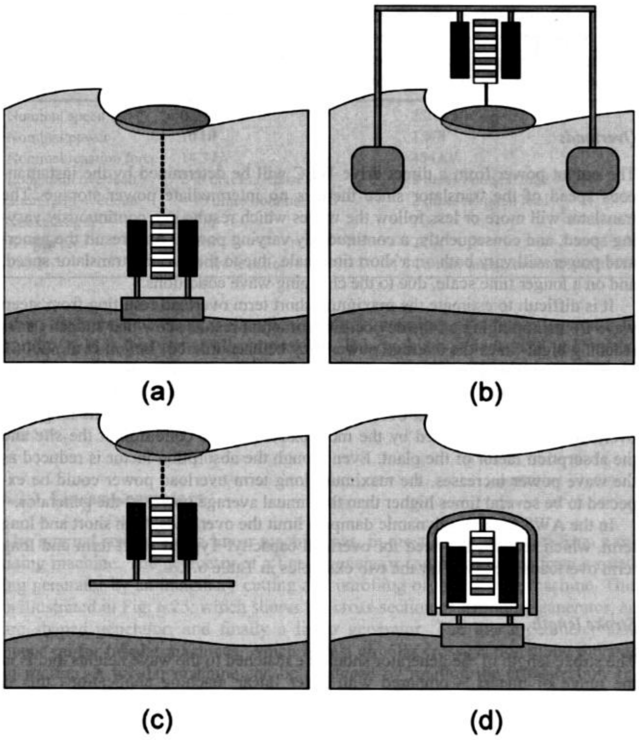

Figure 1.9. *Various solutions for placing the linear generator WEC components.*

Linear generator extracts the power of the waves in the form of a reciprocating motion a low speed and high torque. The linear generator is connected to the grid by a power electronic converter, which is able to process the electric waveform.

Since the linear generator is located at the sea bottom, in a hard to access place, it has to be maintenance free. Furthermore, in order to have as low mass and volume as possible, high values of force density must achieve.

The main features of linear generator depend on the characteristics of the waves in the specified area, generally the common values are [28, 32]:

- power of a few kWs;
- speed up to 1 m/s;
- stroke under 1 m.

These features are achieved by means the use of permanent magnets and tubular linear generator topology.

In literature mainly the following linear generators are proposed for wave energy converting power plants:

- linear permanent magnet synchronous machines, with surface as well as buried permanent magnets [33];
- Vernier hybrid linear machines [34, 35];
- air cored permanent magnet tubular linear machines [36, 37].

1.2 Linear generators

Electrical machines are almost exclusively of a rotary configuration, primarily due to their application. Notable exceptions to this, where some research has been performed, are for transportation purposes (levitating high speed trains, 'Maglev'), projectile launchers or small biomedical actuators. These are all high speed operations, with the electrical machine acting as an actuator / motor.

For the applications presented in the previous chapters, the concept of a linear machine offers the opportunity to simplify the mechanics of the system if it can be used as a slow speed generator. The guiding principles for rotary and linear machines are identical, simply in a different plane of motion. As such, all equations describing a rotary machine are equally applicable to a linear machine, with the slight modification of some terms, such as torque to force. Conceptually, a linear machine can be thought of as the circumference of its rotary counterpart flattened out.

The power absorbed by a linear machine is equal to the product of the reactive force it can deliver and the velocity at which it is displaced. In order to develop greater power for a given velocity, therefore, it is necessary to be able to exert a greater force and thus a high current.

Due to strictly dynamic constraints, the mover iron core mass should be smaller as possible, consequently the mover yoke saturation is generally not negligible [16].

Of the various linear machine topologies which might be employed to convert the kinetic energy into electric energy, tubular configuration is the most interesting solution since it has zero net radial force between mover and stator, no end-windings and volumetrically efficient. One of the disadvantages of tubular topology is the lamination. Because the magnetic flux lines are parallel to the movement direction, mounting the lamination perpendicular to the machine shaft would mean that the magnetic flux should pass from one lamination to the next trough the insulation, resulting a large equivalent air-gap and poor performance, due to high losses. For this reason the lamination should be placed parallel to the translator shaft, raising the problem of aligning them in the air-gap, where they would come in contact, while at the outer part of the stator a gap would appear between adjacent laminations, resulting in a complicated construction process with high costs. Different solutions were taken into account to solve this problem. The first possibility is to use, for the stator core, of molded powder materials, such as soft magnetic composites (SMC). These kinds of materials allow a simple construction of stator core by join different pieces of SMC material. This solution allows, using a simple ring structure as coil, to achieve a high modularity solution. Another way to solve the problem is to replace the tubular topology with a structure with more statoric parts (from 2 to 8), mounted around the translator (Figure 1.10) [38]. Increasing the number of stator parts, the approximation to the tubular structure is more accurate, but it involves a higher cost.

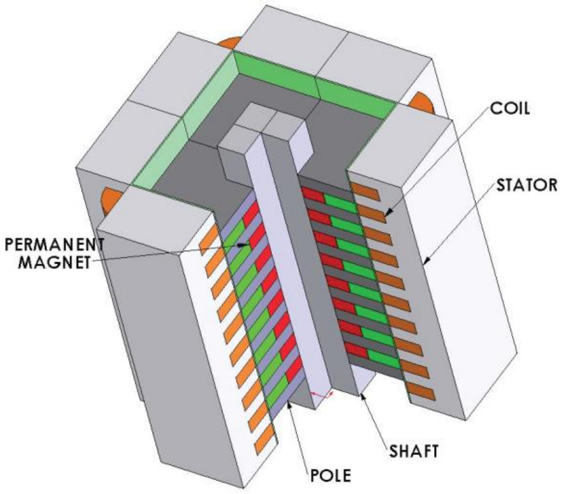

Figure 1.10. *Four-sided linear generators.*

The permanent magnets allow achieving high efficiency, power density and lighter moving part. However, the uses of PMs require a more sophisticated temperature study. There are different ways to magnetize the permanent magnet: radial magnetization, Halbach magnetization and quasi-Halbach magnetization are the most common solutions.

- *Radial magnetization*: is the simplest kind of magnetization. The advantages are the production low-cost cost and the high modularity, the drawbacks are the high values of cogging force and the high value of the back iron mover saturation;
- *Halbach magnetization*: this kind of magnetization is provided by a radial and axial sinusoidal magnetization (as shown in Figure 1.11a), this involves a lower harmonic content. In this case it is generally possible to remove the ferro-magnetic back iron as the axially magnetized magnets essentially provide a return path for the radial air-gap flux, for this reason the moving part results lighter and thus it is possible achieving higher mechanical dynamic. On the other hand, Halbach magnetization does not allow to achieve the same values of linkage flux with the same amount of PM material respect to radial magnetization, furthermore this solution is generally more expensive than the previous one;

- *Quasi-Halbach magnetization*: this kind of magnetization is provided by a radial and axial square wave magnetization pattern (as shown in Figure 1.11b). This solution finds place between the previous two, as it should be possible to remove the ferro-magnetic back iron and it results in a quite simple construction process as well.

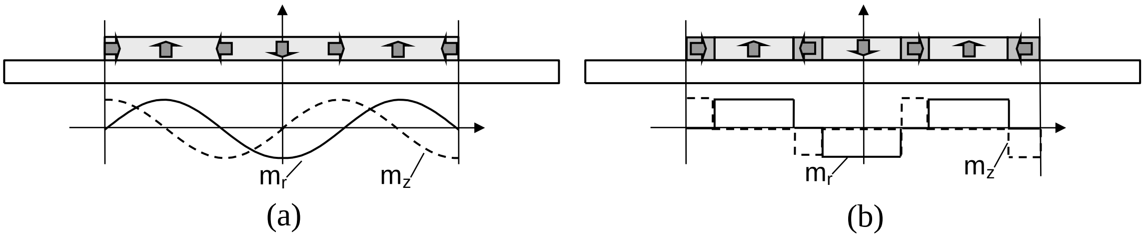

(a) (b)

Figure 1.11. *Halbach magnetization* (a) *and quasi-Halbach magnetization* (b).

1.3 Scope of research

The scope of this research can be summarised as analysis and optimization of linear generators for renewable energy applications, particularly focused on free-piston Stirling engine (FPSE) cogeneration systems. Another topic of this research activity is to develop the dynamic model of the whole cogeneration system, composed by external combustion engine (ECE), linear generator and power electric converter. More specifically, the aim of this thesis is, firstly, to develop a model of linear generator able to describe the behaviour of the machine, in terms of force, flux linkage, electromotive force, losses and efficiency. Then, a parametric analysis, in terms of magnetization pattern, current supply strategy and iron core materials, is carried out in order to optimize the linear generator performance. Finally, a dynamic model of the whole cogeneration system is developed with the aims to describe the dynamic operating condition of the system and achieve the best operation condition, in terms of mechanical parameter (i.e. spring constant) values, oscillating frequency and control strategy. The mathematical model was checked out by some experimental tests, aims to identify more accurately the material magnetic properties, since results evidenced remarkably poorer characteristics with respect to the material reference datasheets, likely due to manufacturing processes.

1.4 Methodology adopted

Analytical models [39-41] would allow to achieve a good parameter estimation, but the complexity of geometry and the several parameter quantity that have to change advise against the use of such kind of models for optimization point of view. Besides, such kinds of models often do not take into account the iron core saturation phenomena, but usually not negligible. On the other hand, finite element analysis (FEA) generally requires a greater computational effort and time consumption for preliminary machine design point of view.

The solution to such problem is given by a semi-analytic model [39], in which a suitable number of FEA is carried out in order to study any linear generator configuration. In order to reduce the computational effort, an approach combining harmonic decomposition and automated magnetostatic FEA sequences (HFEA) is proposed in this thesis. The proposed method allows to simulate the PM motion, different magnetization profiles and different supply strategies, by analysing fixed magnetization space harmonic distributions. The mover saturation, generally not negligible, is taking into account by a suitable number of current sheets on the mover yoke surface, which reproduce the equivalent magnetic permeability decay due to magnetic saturation. The field solution is obtained by superposing the effect of each magnetization space harmonic, the effect of current coil and the effect of equivalent current sheet. The mover axial force is calculated through Maxwell stress tensor evaluation, by radial and axial component of the flux density on the air gap.

The proposed method allows, once carried out FEAs for different magnetization harmonic order and stored the radial and axial component of the air gap flux density, to evaluate the machine performance for different magnetization and supply strategy. Another feature of the proposed method is the possibility to carry out a performance optimization of the machine, adjusting the magnetization profile as well as the current supply waveform.

The efficiency can be estimated as well by evaluating the flux density in some point inside the stator and mover iron cores, in order to calculate the iron core losses.

Finally, a dynamic model of the whole cogeneration system, arranged by free-piston engine (Stirling engine), linear generator and possibly by an electronic power converter, was developed. The dynamic model has a double purpose: one the one hand allows to study the dynamic performances of the system, on the other hand allows optimizing the system in order to achieve the best performances under given constraints. The latter point is an important challenge because the cogeneration system design should be done on the Stirling engine – linear generator system due to their very strict connection.

1.5 Thesis structure

In the chapter 2 a literature review is presented. The state of art is important in order to understand in which point the research activity have to focus. Chapter 3 describes the Stirling engine features and the working principle. Particularly, it focuses the attention on different engine typologies in order to understand which is the best configuration. Chapter 3 presents the advantages and disadvantage of a Stirling engine. Free-piston configuration is described. Chapter 4 describes the linear generator theory. Different typologies and configurations are discussed. The main features of tubular permanent magnet linear generator are pointed out. Chapter 5 presents the research activity focusing the attention on linear generator models utilised to design and optimize the machine. The electromagnetic parameters take into account for a parametric optimization are the magnetization profile, the current supply strategy and the ferro-magnetic materials utilised for iron cores. Then some experimental tests are carried out in order to describe the real behaviour of the permanent magnets and of the iron core materials, which generally may differ to manufacturer data-sheet values. Finally a dynamic model is developed in order to describe the dynamic behaviour of the whole cogeneration system and carry out an optimization. Chapter 6 concludes the thesis by providing an overview of the work carried out in this research listing also possible future work.

Chapter 2

Stirling engines

2.1 Introduction

The Stirling engine (shown in Figure 2.1), sometimes called hot-air engine, converts thermal energy into mechanical energy. It was invented by Robert Stirling in 1816. It is a closed cycle regenerative engine that compresses a fixed amount of working gas at low temperature and then, after heating, expands the gas at high temperature. By cooling the expanded gas it completes the cycle. Since the expansion at high temperature gives a larger amount of work than is consumed by the compression at low temperature, the result is a net mechanical work.

In order to obtain two regions at different temperatures (low and high), a piston called displacer divide the working space of the engine in two spaces: compression and expansion space. As the high pressure gas expands, it moves another piston called power piston, hence doing work. After the gas is expanded, the power piston compresses it by moving inward.

There are three heat exchangers between the compression (cold) and expansion (hot) spaces: cooler, regenerator and heater. The cooler and the heater are used for more effective cooling and heating of the working gas. They bring the gas at compression and expansion temperatures respectively, before it enters these spaces. The regenerator is a heat store, generally made of fine wires in the form of matrix. It captures the heat from the expanded hot gas that flows from the expansion space to the compression space and returns it to the compressed cold gas when it flows back to the expansion space from compression space. This method allows saving a considerable amount of heat energy and thus increasing the engine efficiency.

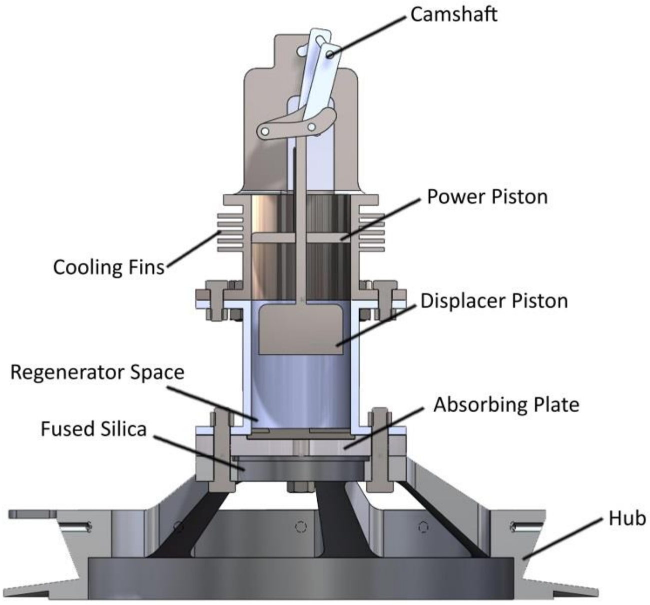

Figure 2.1. *Stirling Engine cross-section.*

Stirling engines working theoretically on the Stirling cycle, or its modifications, in which compressible fluids, such as air, hydrogen, helium, nitrogen or even vapours, are used as working fluids. The Stirling engine offers possibility for having high efficiency engine with less exhaust emissions in comparison with the internal combustion engine. The earlier Stirling engines were huge and inefficient. However, over a period of time, a number of new Stirling engine models have been developed to improve the deficiencies. The modern Stirling engine is more efficient than the early engines and can use any high temperature heat source. Since the Stirling engine is an external combustion engine, most sources of heat can power it (multi-fuel working), including combustion of any combustible material, field waste, rice husk or the like, biomass methane and solar energy. In principle, the Stirling engine is simple in design and construction, and can be operated easily.

The Stirling engine could be used in many applications and is suitable where [42]:

- multi-fuel characteristic is required;
- a very good cooling source is available;
- quiet operation is required;
- relatively low speed operation is permitted;
- constant power output operation is permitted;
- slow changing of engine power output is permitted;
- a long warm-up period is permitted.

From its invention, Stirling engine was used in several different parts of the world, especially in Europe and in the USA, to run a wide variety of appliances including water pumps, cooling fans, sewing machines, laboratory centrifuges and mixers and organ air pumps.

In the beginning of the before century, the Stirling engine was surpassated by the internal combustion engine, which can be easily linked to almost any kind of motor driving systems thanks to its high specific power rate.

A new interest in the Stirling engines was initiated in 1937 by Philips Company. It started a research program to update the old hot-air engine, to produce an electric power generator which could run electronic equipment in remote places. They found out that using, as working fluid, lighter gases then air, such as helium or hydrogen, increase the efficiency and the specific power of the engine.

Further research on Stirling engine was carried out by General Motors in 1958 for space and underwater power systems and vehicle applications. Also the NASA developed several kinds of Stirling engines for aerospace applications. Nowadays, Sunpower Inc. is producing and developing several kinds of Stirling engines.

2.2 Development of Stirling engines

2.2.1 First era of Stirling engines

The Stirling engine was the first invented regenerative cycle heat engine. Robert Stirling patented the Stirling engine in 1816 (patent no. 4081). Engines based upon his invention were built in many forms and sizes until the turn of the century. Because Stirling engines were simple and safe to operate, ran almost silently on any combustible fuel, and were clean and efficient compared to steam engines, they were quite popular [43]. These Stirling engines were small and the power produced from the engine was low (100 W to 4 kW).

In 1853, John Ericsson built a large marine Stirling engine having four 4.2 m diameter pistons with a stroke of 1.5 m producing a brake power of 220 kW at 9 rpm [44]. The first era of the Stirling engine was terminated by the rapid development of the internal combustion engine and electric motor.

2.2.2 Second era of Stirling engines

The second era of the Stirling engine began around 1937 [43], when the Stirling engine was brought to a high state of technological development by the Philips Research Laboratory in Eindhoven, Holland, and has progressed continuously since that time. Initial work was focused on the development of small thermal-power electric generators for radios and similar equipment used in remote areas [2, 4].

New materials were one of the keys to Stirling engine success. The Philips research team used new materials, such as stainless steel [43]. Another key to success was a better knowledge of thermal and fluid physics than in the first era. The specific power of the small ‘102C’ engine of 1952 was 30 times that of the old Stirling engines [46].

The progress in further development made by Philips and many other industrial laboratories, together with the need for more energy resources, has sustained the second era of Stirling engine development until today [43].

2.2.3 Stirling engines for industries

Intensive research by Philips and industrial laboratories led to the development of small Stirling engines with high efficiencies of 30% or more. In 1954, Philips developed an engine using hydrogen as a working fluid. This engine produced 30 kW for a maximum cycle temperature of 977 K at 36% thermal efficiency. The efficiency of the same engine was later improved to 38%. The experimental studies of engines of various sizes up to 336 kW were studied [45].

Other attempts to further develop Stirling engines under license of Philips, were carried out by General Motors from 1958 to 1970 [51]. Other licenses were granted by Philips to United Stirling AB of Malmo, Sweden in 1968 and to the West German consortium of MAN and MWM in 1967 [51]. In 1973, the Philips/Ford 4-125 experimental automotive Stirling engine accomplished a specific power of over 300 times that of the early Stirling engines [44].

2.2.4 Stirling engines for rural and remote areas

Trayser and Eibling [47] carried out a design study to determine the technical feasibility of developing a 50 W portable solar-powered generator for use in remote areas. The results of their study indicate that it is possible to build a solar-powered lightweight portable, reliable, Stirling engine at a reasonable cost.

Gupta et al. [7] developed 1 and 1.9 kW solar-powered reciprocating engines for rural applications. Engine efficiencies were found to be between 5.5 and 5.7% and overall efficiency was found to be 2.02% [49].

Pearch et al. [50] proposed and analysed a 1 kW domestic, combined heat and power (DCHP) system. The results show that 30% of a home’s electrical demand could be generated and electricity cost could be reduced by about 25%.

Podesser [51] designed, constructed and operated a Stirling engine, heated by the flue gas of a biomass furnace, for electricity production in rural villages. With a working gas pressure of 33 bar at 600 rpm and a shaft power of 3.2 kW, an overall efficiency of 25% was obtained. He expected to extend the shaft power to 30 kW in the next step.

Dixit and Ghodke [52] designed compact power generating systems capable of using the combination of a wide variety of solid fuels as a local power source. The system was a heat pipe-based, biomass energy-driven Stirling engine. The macroscopic thermal design of the engine along with the calculation of various energy losses was reported.

2.2.5 Stirling engine optimization

Usually the design point of a Stirling engine will be somewhere between the two limits of: maximum efficiency point and maximum power point. Markman et al. [53] conducted an experiment using the beta-configuration of the Stirling engine to determine the parameters of a 200 W Stirling engine by measuring the thermal-flux and mechanical-power losses. The aim of the project was to optimize and increase the engine efficiency.

Orunov et al. [54] presented a method to calculate the optimum parameters of a single-cylinder Stirling engine. They concluded that mass and size characteristics of the engine could be improved by using the correct choice of the optimal parameters which would result in larger efficiency.

Abdalla and Yacoub [55] studied the feasibility of using waste heat from a refuse incinerator with a Stirling engine. Heat from incineration was used to power the desalination plant and the Stirling engine. Using saline feed raw water as the cooling water and by assuming 50% heat recovery efficiency, they claimed that the engine efficiency could be improved and a thermal efficiency of 27% was obtained.

Nakajima et al. [56] developed a 10 g micro Stirling engine with an approximately 0.05 cm3 piston swept volume. An engine output power of 10 mW at 10 Hz was reported. The problems of scaling down were discussed.

Aramtummaphon [57] tested an open cycle Stirling engines by using steam heated from producer gas. The first engine produced an indicated power of about 1.36 kW at a maximum speed of 950 rpm, while the second engine, improved from the first one, produced an indicated power of about 2.92 kW at a maximum speed of 2200 rpm.

Hirata et al. [58] evaluated the performance of a small 100 W displacer-type Stirling engine Ecoboy-SCM81. An analysis model using an isothermal method considering a pressure loss in the regenerator, a buffer space loss, and a mechanical loss for the prototype engine was developed to improve the engine performance. After the effectiveness of the analysis model was evaluated, some improvements for the prototype engine were discussed.

Costea and Feidt [59] studied the effect of the variation of the overall heat transfer coefficient on the optimum state and on the optimum distribution of the heat transfer surface conductance or area of the Stirling engine heat exchanger. The results pointed out either an optimum variation range for some model parameters, or some significant differences of the power output, source and sink temperature differences, heat transfer characteristic values with respect to each of the studied cases.

Wu et al. [60] analyzed the optimal performance of a Stirling engine. The influences of heat transfer, regeneration time and imperfect regeneration on the optimal performance of the irreversible Stirling engine cycle were discussed. The results of their work provided a new theoretical basis for evaluating performance and improving Stirling engines.

Wu et al. [61] studied the optimal performance of forward and reverse quantum Stirling cycles. The finite time thermodynamic performance bound, optimization criteria and sensitivity analysis were presented. The results showed that the quantum Stirling cycle was different from the classical thermodynamic one. This was because of the different characters of the working fluids.

Wu et al. [62] studied the finite-time exergo-economic optimal performance of a quantum Stirling engine. The maximum exergo-economic profit, the optimal thermal efficiency and power output corresponding to performance bound of an endo-reversible quantum Stirling engine were presented. The result of this work showed a profit bound for designing a real Stirling engine working with a quantum fluid.

Gu et al. [63] attempted to design a high efficiency Stirling engine using a composite working fluid, e.g. two-component fluid: gaseous carrier and phase-change component and single multi-phase fluid, together with supercritical heat recovery process. The results were compared with those of common Stirling engines. The criteria for the choice of working fluid were discussed. Calculation by using sulphur hexafluoride as the working fluid was given as an example to show the thermal efficiency and optimum condensing pressure and temperature.

Winkler and Lorenz [64] described the integration of thin tubular solid oxide fuel cells (SOFCs) and heat engine system. The heat engines investigated were microturbines and Stirling engines. A high system efficiency, low specific volumes, and a small available unit of solid oxide fuel cells was expected from Stirling engine system. Further development for industrial projects was recommended.

Hsu et al. [65] studied the integrated system of a free-piston Stirling engine and an incinerator. The performance of a free-piston Stirling engine was investigated using the averaged heat transfer model. The efficiency and the optimal power output, including the effect induced by internal and external irreversibility, were described.

Petrescu et al. [66] presented a method for calculating the efficiency and power of a Stirling engine. The method was based on the first law of thermodynamics for processes with finite speed and the direct method for closed systems. The results showed good agreement with the actual engine performance obtained from 12 different Stirling engines over a range from economy to maximum power output.

2.3 Development of solar-powered Stirling engines

2.3.1 Solar-powered Stirling engines in the first era

In 1864, Ericsson [67] invented a solar-powered hot air engine using a reflector to heat the displacer cylinder hot-end. Jordan and Ibele [68] reported that between 1864 and 1870, Ericsson used parabolic trough collectors to heat steam and used steam to drive his engine [69]. In 1870, the Stirling engine was adapted by Ericsson to operate with solar energy ([70] cited in Ref. [71]).

Spencer [69] reported that in 1872, Ericsson built an open-cycle hot-air engine using a spherical mirror concentrator. This engine was the first solar-powered hot air engine. It was also reported that the engine could work at 420 rpm at noon on a clear sky day in New York .

Meinel and Meinel [72] commented on the conclusions made by Ericsson pointing out that solar-powered engines would be economical only in remote areas where sunshine was available and pointing out their cost was 10 times higher than conventional engines. The amount of solar-powered Stirling engines built in the first era was quiet small.

Reader and Hooper [73] reported that in 1908 a solar-powered Stirling engine was proposed for a water pumping system.

2.3.2 Solar-powered Stirling engines in the second era

During 1950–1955, Ghai and Khanna worked with an open cycle solar-powered Stirling engine using a parabolic collector in India [45, 49, 71]. The solar energy was focused on the metal engine head but they had problems with heat loss.

Jordan and Ibele [68] described the 100 W solar-powered Stirling engine for water pumping.

Ghai [74] pointed out the point of economy and technical simplicity of a solar powered device even though its competitor was the internal combustion engine.

Later works [75–77] related to solar-powered Stirling engines and heat pipes were previously reviewed by Spencer [49]. Other works concerning the different varieties and arrangements of the cylinder and displacer including construction and operation of solar-powered Stirling engines [71–76] have been reported by Daniels [71]. More details of solar-powered Stirling engines can be found from Jordan and Ibele [68] and Jordan [77].

- ***Stirling engines with transparent quartz window*:** Daniels [71] and Spencer [49] described many research works on solar-powered Stirling engines with transparent quartz windows and related works [47, 79–83]. The problems of this engine could be with the heat transfer and fouling effects. However, Walpita [45] proposed a design for a solar receiver made from a spiral steel tube of 3.175 mm outside diameter for a solar- powered Stirling engine. The heat transfer from solar radiation to the working fluid was analysed and an optimum heat transfer area was obtained.
- ***Stirling engines with concentrating collector*:** the review work on a 15 W solar-powered Stirling engine with concentrating collector was described by Daniels [71]. Other works on Stirling engine with concentrating collectors [83–91] have been comprehensively reviewed by Spencer [90].

  Ahmed et al. [92] reported briefly the operation of a 50 kW solar-powered Stirling engine for electricity production using a single membrane dish concentrator and hydrogen as a working gas. They described the problems of the tracking system due to errors in design and difficulties in starting during the winter season due to improper control part selection.

Childs et al. [93] presented an innovative concept to determine the cost-effectiveness of new approaches to solar-powered desalting technology. These approaches combined modern solar conversion technology with newly developed, hydraulic-driven pumping and energy recovery technology for solar-powered desalting. A solar dish concentrator-Stirling engine electric module, having overall efficiency of 22% for 10 h/day average production, was reported.

Audy et al. [94] reported a solar dynamic power system using a Stirling engine for space station applications. Theoretical models for four different representative orbit configurations were developed. The simulation results were compared to those of a solar dynamic power module using a Brayton gas turbine. Moreover, they showed that the complex unsteady behaviour with either the Brayton cycle or Stirling cycle can be simplified on the basis of parameterizations and energy balances.

- ***Solar dish/engine technology*:** solar dish/engine systems convert solar energy to mechanical energy and then electrical energy. In order to obtain the required temperature for efficient energy conversion, solar dish/engine systems use a mirror array to track the sun. These systems can be characterized by efficiency, modularity, autonomous operation and the capability to work with either a conventional fuel or solar energy. Among many solar technologies, these systems have been accepted to be the systems with the highest solar-to-electrical conversion efficiency [95].

  High-temperature and high-pressure Stirling engines working with hydrogen or helium are normally used in solar dish/Stirling system engines. Modern high performance Stirling engines usually operate with a working fluid temperature of over 973 K and a pressure as high as 200 bar. The efficiencies of conversion from heat to electricity of the best Stirling engines are about 40% [44, 96, 97]. At this moment the kinematic Stirling engines, the Kockums (United Stirling) 4-95 25-kWe, Stirling Thermal Motors STM 4-120 25-kWe, and the SOLO 161 11-kWe are the examples for the engines used for dish/Stirling systems.

  Solar dish/engine technology is one of the oldest solar technologies. In the late 1970s and early 1980s modern solar dish/engine technology was developed by Advanco Corporation, United Stirling AB, McDonnell Douglas Aerospace Corporation (MDA), the US Department of Energy (DOE), and NASA’s Jet Propulsion Laboratory.

It was reported that [95, 98] the Advanco Vanguard system, 25-kWe nominal output module, using the United Stirling Power Conversion Unit (PUC), obtained a solar to electric conversion efficiency of 29.4%. MDA attempted to commercialize a system consisting of their own designed dish and the United Stirling PCU. Before the program was cancelled in 1986, MDA produced eight prototype systems. The rights to the MDA hardware were sold later to Southern California Edison (SCE). In 1988, an annual efficiency of over 23% was expected to be obtained without outages [99–102].

The Dish/Stirling Joint Venture Program (DSJVP) was initiated in 1991 [103]. The aim of the program was to develop a 5–10-kWe dish/Stirling system for applications in remote areas. The Utility Scale Joint Venture Program (USJVP) for 25-kWe dish/engine system was started in late 1993 [105]. The comparably priced systems obtained by the lower-cost stretch-membrane design and its improved operational flexibility were projected by SAIC [106].

The Advanced Dish Development System (ADDS) project plan and technical approach were reported by Diver et al. [106]. The aims of the project were to develop and validate a 9-kWe dish/Stirling solar power system for remote power markets.

The system was composed of the WGAssociates solar concentrator and controls, and the SOLO 161 Stirling power conversion unit. The main system components, features, test results and project status were also reported.

Davenport et al. [107] reported the operational results and experiences from a prototype of the SunDish system at the Salt River Project (SRP). This project was executed through the cooperation of SRP, SAIC, STM, and DOE. The methane gas collected from a landfill was used as fuel when solar energy was not available. They also discussed the design changes and system improvements resulting from operation with the prototype of the SunDish system.

Davenport et al. [108] reported the operation of the second-generation of dish/Stirling power systems (SAIC/STM SunDish systems). Many improvements to both the engine and dish subsystems were made to increase reliability, to improve system performance, to simplify installation, and to correct problems encountered during operation. They reported that the power output was improved from below 20 kW in 1998 to over 23 kW in 2002. An instantaneous peak power of 23.3 kW and efficiency of 26% were observed.

2.3.3 Solar-powered Stirling engine optimization

When a solar collector system is used as a heat input source for power generation, the solar collector and working conditions giving the optimum values of the cost of the system and the optimum power output must be considered. Some theoretical work to optimize solar-powered Stirling engine design was carried out by Umarov et al. [109, 110], however the applications on the engine were not shown in the research papers.

Howell and Bannerot [111] determined the optimum value of the outlet temperature of the solar collector to maximize the work output of Carnot, Stirling, Ericsson, and Brayton cycle engines powered by a solar collector. Eldighidy et al. [112] optimized the conditions for maximum solar energy absorbed by a flat-plate collector used with a plane reflector. A simple flat-plate collector/flat-sheet reflector was analysed completely. Later, Eldighily [113] theoretically investigated the optimum outlet temperatures of the solar collector for the maximum work output for an Otto air-standard cycle with ideal regeneration. This work may be applied to an air-standard Stirling cycle.

Gordon [114] examined the accuracy of the energetic optimization of solar-driven heat engines. The results were obtained for the two limiting cases of maximum efficiency and maximum power. Altfeld et al. [115, 116] minimized the sum of exergy losses, including exergy losses by absorption of radiation at the absorber temperature level by maximizing the net exergy flow. The optimum designs of the absorbers and flow ducts were presented.

Costea et al. [117] studied the effect of pressure losses and actual heat transfer on solar Stirling engine cycle performance. The results indicated that when the engine was operated at the optimum temperature, the real cycle efficiency was approximately half the ideal cycle efficiency.

Chen et al. [118] proposed a non-image focusing heliostat consisting of a number of grouped slave mirrors for solar-powered Stirling engines. An experiment with a low power Stirling engine was reported. They proposed that a solar-powered engine of 20–50 kW was most in demand and would be less costly under stationary conditions.

2.3.4 Development of LTD Stirling engines

Haneman [119] studied the possibility of using air with low temperature sources. An unusual engine, in which the exhaust heat was still sufficiently hot to be useful for other purposes, was constructed. In practice, such an engine would produce only little useful work relative to the collector system size, and would give little gain compared to the additional maintenance required [120].

A simply constructed low temperature heat engine modelled on the Stirling engine configurations was patented in 1983 by White [121]. White suggested improving performance by pressurizing the displacer chamber. Efficiencies were claimed to be around 30%, but this can be regarded as quite high for a low temperature engine.

In 1984, O’Hare [122] patented a device passing cooled and heated streams of air through a heat exchanger for changing the pressure of air inside the bellows. The practical usefulness of this device was not shown in detail as in the case of Haneman’s work.

Kolin [67] experimented with a number of LTD Stirling engines, over a period of many years. In 1983, he presented a model that worked on a temperature difference between the hot and cold ends of the displacer cylinder of as low as 15 °C. After Kolin published his work, Senft [43] made an in-depth study of the Ringbom engine and its derivatives, including the LTD engine. Senft’s research in LTD Stirling engines resulted in the most interesting engine, which had an ultra-low temperature difference of 0.5 °C. It is very difficult to create any development better than this result. Senft’s work [123] showed the principal motivation for Stirling and general heat engines, their target being to develop an engine operating with a temperature difference of 2 °C or lower.

Senft [43] described the design and testing of a small LTD Ringbom Stirling engine powered by a 60° conical reflector. He reported that the 60° test conical reflector producing a hot-end temperature of 93 °C under running conditions, worked very well.

2.4 Mechanical configurations of Stirling engines

Stirling engines can be classified by their drive method: constrained drive (kinematic Stirling engines) and unconstrained drive (free-piston Stirling engines). In the first one typology, the motion of the power piston and the displacer are constrained by cranks and connecting rods. Instead, in the free-piston Stirling engines, the power piston and the displacer are moved by the variation of the pressure of the working gas.

The kinematic Stirling engine can, in turn, be classified in alpha, beta and gamma configuration (Figure 2.2). Each configuration has the same thermodynamic cycle but has different mechanical design characteristics [124].

- ***alpha-configuration***: the displacer is not used. Two pistons, called the hot and cold pistons, are used on either side of the heater, regenerator, and cooler. These pistons move uniformly in the same direction to provide constant-volume heating or cooling processes of the working fluid. When all the working fluid has been transferred into one cylinder, one piston will be fixed and the other piston moves to expand or compress the working fluid. The expansion work is done by the hot piston while the compression work is done by the cold piston.

- ***beta-configuration*****:** the displacer and the power piston are incorporated in the same cylinder. The displacer moves working fluid between the hot space and the cold space of the cylinder through the heater, regenerator, and cooler. The power piston, located at the cold space of the cylinder, compresses the working fluid when the working fluid is in the cold space and expands the working fluid when the working fluid is moved into the hot space.
- ***gamma-configuration*****:** it uses separated cylinders for the displacer and the power pistons, with the power cylinder connected to the displacer cylinder. The displacer moves working fluid between the hot space and the cold space of the displacer cylinder through the heater, regenerator, and cooler. In this configuration, the power piston both compresses and expands the working fluid. The gamma-configuration with double-acting piston arrangement has theoretically the highest possible mechanical efficiency. This configuration also shows good self-pressurization [124]. However, the engine cylinder should be designed in vertical type rather than horizontal in order to reduce bushing friction [126].

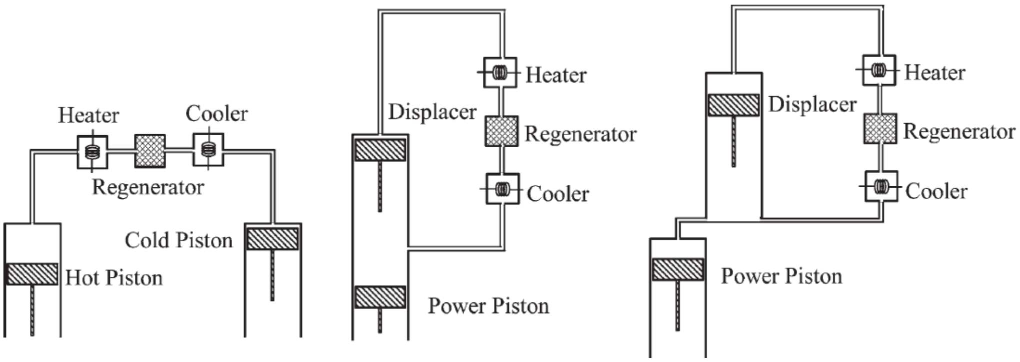

(a) (b) (c)

Figure 2.2. *Stirling engine configurations: alpha (a), beta (b) and gamma (c).*

- ***Free-piston Stirling Engine (FPSE)*****:** In addition to general characteristics of the Stirling engine, the free-piston Stirling engine, shown in Figure 3.3, has its own unique features that make it more appropriate for the use under certain circumstances. These characteristics are:

  - it does not required an external high pressure seal, since it can be hermetically sealed to the environment;
  - it can be produced at low cost, since it has only two moving parts and has no complicated drive mechanism;
  - the power piston and displacer have no loads thanks to the lack of connecting rods, and as a consequence, the engine can operate for a long life without needing lubrication.
  - the FPSE can be made to operate very quietly since all the motions and forces hence the resulting vibrations are in the axial direction to the engine and may be easily isolated.

The FPSE has advantages for operation in remote locations with its potential to run for a long time free from maintenance. For such purpose, FPSE finds applications in all those fields in which maintenance is a problem, such as wave energy converters, army and aerospace applications.

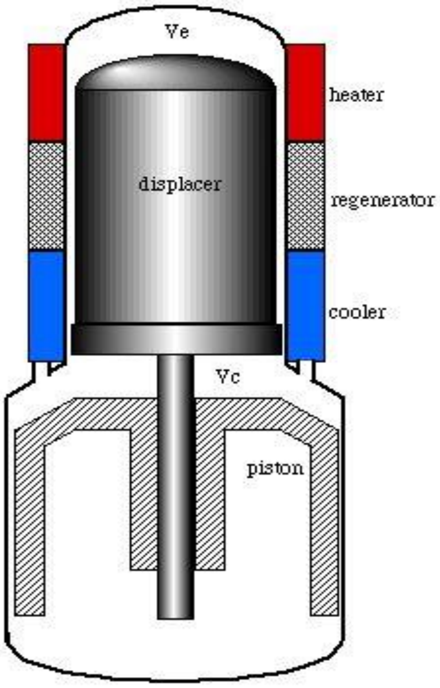

Figure 2.3. *Free-piston Stirling engine.*

- ***Low temperature differential (LTD)*****:** it can be run with small temperature difference between the hot and cold ends of the displacer cylinder [46]. It is different from other types of Stirling-cycle engines, which have a greater temperature difference between the two ends, and therefore the power developed from the engine can be greater. A LTD Stirling engine is shown in Figure 2.4.

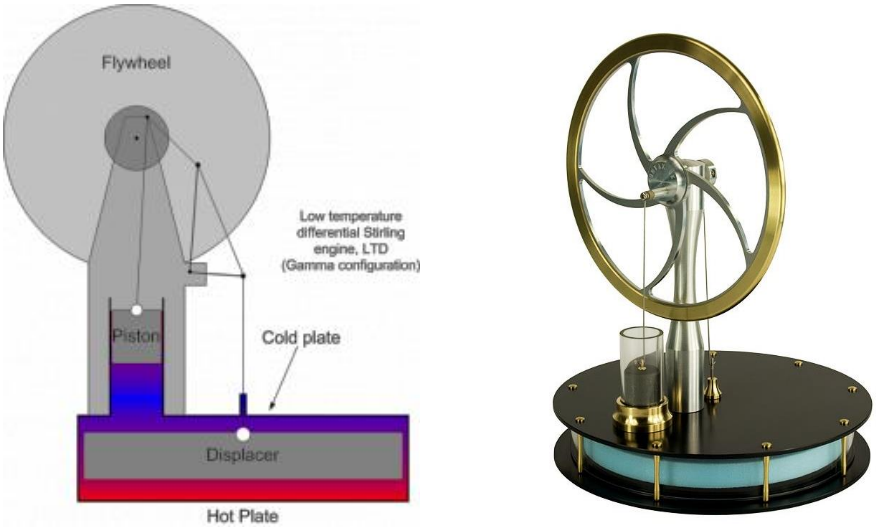

(a) (b)

Figure 2.4. *LTD Stirling Engine:the scheme* (a) *and a prototype* (b).

LTD engines may be of two designs. The first uses single-crank operation where only the power piston is connected to the flywheel, called the Ringbom engine. This type of engine, that has been appearing more frequently, is based on the Ringbom principle. A short, large-diameter displacer rod in a precise-machined fitted guide has been used to replace the displacer connecting rod [67]. The other design is called a kinematic engine, where both the displacer and the power piston are connected to the flywheel. The kinematic engine with a normal 90° phase angle is a gamma-configuration engine [67].

Some characteristics of the LTD Stirling engine are as follows [67]:

- displacer to power piston swept volumes ratio is large;
- diameter of displacer cylinder and displacer is large;
- displacer is short;
- effective heat transfer surfaces on both end plates of the displacer cylinder are large;
- displacer stroke is small;
- dwell period at the end of the displacer stroke is rather longer than the normal Stirling engine;
- operating speed is low.

LTD Stirling engines provide value as demonstration units, but they immediately become of interest when considering the possibility of power generation from many low temperature waste heat sources in which the temperature is less than 100 °C [83]. A calculation using the Carnot cycle formula shows that an engine operating with a source temperature of 100 °C and a sink temperature of 35 °C gives a maximum theoretical thermal efficiency (Carnot efficiency) of about 17.42%. If an engine could be built for achieving 50% of the maximum thermal efficiency, it would have about 8.71% overall Carnot efficiency. Even the calculated thermal efficiency seems rather low, but LTD Stirling engines could be used with free or cheap low temperature sources. This engine should be selected when the low cost engines are put into consideration.

Although the specific power developed by LTD Stirling engines is low, lightweight and cheap materials such as plastics can be used as engine parts.

2.5 Principle of operation

The Stirling hot air engine is a simple type of engine that uses a compressible fluid as the working fluid. Because the working fluid is in a closed system, there are no problems with contamination and working fluid costs. Heat transfer to the working fluid is very important. High mass flow is needed for good heat transfer. The working fluid should be that of low viscosity to reduce pumping losses. Using higher pressure or lower viscosity, or combinations thereof, could reduce the high mass flow required. The Stirling engine could theoretically be a very efficient engine in upgrading from heat to mechanical work with the Carnot efficiency. The thermal limit of the operation of the Stirling engine depends on the material used for construction. Engine efficiency ranges from about 30 to 40% resulting from a typical temperature range of 923–1073 K, and a normal operating speed range from 2000 to 4000 rpm [124].

The ideal Stirling cycle has three theoretical advantages. First, the thermal efficiency of the cycle with ideal regeneration is equal to the Carnot cycle. During the transfer strokes, the regenerator, which is a typical temporary energy storage, rapidly absorbs and releases heat to the working fluid which is passing through. Therefore, the quantity of heat taken from the external heat source is reduced, this results in improving the thermal efficiency (Figure 2.5).

The second advantage, over the Carnot cycle, is obtained by substitution of two isentropic processes with two constant-volume processes. This results in increasing the p–v diagram area. Therefore, a reasonable amount of work from the Stirling cycle is obtained without the necessity to use very high pressures and large swept volumes, as in the Carnot cycle. The Stirling cycle compared with the Carnot cycle between the same given limits of pressure, volume, and temperature, is also shown in Fig. 2.5. The shaded areas 2C-2-3 and 1-4C-4 indicate the additional work available by replacing two isentropic processes with two constant-volume processes. The Carnot cycle isothermal processes (1-2C and 3-4C) are, respectively, extended to process 1–2 and 3–4. The amount of available work is increased in the same proportion as the heat supplied to—and rejected from—the Stirling cycle [44].

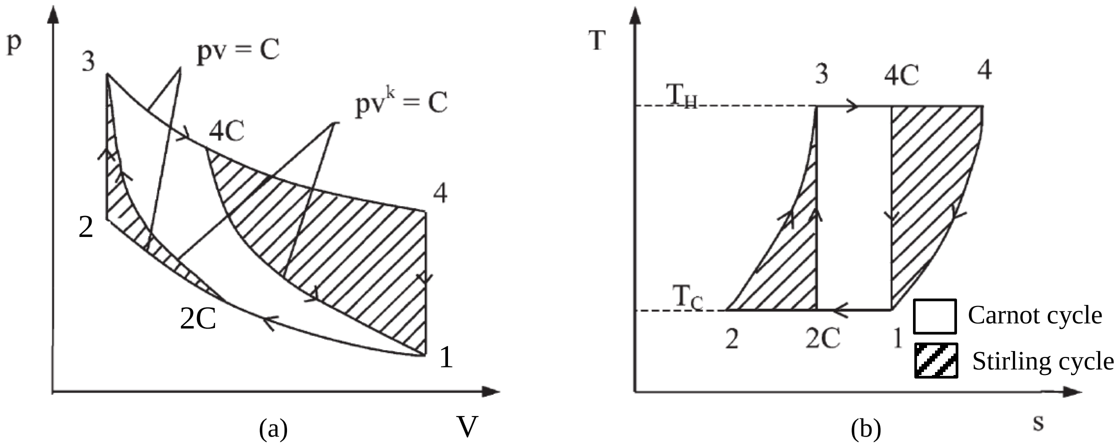

(a) (b)

Figure 2.5. *Comparison between Stirling and Carnot cycles: p-V* (a) *and T-s* (b) *diagrams.*

The third advantage has recently been discovered. Compared with all reciprocal piston heat engines working at the same temperature limits, the same volume ratios, the same mass of ideal working fluid, the same external pressure, and mechanism of the same overall effectiveness, the ideal Stirling engine has the maximum possible mechanical efficiency [43]. These three advantages reveal that the Stirling engine is a theoretical equivalent of all heat engines [43].

The Stirling engine operation can be described as follow (Figure 2.6):

- **Isothermal compression process 1–2 (heat transfer from working fluid at low temperature to an external sink)** (Figure 2.6*a*)**:** After the displacer has pushed the working fluid into the cold space of the cylinder, where it was cooled, it was then held stationary at its top dead center (TDC). This indicated the state 1 and the pressure at this state is p1. The power piston is then being pushed from bottom dead center (BDC) to TDC by flywheel momentum helped by partial vacuum created by the cooling working fluid. The working fluid is in the cold space and is under compression by power piston, which is approaching TDC, and compressing working fluid from 1 to 2 at constant temperature. The work done on the working fluid indicated by the area under process 1–2.
- **Constant-volume heating process 2–3 (heat transfer to the working fluid from regenerator)** (Figure 2.6*b*)**:** The displacer is moving from TDC to BDC

and transferring working fluid from the cold space to the hot space, while the power piston remains stationary at its TDC, awaiting increase in pressure as a result of expanding working fluid. The displacer is pushing the working fluid into the hot space, passing through a regenerator which has stored heat, and already a certain amount is being heated. Heat given up by the regenerator raises the temperature and pressure of the working fluid from 2 to 3 at constant volume. Heat stored in the regenerator is added to the working fluid.

- **Isothermal expansion process 3–4 (heat transfer to the working fluid at high temperature supplied by an external source)** (Figure 2.6*c*)**:** After the displacer has pushed all the working fluid into the hot space, with a corresponding increase in pressure to the maximum, it is then kept at rest at its BDC. The working fluid is in the hot space and is expanding to pressure p4, while a constant temperature process 3–4 is maintained applied at the hot space. The power piston is being pushed from TDC to BDC by the increased pressure, and is applying force to the flywheel, thus creating mechanical energy. This energy will be utilized throughout the remaining processes of the cycle. The work done by the working fluid is indicated by the area under process 3–4.
- **Constant-volume cooling process 4–1 (heat transfer from the working fluid to the regenerator)** (Figure 2.6*d*)**:** After the power piston has reached its BDC and has supplied its energy to the flywheel, it remains stationary and is ready to travel back to TDC under flywheel momentum and the sucking action of the partial vacuum created by the falling pressure. The displacer is moving from BDC to TDC and is transferring working fluid to the cold space where the pressure will fall and a partial vacuum is created, through the regenerator, causing a fall in temperature and pressure of the working fluid from 4 to 1 at constant volume. Heat is transferred from the working fluid to the regenerator.

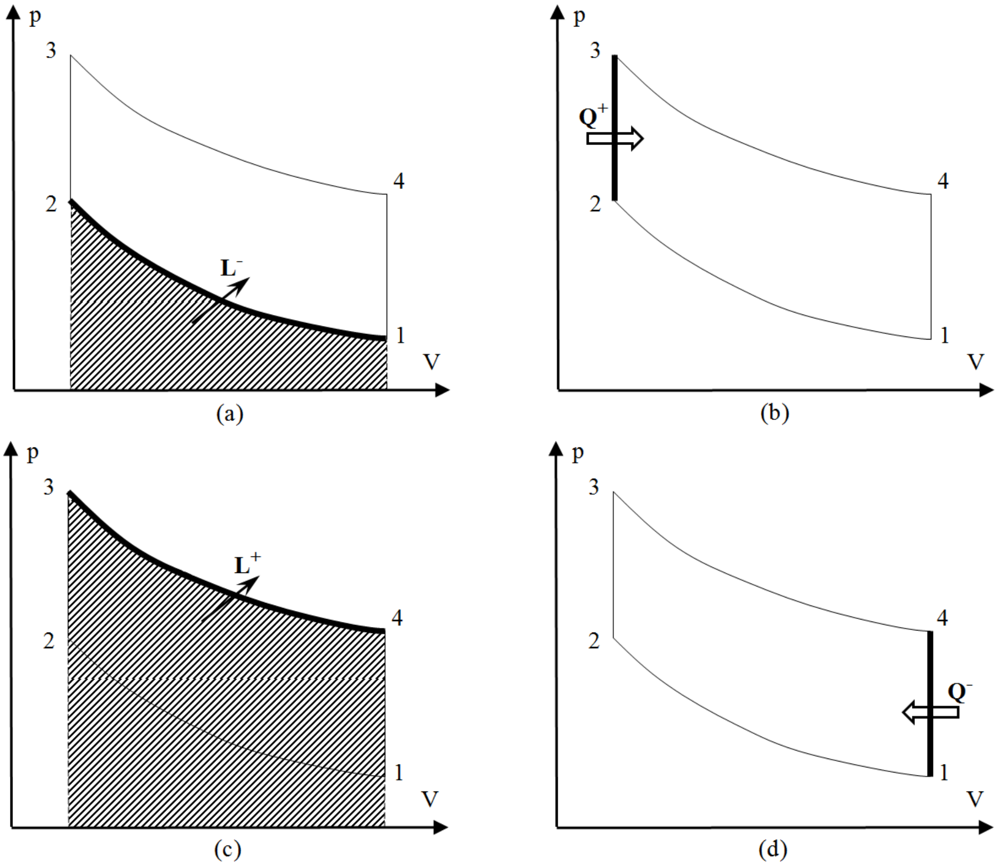

Figure 2.6. *Stirling engine operation process: isothermal compression* (a), *constant-volume heating* (b), *isothermal expansion* (c), *constant-volume cooling* (d).

For an air-standard Stirling cycle, the amounts of heat added Q^+ and rejected Q^- per unit mass of working fluid [J/kg] are as follows [111]:

$$Q^+ = xc_v(T_h - T_c) + RT_h \ln\frac{v_1}{v_2} \tag{2.1}$$

$$Q^- = xc_v(T_c - T_h) + RT_c \ln\frac{v_2}{v_1} \tag{2.2}$$

where x is the fractional deviation from ideal regeneration ($x = 1$ for no regeneration and $x = 0$ for ideal regeneration), c_v is the specific heat capacity at constant volume [J/kgK], T_h is the source (heater) temperature in the Stirling cycle [K], T_c is the sink (cooler) temperature [K], R is the gas constant [J/kgK], v_1 and v_2 are the specific volumes of the constant-volume regeneration processes of the cycle [m^3/kg], respectively.

The Stirling cycle efficiency η_s can be expressed as [111]:

$$\eta_s = \frac{Q^+ + Q^-}{Q^+} = \frac{(T_h - T_c)R\ln\frac{v_1}{v_2}}{xc_v(T_h - T_c) + RT_h\ln\frac{v_1}{v_2}} = \frac{1 - \frac{1}{\theta}}{1 + C_s\left(1 - \frac{1}{\theta}\right)} \tag{2.3}$$

where $\theta = \frac{T_h}{T_c}$ and $C_s = \frac{x c_v}{R \ln\frac{v_1}{v_2}}$.

Equation (2.3) shows that the efficiency is rated to source and sick temperatures and the volume compression ratio $\frac{v_1}{v_2}$, particularly the efficiency increase if increase the temperature differential between heater and cooler or the volume compression ratio.

Beale [15] noted that the power output of several Stirling engines observed could be calculated approximately from the equation:

$$P_{out} = 0.015\, p_m\, f\, V_p \tag{2.4}$$

where P_{out} is the engine power output [W], p_m the mean cycle pressure [bar], f the cycle frequency [Hz], and V_p is displacement of power piston [cm^3]. The Beale formula can be used for all configurations and for various sizes of Stirling engines.

Equation (2.4) may be written in a general form as follows:

$$\frac{P_{out}}{p_m\, f\, V_p} = costant \tag{2.5}$$

The resulting dimensionless parameter $P_{out}/p_m\, f\, V_p$ is called the Beale number. It is clear that the Beale number is a function of both source and sinks temperatures. The solid line in Figure 2.7 indicates the relationship between the Beale number and source temperature. The upper bound represents the high efficiency, well-designed engines with low sink temperatures, while the lower bound represents the moderate efficiency, less well-designed engines with high sink temperatures [15].

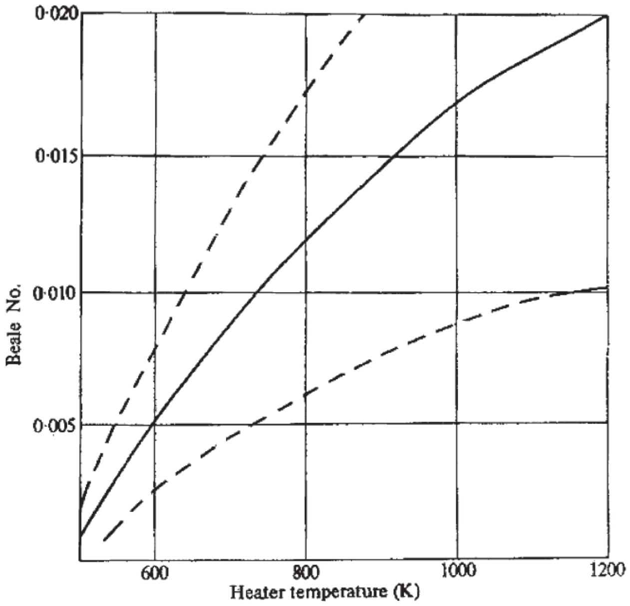

Figure 2.7. *Beale number as a function of source temperature [44].*

2.6 Analytical models of Stirling engine

Models used for calculation of the working process and performance of Stirling engines can be classified as of empirical, analytical and numerical types.

2.6.1 Empirical modelling

A number of studies were performed to develop the empirical correlations for the estimation of the engine power output and the engine efficiency.

West [125] proposed to use a dimensionless parameter called Beale number to predict the engine power (named after Prof. William Beale).

The Beale number is defined in terms of a Stirling engine's operating parameters:

$$B_n = \frac{P_{out}}{p_m \, f \, V_p} \tag{2.6}$$

where B_n is the Beale number [-], P_{out} is the power output of the engine [W], p_m is the mean average gas pressure [bar], f is the engine cycle frequency [Hz] and V_p is swept volume of the power piston [cm^3].

The Beale number with value of 0.015 was suggested to use for a wide range of Stirling engines with different configurations. To take into account the effect of the temperature range in the working cycle, West proposed to introduce into the Beale number the empirical factor F of 0.035 to more accurately calculate the engine's power output. Senft in [126] recommended that for LTD Stirling engines the greater value of the factor F is required to improve the accuracy of predictions.

To find an appropriate correlation for calculating the power output of the LTD Stirling engine of the gamma configuration, Kongtragool and Wongwises in [127] investigated the experimental performance of the engine. They came to the conclusion that the Beale's formula was not valid for conditions in which there were the high temperature ratio. However, they recommended that the original Beale formula and the mean pressure based power output formula with a certain magnitude of the factor F would make it possible to accurately predict the engine's power output.

Other example of development of an empirical correlation for prediction power out of Stirling engines include works of Prieto et al. [128] and Prieto et al. [129]. They analysed a wide range of experimental results and applied methods of the dynamic similarity and quasi-static simulations for various LTD and HTD Stirling engines. To improve the accuracy of predictions of the indicated power of Stirling engines, Prieto and Stefanovskiy [128] used dimensionless analysis to characterise the gas leakage and mechanical power losses. The dimensionless mechanical power losses were determined using the empirical data. Several Stirling engines were modelled using this dimensionless analysis. In [129] Prieto et al. found that such the correlation based on dimensionless analysis of the engine’s working process and different losses in the cycle provided more accurate prediction of the performance of three LTD Stirling engines compared to that obtained using the modified Kolin's model.

2.6.2 Thermodynamic modelling

Numerous mathematical models based on thermodynamic theory have been developed for studying different designs of Stirling engines and their cycles. These models were classified in [130-132] by splitting them in a big number of groups using various criteria. In these investigations, however, the models are categorised into one-dimensional and multi-dimensional model. In turn, one-dimensional model of Stirling engines is subdivided into three subgroups called the first, the second and third-order models.

- ***One-dimensional first-order models*:** the first-order models are based on algebraic equations of mass and energy conservation equations applied to describe the working process of Stirling engines and such approach allows us to obtain analytical equations to estimate power output and efficiency of machines.

  Schmidt model described in [56] was the first in the series of the first-order models and this model made it possible to derive analytical equation [57] to describe pressure variations in the cycle assuming that an engine’s space could be presented as three main spaces, namely the compression space, the expansion space and the dead volume. It was assumed that processes in each of these spaces take place at a corresponding constant temperature levels.

  Toda et al. [58] presented a model which takes into account the effectiveness of the drive mechanism in the Schmidt theory to analyse the engine performance of the LTD Stirling engine of a gamma configuration. The results of experiments on a 10 kW LTD Stirling engine demonstrated that the mechanical effectiveness of the engine has a strong influence on the shaft power of engine.
- ***One-dimensional second-order models*:** the second-order models are superior to the first-order thermodynamic models. Such the models may generally be based on Schmidt analysis. Usually, an engine’s internal gas volume is separated into several spaces. For each space a set of ordinary differential equations of the mass and

energy conservation are used to describe heat and mass transfer processes. Various heat and the pressure losses occurring in real engines are taken into account in the model for a more accurate prediction of the engine’s performance.

Martini [132] presented such the isothermal model based on Schmidt theory and taking into account heat losses and pressure losses. The temperatures of hot and cold gases were obtained by taking into account temperature drops in the heater and cooler. Numerical predictions for the GPU-3 Stirling engine had the 20 % error compared to experimental results.

The first second-order model using an adiabatic analysis was developed by Finkelstein in 1960 and described in [79]. The model defined as adiabatic compression and expansion spaces whilst all heat exchangers were treated as perfect heat exchangers with isothermal processes. Urieli and Berchowitz [138] described the further development of the adiabatic model by Finkelstein. The model was implemented as a computer code and corresponding differential equations were solved using the fourth-order Runge-Kutta method. Additionally, to improve numerical predictions, Urieli and Berchowitz [138] developed a so-called Simple analysis which in fact was the adiabatic model with incorporated non-ideal heat exchangers. Isothermal processes were still assumed in all heat exchangers but the heater’s and cooler’s gas temperatures were then recalculated applying the heat transfer equations.

There have been some Stirling engine models developed based on the Simple analysis approach. Abbas et al. [139] developed method based on the Simple model taking into account a presence of a non-ideal regenerator. The regenerator space was divided into two parts in this work and the model also included calculation of various losses such as the shuttle loss, regenerator loss, regenerator wall heat conduction and pumping loss. The work loss due to a pressure drop was subtracted from the indicated work. Another model using the Simple analysis was developed by Strauss and Dobson [140] in which the pumping work loss and regenerator heat loss described in Urieli [141] were evaluated. The original method to include into calculations the regenerator wall heat conduction was described in this paper. Heat losses and the pumping work loss were included into the value of the rejected heat in the cooler. This caused the reduction of the pressure inside the engine and of the power output. When compared to experimental data, the model demonstrated a good accuracy in predicting performance of the General Motor GPU-3 Stirling engine.

In addition to the Simple analysis method, the quasi steady flow model of Stirling engines was published by Urieli and Berchowitz in [138]. The concept of non-ideal heat exchanger was realised and introduced into the calculation procedure. The heat exchanger wall temperature was defined as a constant during operation of the machine. The model required the use of heat transfer correlations. The fourth-order Runge-Kutta technique was used to solve a set of ordinary differential equations. The pressure drop in heat exchangers was determined and it rectified pressure values in the expansion and compression spaces. Urieli and Berchowitz [138] validated the model with experimental data for the General Motor GPU-3 Stirling engine and reported an improved accuracy of predictions compared to the Simple analysis method.

Several mathematical models for Stirling engines were developed based on the quasi steady flow approach. Thus such models were developed for analysis of the SOLO 161 Stirling engine with the alpha configuration to be used in the Eurodish 10 kWe dish/Stirling system by Granodos et al. [142] and Nepveu et al. [143]. Granodos et al. [142] developed their model which is combined with calculations of the cavity type receiver in MATLAB. In this study the engine’s volume was split into 19 control volumes with ten control volumes being allocated to the regenerator. The developed quasi steady flow model took into account the pressure drop in the channels of heat exchangers. The model developed by Nepveu et al. [143] considered 32 control volumes in the engine’s gas circuit with the regenerator being split into 8 control volumes. As in the previous case, the model described in [143] also coupled to calculations of the heat receiver. This model’s validation was carried out using experimental results obtained by Reinalter et al. [144] on the Eurodish 10 kWe dish/Stirling unit installed at the CNRS-PROME laboratory, France. Parlak et al. [145] analysed the performance of a gamma-type Stirling engine using the developed model based on the quasi steady flow approach. The procedure for determination of the pressure in each working space using the values of the calculated pressure drop was main feature of the model. For calculations of medium temperature difference engines, Tlili et al. [146] developed the second-order adiabatic mathematical model based on the quasi steady flow approach described by Urieli and Berchowitz [148]. They called this the Dynamic model and in the modelling procedure took into account various thermal losses and pressure drops in each component of a MTD Stirling engine. The losses included the energy dissipation due to the pressure drop in all heat exchanges, internal and external conduction losses in the regenerator and shuttle losses caused by reciprocating motion of a displacer. The gas spring hysteresis losses in the compression and expansion spaces were taken into account to improve predictions of the engine performance by Timoumi et al. [147]. In this paper authors also used for calibration experimental data obtained from the General Motor GPU-3 Stirling engine and reported that there was a good correlation between the numerical and experimental results.

Schulz and Schwendig [148] described a mathematical model for simulation of Stirling engines. The pressure drop and heat transfer in the oscillating flow of gas through the heat exchanger were considered at turbulent flow conditions. The ordinary differential equations for each control volume of a Stirling engine were presented and the real gas state equation was used in the model. The absolute value of Nusselt number for laminar and turbulent flow conditions were calculated in the modelling process. It was found that there was a good agreement when theoretical results were compared to experimental data for a Vuilleumier engine.

Mahkamov and Ingham [149] analysed the working process and influence of mechanical losses in a 1-kW solar Stirling engine of an alpha configuration. The second-order mathematical model which considered the hydraulic losses and heat transfer in all control volumes. For the determination of the mechanical losses, cycle variations in the frictional force between the sealing ring and the cylinder (single and double sealing rings), in the sealing of the shaft, the frictional torque in all rolling bearings and the aerodynamic resistance of a flywheel were calculated. As a result of simulations, the predicted indicated power of 3190 W and the brake power of 1585 W were obtained. It was shown that total mechanical losses in the Stirling engine were approximately 50 % of the indicated power.

Ataer and Karabulut in [150] presented a mathematical model for analysis of a V-type Stirling-cycle refrigerator which does not take into account the pressure drop in the cycle. The machine was split into fourteen control volumes and the mass and energy conservation equations were written for each volume. The constant heat transfer coefficient was used to calculate heat transfer in the cooler and heater. Karabulut et al. [151] further developed the model by adding a set of kinematic equations to analyse a Stirling engine with a concentric piston and displacer. However, the constant heat transfer coefficient was still used when considering heat transfer on heater and cooler surfaces.

Anderson et al. [152] developed a Stirling engine model with 13 control volumes with ordinary differential energy and mass conservation equations written for each volume. The model validation was carried out using a 9 kW Stirling engine and there was an acceptable agreement in numerical predictions.

Several mathematical models of LTD Stirling engines were developed which took into account differences in their design compared to conventional Stirling engines. Martaj et al. [153] carried out thermodynamic study of a LTD Stirling engine using the steady state energy, entropy and exergy analysis. The engine was divided into three isothermal cells, namely the heating, cooling and regenerator cells and these were analysed using energy, mass, entropy and exergy balance equations. It was found that the thermal and exergy efficiencies for the whole machine were inversely proportional to the regenerator's dead volume. They found that there was an acceptable agreement between calculated and experimental work outputs for the engine operating with a rotational speed of 199 rpm. Robson et al. [154] developed a mathematical model of a LTD Ringbom Stirling engine which describes parameters of the gas in expansion and compression spaces and in a regenerator. The model takes into account a power piston that is connected to the flywheel with a displacer being a free piston. The mass and energy conservation differential equations for gas in each space were applied. Kinematical and kinetic equations of the transmission mechanism were used to describe the characteristics of piston motions and to determine the engine’s power output. The pressure variation description obtained using the developed mathematical model was in a good correlation with experimental results obtained on the LTD Stirling engine designed by Senft. However, it was concluded that in this model a very small time step is necessary during integration of equations to obtain convergence in the simulation of the unsteady behaviour of the engine.

- ***One-dimensional third-order models*****:** the third-order model is more complex compared to the second-order one and needs much more intensive numerical calculations. In the third-order model mass, volume and momentum equations are written for several control volumes of the gas circuit of the engine in the form of partial differential equations.

  Examples of such models are reviewed by Dyson et al. [155] and Anderson [156]. GLIMPS is the simulation code developed by Gedeon in 1986 and based on a third-order model. The 2D finite difference grid in terms of time and space was used to solve the mass, energy and momentum partial differential equations. The governing equations were applied for both the working gas and the structure of engine. Tew et al. [157] reported that the simulation of Stirling engines using Sage code was performed in a NASA's project.

H-FAST that is Stirling engine analysis code using the harmonic analysis method was presented by Huang cited in [155]. The mass, energy and momentum equations were formed in simplify assumption. Furthermore, the result was deducted with several losses to obtain the correct result.

Anderson in [156] described in details the PROSA software (version 3.0) developed by Thomas. Anderson et al. in [158] presented a one-dimensional modelling approach for a Stirling engine which takes into account the compressibility in the unsteady gas flow. The losses due to the finite temperature heat transfer, the flow friction were described using the empirical correlations. When compared with experimental data, simulation results were in a good agreement with experimental data. It was pointed out that using correct empirical correlations for calculating the heat transfer and friction in the regenerator and heat transfer in the displacer clearance is very important for the accurate prediction of the efficiency and power output. Furthermore, the optimisation study with the use of the shooting method was performed in this work.

- ***Multi-dimensional modelling*****:** in addition to using various one-dimensional models for analysis of a working process of Stirling engines, there have been some investigations performed on application of two-dimensional (2D) and three-dimensional (3D) modelling in order to better predict the working performance of each component of Stirling engines.

  Mahkamov and Ingham [159] demonstrated the application of 2D computational fluid dynamic (CFD) modelling for analysis of the working process of a V-type solar Stirling engine. An axisymmetric CFD model with the standard k-ε turbulence model for compressible flow was chosen to numerically simulate the operational cycle. Preliminary to that, the second-order mathematical model which includes heat and hydraulic losses was used and its results were compared with the results of the CFD model. The better accuracy in the prediction of the engine performance with the CFD model was reported.

  Ibrahim et al. [160] reported on the development of a 2D CFD model for analysing the components of Stirling engines. The so-called CAST model was used to solve the governing equations with the k-ε turbulence model. The predicted gas hysteresis loss from CAST was compared to results obtained from simulations using the commercial CFD software, namely CFD-ACE+. The acceptable agreement between numerical results was found but these significantly differed from experimental results obtained on the test rig.

Further to analysing the working process with application of the 2D CFD modelling, the 3D CFD modelling has been used for the design improvement of a Stirling engine. Thus, Mahkamov and Djumanov [161] analysed the whole Stirling engine operation using 3D CFD modelling with commercial software, namely ANSYS. The modelling deployed the k-ε turbulence model for numerical investigations of the working process inside a gamma-type Stirling engine. Obtained numerical data included temperature, pressure and the velocity contours in the Stirling engine and the indicated power of the Stirling engine was calculated using obtained pressure-volume diagrams in the expansion and compression spaces. Tan et al. [162] presented, using as a tool the 3D CFD (ANSYS) modelling, working process details of a small beta-type kinematical Stirling engine coupled to a parabolic dish concentrator. Two improved design configurations were suggested to increase the indicated power of the engine. Moreover, Mahkamov [163] carried out 3D CFD modelling for the design improvement of a biomass engine. In this paper the working process of a gamma-type Stirling engine run on biomass (heat source) was first investigated by using the developed second-order mathematical model and then the 3D CFD model was applied for calculations. It was demonstrated that the accuracy of the second-order and CFD models was 30 and 12-18 %, respectively, when compared to experimental data. The commercial CFD software, ANSYS, was used for simulating the gas flow and heat transfer in each component of the Stirling engine and the standard k-ε turbulence model for compressible flow was deployed in modelling the cycle. The design improvements were proposed which included a new regenerator with the increased porosity and the change of engine's configuration to the alpha-type. A similar work was performed by Mahkamov and Eid [164] for a Stirling engine heated by synthetic oil. The investigation of the heat transfer phenomena from synthetic oil to the heater of a V-type Stirling engine was performed. The engine was designed for application as a part of a medium temperature solar power plant. The 3D CFD simulations using ANSYS were run to design the heater of the engine.

Dyson et al. [165] reported the computational simulations using 3D CFD modelling based on ANSYS for a part of opposed Stirling convertors. The temperature contours in the cooler, heater and regenerator were presented and also pressure variations in the expansion and compression spaces were determined. The numerical results obtained using the 3D CFD model were compared to results obtained with the use of the one dimensional model software, namely Sage.

Some of the above described mathematical models of Stirling engines were used as tools for optimisation of design of Stirling engines. Such investigations are presented in the next section.

2.7 Optimisation of the design of Stirling engines

This section reviews a number of papers related to the optimisation of Stirling engines using various mathematical models and optimisation methods.

Blank and Wu [166] presented results of investigations of an extra-terrestrial Stirling engine operating with solar heat source using the irreversible thermodynamic cycle analysis. The optimum power and the efficiency at the optimum power condition were calculated using the finite time approach.

Erbay and Yavuz [167] also analysed the performance of the Stirling heat engine at the maximum power conditions. The power and the efficiency were determined by using the model of the thermodynamic cycle of a Stirling engine with a realistic regenerative heat exchanger. The maximum power density technique was used for analysing the engine performance.

Costea et al. [168] optimised the operating temperature for a solar Stirling engine using the mathematical model based on the Stirling thermodynamic cycle. This model took into account fluid friction and mechanical losses in the engine using empirical correlations. Results were obtained by solving a system of nonlinear equations using the method of Lagrangian undetermined multipliers.

Hsu et al. [169] investigated the performance of a free piston Stirling engine operated using the heat from an incinerator. In order to determine the optimal design of an engine, the efficiency and optimal power output at variable heat source and heat sink temperatures were investigated by using a cycle-averaged heat transfer coefficient model. It was found that the efficiency and optimal power output were proportional to the heat source temperature. Additionally, Hsieh et al. [170] studied the feasibility of the power production using the waste heat of an incinerator and a free piston Stirling engine. The performance of a Stirling engine was predicted by using the heat transfer model with irreversible heat transfer processes and the optimisation of the work output was investigated using the Lagrange multipliers method. The maximum power was used as an objective function in the optimisation procedure.

Martaj et al. [171] presented the energy, entropy and exergy analyses of the hot-end and cold-end heat exchangers and the regenerator of a Stirling engine. The mathematical model of the Stirling engine with the finite dimension thermodynamics processes was used in this paper. The engine was analysed using the entropy and exergy balance equations under the steady state condition. In order to optimise the performance of the Stirling engine, this research defined the criteria parameters in terms of the maximum power, the maximum thermal efficiency, the minimum entropy generation and the maximum exergy efficiency. A MATLAB computer program was used to run optimisation calculations.

Boer presented in [172] the one dimensional model for analysing the regenerator of Stirling engines. The model was analytically derived from a simplified model and included viscous and thermal losses. The optimisation performed provided the optimal condition for the regenerator conductance and the piston phase angle for the maximum power output

Yaqi et al. [173] investigated the optimisation of the solar HTD Dish-Stirling engine. The finite heat transfer and heat losses were considered in the model. The optimisation performed in terms of the heat absorber temperature, the concentrating ratio of the system, the effectiveness of the regenerator and the heat leak coefficients resulted in the maximum efficiency of the Dish-Stirling power unit.

Optimisation of Stirling engines based on deploying the Schmidt model is of a particular interest in this subject field. Senft [174] developed the model for optimisation using the principle of the forced work integrated to the classical Schmidt theory. The optimisation calculations provided the values of the optimal swept volume ratio and phase angle to achieve the maximum brake work. The geometry of a gamma-type Stirling engine was optimised and discussed in this work. Schmidt model was also used by Cullen et al. [175] to obtain preliminary results of modelling an Otto/Stirling cycle hybrid engine. The simulations with respect to the engine speed using the Schmidt model were compared to the simulation results obtained using the direct method. The mathematical model based on the Schmidt model was described by Formosa and Despesse in [176]. The regenerator efficiency, the heat exchanger effectiveness and a number of heat loss sources were taken into account in this model. Comparison of the calculated power output with published results from other models for the GPU-3 Stirling engine [177] was carried out to validate the developed model. From optimisation calculations, the effect on the brake power output of the fluid mass, the frequency and the cooler efficiency were determined. However, the author suggested that the proposed model could be used only for the preliminary designing of the engines.

For better accuracy, higher order models of Stirling engines should be used for analysis and optimisation. Altman [177] presented a commercial program for analysing the working process of Stirling engines and obtaining the optimal design parameters. Thus, a numerical analysis program named SNAPpro was first presented in 1999/2000 for designing the various types of Stirling engine. The isothermal second-order model described by Martini [132] was the design tool for simulating the working process. This program written as an Excel program calculated the performance of the Stirling engines and also presented graphs such as P-V diagrams and heat losses. Moreover, it was coupled to Genetic algorithm code and could optimise up to 20 engine design parameters.

Orunov et al. [178] presented the design of the tri-generation power unit on the basis of an alpha Stirling-Stirling cycle for generating electricity and heat/cold production. The first-order model of a Stirling cycle with taking into account hydraulic losses was used at the first stage of the design process. At the second stage, the second-order model taking into hydraulic losses in the all heat exchangers was used for analysing the working gas process. In the optimisation procedure, the dimensionless work parameter and dimensionless length of the heater, cooler and regenerator were used as the optimisation criteria.

Timoumi et al. [146] described the optimisation procedure for the engine parameters of the GPU-3 Stirling engine. The developed quasi steady flow model called Dynamic model was used for the parametric analysis. The effects of the thermal conductivity and heat capacity of materials, the porosity of the regenerator, the temperature of the gas flowing into the regenerator, the regenerator volume, the mass of the working fluid and also the expansion volume on the engine performance were investigated.

Zarinchang and Yarmahmoudi in [179] demonstrated the optimisation of a 20 kW Stirling engine. The optimisation was performed by using so-called OPTIMUM code based on the second-order Stirling engine model. The main heat exchangers such as the heater, cooler and regenerator were redesigned by using the sensitivity analysis. Then the results were recalculated by using the third-order program called STRENG for better predicting the engine performance.

Some studies, though being on the research of conventional Stirling engines, are related to the optimisation of designs of LTD Stirling engines. Some of such papers are reviewed.

Rochelle [180] proposed the mathematical model based on the finite dimension thermodynamics processes and used for simulation and optimisation of a LTD Stirling engine with a gamma configuration. The model uses several operating parameters in the dimensionless form. The ratio between the displacer swept volume and the working volume was optimised so to achieve the maximum efficiency and the maximum work output in the LTD Stirling engine without and with a perfect regenerator. The results of the optimisation provided optimal dimensionless values for both above cases.

Abdullah et al. in [181] analysed the design of the engine by using the first and third order mathematical models for a double-acting LTD Stirling engine operating at the temperature difference of 50 °C with a heat source being a thermo-syphon solar water heater producing the hot water with the temperature of 70 °C. The preliminary design parameters were obtained using the Schmidt analysis and then the third-order model based on Martini's model [181] was deployed to provide the optimal design parameters. It was demonstrated that there were considerable heat and frictional losses inside all heat exchangers of the Stirling engine. The parametric study of the diameter of the cooler and heater tubes were performed.

From review of published paper carried out in this section, it is obvious that the optimisation methods used for designing engines required the mathematical models providing the closed form solution and furthermore the parametric analysis was commonly used for obtaining the optimal engine parameter. Only few published papers describe application of Genetic algorithm method for the optimisation of Stirling engines.

Chapter 3

Linear generators

A linear machine can be defined as being the results of a cylindrical rotary machine which has been mentally split long a radial plane and unrolled, so that instead of produce a torque (as in traditional rotating machines) it produce a linear force along its length.

3.1 Linear generator typologies:

3.1.1 Induction machines

The induction machine is the workhorse of the electric motor industry. Its robustness arises from the simple topology of its rotor, particularly in a squirrel cage motor where there is no requirement for brushes or slip rings. There is a slight preference for induction machines to be used as motors, in particular linear induction machines have previously been of primary interest for transportation actuators. In a linear induction machine a three phase alternating current is used to excite the stator windings, which, in combination with the winding configuration, sets up a synchronous speed travelling magnetic field in the air-gap region. Consequently, if the translator is not moving at synchronous speed, i.e. for all non zero-slip speeds, an emf is induced within the translator, this induce an opposing current in the mover windings that, in turn, create a magnetic field that react again the stator field. The mover accelerates until the force, provided by the magnitude of induced mover current, balance the applied mechanical load. The transition of machine operation from motor to generator occurs as the mover speed overtakes the field speed and goes super synchronous. By feeding the stator coils through a controllable inverter any slip speed can be achieved at any mover velocity. Controlling the output power is hence relatively simple for a variable speed input and as such the rotary version is commonly used in wind turbines. The moving part can have a very simple and light construction, consisting of either conductors embedded in slots of a back iron structure, or possibly just a single conducting sheet. The main drawback of such kind of machine is the low efficiency. In fact, for a linear machine, where there is likely to be a larger air-gap than its rotary counterpart, the inductance and hence reactance of the excitation coil is low. Consequently a large excitation current is required and the overall efficiency of the machine is reduced.

3.1.2 Synchronous machines

Synchronous machines are the primary devices used for high speed rotary power generation in the world's electric power systems today [182]. The rotor is fed with a direct current via brushes and slip rings and so sets up a magnetic field which follows its movement. The stator surrounds the rotor with a set of stationary coils, such that they are cut by the rotor flux pattern. Controlling the excitation currents in these machines, which are generally more efficient than induction machines, provides a way of regulating the output voltage which would otherwise be dependent on speed.

Operating as a motor for high speed transportation devices, linear synchronous machines have been shown to be more favourable than their induction equivalents, with an efficiency of 90 % when compared to 82 % and a power factor of 0.8 as opposed to 0.52 [183]. At low velocities, however, the small pole pitches necessary for rapid flux change limits the current / size of the excitation coils.

There are wear issues associated with field-wound synchronous machines when compared to induction machines. The necessity of physical contact with the translator in order to transfer magnetising current will enforce routine maintenance for inspection or replacement of brushes. The variable speed bi-directional oscillatory motion considered here will only serve to increase wear on the brushes when compared to their rotary counterpart.

3.1.3 Permanent magnet machines

In a machine excited by PMs there is no need for the provision of field excitation, as magnetised material is used to supply pole flux as opposed to current carrying coils. A simple example of such a machine consists of surface mounted ferrous magnets mounted on an iron translator which oscillates within a cylindrical distributed three phase winding, held in place by slotted iron structure.

As the translator moves, so too does the flux pattern resulting from the presence of magnets. An emf is hence induced in the stationary coils as the flux cutting them is changed. The flow of magnetic flux can be simplified by assuming infinitely permeable iron, in which case the total magneto-motive force (mmf) produced by a magnet is dropped across the magnetic gap length (i.e. in the air-gap and within the magnet itself). The flux density in the air-gap B_g [T] is given by:

$$B_g = B_r \frac{t_m}{t_m + \mu_r\, g} \tag{3.1}$$

where B_r is remnant flux density in the magnet [T], t_m is the magnet thickness [mm], μ_r is the permanent magnet relative permeability [-] and g is the air-gap length [mm], respectively.

By use of Lorenz's law, the machine thrust force F [N] on the electrical windings results:

$$F = B_g I L \tag{3.2}$$

where I is the winding current [A] and L is winding length [m], respectively.

The use of PMs allows achieving greater efficiency compared to synchronous machines, due to the lack of mover windings, cause of losses. Furthermore, PMs allow obtaining higher specific power, lighter mover, higher strength and less maintenance.

3.2 Variable reluctance permanent magnet machines

One of the main problems of linear machine is the strength connection between the primary moving source and the mover of linear generator. Accordingly, the output electric frequency is the same of mechanical frequency. In the slow speed applications, this could be a problem, because low frequency means large size of the machine in order to convert the same quantity of energy.

A slow physical velocity may be converted to a high speed flux change by a process known as magnetic gearing. Figure 3.1b shows a single stator pole, split into 3 teeth, interacting with five individual mover poles, each a surface mounted permanent magnet. If the mover moves by one mover pole, the direction of flux flow through the pole can be seen to reverse. In non-toothed designs (Figure 3.1a), the mover would have to move a distance five times this value. This toothed design has therefore increased the rate of change of flux fivefold. However, the mover is only interacting with three stator poles at any one time, reducing the maximum value of flux by a factor of 3/5. The net magnetic gearing of the split mover and stator poles is hence threefold.

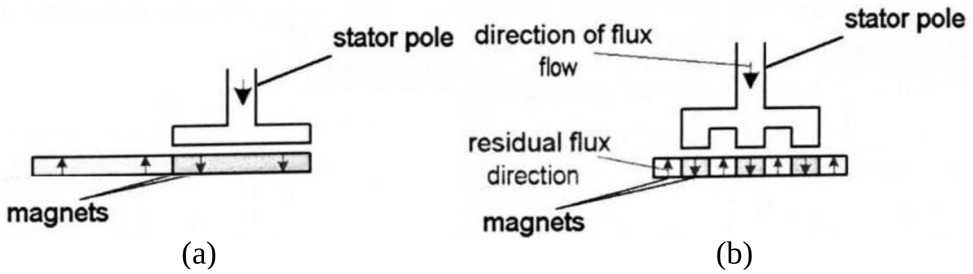

Figure 3.1. *Magnetic gearing: non-toothed* (a) *and toothed* (b) *linear generator designs.*

Recent developments have resulted in a new class of machine, known as Variable Reluctance Permanent Magnet machines (VRPM). There are many topologies of these machines [184-189], all bound by the same principles of operation. Alternative return paths are offered to the magnetic flux through the interaction of rare earth PMs and small pitch iron teeth. Force is developed as the path of minimum reluctance is sought. These machines are capable of shear stresses unmatched by other electrical machines, which has led to a general reduction in the size of machine. These advantages are further amplified if rare earth magnets are used.

A common problem to all VRPMs is that they tend to operate at low power factors under load, values in the range of 0.35-0.55 are typical [190]. The highly effective magnetic circuit of the machine, which is key to its high shear stresses, presents this inherent disadvantage. The problem is compounded by the desire for many turns on the coil to further enhance the change in flux linkage from the slow physical velocity. The result of these factors is that current flowing within the coils produces a strong flux pattern. Any change in this current flow is· hence resisted by a large change in flux flow, producing a back emf. In practice this phenomena manifests itself as a large inductance in series with the electrical machine resisting any change in current. The subsequent phase lag between emf and current results in the terminal voltage collapsing when current flows. The low power factor of VRPMs will hamper their useful power output. The requirements of this topology and the utilisation of magnetic gearing make it an inherent feature which must be overcome by electronic means.

In order to increase the power factor and bring the current and voltage of the generator in phase, reactive power must be provided. This can be done by the addition of a parallel capacitor across the load or by means of an active rectifier that force the output current to be in phase with internal emf, and then bringing the power factor up to unity.

3.2.1 Transversal flux machines

In a transversal flux machine (TFM) (Figure 3.2) the main flux flow is in a direction perpendicular to the direction of travel. The translator consists of surface mounted PMs in a configuration that forces the flux to vary both axially and circumferentially. There are stator coils mounted either side of the translator with a series of iron yokes channelling the flux in such a way that alternate mover poles excite the same coil [184-185]. The result is an inherently three dimensional flux path, and flux from all the magnets contributes to linking one or other of the coils at all times. As such the TFM is the ultimate VRPM machine, producing very high shear stresses values approaching 200 kN/m^2 have been reported [184].

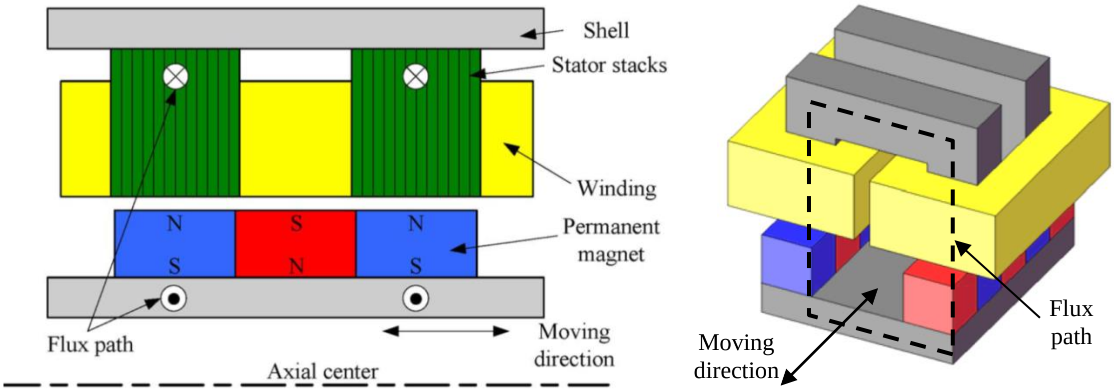

Figure 3.2. *Transversal flux permanent magnet linear machine (TFPMLM).*

The mounting of the stator yokes in combination with the three dimensional flux path present various problems with the support structure of this machine. The typical three dimensional structure does not allow the ferromagnetic elements to be laminated and the necessary small pitch often demands a large number of individual parts, or the use of SMC materials. Furthermore, inherent in this machine is the presence of cogging torque: the tendency of the magnets to align themselves with the path of least reluctance. It has been reported as 30 kN/m^2 in one machine [185].

If the mover magnets are replaced with an equivalent current sheet and the magnets and teeth are misaligned, the force F_n [N] resulting in the interaction of the current sheet and the flux due to the coil current is given by:

$$F_n = B_g \, I_{PM} \, L \tag{3.3}$$

where $B_g = \frac{N\,I}{2}\left(\frac{\mu_r\,\mu_0}{l_{PM}+2\,g\,\mu_r}\right)$ is the flux density in the air-gap [T], $I_{PM} = H_c\, l_{PM} = \left(\frac{B_r}{\mu_{PM}\,\mu_0}\right) l_{PM}$ is permanent magnet equivalent current [A] and L is the permanent magnet axial length [m].

3.2.2 Vernier hybrid machines

The Vernier hybrid machine (VHM) (Figure 3.3) has a significantly more conventional machine structure, and a two dimensional flux pattern [186, 189]. The stator mounted PMs interact with the purely iron toothed mover, in order to produce the flux path shown. This two dimensional path links all four coils, four magnets and four air-gaps. A similar topology has been proposed, [187], which had the magnets on the moving part and the stator face toothed. If the mover moved one magnet pitch, equal to half a mover pitch, in either direction, it can be seen that the teeth would fully align with the opposite poles to those shown, and hence the flow of magnetic flux would be completely reversed.

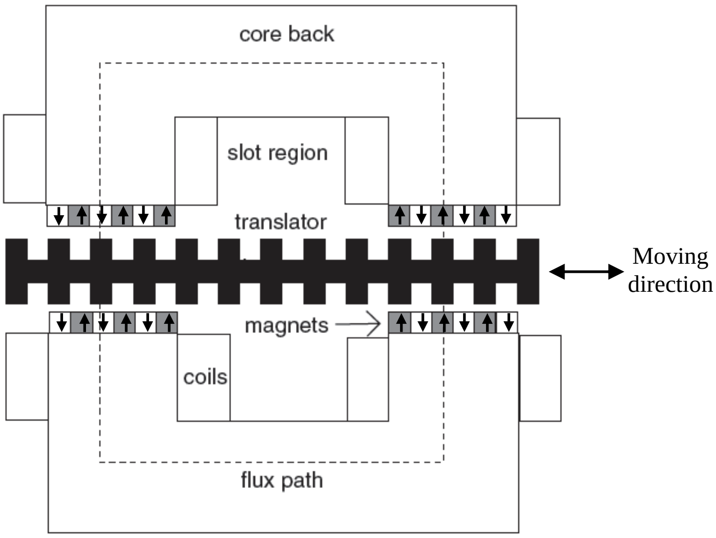

Figure 3.3. *Vernier hybrid machine.*

Because of the slots in the mover the flux density is not constant throughout the width of the airgap. The flux pattern with a higher density is observed under the tooth region than under the slot region. Due to the magnets being alternatively magnetised, the greatest force is reacted when the magnets and teeth are exactly misaligned and hence the equivalent current carrying coils are in the area of highest flux density. The flux under the slot region causes a force which opposes that under the teeth.

The peak resultant force per tooth pitch F_n [N] will be the difference of these opposing forces, given by:

$$F_n = (B_t - B_s)\, I_{PM}\, L \tag{3.4}$$

where B_t is the flux density under the tooth [T] and B_s is the flux density under slot region [T].

3.3 Principle of operation

While rotary motion electric generators are multiphase (generally 3-phase) machines, in general, the linear motion generators (LGs) tend to be single-phase machines, due to linear oscillating motion that forces a change of phase sequence for a change in the motion direction.

Referring to a harmonic motion, the mover position x [m] can be described as follows:

$$x(t) = \hat{x}\sin(\omega t) \tag{3.5}$$

where x̂ is the maximum value of the mover semi-stroke [m] and ω is the oscilating frequency [rad/s].

The electromagnetic force (emf) is, in general:

$$e(t) = -\frac{\partial \Psi_{PM}}{\partial t} = -\frac{\partial \Psi_{PM}}{\partial x}\, v(t) \tag{3.6}$$

where Ψ_{PM} is the PM flux linkage in the phase coil [Wb] and $v = \frac{\partial x}{\partial t}$ is the mover speed [m/s].

Putting equation (3.5) in equation (3.6), results:

$$e(t) = -\frac{\partial \Psi_{PM}}{\partial x}\, \omega\hat{x}\cos(\omega t) \tag{3.7}$$

To obtain a sinusoidal emf waveform, $\frac{\partial \Psi_{PM}}{\partial x}$ has to be constant with mover position. This means that the PM flux linkage in the phase coil has to vary linearly with mover position. The linear variation of PM flux linkage with mover position is met only approximately in practice, due to iron core magnetic saturation. Generally, the Ψ_{PM} flattens toward excursion ends, which leads to the presence of third, fifth and seventh harmonics in $e(t)$.

Ideally, with $\frac{\partial \Psi_{PM}}{\partial x}$ position-independent, emf varies as the speed does.

The thrust force that acts on mover is as follows:

$$F(t) = \frac{e(t)\, i(t)}{v} = -\frac{\partial \Psi_{PM}}{\partial x}\, i(t) \tag{3.8}$$

Ideally, with $\frac{\partial \Psi_{PM}}{\partial x}$ position-invariant, thrust force varies as the current.

From equation (3.8), can be noted that the highest thrust force per given current occurs when the $e(t)$ and $i(t)$ are in phase with each other. Supposing $\frac{\partial \Psi_{PM}}{\partial x}$ position-invariant, from equation (3.7), it follows that $e(t)$ is in phase with mover speed; thus, to achieve the highest thrust force, the current has to be in phase with the speed as well.

The above relation is valid only if $\frac{\partial \Psi_{PM}}{\partial x}$ can be considered position-invariant, this means that the phase inductance L_c [H] is independent of mover position, that is, if the reluctance force is null.

In the hypothesis of ideal LG ($\frac{\partial \Psi_{PM}}{\partial x}$ position-invariant), the complex variables can be used to describe the machine operation, the output voltage $\bar{U}$ [V] results:

$$\bar{U} = \bar{E} - (R_c + j\omega L_c)\,\bar{I} = \bar{E} - \dot{Z}\,\bar{I} \tag{3.9}$$

where R_c is the coil resistance [Ω] and $\dot{Z} = R_c + j\omega L_c$ is the coil impedance.

The delivered apparent power $\bar{S}$ is as follows:

$$\bar{S} = \bar{U}\,\check{I} = P + jQ \tag{3.10}$$

The delivered active power P is:

$$P = \mathrm{Re}\big(\bar{U}\,\check{I}\big) = U\,I\cos\varphi \tag{3.11}$$

where φ is the phase shift between output voltage and current.

To deliver electrical power to a grid the LG output voltage has to be larger than grid voltage U_g. A series of capacitors may be used to reduce the phase shift φ, due to coil inductance L_c.

3.4 Dynamic equations

The motion of LG is regulated by the following force [N] balance:

$$F_{eng} - F_{lg} - F_{cog} - F_{spr} = m\frac{\mathrm{d}^2 x}{\mathrm{d}t^2} \tag{3.12}$$

where F_{eng} is the force provided by primary engine, $F_{lg} = C_{lg}\,i$ is the electromagnetic force of linear generator, $F_{cog} = C_{cog}\,x$ is the cogging force, $F_{spr} = -K\,x$ is the spring force (where K is the spring constant [N/m]) and m is the total moving mass [kg].

In steady-state harmonic motion, the primary engine force has to completely balance by only the electromagnetic force of linear generator. Then, from equation (3.12), has to be:

$$F_{cog} + F_{spr} + m\frac{\mathrm{d}^2 x}{\mathrm{d}t^2} = \big(C_{cog} - K\big)x + m\frac{\mathrm{d}^2 x}{\mathrm{d}t^2} = 0 \tag{3.13}$$

as $x = \hat{x}\sin(\omega_r t)$, it follow that:

$$\big[\big(C_{cog} - K\big) - m\,\omega^2\big]\,\hat{x}\sin(\omega_r t) = 0 \tag{3.14}$$

then, finally:

$$\omega_r = \sqrt{\frac{(C_{cog} - K)}{m}} \tag{3.15}$$

Equation (3.15) spells out the mechanical resonance condition. So the electrical frequency (equals to the mechanical one) results equals to the spring-mass proper frequency.

In this case, the prime mover has to provide only the useful electromagnetic power, while the mechanical spring has to provide the cogging and inertia forces, does the conversion of electrical to kinetic (and back).

To obtain the best condition of energy conversion the spring has to design in order to achieve the resonant frequency for that particular moving mass and working frequency:

$$k = C_{cog} - m\,\omega_r^2 \tag{3.16}$$

3.5 Structures of linear machine

Firstly, the linear machines can be classified based on their planar geometry:

- flat (planar) linear machines, shown in Figure 3.4*a*, that is obtain making an ideally cut and straight a conventional rotating machine. They, in turn, can be classified in single-sided and double-sided if they are assembled in opposite;
- tubular (cylindrical) linear machines (Figure 3.4*b* and Figure 3.5) that is obtain starting from a flat linear generator and then re-rolling the machine in the moving direction.

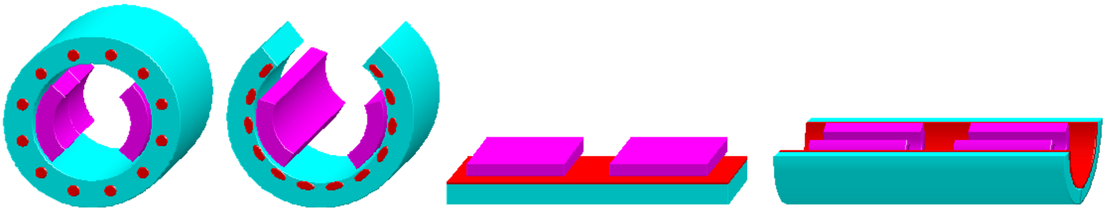
(a) (b)

Figure 3.4. *Process to obtain a linear machine: single-sided flat* (a) *and tubular* (b) *structures.*

The linear machines can be classified according to the stator length respect to mover length:

- long stator (or short mover): the length of the supply part is longer than the excitation way, in most cases the excitation part is mobile;
- short stator (or long mover): the supply part is shorter (or equal) than the excitation way. The supply part is, in most cases, mobile.

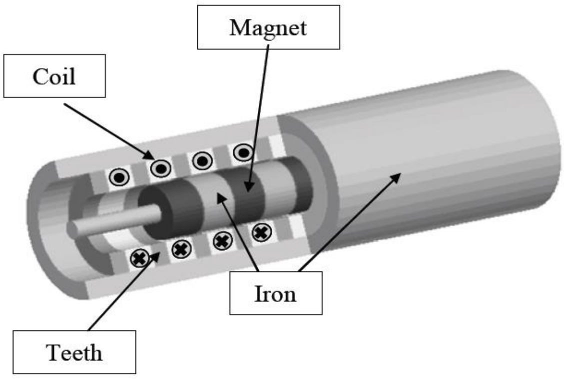

Figure 3.5. *Cross-section of a tubular linear machine.*

The linear machines can be sort by the thrust (propulsion) force is generated, or rather the excitation typology:

- coil: the traveling magnetic field is produced by the current that flow through in a winding (coil exited machines);
- PM: the traveling magnetic field is produced by permanent magnets (PM exited machines).

3.6 Control of permanent magnet linear generators

The control of the PMLGs depends on the prime mover and load characteristics.

Typical prime movers are as follow:

- Free piston engines (Stirling engines) [191];
- Spark-ignited linear internal combustion engines (ICEs) [192];
- Very low-speed reciprocating wave energy converters (average speed from 0.5 to 2.0 m/s) [191].

The control of stroke be instrumented through the prime mover, while the adaptation of alternator voltage to the load – independent or at power grid – is to be performed by power electronics. The motion frequency may be maintained constant and equal to power grid frequency, securing operation at the mechanical resonance frequency. If the frequency of motion varies within some limits, then the complexity of power electronics has to increase, if the load demands constant frequency and voltage output.

The control solution can refer to constant or variable motion frequency solutions and, as concerning the load, a stand-alone non-demanding load or a strong power grid.

In the case of constant motion frequency, the control is decoupled as shown in Figure 3.6. Particularly, the motion amplitude control is provided by prime-mover governor in order to deliver more or less mechanical power while voltage adaption is required in the case of operation at the power grid or at a certain voltage.

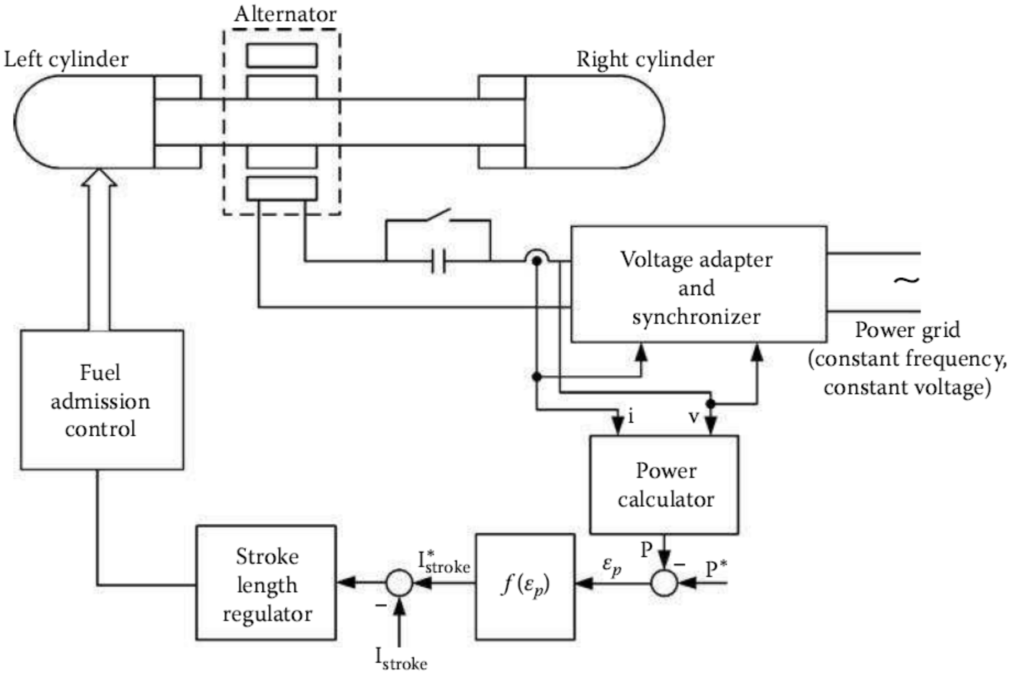

Figure 3.6. *Constant motion frequency solution (power grid connection).*

The power error is the input of a power regulator follower by the stroke length l_{stroke}, regulator. Finally, the fuel injection rate is modified to produce the required motion amplitude l^*_{stroke}, according to electric power requirements.

As the frequency is constant and connection to the grid is required, the motion phase may be modified slowly to provide the synchronization to the grid connections. The voltage adapter may be an autotransformer with variable ratio via a small servomotor. Alternatively, a soft-starter may be used to reduce the transients during connection to the grid. An additional resistance may be added before synchronization, in series with the alternator, and then short-circuited a few second later, as is done with induction generators.

When the motion frequency is allowed to vary, a front-and rectifier plus inverter may be applied, as shown in Figure 3.7. In this case, the series capacitor is no longer required, as the DC link capacitor does the job. The DC link voltage may now be larger than the LMA emf.

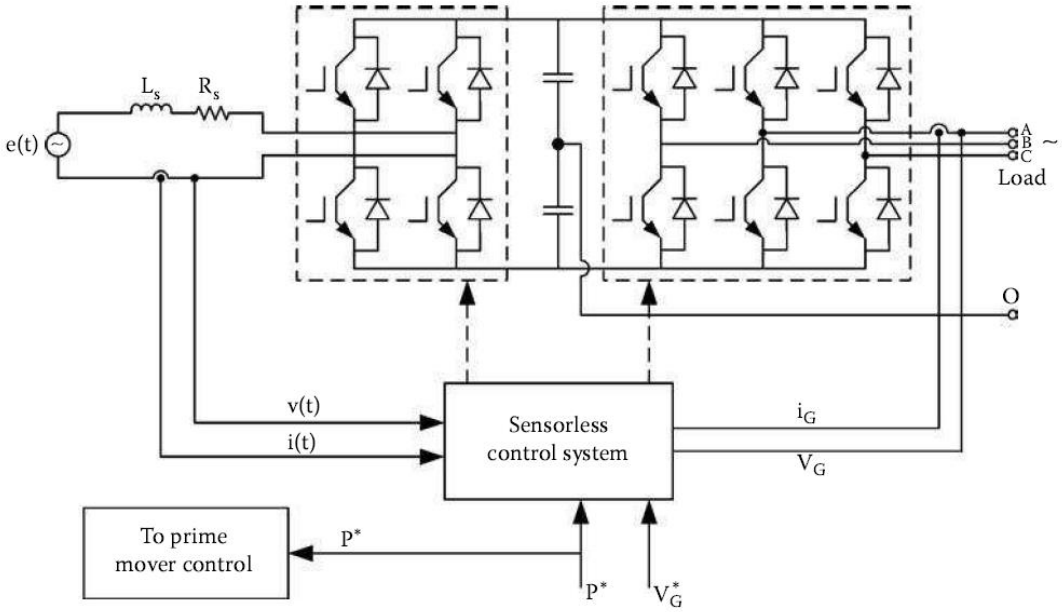

Figure 3.7. *Constant motion frequency solution: front-and rectifier plus inverter.*

A bidirectional converter makes the interface between the variable voltage and frequency of the PMLG and the load requirements. The control of the load-side converter is different for independent load in contrast to power grid operation; it should be similar for the single-phase alternators. The bidirectional converter also allows for motoring and thus, could help in starting or stabilizing the prime mover's motion when the operation takes place at the power grid or with a backup battery. In this case, the smooth connection to the power grid is implicit.

Note that for ocean-wave linear translator alternators, three-phase configurations were proposed [191]. A three-phase bidirectional converter is required in this case. The control of such a system is similar to the case of rotary PM generators.

3.7 History and applications of linear generator

A brief review of the history, types and applications of linear electric actuators and generators was given by Boldea et al. [193].

Amara et al. [194] investigated a tubular linear permanent magnet machine that might offer the highest efficiency and power/force density. The machine studied had a nine-slot, ten pole configuration, with a fractional number of slots per pole per phase. Since the Halbach magnetic array was used for the mover, the flux at the inner bore is quite small, permitting the use of nonmagnetic supporting tube for the magnets. The problem of eddy current reduction is the main design issue for this type of machine configuration.

A typical application of the linear permanent-magnet synchronous generator (LPMSG) is in a wave-energy to electric energy conversion system. The perpetual vertical motion of the sea waves is exploited to drive the mover of a linear generator for producing electricity. A pilot plant using this principle, namely the Archimedes Wave Swing (AWS), was designed for 4-MW peak power [195]. A three-phase linear permanent-magnet generator was designed to extract electric energy from the motion of the floater [196].

Polinder et al. [197] showed that the linear PM generator was cheaper than linear induction generators for such applications. Conventional LPMSG had magnets mounted on the mover, but the authors also proposed a transverse-flux PM generator (TFPMG) which had flux concentrators, magnets and conductors all on the stator, while the translator only consisted of iron. Such a machine configuration was more difficult to build and hence further investigations would be needed.

Wang et al. [198] describe the design and experimental characterization of a reciprocating linear permanent magnet generator. Their paper describes a design methodology which embraces both the electromagnetic and mechanical design. The electromagnetic design synthesis is based around analytical field solutions which allow the optimization of the generator parameters, and it is further verified by non-linear electromagnetic finite element analysis. The design methodology utility is illustrated by a design study and extensive experimental characterisation of a prototype device.

In another paper [199] Wang at al. discuss the issues about the design of a linear permanent magnet generator for application in a free-piston energy converter. To achieve the required high power density, high efficiency and low moving mass, a tubular machine equipped with modular windings and quasi-Halbach magnetization is chosen. Analytical expressions for predicting the open-circuit magnetic field distribution, emf, thrust force and armature reaction, as well as the self and mutual inductances of the machine, are established and verified by means of finite element analysis. It is shown that the machine design can be optimized with respect to three dimensional ratios while satisfying other performance specifications.

Fraiz at al. [200] discuss how to reduce the cogging force in a linear permanent magnet generator. To reduce this force they have design and simulated a tree-phase linear permanent magnet generator for direct wave energy conversion and predicted its performance using the finite element method. They studied the influence of different design parameters (such as PMs length, magnetization orientation and stator slot typologies) on the cogging force and minimized this force by varying the proposed parameters. The results obtained confirm a large reduction in the cogging force and an enhancement in the generator performances.

Delli Colli et al. [201] illustrate the operation of a tubular-machine drive as a linear generator for a heave-buoy wave energy conversion. The paper summarized the principle of marine wave buoy interaction and reports the design analysis and control of a permanent magnet synchronous tubular linear machine based on a scaled generator prototype and on a rotating simulation test bench.

Soheil at al. [202] describe an improved topology of a linear permanent magnet generator for sea wave energy harvesting and presents an electrical model for analysis of this generator. The electrical model is established based on the magnetic equivalent circuit of the machine. The model can be used to design a power electronic interface for capturing maximum power at the resonant frequency of a sea wave. Validity of the model is verified via comparing the calculated inductance of the machine with that of obtained from numerical analysis based on finite element method.

Francois at al. [203] set forth a 3D analytical model of a tubular linear induction generator. The article describes the electromagnetic model of the linear generator and draw comparison with a finite element model, in addiction to identifying the elements of the equivalent electrical diagram and displaying results from the multi-objective optimization study performed using a genetic algorithm.

Chapter 4

Magnetic materials utilized in linear electric machines

4.1 Introduction

The magnetic materials can be classified into three categories: diamagnetic, paramagnetic and ferromagnetic materials. The classification depends on the magnetic dipole moment of atoms of the material and on the interactions among the atoms.

When the different magnetic materials are placed in a uniform magnetic field, the field lines are changed as shown in Figure 4.1.

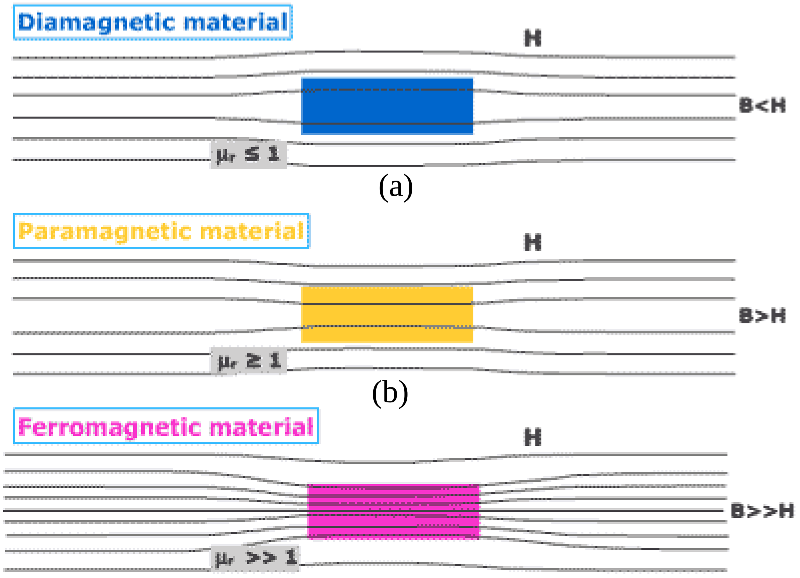

(a)

(b)

(c)

Figure 4.1. *Field lines distribution of diamagnetic materials* (a), *paramagnetic materials* (b) *and ferromagnetic materials* (c) *placed in a uniform magnetic field H.*

- ***Diamagnetism***

  When a diamagnetic material is exposed to a strong magnetic field, electrons in this material rearrange their orbits (orbital motion of electrons) and creating small persistent currents which oppose the external magnetic field. Hence, diamagnetic materials have a very weak and negative susceptibility to external magnetic fields, and also slightly repelled by the magnetic field. In addition, diamagnetic material does not retain the magnetic properties when the external field is removed and does not have permanent net magnetic moment per atom since its orbital are fully-filled.

  Examples of diamagnetic material are bismuth, copper, water, alcohol, mercury etc.

  The permeability of diamagnetic materials is slightly less than or equals to the free space permeability ($\mu_r \leq 1$). The field lines distribution of a diamagnetic material placed in a uniform magnetic field are reported in Figure 4.1a.

  The properties of these materials are independent of temperature.

  Some materials behave like superconductor at very low temperature and they are perfect diamagnetic materials which have $\mu_r = 0$ and $B = 0$ (no magnetic field could be established inside superconductor materials since they expel all the magnetic fields that applied on it). The most popular application of diamagnetic materials is magnetic levitation, where an object can be made to float in the air above a strong magnet.

- ***Paramagnetism***

  Paramagnetic materials are weakly attracted to magnets and have a small positive susceptibility to magnetic fields. Paramagnetic properties are due to the presence of some unpaired electrons that produce the net spin magnetic moments which tend to align themselves in the direction of the external magnetic field. They do not retain the magnetic properties when the external field is removed.

  Paramagnetic materials are sensitive to the temperature: they become more magnetic when theirs temperature reduces. Paramagnetic materials are typically considered nonmagnetic since they have very small positive susceptibility (of the order 10-5) as compared to ferromagnetic materials.

The permeability of paramagnetic materials is slightly more than or equals to the free space permeability ($\mu_r \geq 1$). The field lines distribution of a paramagnetic material placed in a uniform magnetic field are reported in Figure 4.1b.

- ***Ferromagnetism***

  Ferromagnetic materials have a large and positive susceptibility to an external magnetic field. They exhibit a strong attraction to magnetic fields and they are able to retain their magnetic properties after the external field has been removed.

  Ferromagnetic materials have some unpaired electrons so their atoms have a net magnetic moment. They get their strong magnetic properties due to the presence of magnetic domains within which the magnetic moments of all its atoms (10^{19}) are aligned parallel to each other.

  Examples of ferromagnetic materials are iron, nickel and cobalt, and their alloys such as alnico.

  The permeability of ferromagnetic materials is much greater than the free space permeability ($\mu_r \geq 1$). The field lines distribution of a ferromagnetic material placed in a uniform magnetic field are reported in Figure 4.1c.

  When a ferromagnetic material is in the un-magnetised state, the domains are nearly randomly organised as shown in Figure 4.2a and the net magnetic field for the part as a whole is zero. When a magnetising force is applied, the domains become aligned as shown in Figure 4.2b to produce a strong magnetic field within the part. The boundaries between the adjacent domains consist of thin transition regions called as domain walls.

(a)

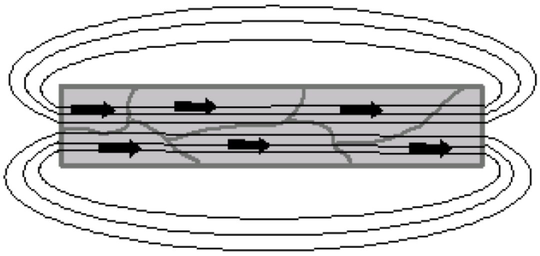

(b)

Figure 4.2. *Domain comparison in a un-magnetised* (a) *and magnetised* (b) *ferromagnetic material.*

In addition, strong magnetic ferromagnetic materials lose all their magnetic properties if they are heated to a critical temperature (Curie temperature). This is because the magnetised domains will organise themselves randomly after theirs atoms are being heated.

The main characteristics of magnetic materials are summarized in Table 4.1.

Table 4.1. *Characteristics of magnetic materials.*

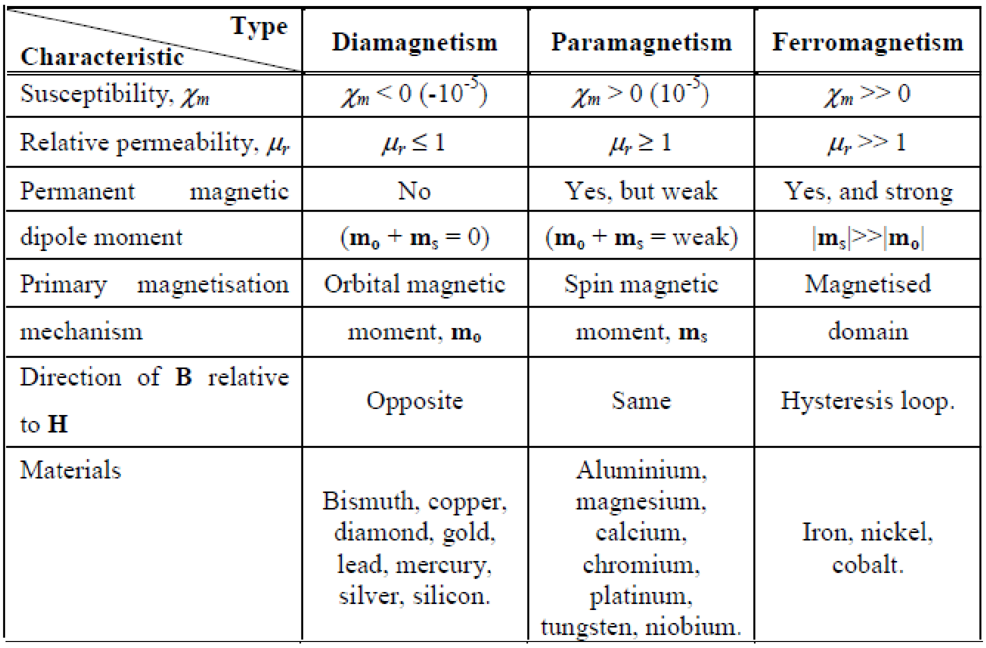

Type / **Characteristic**	**Diamagnetism**	**Paramagnetism**	**Ferromagnetism**
Susceptibility, χ_m	$\chi_m < 0\ (-10^{-5})$	$\chi_m > 0\ (10^{-5})$	$\chi_m >> 0$
Relative permeability, μ_r	$\mu_r \leq 1$	$\mu_r \geq 1$	$\mu_r >> 1$
Permanent magnetic	No	Yes, but weak	Yes, and strong
dipole moment	$(\mathbf{m}_0 + \mathbf{m}_s = 0)$	$(\mathbf{m}_0 + \mathbf{m}_s = \text{weak})$	$\lvert\mathbf{m}_s\rvert >> \lvert\mathbf{m}_0\rvert$
Primary magnetisation	Orbital magnetic	Spin magnetic	Magnetised
mechanism	moment, $\mathbf{m}_0$	moment, $\mathbf{m}_s$	domain
Direction of **B** relative to **H**	Opposite	Same	Hysteresis loop.
Materials	Bismuth, copper, diamond, gold, lead, mercury, silver, silicon.	Aluminium, magnesium, calcium, chromium, platinum, tungsten, niobium.	Iron, nickel, cobalt.

- ***Hysteresis***

The magnetisation behaviour of the ferromagnetic materials is described by the *B-H* magnetisation curve (hysteresis loop) as shown in Figure 4.3*b*.

The loop is generated by measuring the magnetic flux *B* of a ferromagnetic material while the magnetising force *H* is changed. A ferromagnetic material that has never been previously magnetised or has been thoroughly demagnetised will follow the dashed line (initial magnetization curve) as *H* is increased, as shown in Figure 4.3*a*. As the line demonstrates, the greater the amount of current applied, the stronger the magnetic field in the component. At point “a” almost all of the magnetic domains are aligned and an additional increase in the magnetising force will produce very little increase in magnetic flux. The material has reached the point of magnetic saturation.

When H is reduced down to zero, the curve will move from point "a" to point “b”. At this point, it can be seen that some magnetic flux remains in the material even though the magnetising force is zero. This is referred to as the point of retentivity on the graph and indicates the remanence or level of residual magnetism in the material, where some of the magnetic domains remain aligned but some have lost their alignment. As the magnetising force is reversed, the curve moves to point “c”, where the flux has been reduced to zero. This is called the point of coercivity on the curve: the reversed magnetising force has flipped enough of the domains so that the net flux within the material is zero. The force required to remove the residual magnetism from the material, is called the coercive force or coercivity of the material.

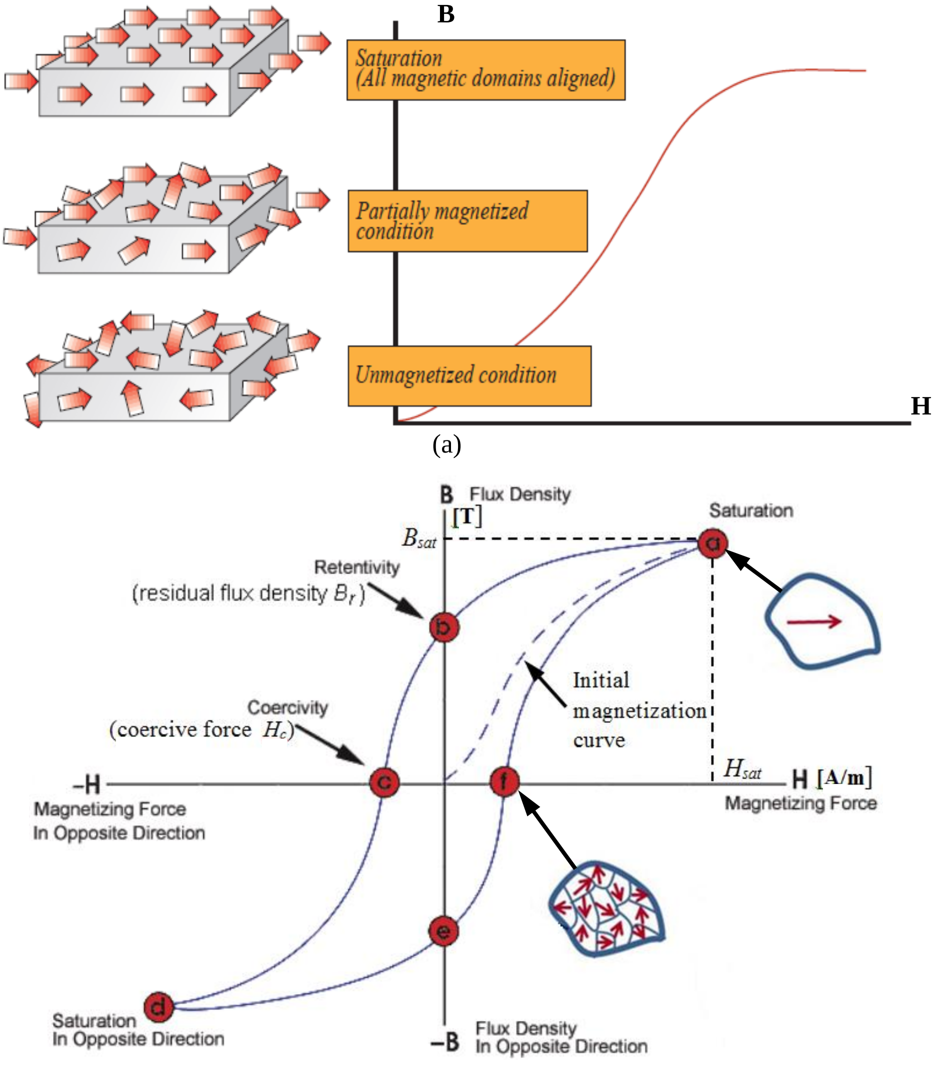

(a)

(b)

Figure 4.3. *Hysteresis loop: initial magnetization curve* (a) *and hysteresis loop profile* (b).

As the magnetising force is increased in the negative direction, the material will again become magnetically saturated but in the opposite direction (point “d”). Reducing *H* to zero brings the curve to point “e”. It will have a level of residual magnetism equal to that achieved in the other direction. Increasing H back in the positive direction will return B to zero. Notice that the curve did not return to the origin of the graph because some force is required to remove the residual magnetism. The curve will take a different path from point “f” back to the saturation point where it completes the loop. The complete close loop “abcdefa” is called as a hysteresis loop.

The *saturation field strength* H_{sat} [A/m] is the minimum field strength that has to expend to reach the region of magnetic saturation. For field strength $H \geq H_{sat}$ the ferromagnetic material behaviour is like to free space, thus:

$$\frac{dB}{dH} = \mu_0 \tag{4.1}$$

The *remanence induction* or *residual flux density* B_r [T] is the induction remaining in a closed magnetic circuit if after achieve the saturation condition ($H \geq H_{sat}$), the field strength return to zero.

The *coercive force* or *coercivity* H_c [A/m] is the magnetic field strength at which the induction of a magnetic material previously magnetised up to saturation becomes zero.

The *maximum energy product* $(BH)_{max}$ [GOs (Gauss-Oersted) = $8\cdot10^3$ Ws/m^3] is the maximum product of the flux density and field strength attained on the demagnetization curve (Figure 4.4).

The values of B and H at $(BH)_{max}$ are designated as B_a and H_a.

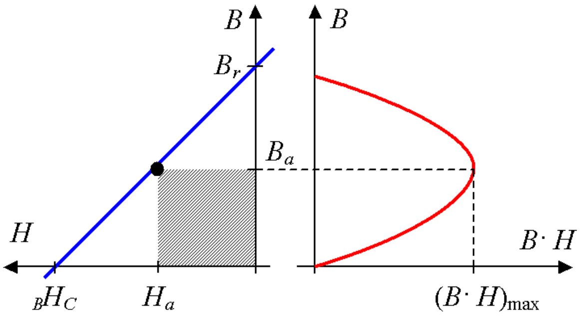

Figure 4.4. Energy product of a magnetic material, the dot represents the maxim value $(BH)_{max}$.

The maximum energy product occurs at the point on the demagnetisation curve where a contour line would just touch it. Such feature is a very important characteristic of permanent magnet materials, because it is a measurement of the maximum amount of magnetic energy stored in a magnet.

In general, magnetic materials can be classified as magnetically "soft" and "hard" materials. The first ones have a smaller hysteresis loop (Fig. a), while the second ones have a bigger hysteresis loop (Fig. b).

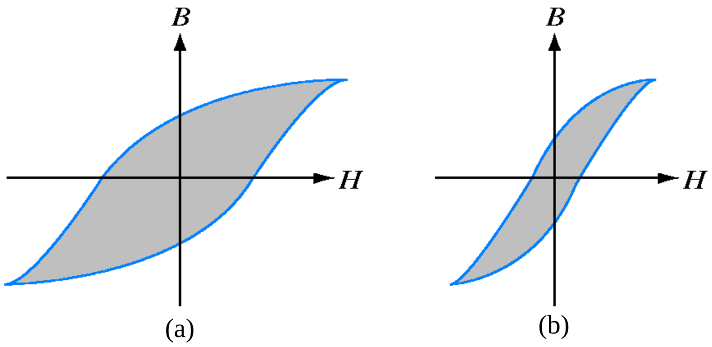

Figure 4.5 *Comparison between hysteresis loop of a hard material* (a) *and of a soft material* (b).

The characteristics of soft magnetic materials are: the facility to magnetize and demagnetize, they have low hysteresis loss, high permeability and low magnetic stored energy. On the other hand, hard magnetic materials retain their magnetism and are difficult to demagnetize even after the removal of applied magnetic field. They have large hysteresis loss and a high magnetic stored energy.

For such reason, soft magnetic materials are used to build iron cores of electrical machines, whereas hard magnetic materials are used for to build permanent magnets.

4.2 Hard ferromagnetic materials - permanent magnets

The hard ferromagnetic materials are used to build permanent magnets.

The most popular permanent magnet materials are: ferrite, alnico, SmCo and NdFeB. While there are several processing options, magnets can be divided into fully dense or bonded, leading to isotropic or anisotropic magnets.

The historical trend of permanent magnets is reported in Figure 4.6, and in Figure 4.7 shows the magnetization curve.

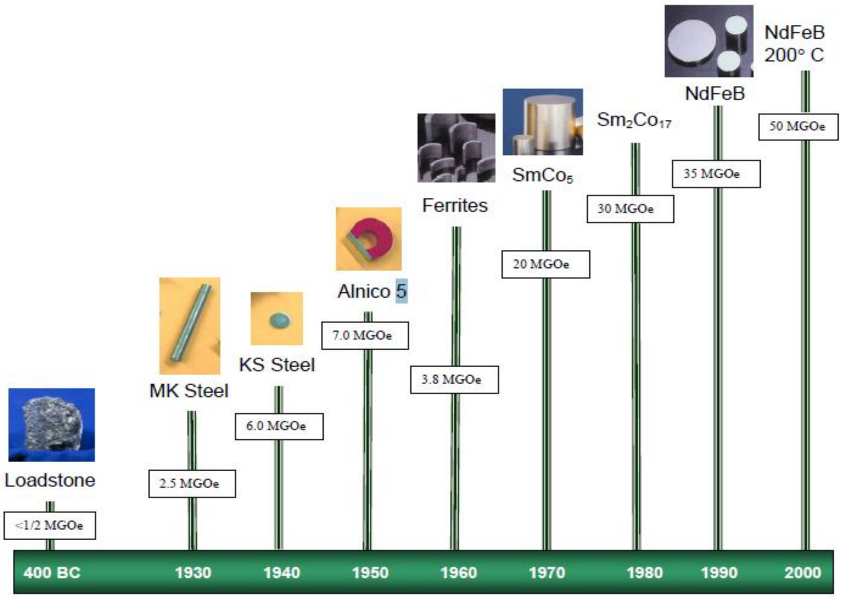

Figure 4.6. *Historical trend of permanent magnets.*

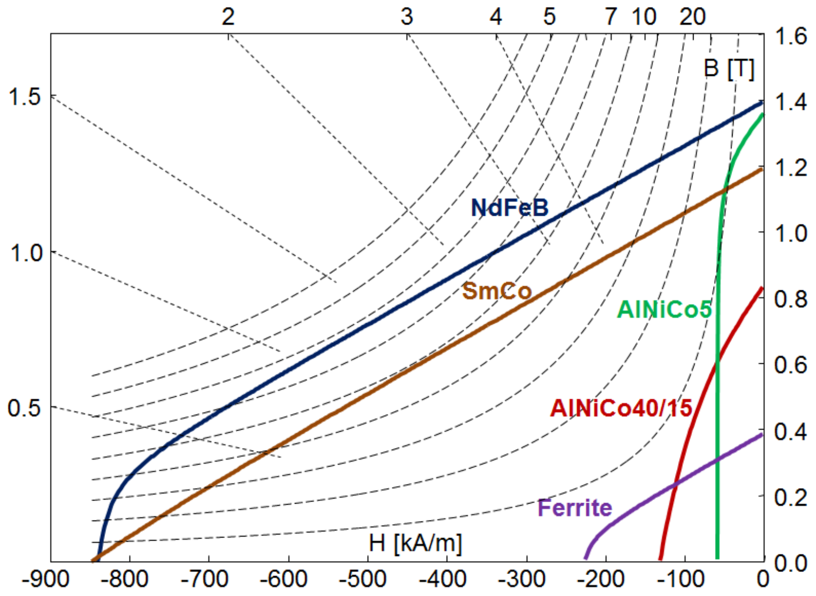

Figure 4.7. *Magnetization curves of hard ferromagnetic materials.*

The main properties, in terms of residual flux density, coercivity, intrinsic coercivity and maximum energy product are reported in Table 4.2.

Table 4.2. *Comparison of the main properties of PM materials in terms of: residual flux density, coercivity, intrinsic coercivity and maximum energy product.*

Material	Grade	B_r [kG]	H_c [kOe]	H_{ci} [kOe]	BH_{max} [MG Oe]
NdFeB	39H	12.8	12.3	21.0	40.0
NdFeB	26	6.8	5.8	10.3	26.0
SmCo	B10N	10.5	9.2	10.0	10.0
Alnico	5	12.5	0.6	0.6	5.5
Ceramic	8	3.9	3.2	3.3	3.5

- ***Ferrite***

  Ferrite magnets, also called ceramics, are made of a composite of iron oxide and barium carbonate ($BaCO_3$) or strontium carbonate ($SrCO_3$). Widely available since the 1950's, this materials is commonly available and at lower cost than other types of materials used in permanent magnets.

  They are made using pressing powder in a die and then fusing the powder into a solid material with heat. While the sintered magnets are solid, their physical properties are more similar to a ceramic and are easily broken and chipped.

  Ferrite magnets are brittle and hard, they generally require diamond wheels to grid and shape. These magnets come in a number of different grades: they can be isotropic, namely with equal magnet properties in all directions; or they can be anisotropic, that are magnetised in the pressing direction. The anisotropic method delivers the highest energy product among ceramic magnets at values up to 3.5 MGOe.

  Ferrite magnets have a good balance of magnetic strength, resistance to demagnetizing and economy. Nowadays, they are the most widely used magnets in cheap applications.

  Beneficial characteristics of ferrite magnets include their low cost, high coercive force, resistance to corrosion, and high heat tolerance. Drawbacks include their low energy product or "strength", low mechanical strength, and the ferrite powder on the surface of the material which can rub of and cause soiling.

- ***Alnico***

  Alnico magnets are made up of an alloy of aluminium (Al), nickel (Ni) and cobalt (Co), with small amounts of other elements added to enhance the properties of the magnet. They have good temperature stability, good resistance to corrosion, but are prone to demagnetization.

  Alnico magnets are produced by two typical methods: casting or sintering. Sintering offers superior mechanical characteristics, whereas casting delivers higher energy products (up to 5.5 MGOe) and allow for the design of intricate shapes. There are anisotropic grades that provide for a preferred direction of magnetic orientation.

  Beneficial characteristics of Alnico magnets include their high corrosion resistance, high mechanical strength and very high working temperatures. Drawbacks include their higher cost, low coercive force, easy of demagnetization and low energy product.

- ***Samarium cobalt (SmCo)***

  Samarium cobalt is a type of rare earth magnet material that is highty resistant to oxidation, has a higher magnetic strength than ferrite and alnico and better temperature resistance than neodymium materials. They offer the best temperature characteristics of all rare earth magnets and can withstand temperatures up to 350 °C.

  Sintered SmCo magnets are brittle and prone to chipping and cracking and may fracture when exposed to thermal shock.

  Due to the high cost of samarium, SmCo magnets are used only in application where high temperature and corrosion resistance is critical.

  Beneficial characteristics of SmCo magnets include their high corrosion resistance, high energy product and high temperature stability. Drawbacks include their high cost and very low mechanical strength.

- ***Neodymium iron boron (NdFeB)***

  Neodymium iron boron is another type of rare earth magnetic material. NdFeB is the most advanced commercialized permanent magnet material available nowadays. This magnet has similar properties as the SmCo magnets except that it is more easily oxidized and generally does not have the same temperature resistance. However, NdFeB magnets have the highest energy products approaching 50 MGOe and they are mechanical stronger than SmCo magnets.

  NdFeB material is more costly by weight than ferrite or alnico, but produces the highest amount of flux per unit of volume or mass making it very economical for many applications. Their high energy products lend themselves to compact designs that result in innovative applications and lower manufacturing costs.

  NdFeB magnets have to protect again the corrosion. Surface treatments have been developed that allow them to be used in most applications. These treatments include copper, silver, gold, nikel, zinc and tin plating and epoxy resin coating.

  Beneficial characteristics of NdFeB magnets include their very high energy product, very high coercive force and moderate temperature stability. Drawbacks include lower mechanical strength and low corrosion resistance when not properly coated or plated.

- ***Bonded magnets***
  All of the above mentioned materials are available as bonded grades by either extrusion, compression, calendaring or injection molding processes. The magnetic properties are lower because they sometimes lose their anisotropy and they are not fully dense due to the introduction of resins and epoxies. The main advantage to this group is that they can be made in complex shapes and can be insert, over-molded and co-molded with other materials.

The main properties of above mentioned PM materials, with advantages and drawbacks, are listed in Table 4.3. In Table 4.4 are reported the Curie T_c and the maximum T_M temperatures of main PM materials.

Table 4.3. *Comparison of the main characteristics (advantages and drawbacks) of the main PM materials.*

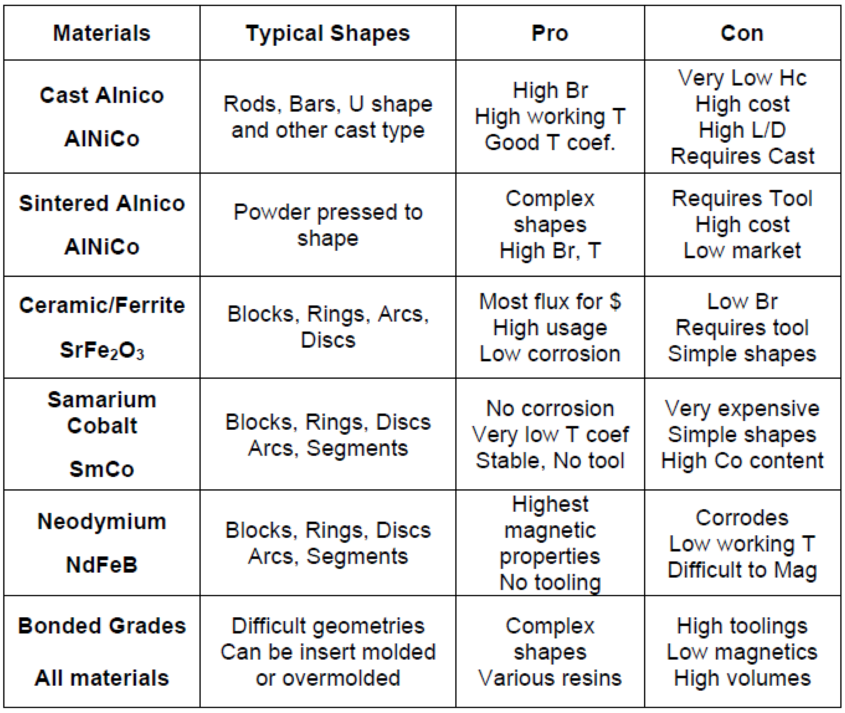

Materials	Typical Shapes	Pro	Con
Cast Alnico **AlNiCo**	Rods, Bars, U shape and other cast type	High Br High working T Good T coef.	Very Low Hc High cost High L/D Requires Cast
Sintered Alnico **AlNiCo**	Powder pressed to shape	Complex shapes High Br, T	Requires Tool High cost Low market
Ceramic/Ferrite **$SrFe_2O_3$**	Blocks, Rings, Arcs, Discs	Most flux for $ High usage Low corrosion	Low Br Requires tool Simple shapes
Samarium Cobalt **SmCo**	Blocks, Rings, Discs Arcs, Segments	No corrosion Very low T coef Stable, No tool	Very expensive Simple shapes High Co content
Neodymium **NdFeB**	Blocks, Rings, Discs Arcs, Segments	Highest magnetic properties No tooling	Corrodes Low working T Difficult to Mag
Bonded Grades **All materials**	Difficult geometries Can be insert molded or overmolded	Complex shapes Various resins	High toolings Low magnetics High volumes

Table 4.4. *Curie temperature and maximum temperature of main PM materials.*

Material	**T_c [°C]**	**T_M [°C]**
NdFeB	310	150
SmCo	750	300
Alnico	860	540
Ceramic	460	300

4.3 The effect of temperature variation

All permanent magnet materials are temperature sensitive and it is important to take this into consideration when designing magnetic circuits where a high degree of temperature stability is necessary or where high maximum temperatures are likely to be reached in operation.

Temperature changes have an effect on the demagnetisation curves with different coefficients of both remanence and coercivity. As can be seen from Figure 4.8, the general shape of the curve remains the same but has varying values of remanence and coercivity with temperature changes.

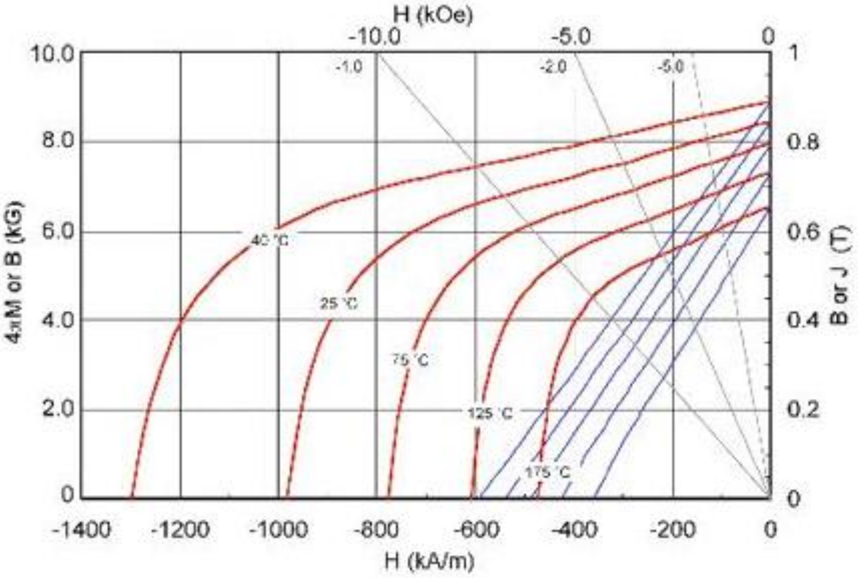

Figure 4.8. *Hysteresis loop changing as a function of temperature (material: MQP-14-12).*

To minimise the effect of temperature on the field produced by a permanent magnet, it is advisable to operate above the ‘knee’ in the demagnetisation curves.

However the temperature effects are of two types. The reversible changes where the initial flux is restored when the magnet returns to the original temperature; and the irreversible changes where the losses are permanent, but can be restored by re-magnetising the ferromagnetic material.

The reversible changes are usually only dependent upon the material composition, whereas the irreversible losses are largely dependent on the working point and intrinsic coercivity of the material grade.

The manufacturer data-sheet usually report two type of temperature:

- T_{Curie}: is the Curie temperature at which the elementary magnetic moments are randomized and the material is demagnetized, the magnetism can only be restored by renewed magnetization below this temperature;

• T_{max}: is the maximum practical operating temperature in air, for general classes of major materials.

Table 4.4 reports these temperatures for the mentioned PM materials.

Changes in temperature affect both flux output, which is proportional to B_r, and resistance to demagnetization, which is proportional to H_c (Fig.). The amount to which these change is called the reversible temperature coefficient of induction (α) or the reversible temperature coefficient of coercivity (β). The change in B_r and H_c as a function of temperature is generally not linear.

The induction and coercivity as function of the temperature variation is given by:

$$B(T) = B_0\,[1 + \alpha\,(T - T_0)] \tag{4.2}$$

$$H(T) = H_0\,[1 + \beta\,(T - T_0)] \tag{4.3}$$

where B_0 and H_0 are the induction and coercivity at temperature T_0, respectively.

Table 4.5 reports the reversible temperature coefficients of induction and coercivity for different PM materials. Note also, that ferrite has a large positive reversible coefficient of coercivity. That means as temperature is reduced, intrinsic coercivity decreases resulting in a knee developing in the normal curve.

Table 4.5. *Reversible temperature coefficients of induction (α) and coercivity (β).*

Material	α [°C^{-1}]	β [°C^{-1}]
NdFeB	-0.12	-0.60
SmCo	-0.04	-0.30
Alnico	-0.02	0.01
Ceramic	-0.20	0.30

4.4 Manufacturing and magnetization process

Depending on the type of material, the following processes are used to manufacture permanent magnets:

- ***Sintering***: the sintering process involves compacting fine powders at high pressures in an aligning magnetic field, then sintering it into a solid shape. After sintering, the “ingot” is rough and must be machined to achieve close tolerances. The complexity of shapes that can be pressed using this process is limited. Neodymium and Samarium cobalt powders are compressed to form magnets by:
  - *Isostatic pressing*: the powder is compacted with the same force from all directions. These magnets have the highest possible magnetic values because of the higher density achieved using this technique.

  - *Compressing in tools*:
    a. *Transverse Field Pressing*. The powder is compacted at right angles to the magnetic flux. These magnets have a weaker field compared to the isostatic pressed ones, but stronger compared to the parallel pressed magnets.
    b. *Parallel Compressing*. The powder is compacted parallel to the magnetic field.
- ***Compression Molding***: this method is commonly used to make NdFeB magnets using melt spun Nd powders that are epoxy coated. The powders are compacted and then heat cured for the epoxy to perform the binding function. These magnets are typically isotropic.

  Injection Molding Neodymium, Samarium Cobalt, and Ferrite Materials can be manufactured by injection molding. Common binders for injection molding are polyamides. The advantage of using this method is the possibility to get a better tolerance directly from the tool with no required heat treatment, and the magnets can be produced in complex shapes. They can be combined with other materials for over-molding or insert molding.
- ***Casting***: this process is used for manufacturing Alnico. Process is similar to the casting of other metals. Parts are formed in sand casts which can be complex.
- ***Calendering and Extruding***: flexible NdFeB and Ferrite magnets with Nitrile rubber binders are made using this method. The process is similar to that for vinyl sheets. Parts are later die cut or stamped from sheets of various thicknesses.

As regard the magnetization process, magnets can be delivered magnetized and un-magnetized. Many automated production methods rely on the megnets being incorporated into assemblies in a un-magnetized state and later magnetized once the assembly is completed. A magnet can be magnetized in a variety of directions (Figure 4.9).

Anisotropic material must be magnetically orientated during the production of the material. They therefore are inclined to a fixed orientation. The radial orientation is quite difficult to produce and it is only available in some isotropic materials.

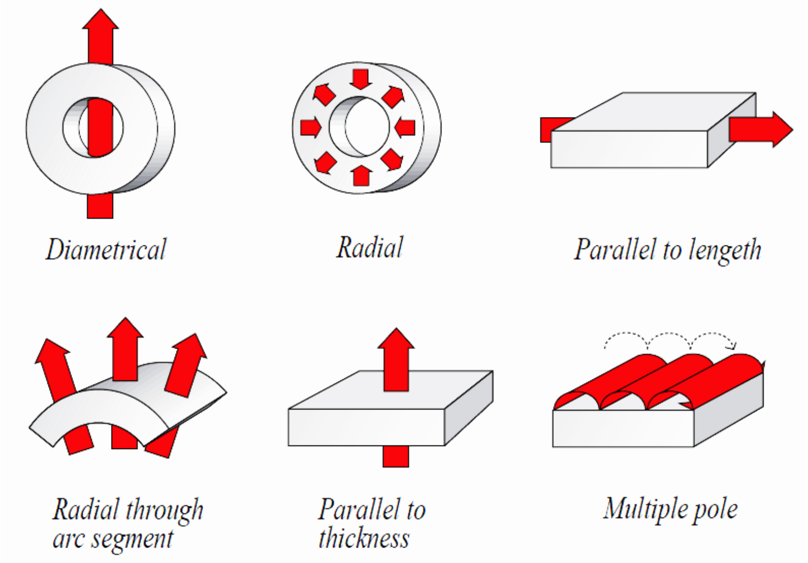

Figure 4.9. *Magnetizing patterns.*

Permanent magnet materials are believed to be composed of small regions or “domains” each of which exhibit a net magnetic moment. An un-magnetized magnet will possess domains which are randomly oriented with respect to each other, providing a net magnetic moment of zero. Thus a magnet when demagnetized is only demagnetized from the observer’s point of view. Magnetizing fields serve to align randomly oriented domains to give a net, externally observable field.

The objective of magnetization is initially to magnetize a magnet to saturation, even if it will later be slightly demagnetized for stabilization purposes. Saturating the magnet and then demagnetizing it in a controlled manner ensures that the domains with the least commitment to orientation will be the first to lose their orientation, thereby leading to a more stable magnet. Not achieving saturation, on the other hand, leads to orientation of only the most weakly committed domains, hence leading to a less stable magnet.

Anisotropic magnets must be magnetized parallel to the direction of orientation to achieve optimum magnetic properties. Isotropic magnets can be magnetized through any direction with little or no loss of magnetic properties. Slightly higher magnetic properties are obtained in the pressing direction.

4.5 Soft ferromagnetic materials - iron core materials

Soft magnetic materials are used to build the iron cores of the electric machines, thanks to their low hysteresis loss.

- ***Hysteresis losses***
  The hysteresis losses can be calculated considering a magnetic circuit of length L and section S, supply by a sinusoidal current with I RMS value. The supply power results:

$$P = \frac{dW}{dt} = E\ I = N\frac{d\varphi}{dt}\ I = N\ I\ A\ \frac{dB}{dt} = H\ L\ A\ \frac{dB}{dt} = H\ V\ \frac{dB}{dt} \tag{4.4}$$

Thus, the energy supply by the source in going from point “g” to point “b” (Fig. a), results:

$$W_s = \int_g^b H\ V\ dB = V\int_g^b H\ dB \tag{4.5}$$

This integral corresponds to the shaded area, shown in Figure 4.10a; it is equal to the energy supplied per unit volume of the magnetic core.

When the current is in the same direction but is decreasing (from point “b” to point “c” of Figure 4.10b), the polarity of the induced e.m.f. is reversed, according to Lenz’s law, the result that the energy return to the source is:

$$W_r = V\int_b^c H\ dB \tag{4.6}$$

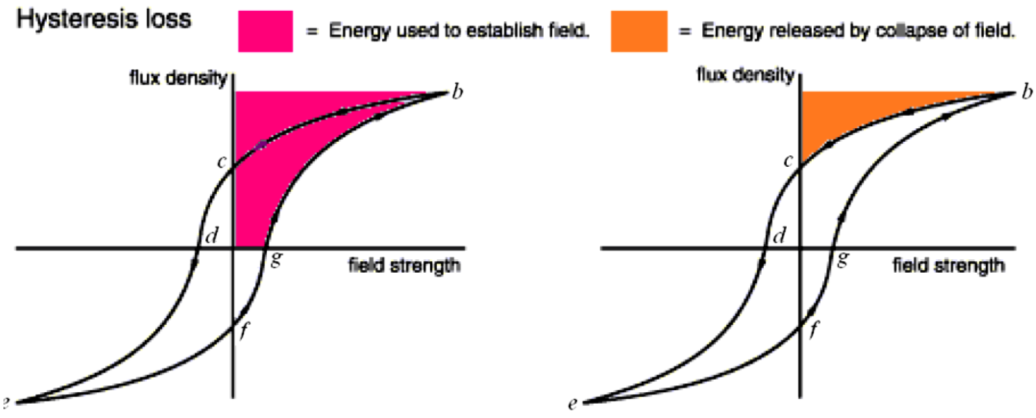

(a) (b)

Figure 4.10. *Hysteresis losses: energy supply by the source* (a) *and energy return to the source* (b).

Finally, considering a complete loop "$gbcdefg$", the energy supply by the source W_h [J], results:

$$W_h = V \oint H \, dB \tag{4.7}$$

The area of the hysteresis loop in tesla-ampere turns/meter or in weber-ampere turns/m^3 is therefore the number of joules dissipated per cubic meter and per cycle in the core (energy dissipated per unit volume per cycle). The energy dissipated per unit volume per cycle is named as the hysteresis loss (Figure 4.11). This energy loss is due to the friction encountered during domain-wall motion and rotation.

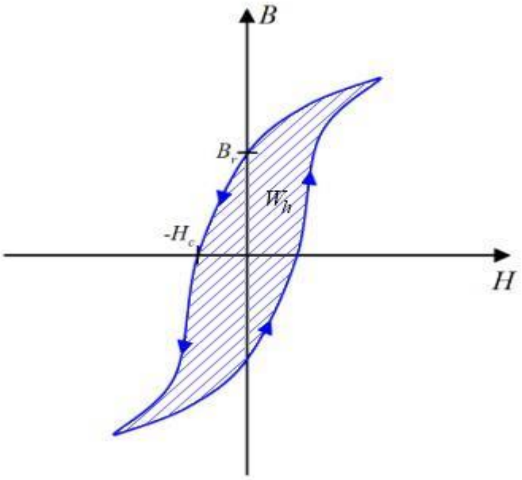

Figure 4.11. *Hysteresis losses.*

Hysteresis loss can be minimised only by selecting a soft magnetic material with a narrow hysteresis loop. This is because the small loop area corresponds to a low hysteresis loss. Thus, soft magnetic materials are suitable for armature and transformer core. On the other hand, hard magnetic materials have larger loop areas which correspond to higher hysteresis loss. Due to this reason, hard magnetic materials are not suitable for alternating magnetisation but they are suitable for permanent magnet.

The specific power of the hysteresis loss P_h [W/m^3] is empirically given by Steinmetz hysteresis law:

$$P_h = k_h \, f \, \hat{B}^n \tag{4.8}$$

where k_h is the coefficient of hysteresis losses (it depends on the nature of the ferromagnetic material), f is the frequency [Hz], $\hat{B}$ is the peak value of the flux density [T] and n is a coefficient included between 1.5 and 2.5

- ***Eddy current losses***

When a changing magnetic field cuts through a sample of metal or magnetic materials that is not connected to a circuit, by Faraday's law, a circulating current is induced. This current is known as eddy current, it is localised within that material and has a flow pattern as shown in Figure 4.12.

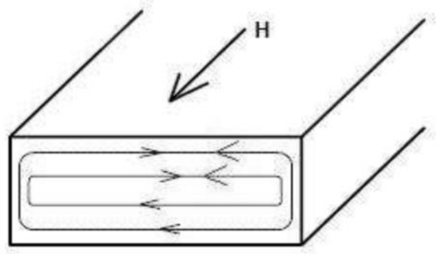

Figure 4.12. *Eddy current (black arrows) induced within the metal or magnetic material and the current induced by the external magnetic field (red arrows).*

Eddy current creates losses through Joule heating, and it reduces the efficiency of device that operates under alternating magnetic field condition such as iron core of transformers and alternating current motors. This power loss is known as eddy current loss due to the induced eddy current in the metal or magnetic materials.

In general, the resistance R [Ω] of a material is given by:

$$R = \rho \frac{l}{S} \tag{4.9}$$

where ρ is the resistivity of the material [Ω m],l is the length of the piece of material [m], and S is the cross-sectional area of the piece of material [m^2].

In order to reduce the resistance the material resistivity can be increased by adding silicon. Another effective way to achieve low eddy current loss is by using lamination of electrical metal sheets, this means to reduce the surface available for the eddy current. These metal sheets are coated with insulator which breaks the eddy currents path.

As for the hysteric losses, the eddy current losses P_e [W/kg] can be expressed by analytically way:

$$P_e = k_e\, f^2\, \hat{B}^2 \tag{4.10}$$

where k_e is the eddy current losses coefficient (it depends on the nature of the ferromagnetic material).

The total eddy current caused by the local eddy currents is generally higher than that predicted by the formulation under the global eddy current assumption. The different is known as the excess loss. Since it is very difficult to calculate the total average eddy current loss analytically, by statistical analysis, it was postulated that for most soft magnetic materials under a sinusoidal magnetic field excitation, the excess loss P_{ex} [W/kg] can be predicted by:

$$P_{ex} = k_{ex}\, f^{3/2}\, \hat{B}^{3/2} \tag{4.11}$$

where k_{ex} is the excess losses coefficient (it depends on the nature of the ferromagnetic material).

The total loss can be calculated by summing equations (4.9), (4.10) and (4.11)

The Figure 4.13 illustrates the separation of alternating core loss of Lycore-140, 0.35 mm non-oriented sheet steel at 1 T. By equations (4.9), (4.10) and (4.11) the coefficients of different loss components can be obtained by fitting the total core loss curves, as shown in Figure 4.13.

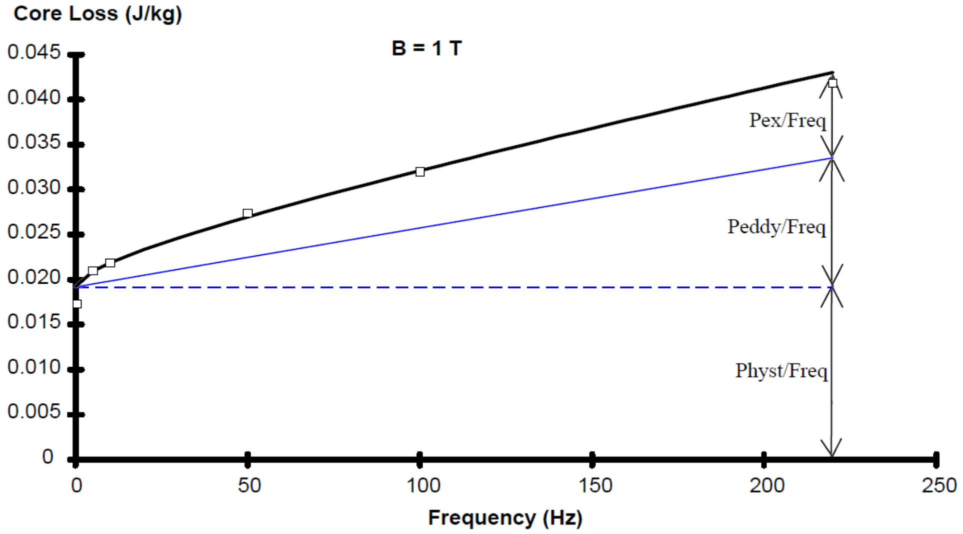

Figure 4.13. *Separation of alternating core loss of Lycore-140 at B=1 T.*

Although eddy current reduces the efficiency of an electromagnetic device, but in proper circumstances, it can be used as a non-destructive tool to measure material thickness and coating thickness. It also can be used in the crack detection, material identification, heat damage detection, and heat treatment monitoring.

4.6 Soft magnetic composite materials

The ideal soft magnetic composites (SMC) material would be an isotropic electric insulator with very high magnetic permeability, low coercivity and high saturation induction. In addition the material should be easy to shape into 3-dimensional structures in order to fully take advantage of the material's isotropic nature.

The most common soft magnetic material used today is steel sheet, either as pure iron or alloyed with elements like Si in order to enhance performance. The steel sheets (with an electrically insulating coating) are punched into 2-dimensional sheets and stacked to form 2-dimensional laminated structures. Steel laminate is clearly the dominant material for applications up to several hundred Hz. There are many reasons for this, good magnetic properties (high induction, low losses at lower frequencies) and normally low cost. However, this material also has drawbacks; it is by its laminated nature essentially a 2-dimensional material. For higher frequencies, very thin and often alloyed sheets must be used in order to minimize the eddy current losses. In these cases, the cost for both rolling the steel sheets and punching those increases dramatically. Saturation induction will also decrease due to the increased air-gaps between the sheets. The punching operation also results in plastic deformation (distortion of the crystal lattices), which causes deterioration of the magnetic properties.

From this we can conclude that none of the traditional materials fully meet the requirements for an ideal soft magnetic material as outlined above.

Powdered Soft Magnetic Composites (SMCs) do however in many respects resemble the ideal material, as they are isotropic materials consisting of small insulating iron particles. Intricate 3D-shapes could be obtained by the well-established, cost-effective P/M-compaction process. Saturation induction is close to the laminates and eddy current losses are significantly lower due to the smaller size of the particles (typically 5-200μm) compared to the thickness of the steel sheets (normally 200-1000μm). However SMCs have a distributed air-gap, leading to lower permeability and further, due to the plastic deformation of the particles that takes place during the compaction step, higher hysteresis losses. A heat treatment operation after the compaction will partly relieve the stresses.

The benefits of replacing the conventional laminated core in an electric machine with the powdered iron composites are considerable, and include:

- Essentially unity iron stacking factor, due to the fact that a SMC core is of compact structure.
- Potential for reduced air gap length as a result of the tight tolerances maintained in manufacturing SMC material.
- Increased copper fill factor (up to 66% vs. the typical value of 33%); reduced copper volume as a result of increased fill factor and reduced end winding length.
- Reduced copper loss as a result of the reduced copper volume;

- Reduced high frequency tooth ripple losses since the SMC has essentially no eddy current losses;
- The above two items suggest a potential increase in the overall efficiency;
- Modular construction allows the possibility of easy removal of an individual modular unit for quick repair or replacement;
- Possibility of producing three dimensional flux patterns in the SMC material and thus, to improve the electric machine performance.
- Reduced axial length–over–end–winding dimension as a result of the more compact end winding.
- Absence of the phase insulation as a result of using non–overlapping windings; also, there is an additional potential elimination of the ground wall insulation since the SMC core (stator) itself acts as an insulator.
- There is no need to stress relief, as in the case of the stator lamination after punching and assembling the stack; this is a relatively costly and time consuming task, (stress relief is, however, included in the process of manufacturing the SMC parts).
- Reduced bearing currents in the presence of PWM waveforms, because of the use of SMC which acts as insulation against this type of current flow.
- Stator is easily recyclable since the stator can again be compressed back into powered form with pressure and the copper windings readily removed.

These advantages are, of course, accompanied by a number of drawbacks. The most significant of these is the relatively low relative permeability of roughly 500 for the most commonly used SOMALOY 500. Other concerns include relatively low rupture strength, as well as an important portion of iron losses at lower frequency, due to the increased hysteresis loss, although there is almost no eddy–current loss.

The SMC concept is very flexible as the final properties of the component will depend on the properties of the iron powder, coating, lubricant / binder, compaction and heat treatment. A schematic of the factor that affect the SMCs properties is show in Figure 4.14.

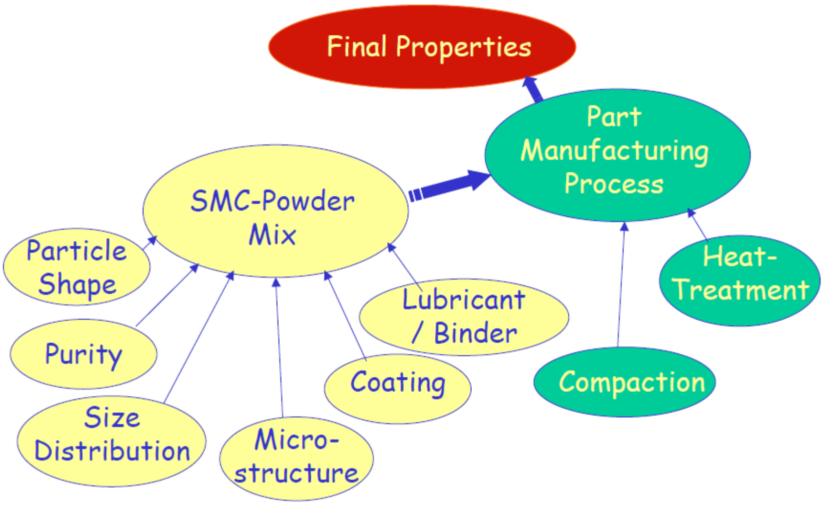

Figure 4.14. *Factor affecting SMCs properties.*

4.6.1 Powder characteristics

Particle shape

In principle an SMC material could be built up by particles having different shapes. The widely used particle shape to build SMC materials are: fibres, flakes and spheres (Figure 4.15).

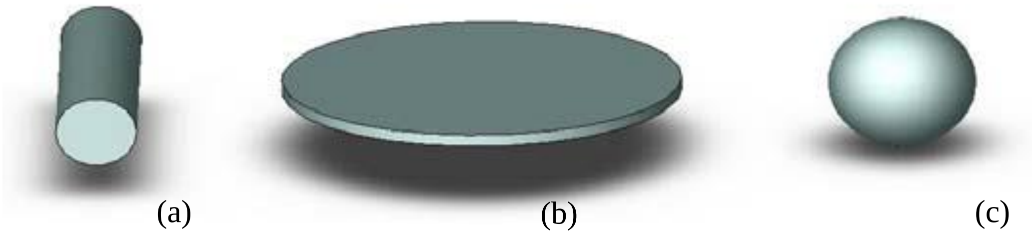
(a) (b) (c)

Figure 4.15. *An example of tree possible particle shape of SMC materials: fibre* (a), *flake* (b) *and sphere* (c).

- *Fibre*: The individual fibre is essentially a 1-dimensional element and its ability to carry a magnetic flux is much better in the direction along the fibre than across it. If fibres are filled into a die and compacted, the fibres will, due to the prevailing pressure situation in the die, essentially be aligned in a plane perpendicular to the compaction direction. This means a 2-dimensional material, but because the distributed air-gap will be large in all directions in this material it makes no sense.

  The most effective packing of the fibres will occur if they, in the plane perpendicular to the compaction direction, all were aligned in the same direction. Although difficult to obtain in practice, an essentially 1- dimensional material would be created. The distributed air-gap along the fibres would in this direction be relatively small and eddy currents limited to the thickness of the fibres. The fibres would probably be effectively packed, thus the material could be expected to have very good magnetic properties in this direction. In the transverse directions the situation would however be the opposite; a very large distributed air-gap and thus a poor permeability.

- *Flake*: Flaky particles will upon compaction, for the same reasons as discussed above, essentially be aligned perpendicular to the compaction direction in order to create an efficient 2-dimensional material. The distributed air-gap in this plane will be small and eddy currents limited to the thickness of the flakes.

  Therefore good properties in this plane could be expected, while the opposite situation occurs in the plane perpendicular to the flake surfaces. Nevertheless, this would be the superior 2-dimensional SMC-material.

  Another factor influencing the anisotropy for both the fibre and the flake is the demagnetisation factor, N_d.

  The demagnetisation factor determines the strength of the demagnetisation field H_d opposed to the magnetization field M, in each particle.

  $$H_d = N_d M \tag{4.12}$$

  where N_d is influenced by the shape of the particles and the direction of magnetization in such a way that it will be small in directions parallel to the fibre length and flake surface, while the opposite will occur in transverse directions. This fact makes the anisotropy even more pronounced for these materials while the demagnetizing factor is constant for isotropic shapes i.e. spheres.

- *Sphere*: This shape, is by its nature, not possible to align in any direction and a true 3-dimensional, isotropic structure is created upon compaction. As the shape is isotropic, the distributed air-gap is larger compared to the optimal directions for the fibre and flake materials, but much smaller in other transverse directions. Even if the isotropic material can in some respects be considered as a compromise, this is the only alternative that will clearly benefit from the unique shaping opportunities of the compaction process. The sphere makes it possible to manufacture parts with 3-dimensional shapes that can carry a 3-dimensional flux. This combination opens up new avenues to improve existing designs for electrical motors, linear actuators and ignition coils etc.

Purity

For steel sheets, purity of the iron is known to be of considerable importance to the magnetic properties. The same will in principle apply to iron powders. It is well known from traditional P/M that impurities affect compressibility negatively. A lower density means a larger distance between particles, i.e. a larger distributed air-gap and poorer magnetic properties. Interstitials such as O, N & C are perhaps the most poisonous and are known to have a negative effect on both compressibility, which indirectly affects the properties, and also directly on the base material, causing a significant drop in permeability and increase of coercivity. Secondary effects like so called magnetic ageing might also occur after long term operation whereupon interstitials are diffused to certain areas in the material causing pinning of magnetic domains. The effect of other alloying elements will depend from case to case. Normally the small trace elements of other metals in iron powder will not significantly affect the properties. Nowadays iron powders used for SMC materials are very pure with an extremely low content of interstitials and harmful alloying elements and hence very suitable as soft magnetic material.

The size of the particles will significantly affect the characteristics of the material. Decreasing the particle size will increase the distributed air-gap, leading to lower permeability and induction. Eddy currents will, however, decrease due to the smaller particle size. Smaller eddy currents mean a larger skin depth and as a consequence improved frequency stability and lower losses at higher frequencies. These facts are illustrated in Figure 4.16, in which two high frequency materials, Permite$^{\text{TM}}$ 55K(< 45 micron) and Permite$^{\text{TM}}$ 75K(< 150 micron) with different particle sizes are compared.

Depending on the demands of the application, the appropriate particle size should be selected.

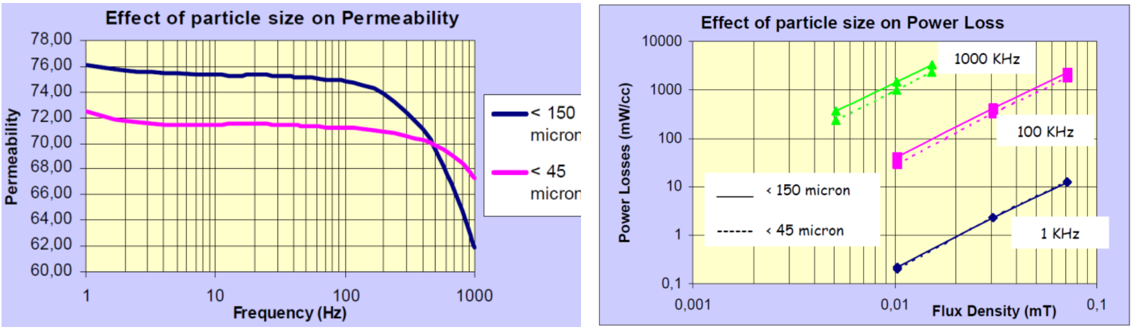

(a) (b)

Figure 4.16. *Effect of SMC particle size on permeability* (a) *and core loss* (b).

Insulating Coating

The demands on the insulating coatings of SMC materials are extremely high. Firstly they must not be too thick, as that would increase the distributed air gap. Secondly, the coating must be chemically stable in order not to be destroyed by chemical reactions during processing of the material or service in the application. Thirdly, the coating must be both hard and ductile in order to survive the pressures and friction during compaction.

In this study the influence of insulating coating on the magnetic performance was investigated. Two 100-mesh powders, uncoated and coated, were mixed with 0.5% Kenolube^{TM}, compacted at 800 MPa and heat treated at 500°C for 30min in air. The coated material resembles Somaloy^{TM} 500. The results are presented in Figure 4.17.

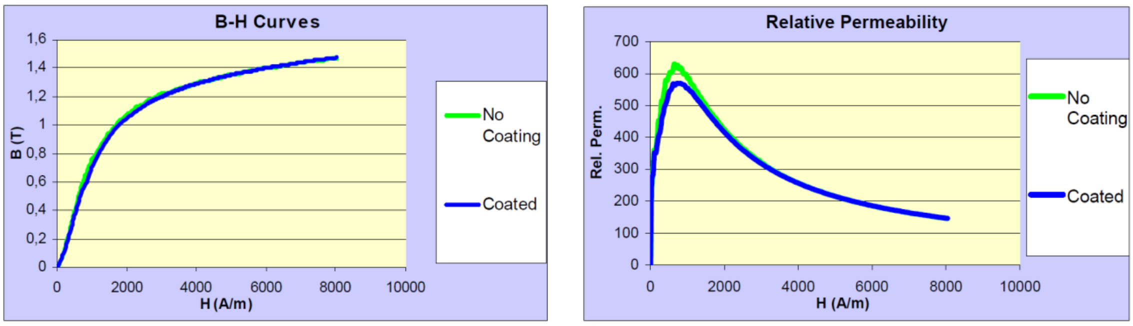

(a) (b)

Figure 4.17 *Effect of SMC insulation coating on induction* (a) *and permeability* (b).

As shown, the coating will hardly affect the induction and permeability compared to the uncoated material. In fact, the inorganic coating on the particles will facilitate the compaction, as smearing in the compaction tool will be less of a problem. From this we can conclude that the coating typically used is extremely thin and that a very small additional air-gap is being introduced.

Looking at the losses, the very positive effect of the coating is obvious. The coating significantly improves the frequency stability. This is a result of increased resistivity and means also that the coating will significantly increase the skin depth for the materials.

4.6.2 *Manufacturing process*

Compaction

SMC-materials could take direct advantage from the well-established compaction technology for traditional PM-materials.

The most critical compaction parameter influencing material performance is the compaction pressure. It is always beneficial to compact at as high compaction pressure as possible, see B-H curves in Figure 4.18.

Higher density means higher induction for a certain applied field, leading to benefits such as higher torque in rotating machine applications.

At the same time, increasing the compaction pressure makes compaction more difficult. The tool wear increases as well as the risk for tool failure. However, as the general trend for powder metallurgy is towards higher density, knowledge on how to successfully compact at high pressures is continuously improving and many companies already today are using pressures up to 800 MPa or higher.

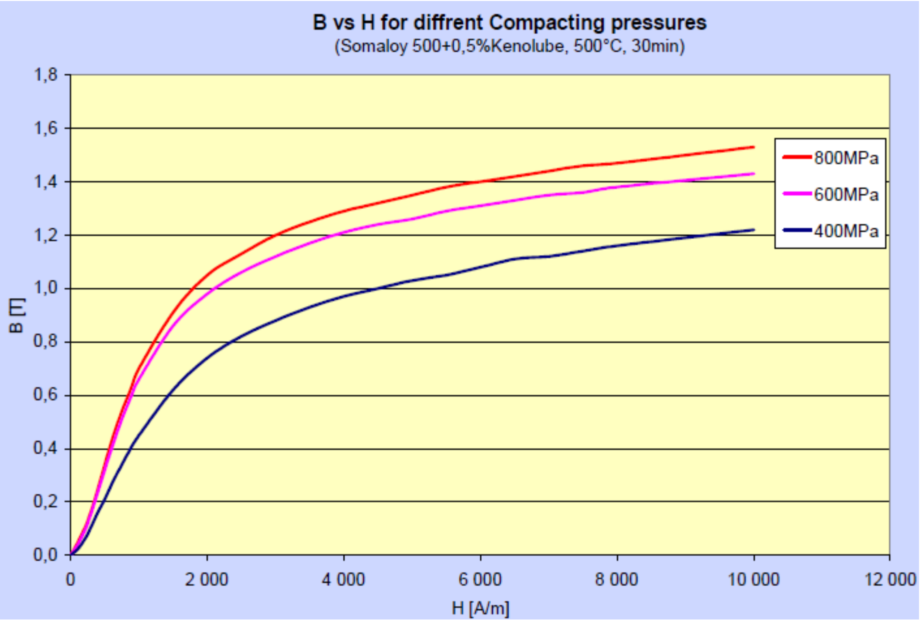

Figure 4.18. *Effect of the compaction pressure on induction.*

Heat Treatment

During compaction, plastic deformation in the particles occurs which leads to distortion of the crystal lattices. This distortion acts as an energy barrier which the domain wall motion and rotation have to overcome. As a consequence, the coercivity of the material will increase and the response to an applied field will not be so strong, i.e. a flatter and wider B-H curve. Therefore a stress-relieving operation of the compacted SMC-part, allowing for a recovery of the crystal lattice will be very beneficial for the soft magnetic properties. The inorganic coating used for the Somaloy^{TM}-type of materials has been optimised in order to withstand heat treatment to about 500°C and at this temperature the stress relaxation of the material is significant. Lowering the temperature leads to less efficient stress relaxation while higher temperatures destroy the inorganic coating, as seen in Figure 4.19.

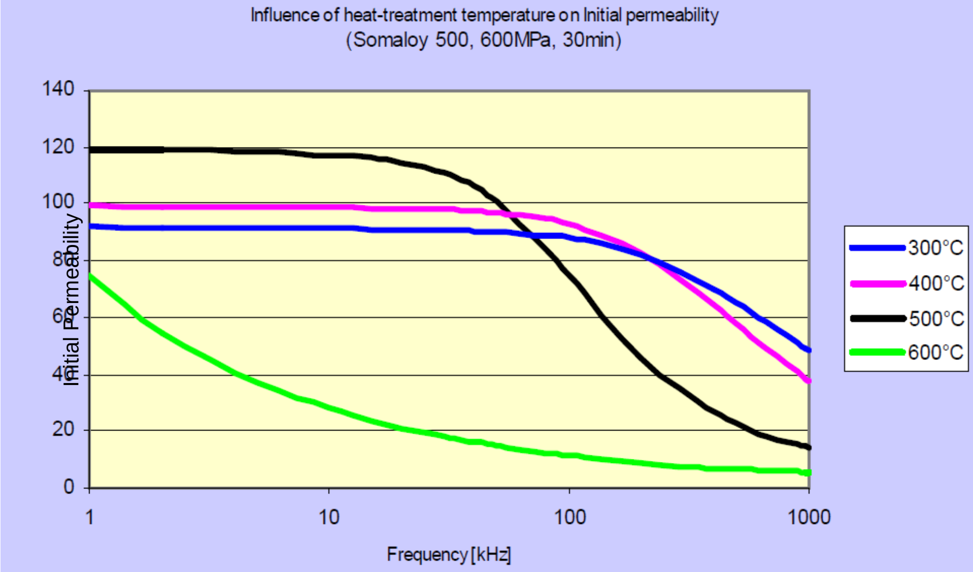

Figure 4.19. *Effect of heat treatment temperature on frequency stability.*

4.7 Analytical analysis of magnetic circuits

4.7.1 Equivalent electric circuit

Consider a simple structure consisting of a current carrying coil of N turns and a magnetic core of mean length l_c [m] and a cross sectional area A_c [m^2] as shown in the Figure 4.20. The permeability of the core material is μ_c [H/m]. Assume that the size of the device and the operation frequency are such that the displacement current in Maxwell's equations are negligible, and that the permeability of the core material is very high so that all magnetic flux will be confined within the core.

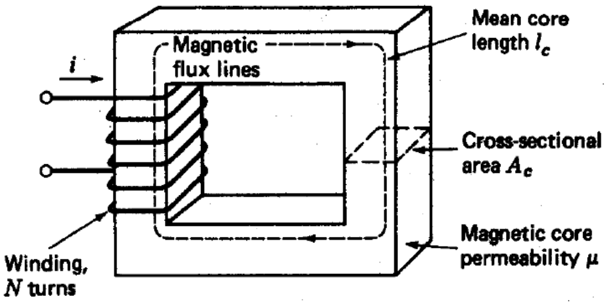

Figure 4.20. *Structure of a simple magnetic circuit.*

By Ampere’s law:

$$\oint_l H\,dl = \oint_A J\,dA \tag{4.13}$$

results:

$$H_c\, l_c = M \tag{4.14}$$

where H_c is the magnetic field strength [A/m] in the core and $M = N\,i$ the magnetomotive force [A].

The magnetic flux ϕ_c [Wb] through the cross section of the core can express as:

$$\phi_c = B_c\, A_c \tag{4.15}$$

where $B_c = \mu_c\, H_c$ the flux density in the core.

Therefore, results:

$$\phi_c = \mu_c\, H_c\, A_c = \frac{M}{\mathcal{R}_c} \tag{4.16}$$

where $\mathcal{R}_c = l_c/(\mu_c\, A_c)$ is the reluctance of magnetic circuit.

It is worth to point out, that if we take the magnetic flux ϕ_c as the “current”, the magnetomotive force M as the “emf of a voltage source” and $\mathcal{R}_c$ as the “resistance”, we have an analogy with Ohm’s law of an electrical circuit theory.

Some corresponding quantities in electric and magnetic circuit are listed in Table 4.6.

Table 4.6. *Corresponding quantities in electric and magnetic circuit.*

Electric quantities	**Magnetic quantities**
Current I	Magnetic flux Φ
Current density **J**	Magnetic flux density **B**
Conductivity σ	Permeability μ
Resistance $R = l/(\sigma\, A)$	Reluctance $\mathcal{R} = l/(\mu\, A)$
Conductance $G = 1/R$	Permeance $\mathcal{P} = 1/\mathcal{R}$
Electromotive force $V = R\, I$	Magnetomotive force $M = \mathcal{R}\,\Phi$
Electric field intensity **E**	Magnetic field intensity **H**

For nonlinear magnetic circuits, where the nonlinear magnetization curves need to be considered, the magnetic reluctance is a function of magnetic flux since the permeability is a function of the magnetic field strength or flux density (Figure 4.17*b*). Numerical or graphical methods are generally used to solve this kind of problems.

The equivalent electric circuit of a magnetic circuit is shown in Figure 4.21.

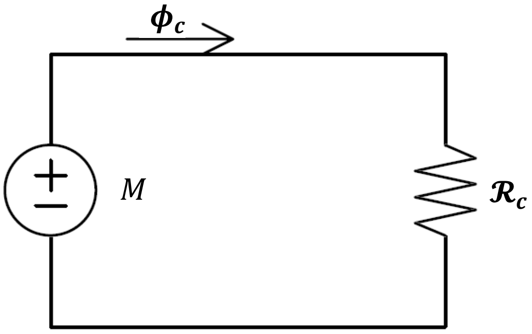

Figure 4.21. *Equivalent electric circuit of a simple magnetic circuit.*

The differences between electric and magnetic circuits are as below:

- The path of the magnetic flux flows is perpendicular to the current flows in the circuit. In other words, the directions of B and J are perpendicular.
- For a given temperature, electric resistance is constant and does not depend on current density. However, the magnetic reluctance depends on magnetic field and flux intensity since the permeability is not constant.
- Current flowing in an electric circuit involves dissipation of energy, but for magnetic circuit, energy is needed to generate magnetic flux.

Now, consider a magnetic circuit with an air gap of length l_g cut in the middle of a leg, as shown in Figure 4.22*a*. As they cross the air gap, the magnetic flux lines bulge outward somewhat, as illustrated in Figure 4.22*b*. The effect of the fringing field is to increase the effective cross sectional area A_g of the air gap.

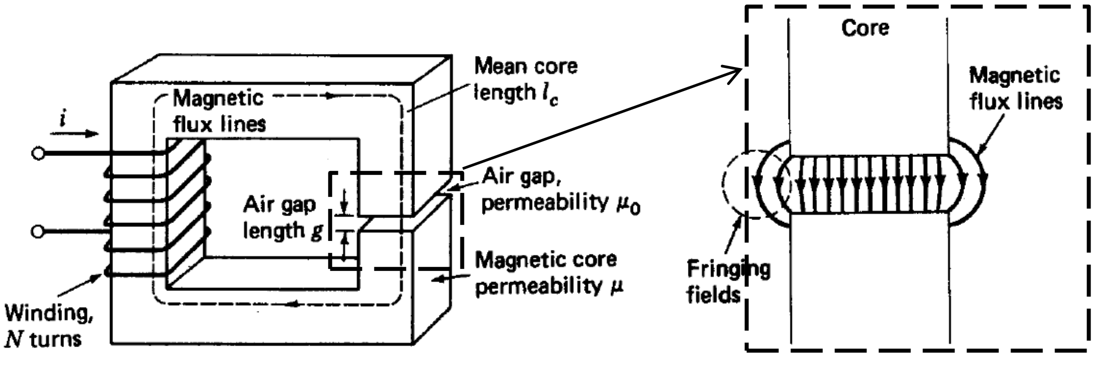

(a) (b)

Figure 4.22. *Structure of a magnetic circuit with an air gap* (a) *and flux line distribution in the air gap* (b).

By Ampere's law, results:

$$M = N\,i = H_c\,l_c + H_g\,l_g \tag{4.17}$$

where

$$H_c\,l_c = \mathcal{R}_c\,\phi_c \tag{4.18}$$

and

$$H_g\, l_g = \mathcal{R}_g\, \phi_g \tag{4.19}$$

According to Gauss' law in magnetics:

$$\oint_A B\, dA = 0 \tag{4.20}$$

Results:

$$\phi_c = \phi_g = \phi \tag{4.21}$$

Therefore:

$$M = \left(\mathcal{R}_c + \mathcal{R}_g\right) \phi \tag{4.22}$$

That is, the above magnetic circuit with an air gap is analogous to a series electric circuit. Further, if we regard $H_c l_c$ and $H_g l_g$ as the "voltage drops" across the reluctance of the core and the air gap respectively, the above equation from Ampere's law can be interpreted as an analogy to the Kirchhoff's voltage law (KVL) in electric circuit theory, that is:

$$\sum M = \sum \mathcal{R}\, \phi \tag{4.23}$$

The Kirchhoff's current law (KCL) can be derived from equation (4.20), that is:

$$\sum_{i=1}^{N} \phi_i = 0 \tag{4.23}$$

Where N is the total number of branches with currents flowing towards or away from the node.

The equivalent electric circuit of the magnetic circuit with an air gap is shown in Figure 4.23.

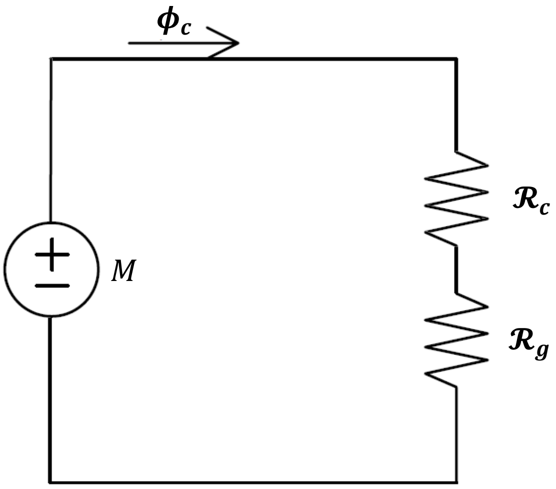

Figure 4.23. *Equivalent electric circuit of a magnetic circuit with an air gap.*

Consider a piece of permanent magnet of a uniform cross sectional area of A_{PM} and a length l_{PM}, as shown in Figure 4.24*a*. The demagnetization curve of the magnet is a straight line with a coercive force of H_c and a remanent flux density of B_r, as shown in Figure 4.24*b*. The demagnetization curve can be expressed analytically as:

$$\mathrm{B}_{PM} = \mu_{PM}\,(H_{PM} + H_c) \tag{4.25}$$

where $\mu_{PM} = B_r/H_c$ is the permeability of the permanent magnet, which is very close to μ_o, the permeability of free space (for a NdFeB magnet, $\mu_{PM} = 1.05\,\mu_0$).

The magnetic “voltage drop” across the magnet can be expressed as:

$$H_{PM}\,l_{PM} = \left(\frac{B_{PM}}{\mu_{PM}} - H_c\right) l_{PM} = \mathcal{R}_{PM}\,\phi_{PM} - M_{PM} \tag{4.26}$$

where $\mathcal{R}_{PM}$ is the reluctance and M_{PM} is the magnetomotive force (“voltage source”) of the magnet. It should be noted that in the magnet, B_{PM} and H_{PM} are in opposite directs.

The equivalent electric circuit of a permanent magnet is reported in Figure 4.24*c*.

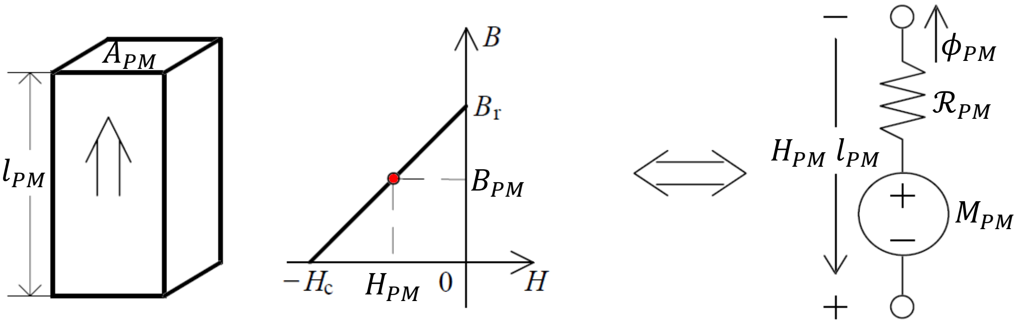

Figure 4.24. *Structure* (a), *demagnetization curve* (b) *and equivalent electric circuit* (c) *of a permanent magnet.*

4.7.2 Limitations of the magnetic circuit approach

The number of problems in practical magnetic circuits that can be solved by the magnetic circuit approach is limited, despite the similarity of this approach to simple dc electric circuit theory. The purpose of introducing magnetic circuits is to state some very fundamental principles and definitions that are necessary in order to understand electromagnetic systems. The limitations of magnetic circuit theory rest primarily in the nature of magnetic materials as contrasted with conductors, insulators, and dielectric materials. Most of these limitations have already been introduced as "assumptions" in the discussion of magnetic circuits. Let us assess the significance of these assumptions.

- ***Homogeneous magnetic material:*** most materials used in practical electromagnetic systems can be considered homogeneous over finite regions of space, allowing the use of the integral forms of Maxwell's equations and calculations of reluctances and permeances.

- ***Isotropic magnetic materials**:* many sheet steels and ferrites are oriented by means of the metallurgical process during their production. Oriented materials have a "favored" direction in their grain structure, giving superior magnetic properties when magnetized along this direction.
- ***Non-linearity**:* this is an inherent property of all ferro- and ferrimagnetic materials.

  However, there are many ways of treating this class of nonlinearity analytically:
  - as can be seen from the B-H curve, a considerable portion of the curve for most materials can be approximated as a straight line, and many electromagnetic devices operate in this region;
  - numerous analytical and numerical techniques have been developed for describing the B-H and other nonlinear magnetic characteristics;
  - the nonlinear B-H characteristic of magnetic materials manifests itself in their relationship between flux and exciting current in electromagnetic systems; the relationship between flux and induced voltage is a linear one, as given by Faraday's law. It is possible to treat this nonlinear excitation characteristics separately in many systems, such as is done in the equivalent circuit approach to transformers and induction motors;
  - an inductance whose magnetic circuit is composed of a magnetic material is a nonlinear electric circuit element, such as a coil wound on a magnetic toroid;
  - with an air-gap in the magnetic toroid, however, the effect of the nonlinear magnetic material on the inductance is lessened. Actuators have air-gaps in their magnetic circuits, permitting the basic theory of these devices to be described by means of linear equations;
- ***Saturation**:* all engineering materials and devices exhibit a type of saturation when output fails to increase with input, for instance, in the saturation of an electronic amplifier. Saturation is very useful in many electromagnetic devices, such as magnetic amplifiers and saturable reactors.
- ***Leakage and Fringing Flux**:* this is a property of all magnetic circuits. It is best treated as a part of the generalized solution of magnetic field distribution in space, often called a boundary value problem. In many actuator magnetic circuits, boundaries between regions of space containing different types of

magnetic materials (usually a boundary between a ferromagnetic material and air) are often planes or cylindrical surfaces that, in a two-dimensional cross section, become straight lines or circles. Leakage inductances can frequently be determined in such regions by calculating the reluctance or permeance of the region using fairly simple integral formulations. The spatial or geometric coefficients so obtained are known as permeance coefficients.

Chapter 5

Semi-analytical model of a linear machine

5.1 Introduction

The previous chapters described the working principle of Stirling engines and the different typology of linear machine, utilized in the cogeneration system and renewable energy converter. The application is referred to a micro co-generation system − based also on renewable energy sources – to supply domestic or isolated low rated loads.

Mechanical energy is provided by a free-piston energy converter (FPEC), which converts thermal energy produced by a thermal source into mechanical energy; specifically, an external combustion engine, based on Stirling cycle, was considered [204]. Mechanical energy is then converted into electrical energy by means of linear generator (LG). The FPEC systems can be connected to the distribution grid by a back-to-back converter according the schemes adopted for variable speed generators; as for the LG operation, this scheme allows optimal starting and synchronization by switching the generator to motoring operation, motion regularization and optimization of the energy output by a proper current control strategy [205]. The general scheme of such system is reported in Figure 5.1.

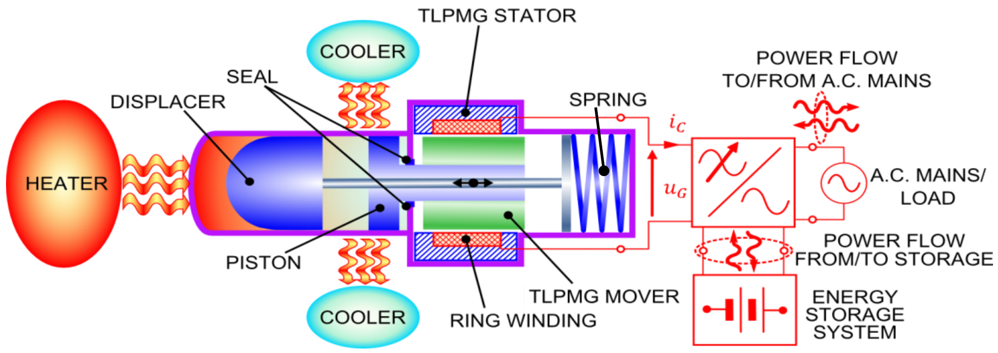

Figure 5.1. *Scheme of a free-piston energy converter integrating a Stirling engine and a single phase TLPMG.*

The main advantages of FPECs with respect to conventional crank–rod based on rotary machine systems are:

- high specific power thanks to their greater compactness;
- high reliability thanks to the reduction of the moving parts;
- high efficiency;
- cheapness thanks to their constructive simplicity;
- low maintenance;
- low noise pollution.

The short stroke permanent magnet linear generator (TPMLG) can be convenient as it represents a good compromise between the production costs and the output performances.

The main advantages of tubular configuration are:

- higher specific power respect to flat configuration;
- no normal component of the force;
- high modularity;
- high manufacturing simplicity;
- possibility to adopt ring winding.

The core lamination of tubular configuration results quite difficult because the lamination, in order to reduce the eddy current loss, should be arranged in the axial direction and this involves a hard manufacturing production. The axial lamination of a tubular linear machine is reported in Figure 5.2 [206].

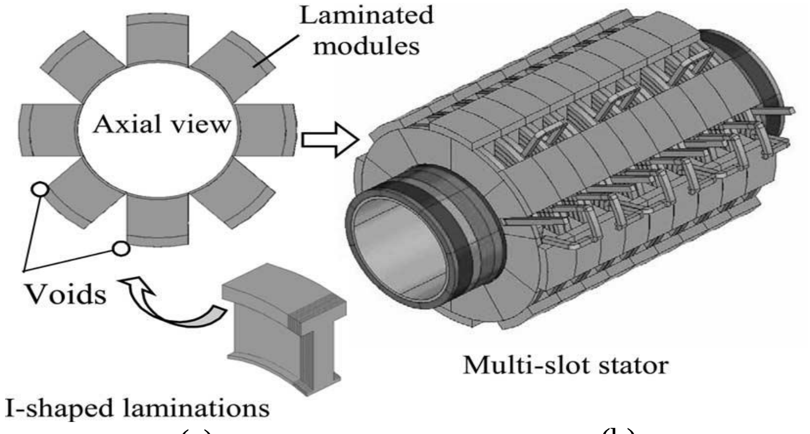

(a) (b)

Figure 5.2. *Stator core fabricated from modules formed from I-shaped laminations (a), schematic of laminated linear generator [206].*

For such reason, the use of SMC materials is practically binding to obtain complex core shapes by suitable molding process. In addition, the SMC materials present a lower eddy current loss but a lower permeability than conventional lamination.

Finally, the use of PMs involves the following features:

- higher efficiency respect to electrically excited machines thanks to absence of copper loss in the mover;
- lighter mover, this feature allows achieving a greater dynamic performance;
- higher costs due to the rare earth utilization to build the PMs;

Magnetization pattern is a relevant issue for the electromagnetic design of the machine, since it can heavily affect the TPMLG performances. Several papers [207,208] suggest Halbach or quasi-Halbach arrangement as the more appropriate magnetization pattern for such kind of applications. The main features given by the Halbach and quasi-Halbach magnetization arrangement are:

- the axially magnetized magnets essentially (or the axial component of magnetization in the case of Halbach arrangement) provide a return path for the radial airgap flux, and, hence, the flux in the mover yoke is relatively small;
- the permanent magnets may be mounted on a non-magnetic support tube without significantly compromising the thrust force capability [208];
- the mass of the moving piston and permanent magnet armature assembly can be greatly reduced, which is essential for achieving a high output power and dynamic performances of the cogeneration system;
- sinusoidal distribution of air-gap flux density.

The Halbach magnetization enhances the quasi-Halbach advantages, but with the drawback of more complicated manufacturing and uncertain resulting profile.

The aim of the research was to develop a model that allows analysing, optimising and thus designing a TPMLG; so the goal is achieving the results, in terms of thrust force, output power and efficiency, varying the main electromagnetic quantities that affect the TPMLG performances.

One of the most important issues to investigate, from electromagnetic design point of view, is the magnetization pattern, since it can heavily affect PM amount and consequently the mover mass and, in turn, dynamic performances. For this purpose, analytical and numerical methods are proposed to study tubular configurations [209,210]. Due to the asymmetrical magnetic configuration and to the remarkable fringing end effects, analytical methods – generally relying on the assumption of periodic boundary conditions – can be hardly applied.

On the other side, finite element analyses (FEAs) carried out on the whole configuration for different mover positions can be excessively time-consuming for a preliminary design, when the influence of several PM magnetizations must be investigated.

In order to reduce the computational effort, an approach combining harmonic decomposition and automated magnetostatic FEA sequences is proposed, to simulate the PM motion and different magnetization profiles by analysing fixed magnetization space harmonic distributions.

Another important issue is the current supply strategy definition. Such matter is essential in order to determine the best solution to maximize the power conversion.

The method is based on the superposition of the effects of each magnetization space harmonic and the effect of the supply current, while the geometry is being unvaried. In order to apply the superposition principle the magnetic linearity of iron cores (stator and mover) materials is assumed, that means to consider a constant magnetic permeability for the ferromagnetic parts.

Actually, the mover yoke saturation is generally not negligible, due to high dynamic requirements that constrain the mover mass reduction as much as possible. Thus, the demagnetizing effect due to mover yoke saturation is taken into account by a suitable current sheet distribution on the mover surface, determined by an iterative procedure.

The proposed semi-analytical method allows overcoming the inherent limitations of analytical methods (asymmetrical magnetic configuration, remarkable fringing end effects and mover local magnetic saturation) that can be simply managed only in some simplified cases or by adopting a complex formulation and appropriate corrections [211]. On the other hand less computational effort is required than normal FEAs in the case of high number of electromagnetic parameter variation, as it usually occurs for a machine design and optimization (i.e. several mover positions, different magnetization and current supply solutions).

In fact, the proposed method, after a suitable number of FEAs, allows investigating of several magnetization patterns and supplying strategies, without requiring any other FEAs.

The method allows taking into account several SMC materials for the ferromagnetic parts in the hypothesis of unvaried linear magnetic permeability (the permeability value before the saturation effect becomes remarkable). In this condition is possible utilize the same space harmonic FEAs, adjusting only the mover current sheet distribution according to BH curve of specific SMC material.

5.2 Preliminary design

The proposed procedure is applied to the analysis of a short-stroke 3-poles TPMLG (Figure 5.3), using a commercial software package (Ansys Maxwell®).

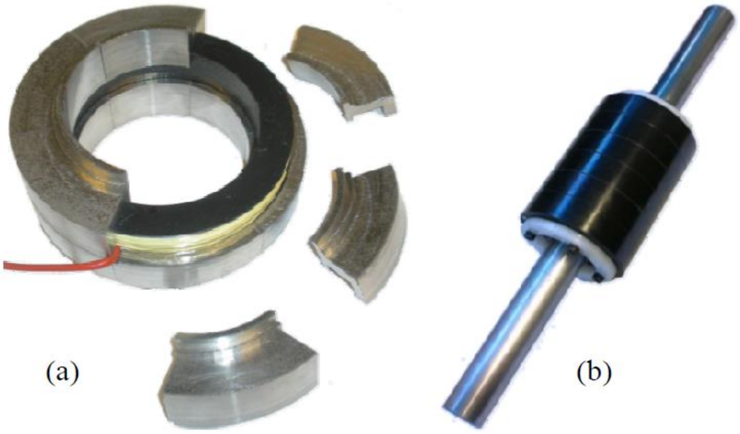

Figure 5.3. *TPMLG prototype; (a): stator assembly with twelve SMC modular cores; (b): mover consisting of bonded PM ring mounted on a steel shaft.*

The main TLPMG ratings and material magnetic properties are shown in Table 5.1. In particular the maximum PM magnetization M_{PM}, is typical of a bonded rare-earth PM material, and it is kept unvaried for all the examined magnetization schemes, including pure radial, Halbach and quasi-Halbach magnetization patterns.

Table 5.1. *Main ratings design data and magnetic properties.*

$\boldsymbol{\tau = 40}$ **mm**	$\boldsymbol{v_{max} = 4}$ m/s	$\boldsymbol{E_{G0} = 400}$ $\mathbf{V_{rms}}$
$\boldsymbol{\mu_{PM} = 1.2 \cdot \mu_0}$	$\boldsymbol{M_{PM} = 400}$ kA/m	$\boldsymbol{\mu_{m,lin} = 400\ \mu_0}$
$\boldsymbol{\delta_C = 4.5}$ A/$\mathbf{mm^2}$	$\boldsymbol{I_G^*} = 1.32$ A	$\boldsymbol{N_C} = 760$

The TPMLG is preliminarily sized according to the maximum flux density allowable in the SMC cores (≅ 1.3 T) [212] and assuming simple harmonic motion and sinusoidal current waveform. The asymmetrical pole shoe profile is devised to increase the side flux linkage and to reduce both the cogging effects F_{z0} and the coil inductance L. A parametric analysis, varying the pole shoes height ($h_s =$ 3, 4 mm) and the external ($w_{s,e} =$ 16, 18, 20 mm) and internal ($w_{s,i} =$ 12, 14, 16 mm) width, was carried out for Halbach magnetization and current $I_G = 3$ A. The parametric data are reported in Table 5.2.

Table 5.2. *Parametric analysis per preliminary design of pole show profile (Halbach magnetization,* $\boldsymbol{I_G} = 3$ A*).*

N.	h_s [mm]	$w_{s,e}$ [mm]	$w_{s,i}$ [mm]	F_{z0} [N]	L [mH]
1	3	16	12	79.3	441.7
2	4	16	12	87.6	448.8
3	3	18	12	22.8	453.2
4	4	18	12	27.7	460.4
5	3	20	12	32.9	465.2
6	4	20	12	34.3	470.1
7	3	16	14	22.7	464.6
8	4	16	14	18.8	474.9
9	3	18	14	58.4	476.7
10	4	18	14	57.9	486.3
11	3	20	14	93.7	489.1
12	4	20	14	90.8	493.1
13	3	16	16	64.6	499.9
14	4	16	16	55.7	512.8
15	3	18	16	117.3	511.8
16	4	18	16	123.5	525.7
17	3	20	16	159.9	525.6
18	4	20	16	152.3	534.2

From Table 5.2 results that the minimum value of cogging force and inductance is achieved for the analysis number 3 and number 7. Fur such reason it is chosen $h_s = 3$ mm, $w_{s,e} = 17$ mm and $w_{s,i} = 13$ mm. Main geometrical data of the reference and simplified models are reported in Table 5.3.

Table 5.3. *Main geometrical model data (see Figure 5.4; sizes in mm).*

$r_g = 44.5$	$h_{PM} = 6$	$w_{my} = 300$	$h_{my} = 8$	$w_p = 10$	$w_{s,e} = 17$	$w_{s,i} = 13$	$h_s = 3$
$h_{sy} = 29.4$	$w_{sy} = 52$	$\tau = 40$	$h_y = 6.4$	$h_p = 14$	$g = 1$	$\tau' = 200$	$w'_{my} = 90$

Being the coil section is 448 mm^2 and assuming a 50% filling factor, the coil resistance at operating temperature is estimated at $R_G = 20.5\Omega$.

In order to limit the mover mass, an adequate shaft stiffness being maintained, mover yoke thickness h_{my} must be limited as much as possible, provided an excessive magnetic saturation is avoided.

5.3 Simplified FEA model

The simplified FEA model (called HFEA: harmonic finite element analysis) aims to improve the performance and optimize the linear generator after the preliminary design with a significant reduction of the computational effort [213-214].

The semi-analytical model is based on the superposing the effect of different order of magnetization space harmonics, which are fixed with respect to the stator reference. The magnetization space harmonics are obtained by means of the Fourier analysis of PMs magnetization profile. The PMs magnetization distribution can be reproduced recombining, through the relative Fourier coefficients, every magnetization space harmonic order. For such purpose, the PMs are replaced with a PM band with the same permeance of PMs and with a sinusoidal magnetization with different harmonic orders.

The geometrical model utilized for simplified FEA derives from real LG geometry (reference model, shown in Figure 5.4*a*). Thank to symmetry (in this case the mover is kept fixed respect to stator) is possible to use a simplified model, considering only half geometry (Figure 5.4*b*).

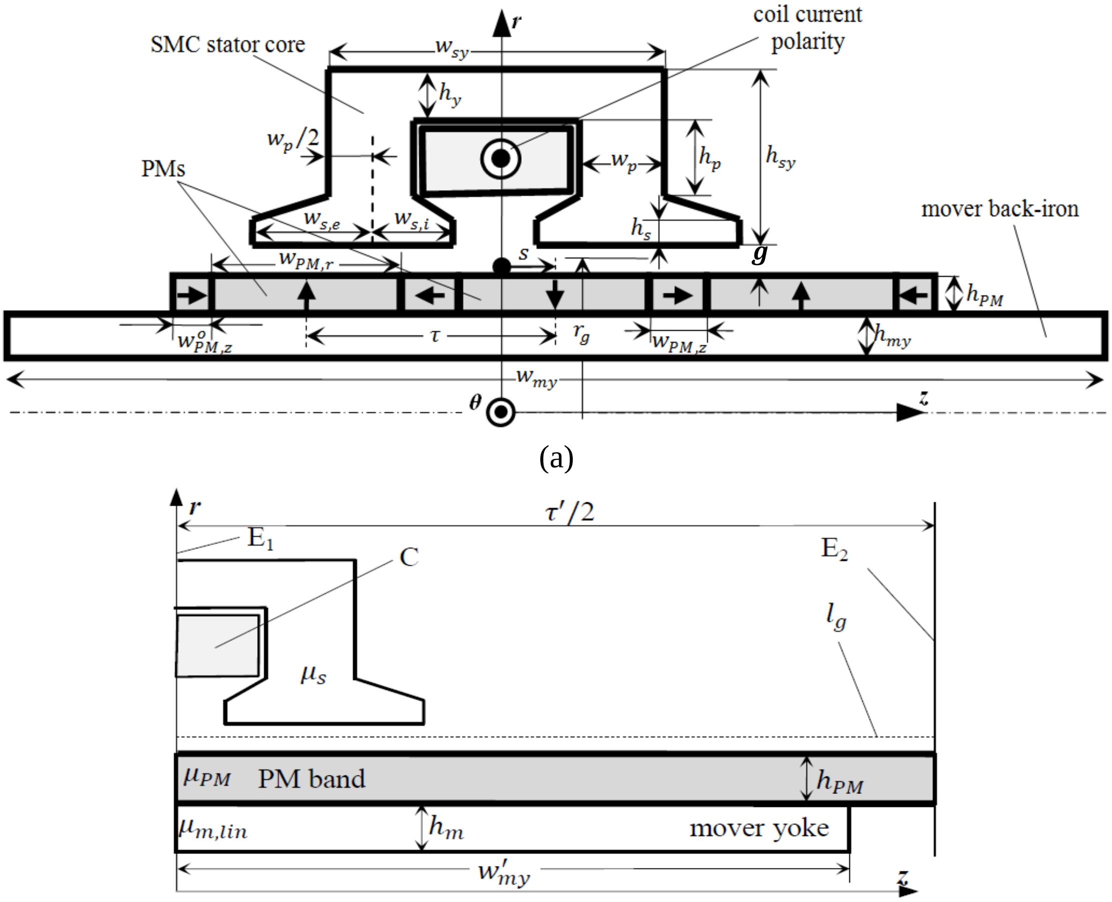

(a)

(b)

Figure 5.4. *FEAs geometrical models: reference model* (a), *simplified model* (b). *E1, E2: symmetry boundaries;* l_g*: sample air-gap line for the flux density; C: coil section.*

In such model the stator ferromagnetic parts are unchanged and modelled with a constant permeability value. Differently, the PM band length w'_{PM} must be extended with respect to PM length w_{PM} to cover the maximum value of the stroke s_M, in order to enable the reproduction of the spatial magnetization function, that is:

$$w'_{PM} \geq \frac{3}{2}\,\tau + s_M = 2\,\tau \tag{5.1}$$

The best solution is obtained with infinite-length PM band, in fact this solution allows considering only the odd harmonics and neglecting the even ones. In order to obtain such condition, even/odd condition is applied to the boundary edge. In this case the mover yoke length has to extend. However, the mover yoke length cannot reach the maximum value (continuous mover yoke between adjacent TPMLGs) in order to avoid fictitious flux leakage on the E2 boundary. Figure 5.5 shows the cogging force profile for different mover yoke configuration. As can be seen the complete mover configuration (red line) does not reproduce the force profile in the correct way due to the flux path between adjacent models (real and fictitious models).

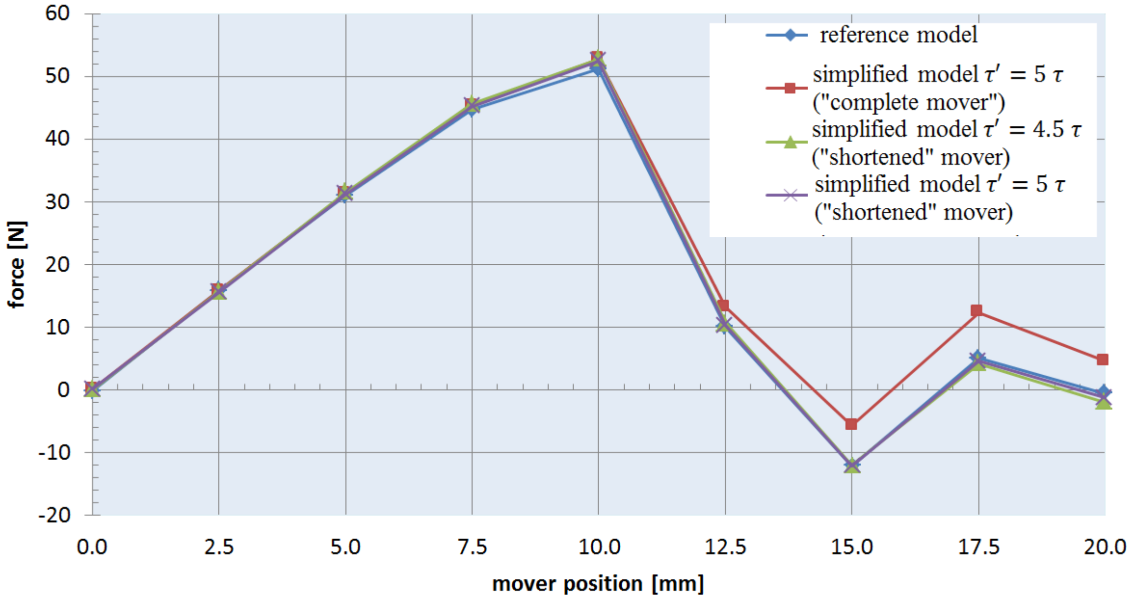

Figure 5.5. *Cogging force profile for different mover yoke configuration.*

In order to deal with mover yoke saturation an iterative procedure was developed, introducing in the former linear model a set of *2Z* fictitious current sheet coils wound around suitable zones of the mover yoke – where saturation is more remarkable – to simulate the demagnetizing effect due to saturation, the permeability value $\mu_{m,lin}$ at linearity being unvaried (Figure 5.6). These coils are fixed with respect to the stator reference frame and symmetrical with respect to r-axis.

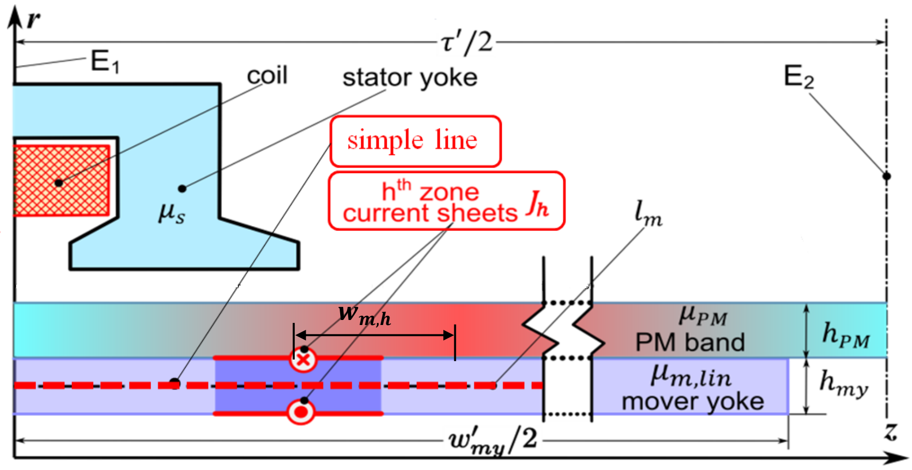

Figure 5.6. *Scheme of the current sheet distribution on the mover surface in the generic h*th *zone.*

In order to choose the number and the width of the zones a preliminary FEA was carried out, in order to identify the zones where the flux density remain approximately constant for the different mover positions. Alternatively, the zones widths can be choose analytically. Particularly, has been chosen $Z = 2$ zones of width equals to $w_{m,1} = w_{m,2} = \tau/\pi = 12.7\ mm$.

In the hypothesis of magnetic linearity is possible to apply the superposition principle, analysing separately the effect of each magnetization harmonic, current supply, and mover current sheet.

In order to study any magnetization patterns, two different magnetizations are considered for PM band: radial (indicated with letter "*r*") and axial (indicated with letter "*z*"). The PM band magnetization is set a space harmonic at a time, with radial and axial magnetization separately. In the case that the software does not allow setting the magnetization profile, is possible to reproduce it through suitable current densities (for the radial magnetization) and current sheets (for the axial magnetization).

To reconstruct the PMs magnetization profile by means of Fourier principle, we have to impose two different magnetization profile that results with a 90° phase difference between them. These two magnetizations have the magnetic axes along the *d* and *q* axes respectively, as shown in Figure 5.7 that report the decomposition of the fundamental harmonic ($m_{r,1}$) of a square wave radial magnetization profile (m_r) in two components ($m_{rd,1}$ and $m_{rq,1}$) for a generic stroke *s*.

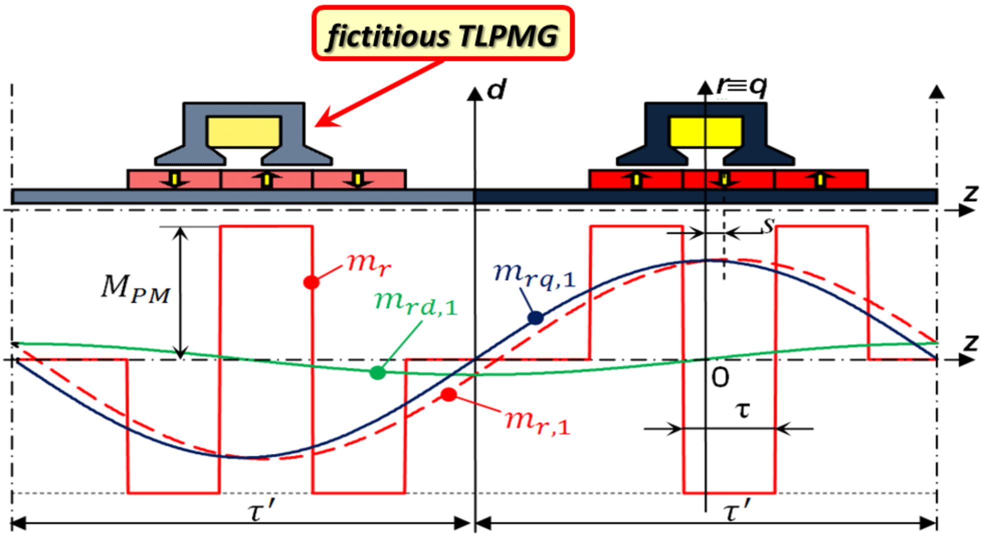

Figure 5.7. *Components $m_{rd,1}$ and $m_{rq,1}$ in the d - q and stator reference frame of the fundamental harmonic $m_{r,1}$ related to a pure radial magnetization m_r; M_{PM}: maximum PM magnetization.*

To summarise, for each harmonic order we carried out four FEAs, with the follow magnetizations: $m_{r,d}$, $m_{r,q}$, $m_{z,d}$ e $m_{z,q}$. Four different FE models were developed, with the same geometrical model but different magnetization profile, as shown in Figure 5.8.

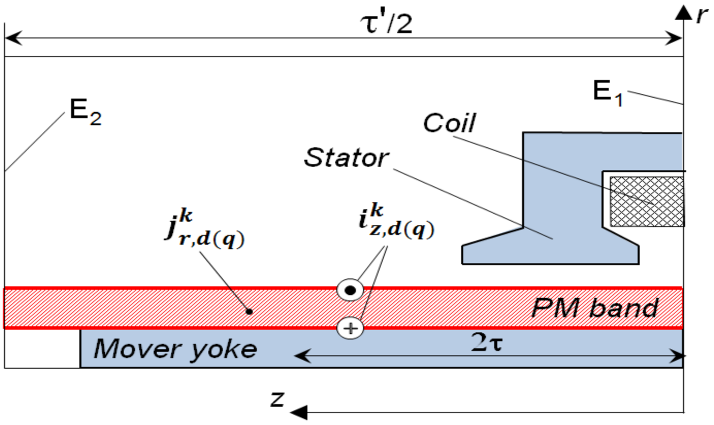

Figure 5.8. *FE geometrical model with current density and current sheet utilised to reproduce the magnetization.*

In the follow are reported the magnetization (just for simplicity with unitary amplitude) for the four different models for the generic harmonic n:

a) Radial component, d-axix: $m_{r,d}$. The current density in the PM band $j_{r,q}$ [A/m^2] results:

$$j_{r,q}^{n} = \frac{\pi}{\tau'}\cos(n\frac{\pi}{\tau'}z) \tag{5.2}$$

The boundary conditions on the edges are:

E$_1$: odd;

E$_2$: even.

b) Radial component, q-axix: $m_{r,q}$. The current density in the PM band $j_{r,d}$ [A/m^2] results:

$$j_{r,d}^{n} = \frac{\pi}{\tau'} \sin(n \frac{\pi}{\tau'} z) \tag{5.3}$$

The boundary conditions on the edges are:

E$_1$: even;

E$_2$: odd.

c) Axial component, d-axix: $m_{z,d}$. The current on the PM band surface $i_{z,d}$ [A/m] results:

$$i_{z,d}^{n} = \sin(n \frac{\pi}{\tau'} z) \tag{5.4}$$

The boundary conditions on the edges are:

E$_1$: odd;

E$_2$: even.

d) Axial component, q-axix: $m_{z,q}$. The current on the PM band surface $i_{z,q}$ [A/m] results:

$$i_{z,q}^{n} = \cos(n \frac{\pi}{\tau'} z) \tag{5.5}$$

The boundary conditions on the edges are:

E$_1$: even;

E$_2$: odd.

As can be noted, the magnetization is independent to mover position and results fixed with respect to stator reference. For such reason is possible to consider only odd harmonics because the even harmonics give a null contribution.

The only models that give a non-null contribution to the flux linkage are the “b” and “c”.

As regards the contribution due to current supply, a unitary value is set in “b” or “c” model, after setting to zero the magnetization.

As regards the current sheet distributions on the mover yoke, utilised to reproduce the demagnetising effect due to magnetic saturation, they are reproduced in the “c” or “d” model. In fact, they are the unique models that give an axial component of the flux density and thus can represent the demagnetizing effect of the saturation. Also in this case, just for simplicity, the values are set, one at a time, to unitary value, while the PM band magnetization is virtually switched off.

To summarise, the carried out FEAs are (let N number of harmonics considered to reconstruct the PMs magnetization and Z number of zones of mover division):

- $2N$ analyses by only applying the PM current distributions;
- one analysis by applying only the coil current;
- Z analyses by only applying the current sheet on the mover surface.

As can be seen, the most computational effort of the HFEA method is due to the simulations for the space harmonics magnetization. This suggests choosing carefully the number of the harmonics N, in order to reconstruct correctly the PMs magnetization without an excessive computational time.

Another important issue which affects the computational effort of the HFEA is the length τ' of the model.

To choose the number of harmonic to consider, the cumulative contribution of the harmonic is compared to the FEA carries out for the reference model. This process has been done for some different mover positions, Figure 5.9 shows the cogging force trend for no-load condition and s=10mm.

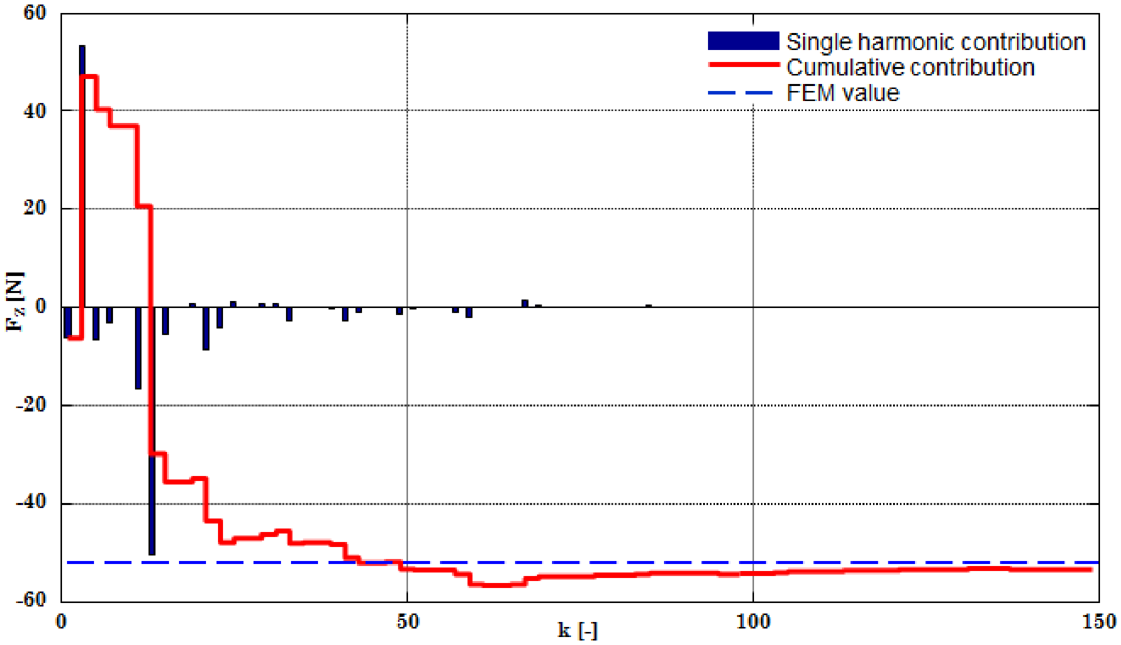

Figure 5.9. *Harmonic contribution on cogging force (no-load, s=10mm).*

It can be concluded that, after about 50 harmonics, the force value is reconstructed well enough. Moreover this solution does not involve an excessive effort in terms of time consuming, in fact it require about 25 simulations for each model.

In conclusion, considering $N = 51$ harmonics, HFEA method requires little more than 100 simulations. Considering that, during the analysing stage of the machine, we should consider different mover positions (at least 30 positions) and different current supply values (at least 10 values), that means at least 300 simulations; it is clear the advantage to use the simplified method. Besides, the simplified model considers only half geometry of the TPMLG, and this involves a further time consuming reduction. In the case of machine optimization the HFEA results even more convenient, since different magnetization patterns and different current strategy have been considered.

The HFEA execution to obtain the complete model on an ordinary PC requires about 25 minutes. Even if preliminary calculation time for each harmonic increases with N_h^3 the subsequent solution takes only some tenth of a second per configuration, including non-linear iterative procedure. On the contrary, a full model direct FEA takes about 1 min per solution, the same HFEA energy error threshold being maintained. Accordingly, direct FEA is likely more convenient to analyse a single magnetization pattern and a limited number of mover positions; instead, HFEA seems to be more profitable for taking into account multiple magnetization schemes, finer position samplings and variation of the supply strategy.

Another item to take into account is the meshing process of the FEA. One of the main problems is the meshing the object near the airgap, because a not thick enough mashing may result in a not correct reconstruction of the solution fields. On the other hand, if the mesh is thick enough near the airgap, this may involve an excessive mesh in the other part of the model, and this result in excessive time consumption.

This problem can be solved by subdividing the airgap between the stator core and PMs into several smaller parts. In this way is more simple to control the number of the mesh elements in the object, and thus find the right balance between the solution accuracy and the computational effort require for the solution.

5.4 Working principle of simplified model

In the previous paragraph the geometrical models utilised for FEAs have been described.

The HFEA procedure aims at the calculation of the following quantities:

- radial and axial components of the airgap flux density: $B_{g_{r(z),k}}^{r(z),d(q)}$ (the superscripts indicate: magnetization direction (radial or axial), axis direction (d-axis or q-axis); the subscripts indicate: component direction (radial or axial), harmonic order).

  Such quantities are sampled on suitable points P_g in air-gap lines (see l_g in Figure 5.3 as an example). The sampling should be dense enough to reconstruct the flux density profile in the correct way; particularly, the flux density was sampled on 1500 points. The flux density samples are utilised to calculate the force value by means of the Maxwell stress tensor;

- radial and axial components of the flux density in the stator $B_{s_{r(z),k}}^{r(z),d(q)}$ and mover $B_{g_{z,k}}^{r(z),d(q)}$ cores. To the purpose, a grid inside the cores is defined to sample with enough accuracy the flux density distribution. The samples are utilised to estimate the core loss, by means of the hysteresis, eddy current and excess coefficients;
- the coil flux linkage ($\phi_k^{r,d}$, $\phi_k^{z,q}$). Only d-axis magnetization component gives a non-null contribution to the flux linkage. It is utilised to evaluate the total flux linkage and thus to calculate the electromotive force (emf).

As mentioned in the previous paragraphs, the HFEA method is based on the superimposing the effect of the different harmonics. The process that has been used is reported in the following, firstly referring to a non-saturated condition:

1) the PMs magnetization profile has been decomposed in Fourier series in order to determine the Fourier coefficients with reference to simplified model PM band width τ'. The Fourier coefficients depend on mover position s and geometrical quantities. In the case of two magnetization components (radial and axial), they have to be considered separately, calculating the Fourier coefficients for each one;
2) the HFEA is carried out to obtain the TPMLG electromagnetic model. In particular it consists of the calculation of the flux density components, in the airgap and in the stator and mover cores, and of the coil flux linkage for each magnetization harmonic and coil current. Such data are then stored for subsequent elaborations;
3) thank to linearity condition, the total quantity values can be reconstructed (those that are related to the real model), in terms of airgap flux density and flux linkage, multiplying the electromagnetic quantity of a specific harmonic order by the related Fourier coefficient and after summing the contribution for each harmonic order. As regards the current supply contribution, the electromagnetic quantities related to unitary current supply are multiplied for the real current supply value. Thus, for a generic load condition, the total quantity values are given by the sum of the harmonic contributions and current supply contribution.

By such approach, mover position dependence is taken into account by the Fourier coefficients, without requiring additional FEAs.

4) starting from airgap flux density and from flux linkage is possible to calculate the thrust force and electromotive force values respectively. These values are affected by the number of the harmonics considered.
5) the demagnetizing effect on the mover yoke, due to magnetic saturation, is to take into account by a suitable procedure described in the next paragraph;
6) the TPMLG performances are evaluated with the estimation of the core losses and efficiency.

The first point regards the decomposition of PMs magnetization profile in Fourier series to obtain the Fourier coefficients. For a general function $f(x)$ with period τ, from the definition of the Fourier series results:

$$f(x) = \frac{a_0}{2} + \sum_{k=1}^{\infty} \left(a_k \cos\left(\frac{2\pi k}{\tau} x\right) + b_k \sin\left(\frac{2\pi k}{\tau} x\right) \right) \tag{5.6}$$

where k is the order of harmonic the coefficients a_k and b_k are calculated according to the specific magnetization distribution.

The more utilized magnetization patters are: radial, quasi-Halbach and Halbach. All the considered magnetization profiles are symmetrical with respect to r-axis (or rather q-axis) for s = 0. The Fourier coefficients relative to these magnetization outlines are:

- ***Radial:*** the radial magnetization corresponds to a square-wave profile with only the radial component m_r (Figure 5.10).

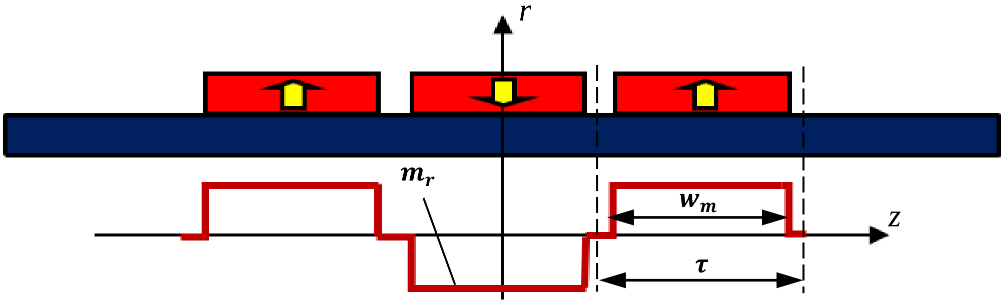

Figure 5.10. *Radial magnetization scheme.*

For such kind of magnetization, the PMs could not be contiguous but can be an air gap between them (quasi-square wave distribution): $k_m < 1$ where $k_m = w_{PM}/\tau$.

The Fourier coefficients results:

$$a_k = \frac{2}{\tau'} \int_{-\frac{\tau'}{2}}^{\frac{\tau'}{2}} m_r(z-s) \cos\left(\frac{2\pi k}{\tau'} z - s\right) \, dz = K_{r,k} \, \cos\left(\frac{2\pi k}{\tau'} s\right) \tag{5.7}$$

$$b_k = \frac{2}{\tau'} \int_{-\frac{\tau'}{2}}^{\frac{\tau'}{2}} m_r(z-s) \sin\left(\frac{2\pi k}{\tau'} x - s\right) \, dz = K_{r,k} \, \sin\left(\frac{2\pi k}{\tau'} s\right) \tag{5.8}$$

where:

$$\begin{aligned} K_{r,k} &= \frac{2}{\tau'} \int_{-\frac{\tau'}{2}}^{\frac{\tau'}{2}} m_r(z) \cos\left(\frac{2\pi k}{\tau'} x\right) \, dz = \\ &= \frac{4}{\pi} M \left[\sin\left(k \frac{k_m \, \alpha}{2}\right) - 2\cos(k \, \alpha) \sin\left(k \frac{k_m \, \alpha}{2}\right)\right] \end{aligned} \tag{5.9}$$

with:

$$\alpha = \pi \, \frac{\tau}{\tau'} \tag{5.10}$$

- ***quasi-Halbach****:* the quasi-Halbach magnetization corresponds to a square wave distribution for both m_r and m_z (Figure 5.11).

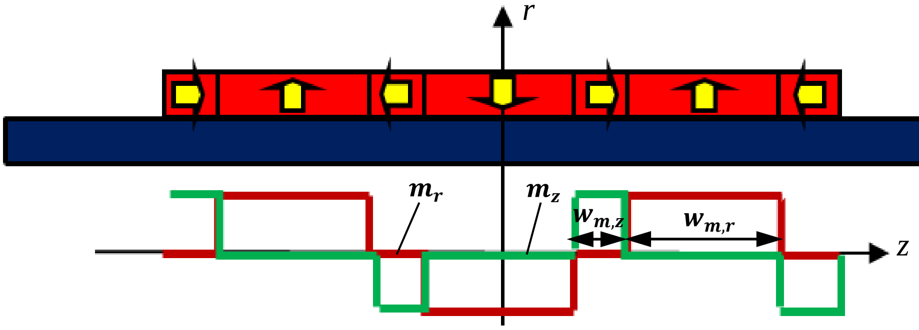

Figure 5.11. *Quasi-Halbach magnetization scheme.*

For such kind of magnetization profile, the PMs are alternately magnetized in radial and axial directions in order to the axially magnetized magnets essentially provide a return path for the radial air-gap flux, and, hence, the flux in the inner bore of the armature is relatively small.

For the radial component of magnetization the Fourier coefficients results:

$$a_{r,k} = \frac{2}{\tau'} \int_{-\frac{\tau'}{2}}^{\frac{\tau'}{2}} m_r(z-s) \cos\left(\frac{2\pi k}{\tau'} z - s\right) \, dz = K_{r,k} \, \cos\left(\frac{2\pi k}{\tau'} s\right) \tag{5.11}$$

$$b_{r,k} = \frac{2}{\tau'} \int_{-\frac{\tau'}{2}}^{\frac{\tau'}{2}} m_r(z-s) \sin\left(\frac{2\pi k}{\tau'} z - s\right) \, dz = K_{r,k} \, \sin\left(\frac{2\pi k}{\tau'} s\right) \tag{5.12}$$

where

$$K_{r,k} = \frac{2}{\tau}\int_{-\frac{\tau}{2}}^{\frac{\tau}{2}} m_r(z)\cos\left(\frac{2\pi k}{\tau}z\right)\,dz = \frac{4}{\pi}M\left[\sin\left(k\frac{\pi}{\tau'}\left(-\tau-\frac{w_{PM,r}}{2}\right)\right)+ \right.$$
$$\left. + \sin\left(k\frac{\pi}{\tau'}\left(\tau-\frac{w_{PM,r}}{2}\right)\right) + \sin\left(k\frac{\pi}{\tau'}\frac{w_{PM,r}}{2}\right)\right] \tag{5.13}$$

For the axial component of magnetization the Fourier coefficients results:

$$a_{z,k} = \frac{2}{\tau'}\int_{-\frac{\tau'}{2}}^{\frac{\tau'}{2}} m_z(z-s)\cos\left(\frac{2\pi k}{\tau'}z - s\right)\,dz = K_{z,k}\,\cos\left(\frac{2\pi k}{\tau'}s\right) \tag{5.14}$$

$$b_{z,k} = \frac{2}{\tau'}\int_{-\frac{\tau'}{2}}^{\frac{\tau'}{2}} m_z(z-s)\sin\left(\frac{2\pi k}{\tau'}z - s\right)\,dz = K_{z,k}\,\sin\left(\frac{2\pi k}{\tau'}s\right) \tag{5.15}$$

Where

$$K_{z,k} = \frac{4}{\pi}M\left[\cos\left(k\frac{\pi}{\tau'}\left(-\frac{3}{2}\tau\right)\right) + \cos\left(k\frac{\pi}{\tau'}\left(-\frac{3}{2}\tau+\frac{w_{PM,z}}{2}\right)\right)+ \right.$$
$$\left. +\cos\left(k\frac{\pi}{\tau'}\left(-\frac{\tau}{2}+\frac{w_{PM,z}}{2}\right)\right) - \cos k\left(\frac{\pi}{\tau'}\left(-\frac{\tau}{2}-\frac{w_{PM,z}}{2}\right)\right)\right] \tag{5.16}$$

- ***Halbach****:* the Halbach magnetization corresponds to sinusoidal spatial distributions for m_r and m_z (Figure 5.12).

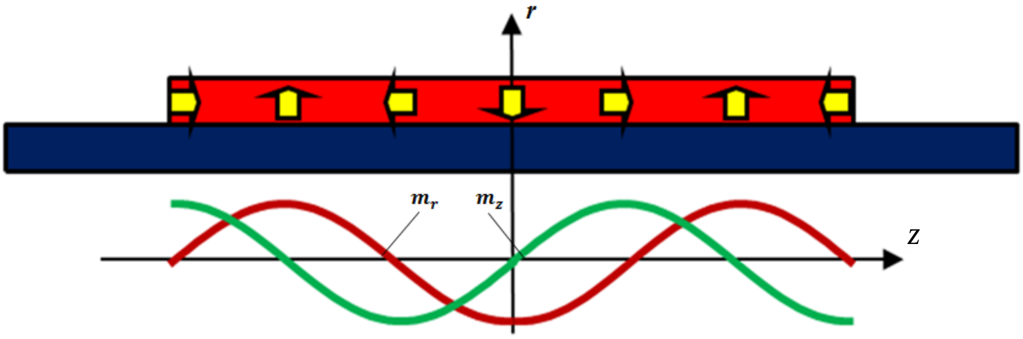

Figure 5.12. *Halbach magnetization scheme.*

For such kind of magnetization the axially magnetization provides a return path for the radial air-gap flux giving the same benefit provided from quasi-Halbach magnetization, furthermore the air-gap flux density distribution approximate in a better way the sinusoidal profile, and thus the emf results with a lower harmonic content.

The radial (axial) component of magnetization the Fourier coefficients results:

$$a_{r(z),k} = \frac{2}{\tau'} \int_{-\frac{\tau'}{2}}^{\frac{\tau'}{2}} m_{r(z)}(z-s) \cos\left(\frac{2\pi k}{\tau'} z - s\right) dz = K_{r(z),n} \cos\left(\frac{2\pi k}{\tau'} s\right) \tag{5.17}$$

$$b_{r(z),k} = \frac{2}{\tau'} \int_{-\frac{\tau'}{2}}^{\frac{\tau'}{2}} m_{r(z)}(z-s) \sin\left(\frac{2\pi k}{\tau'} z - s\right) dz = K_{r(z),n} \sin\left(\frac{2\pi k}{\tau'} s\right) \tag{5.18}$$

where:

$$K_{r,k} = \frac{4}{\pi} M \frac{k\,\rho^2 \cos\left(k\frac{\pi}{2\rho}\right)\left[1 - 2\cos\left(k\frac{\pi}{\rho}\right)\right]}{(\rho - k)(\rho + k)} \tag{5.19}$$

$$K_{z,k} = \frac{K_{r,k}}{\rho} \tag{5.20}$$

with:

$$\rho = \frac{\tau'}{\tau} \tag{5.21}$$

After executing the FEAs for the four models (step 2), is possible to reconstruct the total values of the electromagnetic quantities as radial and axial component of airgap flux density and total coil flux linkage.

The no-load radial (axial) component of the flux density $B_{r(z)0}$ results:

$$\begin{aligned} B_{r(z)0}(P_g, s) = \sum_{k=1}^{N} \Big[& a_{r,k}(s)\, B_{r(z),k}^{r,q}(P_g) + b_{r,k}(s)\, B_{r(z),k}^{r,d}(P_g) + \\ & + a_{z,k}(s)\, B_{r(z),k}^{z,q}(P_g) + b_{z,k}(s)\, B_{r(z),k}^{z,d}(P_g) \Big] \end{aligned} \tag{5.22}$$

This is a general formulation; it can be used to calculate the airgap flux density$B_{g0_{r(z)}}$ as well as the flux density inside the mover $B_{m0_{r(z)}}$ and stator $B_{s0_{r(z)}}$ cores.

According to Figure 5.4a reference frame, only d-axis magnetization components contribute to coil flux, so the no-load flux linkage results:

$$\phi_0(s) = \sum_{k=1}^{N} b_{r,k}(s)\, \phi_k^{r,d} + a_{z,k}(s)\, \phi_k^{z,q} \tag{5.23}$$

By the no-load airgap flux density formulation and according to Figure 5.4a, the no-load (cogging) force F_{z0} and is determined by Maxwell stress tensor:

$$F_{z0}(s) = \frac{2\pi l_g}{\mu_0} \int_{l_g} B_{g0_r}(P_g, s)\, B_{g0_z}(P_g, s)\, dl \tag{5.24}$$

By (23), the no-load emf e_{g0} results:

$$\begin{aligned} e_{G0}(s) &= -N_c \frac{d\phi_0}{dt} = -vN_c \frac{d\phi_0}{ds} = \\ &= -vN_c \sum_{k=1}^{N} \left(\frac{db_{r,k}(s)}{ds} \phi_k^{r,d} + \frac{da_{z,k}(s)}{ds} \phi_k^{z,q} \right) \end{aligned} \tag{5.25}$$

where v is the mover speed and N_c is the number of coil turns. It’s worth pointing out that the flux linkage derivative obtained from the analytical expressions of the coefficients $b_{r,k}$ and $a_{z,k}$ is much more robust from the numerical point of view than other numerical procedures.

A separate FEA is executed with unitary total coil current and de-energized PMs. The flux density components $B_r^{I_{c,d}}$ and $B_z^{I_c,d}$ as well as the flux linkage $\phi^{I_c,d}$ are then determined as at no-load.

The radial and axial flux density components B_r, B_z and flux linkage ϕ at load are calculated as:

$$B_{g_{r(z)}}(P_g, s) = B_{g0_{r(z)}}(P_g, s) + M_C(s)\, B_g^{I_c}{}_{r(z)}(P_g) \tag{5.26}$$

$$\phi(s) = \phi_0(s) + M_C(s)\, \phi^{I_c,d} \tag{5.27}$$

where $M_C = N_c\, I_c$ [A] is the total coil supply ampere-turns.

The force F_z and the emf e_G at load are obtained as in equation (5.24) and (5.25), where B_{g0_r}, B_{g0_z} and ϕ_0 are replaced by B_{g_r}, B_{g_z} and ϕ, respectively. An alternative formulation including the dependence of F_z and e_G on the variation of ϕ_0 with s can be written as (assuming the flux linkage $\phi^{I_c,d}$ nearly independent on s):

$$F_z(s) = F_{z0}(s) + M_C(s)\, \frac{d\phi_0}{ds} \tag{5.28}$$

$$e_G(s) = -v\, N_c \frac{d\phi_0}{ds} + \phi^{I_c,d} \frac{dM_C}{ds} \tag{5.29}$$

5.5 Analysis take into account the mover saturation

In order to limit the mover mass, an adequate shaft stiffness being maintained, mover yoke thickness h_m must be limited as much as possible, provided an excessive magnetic saturation is avoided. In principle mover yoke saturation cannot be nevertheless neglected (as shown in Figure 5.13), so, at a first glance, the above described procedure, relying on the superposition principle, is invalidated.

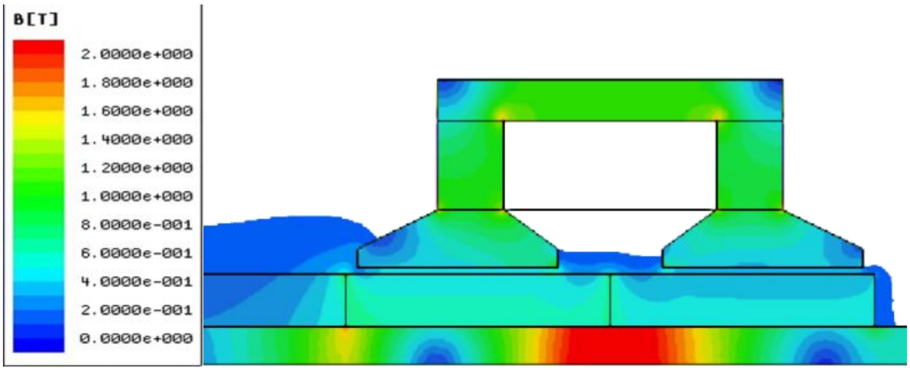

Figure 5.13. *Flux density distribution for radial magnetization, s = 20mm,* M_c *= 1000 A.*

Therefore an iterative procedure is developed to include saturation, introducing in the former linear model a set of 2*Z* fictitious current sheet coils wound around suitable zones of the mover yoke – where saturation is more remarkable - to simulate the demagnetizing effect due to saturation, the permeability value $\mu_{m,lin}$ at linearity being unvaried. These coils are fixed with respect to the stator reference frame and symmetrical with respect to *r*-axis.

Let J_h the linear current density of each h-th coil (with $h = 1 \div 2Z$), the effect of each pair of symmetrical coils (i.e., h-th and (2*Z*+1-*h*)-th coils) (Figure 5.14*a*) can be obtained by summing the effect of two even-symmetrical current sheets $J_{d,h}$ (Figure 5.14*b*) and two odd-symmetrical current sheets $J_{q,h}$ (Figure 5.14*c*), given by:

$$J_{d,h} = \frac{J_{2Z+1-h} + J_h}{2} \tag{5.30}$$

$$J_{q,h} = \frac{J_{2Z+1-h} + J_h}{2} \tag{5.31}$$

As a result, the analysis can be restricted to a halved FE model for both the cases, changing only boundary conditions on E_1 and E_2. This model is analysed by a set of 2*Z* FEAs, supplying each *k*-th coil one by one with $J_{d(q),k} = 1$ A/m, setting $M_C = 0$, de-energized PMs. As a result, the flux density values $B_{m_z}^{J_k,d(q)}$ in the points P_{m,i_h} ($i_h = 1 \div N_h$, with N_h points in the h-th zone) along the line l_m of Figure 5.14*a* in the middle of the mover yoke are obtained.

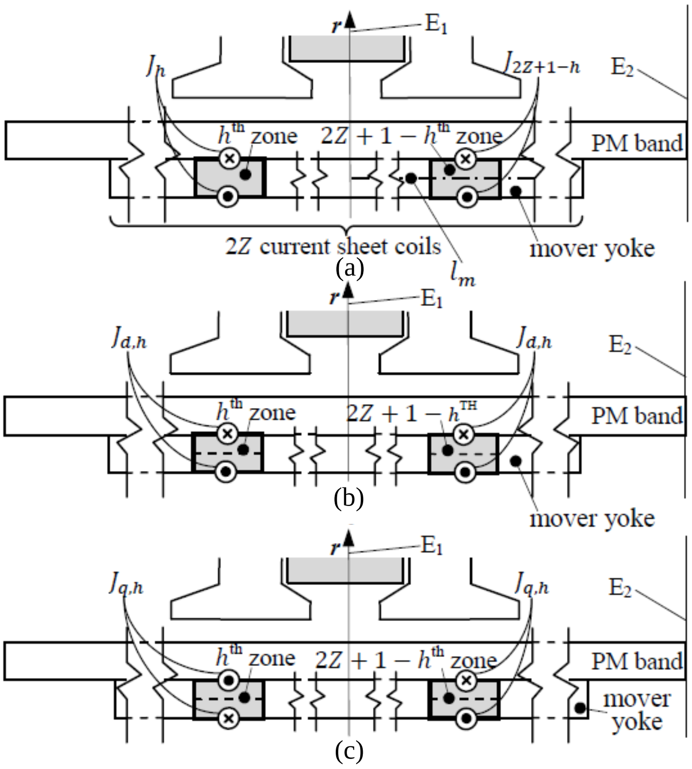

Figure 5.14. *Fictitious current sheets* J_h *introduced to allow for saturation (*l_m*: sample line for evaluation of* $B_{m_z}^{J_k,d(q)}$*)* (a) *and decomposition into even* $J_{d,h}$ (b) *and odd* $J_{q,h}$ (c) *current sheets.*

The current density J_h is determined according to the mismatch ΔH between the magnetic field value H at saturation and the corresponding value H_{lin} at linearity (permeability $\mu_{m,lin}$), the same flux density being maintained (Figure 5.15).

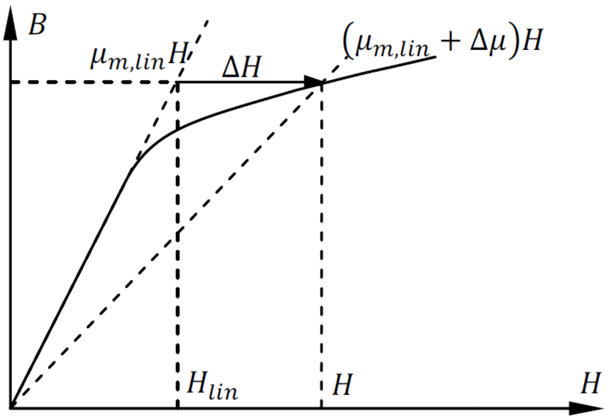

Figure 5.15. *Definition of the magnetic field mismatch* $\Delta\boldsymbol{H}$ *to take into account magnetic saturation.*

Applying the method of images, the magnetic field due to the current sheet outside (in the PMs) $H_{z,h}^{PM}$ and inside the mover $H_{z,h}^{m}$ is given by, respectively:

$$H_{z,h}^{PM} = \frac{\mu_{m,lin}}{\mu_{m,lin} + \mu_{PM}} J_h \tag{532.}$$

$$H_{z,h}^{m} = -\frac{\mu_{PM}}{\mu_{m,lin} + \mu_{PM}} J_h \tag{5.33}$$

and consequently the boundary continuity conditions for the magnetic field yield (H_z: magnetic field at linearity):

$$\frac{\mu_{PM}\left(H_z + H_{z,h}^{PM}\right)}{\mu_{m,lin}\left(H_z + H_{z,h}^{m}\right)} = \frac{\mu_{PM}\left(H_z + \frac{\mu_{m,lin}}{\mu_{m,lin} + \mu_{PM}} J_h\right)}{\mu_{m,lin}\left(H_z - \frac{\mu_{PM}}{\mu_{m,lin} + \mu_{PM}} J_h\right)} = \frac{\mu_{PM}}{\mu_{m,lin} + \Delta\mu} \tag{5.34}$$

with $\Delta\mu$ permeability variation with respect to $\mu_{m,lin}$ expressed as a function of ΔH by:

$$\Delta_{\mu} = -\frac{\Delta H \; \mu_{m,lin}}{\frac{B_{m_z}}{\mu_{m,lin}} + \Delta H} \tag{5.35}$$

where B_{m_z} is the total (the resultant effect of magnetization, coil current and mover current sheet densities) flux density in the points $P_{m,i}$.

Substituting (5.35) in (5.34) and solving for J_h gives finally:

$$J_h = \frac{\Delta H}{1 + \frac{\mu_{m,lin} \, \mu_{PM}}{\mu_{m,lin} + \mu_{PM}} \frac{\Delta H}{B_{m_z}}} \tag{5.36}$$

Since the field generated by the fictitious coils affects in turn the flux density inside the mover, the mismatch ΔH is iteratively re-adjusted, according to the flow diagram of Figure 5.16. Starting from an initial set of the estimated current density values J_k (with $k = 1 \div 2Z$), the even/odd components $J_{d(q),k}$ can be obtained by (5.30) and (5.31).

Multiplying the corresponding unit-current flux density values $B_z^{J_k,(d,q)}$ by $J_{d(q),k}$ yields the estimated flux density contributions $\Delta B_z^{k,(d,q)}$ to the flux density variation on each sample point P_{m,i_h} due to each k-th current sheet. Summing such contributions for all the Z $J_{(d,q),k}$ pairs to the linear flux density value $B_{m_{z,lin}} = B_{m_z}^{r(z),d(q)} + B_{m_z}^{I_c}$ due to magnetization and coil current, the updated flux density values $B_{m_z}(P_{m,i_h})$ and the corresponding permeability $\mu(P_{m,i_h})$ and magnetic energy $W_m(P_{m,i_h})$ are obtained, according to the mover magnetic characteristic.

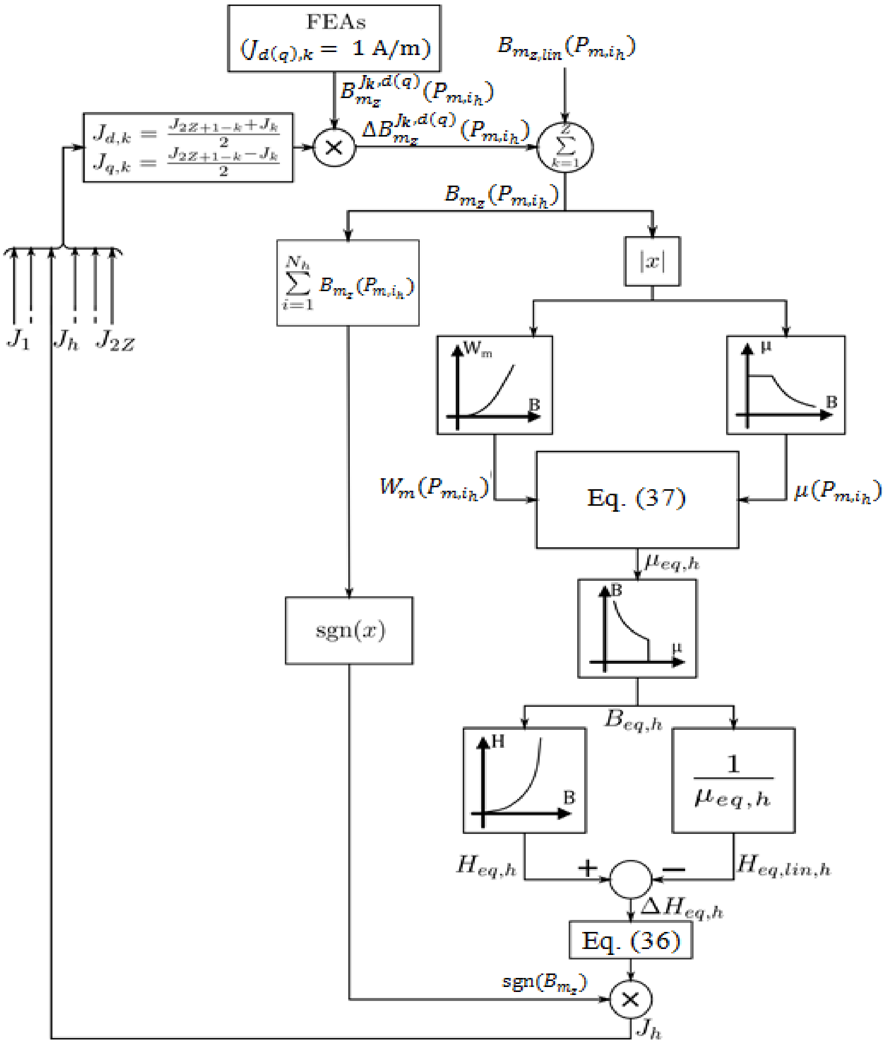

Figure 5.16. *Conceptual scheme of the iterative procedure to define the h-th zone current density.*

Let the h-th zone equivalent permeability $\mu_{eq,h}$, the weighted average of μ taking W_m as weighting function, is calculated as:

$$\mu_{eq,h} = \frac{\sum_{i_h=1}^{N_h} \mu(P_{m,i_h})\, W_m(P_{m,i_h})}{\sum_{i_h=1}^{N_h} W_m(P_{m,i_h})} \tag{5.37}$$

The corresponding flux density value $B_{eq,h}$, the linear $H_{eq,lin,h}$, non-linear $H_{eq,h}$ and mismatch $\Delta H_{eq,h}$ values of the magnetic field are obtained. J_h value is updated putting $\Delta H_{eq,h}$ in (5.36) and multiplying by the due sign.

This process is repeated for each zone to obtain a new current density set for a further step of the iterative procedure, stopped according to a suitable convergence test. It is worth remarking that, even if the above described procedure must be repeated for each mover position, i.e. s value, the re-evaluation of the unit-current flux density $B_{m_z}^{J_k,(d,q)}$ is not required, since fictitious coils are fixed with respect to the stator. These values are therefore evaluated and stored not only in the mover sample points $P_{m,i}$ but also in the air-gap point set P_g, as well as the corresponding per-turn coil flux linkage $\phi^{J_k,d}$ due to current density $J_{d,k} = 1$A/m (q-component does not contribute to coil flux linkage).

Evidencing the dependence on s and adopting the above notations, the expressions (5.26) and (5.27) of the airgap flux density and the coil flux linkage at linearity (denoted by $_{lin}$ subscript) are adjusted taking into account the current sheets contributions as follows:

$$\begin{aligned} B_{g_{r(z)}}(P_g, s) &= B_{g_{r(z),lin}}(P_g, s) + \Delta B_{g_{r(z)}}(P_g, s) = \\ &= B_{g_{r(z),lin}}(P_g, s) + \sum_{k=1}^{Z} \left(J_{\mathrm{d(q)},k}(s)\, B_{g_{\mathrm{r(z)}}}^{J_k,\mathrm{d(q)}}(P_g) \right) \end{aligned} \tag{5.38}$$

$$\phi(s) = \phi_{lin}(s) + \sum_{k=1}^{Z} \left(J_{d,k}(s)\, \phi^{J_k,d} \right) \tag{5.39}$$

Correspondingly, force and emf are obtained, respectively:

$$F_z(s) = \frac{2\pi l_g}{\mu_0} \int_{l_g} B_{g_r}(P_g, s)\, B_{g_z}(P_g, s)\, dl \tag{5.40}$$

$$e_G(s) = e_{G,lin}(s) - v\, N_C \sum_{k=1}^{Z} \frac{\partial J_{d,k}}{\partial s} \phi^{J_k,d} \tag{5.41}$$

where the derivative $\partial J_{d,k} / \partial s$ is now determined by numeric interpolation.

The influence of the sheet coil pairs number Z on the HFEA accuracy with magnetic saturation was investigated. With reference to a pure Halbach magnetization and a constant current supply $i_G = 2\ I_G$, the results related to a linear HFEA, HFEAs with $Z = 1$ and $Z = 2$ and non-linear FEA were compared. The values of the axial force, reported in Figure 5.17, shows that the HFEA with $Z = 2$ and non-linear FEA results match very well, so $Z = 2$ is adopted for the further analyses.

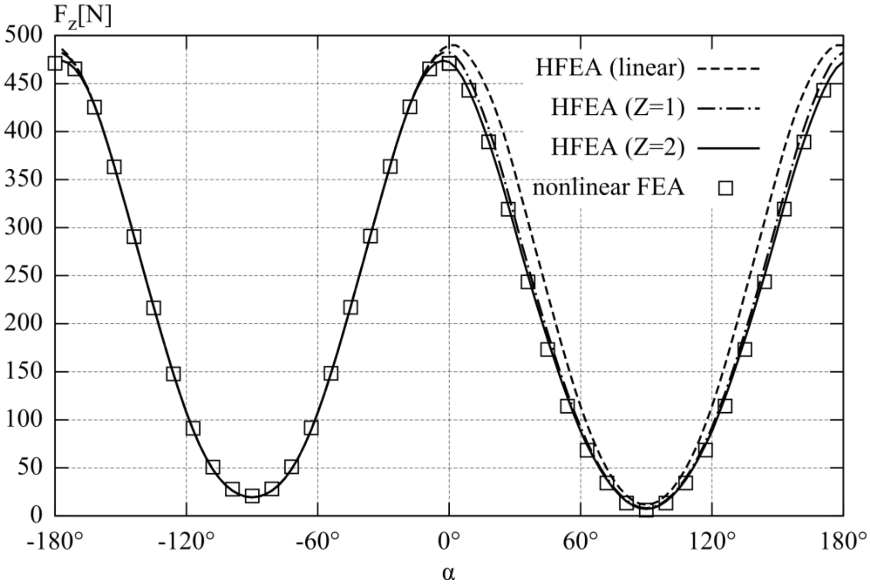

Figure 5.17. *Mover axial force F_z with saturated mover yoke ($i_G = 2\ I_G$): influence of the zone number Z on the accuracy.*

In Table 5.4 are reported the FEAs stored quantities, such as the flux density in the airgap and in the mover and stator cores, and the flux linkage) due to magnetization, coil current and mover sheet current. Inside the square brackets are reported the dimension of the stored matrix.

Table 5.4. *HFEA storage quantities: in the bracket array dimension.*

	Magnetization $\boldsymbol{m_{r,d}, m_{r,q}, m_{z,d}, m_{z,q}}$	**Coil current** $\boldsymbol{I_{c,d}}$	**Mover sheet current** $\boldsymbol{J_{1,d}, J_{1,q}, J_{2,d}, J_{2,q}}$
Airgap flux density $\boldsymbol{B_g}$	${B_g}_{r,k}^{r,d}, {B_g}_{z,k}^{r,d}, {B_g}_{r,k}^{r,q}, {B_g}_{z,k}^{r,q},$ ${B_g}_{r,k}^{z,d}, {B_g}_{z,k}^{z,d}, {B_g}_{r,k}^{z,q}, {B_g}_{z,k}^{z,q}$ $[8 \times (N_h, N_g)]$	${B_g}_r^{I_c,d}, {B_g}_z^{I_c,d}$ $[2 \times (1, N_g)]$	${B_g}_r^{J_1,d}, {B_g}_z^{J_1,d}, {B_g}_r^{J_1,q}, {B_g}_z^{J_1,q},$ ${B_g}_r^{J_2,d}, {B_g}_z^{J_2,d}, {B_g}_r^{J_2,q}, {B_g}_z^{J_2,q}$ $[8 \times (1, N_g)]$
Mover flux density $\boldsymbol{B_m}$	${B_m}_{z,k}^{r,d}, {B_m}_{z,k}^{r,q}, {B_m}_{z,k}^{z,d}, {B_m}_{z,k}^{z,q}$ $[4 \times (N_h, N_m)]$	${B_m}_z^{I_c,d}$ $[1 \times (1, N_m)]$	${B_m}_z^{J_1,d}, {B_m}_z^{J_1,q}, {B_m}_z^{J_2,d}, {B_m}_z^{J_2,q}$ $[4 \times (1, N_m)]$
Stator flux density $\boldsymbol{B_s}$	${B_s}_{r,k}^{r,d}, {B_s}_{z,k}^{r,d}, {B_s}_{r,k}^{r,q}, {B_s}_{z,k}^{r,q},$ ${B_s}_{r,k}^{z,d}, {B_s}_{z,k}^{z,d}, {B_s}_{r,k}^{z,q}, {B_s}_{z,k}^{z,q}$ $[8 \times (N_h, N_s)]$	${B_s}_r^{I_c,d}, {B_s}_z^{I_c,d}$ $[2 \times (1, N_s)]$	${B_s}_r^{J_1,d}, {B_s}_z^{J_1,d}, {B_s}_r^{J_1,q}, {B_s}_z^{J_1,q},$ ${B_s}_r^{J_2,d}, {B_s}_z^{J_2,d}, {B_s}_r^{J_2,q}, {B_s}_z^{J_2,q}$ $[8 \times (1, N_s)]$
Flux linkage $\boldsymbol{\phi}$	$\phi_k^{r,d}, \phi_k^{z,q}$ $[2 \times (N_h, 1)]$	$\phi^{I_c,d}$ $[1]$	$\phi^{j_1,d}, \phi^{j_2,d}$ $[2]$

5.6 Core losses and efficiency estimation

The SMC core losses, affecting the TLPMG electromagnetic efficiency, can be estimated by evaluating the radial and axial component of flux density as a function of time on a suitable grid of sampling points P_s. The density of spatial and time sampling is a compromise between the requirements of limited computational effort and accurate prediction of the loss distribution. Therefore, the samples along l_m inside the mover are used for both $J_h$calculation (for equivalent mover yoke saturation) and core loss calculation. As for the stator core, three distinct sampling subsets are defined (Figure 5.18): S_1 in the horizontal yoke, where only B_z is evaluated, S_2 in the vertical yoke, where only B_r is evaluated, and S_3 in the pole shoe, where both the components must be taken into account, since flux density direction varies with time.

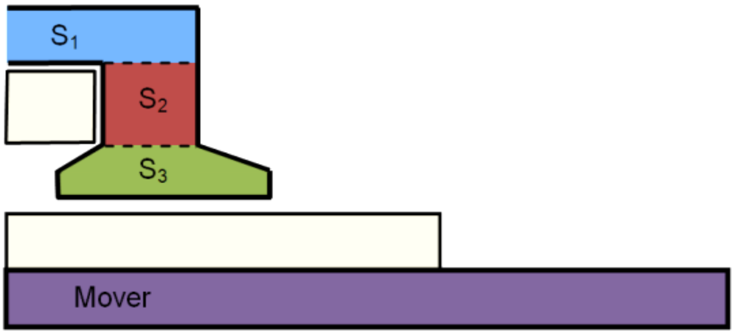

Figure 5.18. *Stator zones division for core loss estimation: S_1: horizontal yoke, S_2: vertical yoke and S_3: pole shoe.*

Assuming a steady-state condition, the flux density time dependence can be expressed by truncated Fourier series expansions, harmonic coefficients being derived by interpolating the magnetostatic FEA results. This approach smooths the numerical errors due to FE solution and consequently reduces noise in time derivative evaluation, provided that an adequate sample number is considered. The average value of the core loss density p_c [W/m^3] is determined elaborating the formulation suggested in [213] as:

$$p_c = k_h\, f \max|_T\{(B_r - \langle B_r\rangle)^2 + (B_z - \langle B_z\rangle)^2\} + \\ + \frac{1}{T}\int_0^T \left(\frac{k_{ec}}{2\pi^2}\left|\frac{dB}{dt}\right|^2 + \frac{k_{ex}}{8.76}\left|\frac{dB}{dt}\right|^{\frac{3}{4}} \right) dt \tag{5.42}$$

where $\langle\ \ \rangle$ brackets stands for time averaged values and $\left|\frac{dB}{dt}\right| = \sqrt{B_r^2 + B_z^2}$ is the absolute value of flux density vector, $f = 1/T$ is the fundamental frequency, k_h, k_{ec} and k_{ex} are the hysteresis, eddy current and excess loss coefficients, respectively.

Such coefficients are obtained by the elaboration of the specific loss data as functions of the maximum flux density at different frequencies [215-217]. The total core losses P_c

are finally obtained by the integration of p_c on the volume of the predefined stator and mover regions.

Preliminary elaborations evidence that the hysteresis loss contribution is largely predominant in the frequency range below 1 kHz. Consequently, a current-controlled supply strategy could be profitably adopted to limit current peaks, the same rms value being maintained, to improve efficiency by reducing the maximum flux density magnitude at load.

The instantaneous input electromagnetic power $p_{em}(t)$ and the output power $p_G(t)$ are given by:

$$p_{em}(t) = F_z(s)\, v(t) \tag{5.43}$$

$$p_G(t) = u_G(t)\, i_G(t) = [e_G(t) - R_G\, i_G(t)]\, i_G(t) \tag{5.44}$$

where $u_G(t)$ and R_G are the TPMLG instantaneous output voltage and coil resistance, respectively.

Neglecting friction and windage losses, the mean values of the input mechanical power P_m and the output electric power P_G can be therefore calculated as:

$$P_m = \frac{1}{T}\int_0^T p_{em}(t)\, dt + P_c \tag{5.45}$$

$$P_G = \frac{1}{T}\int_0^T p_G(t)\, dt \tag{5.46}$$

Using the above quantities, further indexes are considered, mainly related to the electrical system performance and requirements. In particular, the following calculations are useful for design purpose:

- the efficiency, which accounts for the contribution of electromagnetic losses, results:

$$\eta = \frac{P_G}{P_m} \tag{5.47}$$

- the total power factor, which is related to the grid converter sizing, results:

$$\lambda = \frac{P_G}{U_G\, I_G} \tag{5.48}$$

  where $U_G = \frac{1}{T}\int_0^T u_G(t)\, dt$ is the output voltage rms value;

- the power ripple, which is involved in the sizing of appropriate filters or storage systems at the converter output terminals, results:

$$\Delta P_G = \frac{\max\{p_G(t)\} - \min\{p_G(t)\}}{2\, P_G} \tag{5.49}$$

5.7 Model validation

The main HFEA parameters (number of harmonics n_m and of sheet coil pairs Z) should assure a good accuracy without an excessive calculation time. To this purpose, a quasi-Halbach configuration ($w_{m,r} = 0.9\,\tau$, $w^i_{m,z} = 2\,w^o_{m,z} = 0.1\,\tau$) was preliminary analysed, comparing the B_r air-gap profiles obtained by HFEA and by a direct FEA of the full model to check the influence of saturation on HFEA accuracy. The very good agreement between the two methods for both unsaturated and saturated mover core (linear and non-linear HFEA, respectively) is shown in Figure 5.19 (results related to $N = 55$ and $Z = 2$ for $s = \tau/2$ and $i_G = I_G$). It's worth noticing the mover saturation is quite relevant, causing about 13% reduction of the maximum flux density.

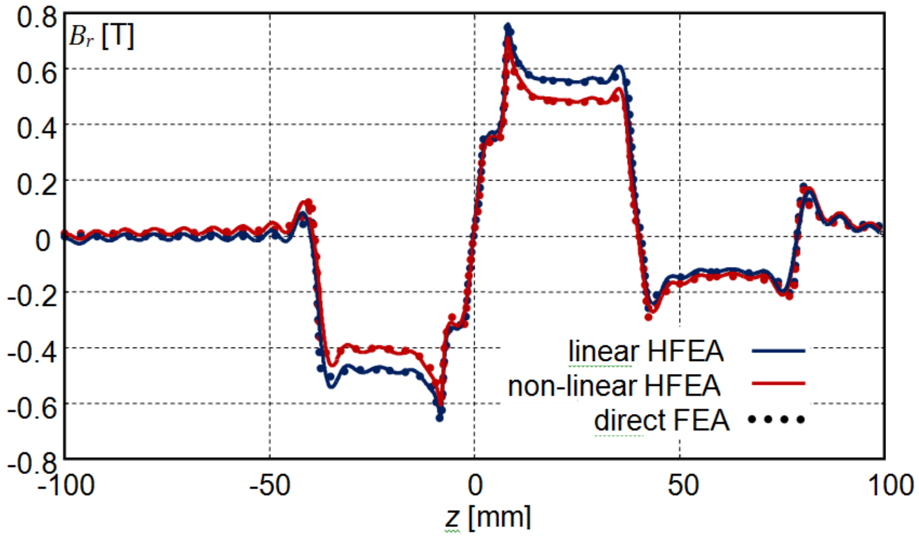

Figure 5.19. *Radial component of the flux density calculated on the air-gap line l_g by HFEA procedure and direct FEA ($N = 55$ and $Z = 2$ for $s = \tau/2$ and $i_G = I_G$).*

As can be seen, the HFEA method reproduces correctly the airgap flux density. This means that the thrust force, given by the product between radial and axial components of airgap flux density, is reproduced in the correct way as well.

In order to validate the proposed model, a condition of significant mover magnetic saturation is chosen. In Figure 5.20 is reported the no-load flux linkage for pattern III in the case of linear and non-linear magnetic characteristics of SMC material. The flux linkage reduction of non-liner with respect to linear characteristic is remarkable ($\cong -12\%$).

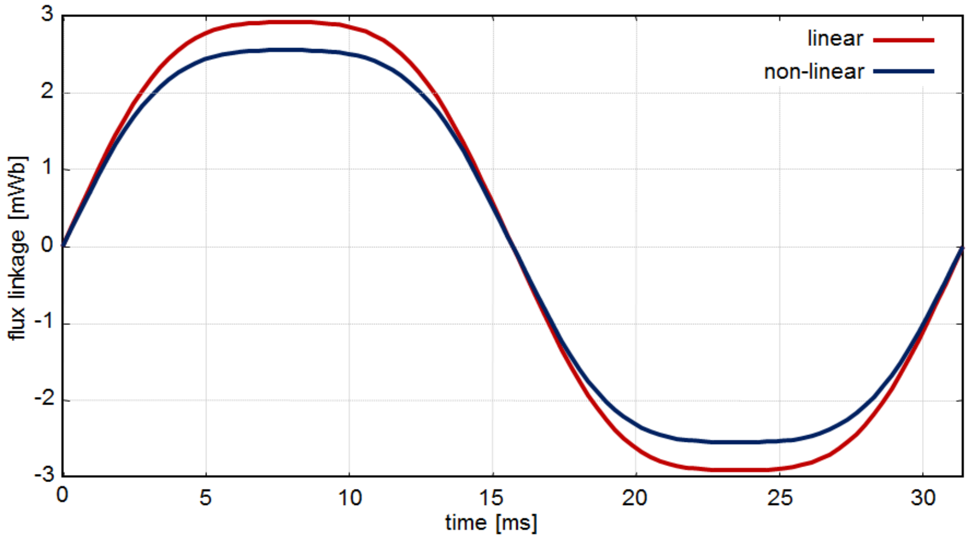

Figure 5.20. *Comparison of no-load flux linkage between linear and non-linear magnetic characteristics (pattern III).*

Figure 5.21 shows the no-load force and flux linkage as functions of the mover position for both the Halbach magnetizations. With regard to such figures, the following aspects can be evidenced:

- the agreement with the actual FEM model is very good for both the magnetization schemes;
- the ideal Halbach scheme presents very low cogging force and higher flux linkage (+11% with respect to quasi Halbach), the latter being practically sinusoidal;
- the cogging force related to quasi Halbach scheme has higher harmonic content, which can harmfully affect the mover dynamics.

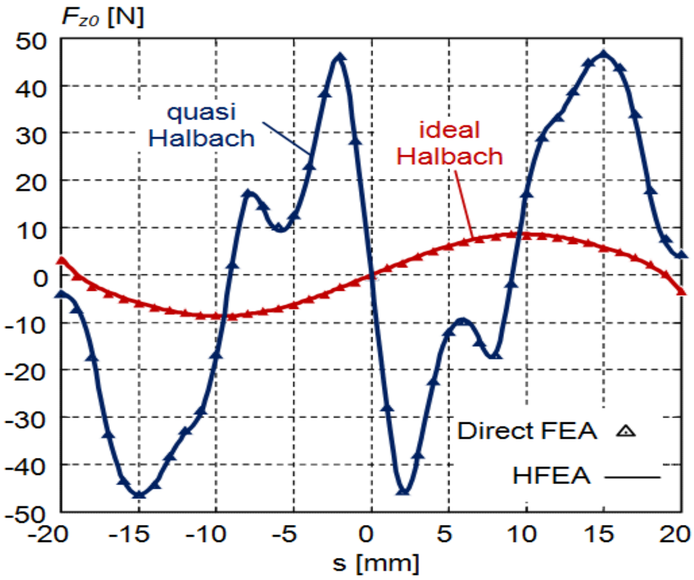

Figure 5.21. *No-load force for ideal Halbach and quasi Halbach magnetizations (w_{mr}=w'_{mz}= 20 mm, w''_{mz}= 10 mm).*

To check the effectiveness of the calculation procedure, the core losses at both no-load and $I_G = I_G^*$ are evaluated by HFEA and by direct FEA, with a very good agreement (Table 5.5). It is worth to point out that transient package required by the latter analysis is considerably more time consuming than a magnetostatic FEA. Losses are mainly confined in the stator core (about 85% of the total value) and particularly in the zone S_3; at load, core losses further increase due to the magnetizing effect of the coil mmf.

Table 5.5. *Core losses in W calculated by HFEA and direct FEA.*

Operating condition	**HFEA**					**Direct FEA**
	Zone S_1	***Zone S_2***	***Zone S_3***	***Mover***	***Total***	
No-load	3.6	1.8	3.3	1.4	10.1	10.2
$I_G = I_G^*$	4.6	2.1	4.2	2.3	13.2	12.8

5.8 Example of application

The HFEA can be utilised to study and analyse the performance of different magnetization profile and different current supply strategy [214]. Through a parametric analysis, an optimization of TPMLG can be carried out.

For the example of application, a simple harmonic motion and a load current source with a predefined number n_G of odd harmonics are considered:

$$v(t) = \hat{V}\cos(\omega t) \tag{5.50}$$

$$i(t) = \sum_{k=1}^{n_G} I_{G,k}\cos(k\omega t) \tag{5.51}$$

To such purpose, three different PM magnetization patterns are compared by HFEA, namely:

- ***pattern I*:** pure Halbach magnetization, corresponding to sinusoidal spatial distributions for m_r and m_z;
- ***pattern II*:** radial magnetization corresponding to a square-wave m_r distribution, with $w_{m,r} = 3\,\tau/4$;
- ***pattern III*:** quasi-Halbach magnetization corresponding to square wave distributions for both m_r and m_z, the PM width ratio being $\alpha_r = w_{PM,z}/w_{PM,r}$, with $w_{PM,z} = 2\,w_{PM,z}^o$ to maximize the no-load flux at $s = \tau/2$.

As regards the current supply, two possible strategies are considered:

- ***strategy A:*** sinusoidal current supply (*nG* = 1, current in phase with no-load e.m.f. e_{G0}) with $I_{G,1} = \sqrt{2}\, I_G^*$, wher$I_G^*$e is rated value of the coil current;
- ***strategy B:*** current supply by suitable harmonic components in order to maximize the mean converted power, the total current rms value being equal to I_G^*.

The condition is fulfilled by choosing the harmonic amplitudes according to the following equations:

$$\begin{cases} I_{G,\mathrm{k}} = \dfrac{E_{G0,k}}{E_{G0}}\, I_G^* = \beta_{I,k}\, I_G^* \\ \displaystyle\sum_{k=1}^{n_G} I_{G,k}^2 = {I_G^*}^2 \end{cases} \tag{5.52}$$

with $\mathrm{E}_{\mathrm{G0,k}}$ harmonic amplitudes and E_{G0} rms value of the no-load emf calculated by the magnetostatic analyses.

As regards the *pattern III*, the calculation of the no-load flux linkage by (5.23) in the range $0.5 \leq \alpha_r \leq 0.95$ by a parametric analysis defines the optimal value $\alpha_r \cong 0.75$ (Figure 5.22): for lower and higher values the flux decreases due to the lower B_r contribution and to the higher mover saturation, respectively.

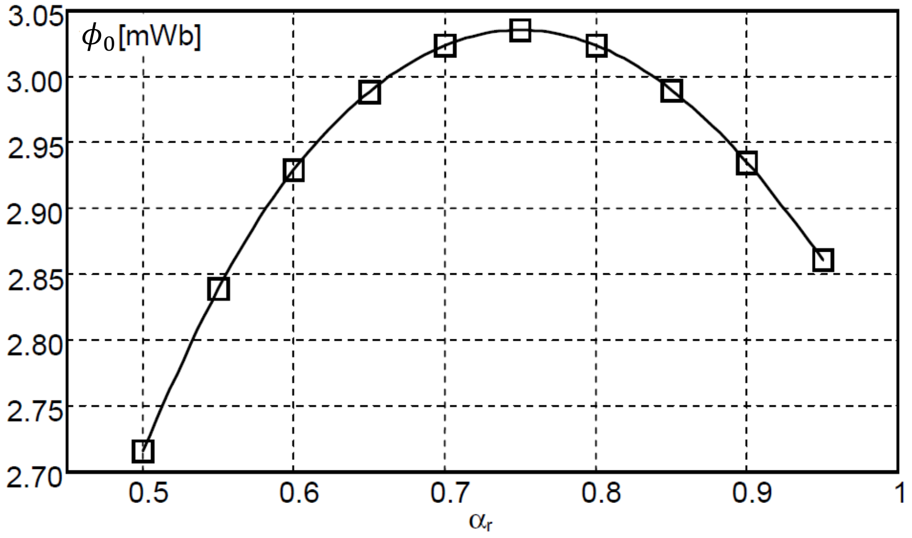

Figure 5.22. *No-load flux linkage* $s = \tau/2$*at as a function of the PM width ratio related to pattern III.*

An example of parametric analysis can be also carried out in order to optimize the no-load flux, by changing the PMs width w_{PM}. Such analysis can be straightforwardly accomplished by HFEA, since it requires only the analytical elaboration of the results obtained by the preliminary FEA sequence, according to (5.23).

An example of this calculation is shown in Figure 5.23: an almost perfectly sinusoidal waveform is achieved by a very limited number of iterations for w_{PM}=5/8 τ = 25 mm. This case allows achieving a sinusoidal waveform for the emf as well. A low harmonic content in emf reduces the core losses and thus results in an efficiency improving.

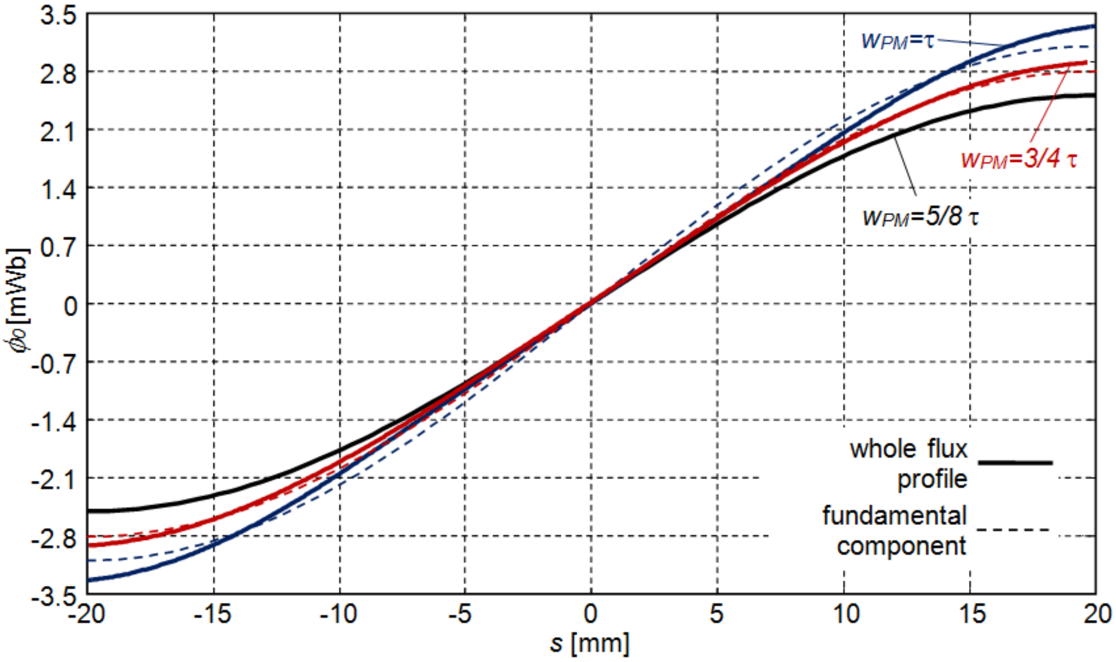

Figure 5.23. *No-load flux linkage as a function of position for different* w_{PM} *values.*

In the same figure, the curve related to w_{PM}=3/4 τ = 30 mm is also reported, as it matches different requirements of limitation of PM amount, flux maximization and reduction of the harmonic content. This condition maximize the flux/PM amount ratio, that means, at the same time, the maximization of the flux/cost ratio, since the PM cost is the highest one in relation to the other TPMLG active parts.

Another important issue to investigate is the cogging force F_{z0}, because it affects the starting of linear generator and in general its dynamic behaviour. The cogging force results from the interaction between the iron-structure stator teeth and the permanent magnets mounted on the translator part.

For such purpose four other different magnetization patterns have been considered:

- ***pattern I*****:** pure Halbach magnetization;
- ***pattern II*****:** quasi Halbach magnetization with $w_{PM,r} = w_{PM,z} = 2\,w^{o}_{PM,z} = \tau/2$;
- ***pattern III*****:** quasi Halbach magnetization with $w_{PM,r} = 4\tau/5$ and $w_{PM,z} = 2\,w^{o}_{PM,z} = \tau/5$;
- ***pattern IV*****:** radial magnetization with $w_{PM,r} = 4\tau/5$.

Figure 5.24 shows the influence of the magnetization pattern on the cogging force F_{z0}. The agreement with nonlinear FEAs was confirmed for all the configurations. The lowest cogging force is achieved in the pure Halbach scheme, thank to more smoothed magnetization profile and thus lower interaction between the magnet and the stator core. The worst condition is represented by *pattern III*.

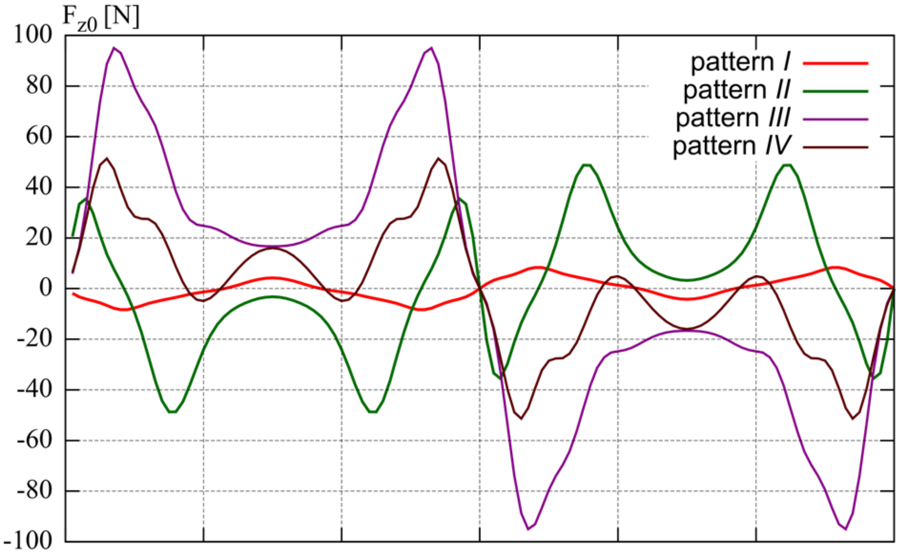

Figure 5.24. *Cogging force F_{z0} for different magnetization patterns obtained by HFEA with Z=2.*

As for the comparison at load condition, the calculation of the current harmonic content for *strategy B*, carried out by (5.52) with n_G=5, evidences the presence of an appreciable 3rd harmonic, mainly for *pattern II* ($\beta_{I,3} = 0.35$); on the other side, *pattern III* is characterized by the higher fundamental and 5th harmonics $\beta_{I,1} = 0.97$, $\beta_{I,5} = 0.04$). The main performances for both the supply *strategy A* and *B* are compared in Table 5.6: mean power and efficiency values are close and satisfactory for both *patterns I* and *III*. It's worth pointing out that *strategy B* generally leads to lower flux density peak values inside cores and consequently to lower hysteresis losses. Though benefitting by PM amount saving and an easy-to-manufacture magnetization profile, *pattern II*, yielding about 17% less mean power, has poorer efficiency and power factor.

Table 5.6. *Performance comparison for different magnetization schemes and current supply strategy.*

Pattern	**Supply strategy**	**P_G [W]**	**ΔP_G [-]**	**P_{Fe} [W]**	**η [%]**	**λ [-]**
I	A	452.0	1.57	15.1	89.9	0.856
	B	488.0	2.09	14.1	90.7	0.831
II	A	368.0	1.49	10.8	88.8	0.852
	B	387.0	1.99	10.1	89.4	0.787
III (α_r=0.75)	A	439.0	1.41	14.0	89.8	0.881
	B	456.0	1.80	13.0	90.3	0.812

The most remarkable P_G improvement (≈ +8%) is obtained by applying strategy B to pattern I, with a slight efficiency increase as well, with the drawback of a higher power fluctuation, as shown by Figure 5.25. Generally, it can be seen that the greater is the deviation of the e_{G0} waveform from sinusoid (due to non-uniform speed) the more profitable is the pulsed current supply in comparison with other control strategies.

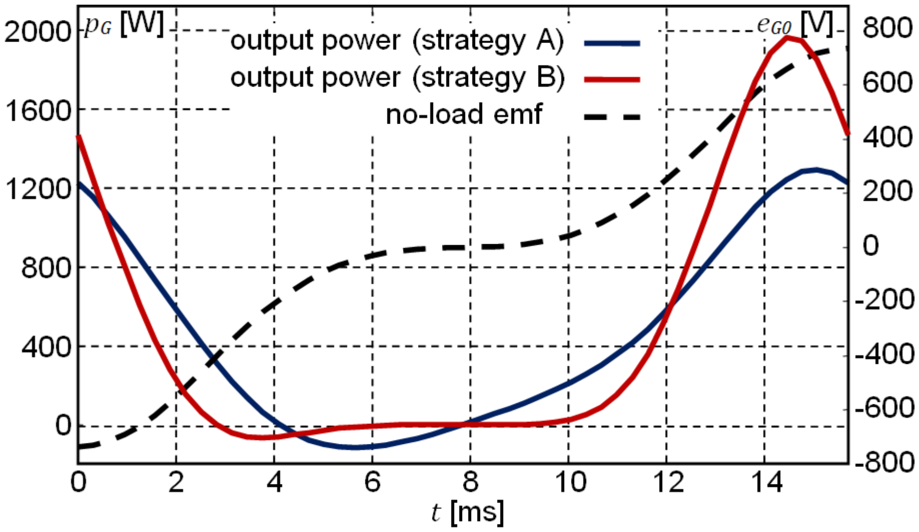

Figure 5.25. *Instantaneous output power and no-load emf related to pattern I.*

HFEA flexibility and computational effectiveness enables also a fast parametric analysis of the TLPMG performances as functions of the current load ratio I_G/I_G^*, as shown in Figure 5.26, related to strategy B. Efficiency is satisfactory in a pretty wide load range, and power rate is only a little less than linear, due to saturation.

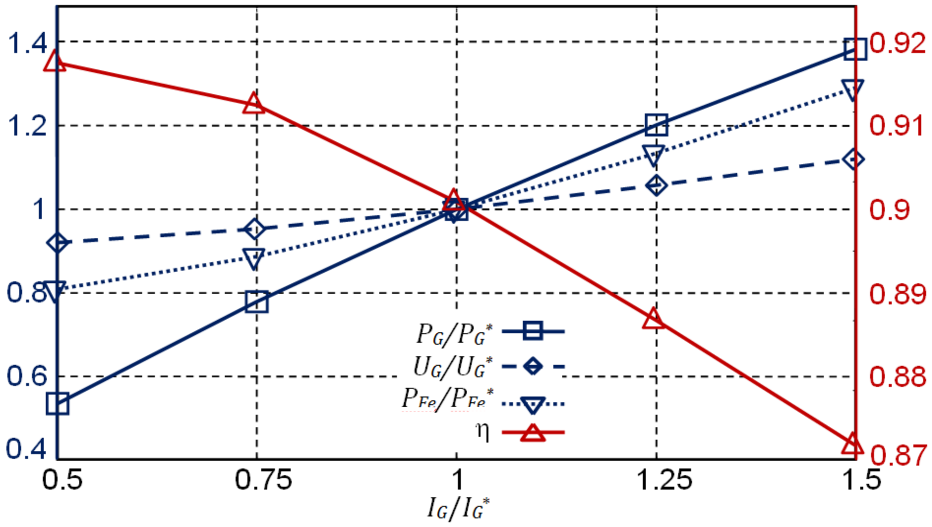

Figure 5.26. *TPMLG performances as functions of load (pattern I - strategy B).*

Since a wide SMC commercial variety is available, differing from each other by magnetic properties as well as cost, it is convenient to investigate how the former affect both the TLPMG flux linkage and core losses, especially in presence of distorted flux density time variation. Such parametric analysis, useful to identify the most convenient material for the ferromagnetic cores, is applied to the materials reported in Table 5.7 [216-218]. Even if the linearized magnetic permeability values are close, these materials differ by both BH curve saturation and specific core loss values.

Table 5.7. *Magnetic properties (magnetic field and core losses) of SMC materials.*

N.	Material type	$\frac{\mu_{m,lin}}{\mu_0}$	H [kA/m] @ 1 T	H [kA/m] @ 1.5 T	p_{FE} [W/kg] @ 1 T	
					60 Hz	*400 Hz*
1	GKN 304913	400	1.5	4.9	-	71.7
2	Ancorlam®	400	2.2	7.9	9.0	67.0
3	Ancorlam® HR	300	2.7	8.5	7.6	53.0
4	Somaloy® Prototyping	400	2.5	12.0	5.9	47.0

With reference to pattern I (the most effective as for the output characteristics) and to supply strategy B, the results of comparison are reported in Table 5.8: the highest P_G value is obtained by the N.1 material with less saturated BH curve. As for efficiency, the material N.4 could be preferable due to its lower core losses. However, the relatively low operating frequency is not worth using expensive materials with high bulk resistivity, making preferable the achievement of other benefits in terms of manufacturing features and power performance.

Table 5.8. *Performance comparison for different SMC materials.*

N.	Material type	U_G [V]	P_G [W]	P_{Fe} [W]	η [%]	λ [-]
1	GKN 304913	443	488	14.1	90.7	0.831
2	Ancorlam®	434	474	15.9	90.2	0.824
3	Ancorlam® HR	439	483	15.8	90.4	0.829
4	Somaloy® Prototyping	428	465	10.7	90.9	0.819

5.9 Conclusion

In this chapter an analytical procedure based on magnetization space harmonic was developed. The proposed HFEA method combines the results of linear FEAs related to the space magnetization harmonics with an iterative procedure to define suitable surface current sheets, effectively taking into account the heavy mover saturation. The method is based on the superposing of the effects due to the different magnetization harmonic orders, the effect of coil current and the effect of the fictitious current sheets on the mover surface. By this procedure is possible to reconstruct some interesting quantities such as the airgap flux density, utilised to estimate the thrust force value by means of the Maxwell stress tensor; the flux density inside the stator and mover cores, utilised to estimate the core losses.

After the preliminary elaborations, any magnetization pattern can be analysed and therefore HFEA can be effectively adopted for parametric analyses and design optimization.

The HFEA procedure enables a considerable time saving with respect to direct FEAs, since it operates on fixed geometric configurations with predefined sinusoidal magnetization patterns. It is particularly convenient to improve the TPMLG performance by comparing different magnetization schemes and supply strategies and can apply to parametric variations and optimization analyses as well. Its effectiveness is confirmed by the good agreement with the corresponding direct FEA results even with heavy mover saturation.

The example of application shows that, assuming a simple harmonic motion, the best performances as for output power and efficiency are obtained by Halbach-type magnetization and non-sinusoidal current-controlled supply. The procedure enabled also to investigate on the convenience of adoption of high permeable SMC material for the cores.

Chapter 6

Characterization of electromagnetic parameters

6.1 Introduction

The tubular permanent magnet (TPM) LG results the more indicated electromagnetic configuration for the free-piston co-generation system, as the mover can be easily integrated with the engine piston, resulting in a very compact arrangement. Furthermore, it is possible to scale up the power rating simply by lining up more stator and PM elements.

Remarkable benefits can derive from the use of molded powder materials, such as soft magnetic composites (SMC) for the stator core and bonded rare-earths for the PM ring, which can be magnetized after the installation on the mover shaft. Among them, the high manufacturing automation of the TPMLG active parts, the compact design, the isotropic magnetic properties of the stator SMC core (no complicated laminated structures are requested) [218] and the option to adopt different PM magnetization patterns to achieve particular design objectives make the TPMLG a very promising solution.

To check the effectiveness of the procedure used to analyse and design a TPMLG, presented in the previous chapter, a prototype of TPMLG was built. The stator and mover of the three-pole single-phase TPMLG prototype is reported in Figure 6.1.

The stator assembly (Figure 6.1*a*) consists of twelve SMC modular core segments, held together by the insulation box including a ring coil. The PM ring (Figure 6.1*b*) is divided into six identical pieces mounted on a solid iron hollow cylinder, suitably sized to reduce the moving mass, without appreciably affecting the magnetic saturation. This structure is joined to the inner shaft of the linear motion transmission. To optimize the output power/PM mass ratio, the coil flux linkage at the mover stroke ends should be maximized. For this purpose, the moving PMs should be always aligned to the stator pole axis at the stroke end.

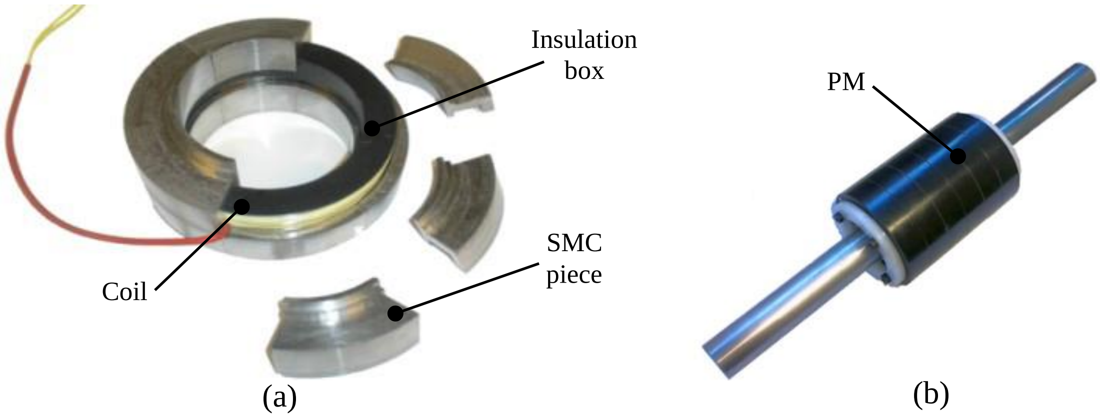

Figure 6.1. *3-poles single phase TPMLG prototype;* (a)*: stator with SMC modules and ring coil;* (b)*: mover with surface PM ring.*

Though general simplified assumptions can be used for a preliminary analytical design [210], a reliable assessment of the TPMLG output performances requires an accurate definition of the material properties, to be identified by suitable numerical procedures. Uncertainties related to coarse supplier specifications, process variability and heavy machining may lead to unreliable results and then to unsatisfactory set-up of the generator system, as for the design optimization as well as the control strategy assessment [219].

This chapter describes a procedure elaborating the results of both measurements and finite element analyses (FEAs) aiming to the determination of the main magnetic properties, such as the magnetization curve and the core loss coefficients of the SMC material as well as the actual PM magnetization function. The parameters defining the magnetic properties, obtained by the proposed procedure, are then implemented in the FE model to evaluate the expected performances in terms of voltage, force and core loss values, enabling both possible design improvements and the definition of the TPMLG mathematical model for the dynamic operation analysis [220].

The TPMLG prototype allows to check the procedure elaborated in the chapter 5, as well as to obtain an effective characterization of the magnetic material properties. Such quantities can be remarkably affected by the manufacturing process, leading to unexpected performance worsening. Then an appropriate procedure should be set up to evaluate possible mismatch with respect to the provider's specifications and to enable the definition of reliable models for design optimization and control strategy assessment.

Generally, the uncertainties are related to:

- the SMC magnetization curves and core loss coefficients, heavily affected by the raw sample manufacturing, the machining process, possibly deteriorating the particle insulation of the magnetic powder, and by the number of core segments;
- the magnetization distribution along the PM ring depending on the magnetizer arrangement, on the back-iron conductivity and on the material magnetic characteristic.

The preceding issues can be crucial for the performance prediction of the prototype under consideration. For such purpose, a procedure is developed to derive the main magnetic properties of the SMC material (linear and saturated permeability values, core loss coefficients) from the analytical elaboration of suitable experimental tests.

The experimental setup consists of $N_e = 4$ regularly spaced identical coils (excitation coils) with $N_t = 180$ turns each, placed around one half part of the stator core to obtain a quasi-toroidal field distribution (Figure 6.2), with low leakage fluxes and almost uniform magnetic flux on every transversal section of the stator core. Taking into account the isotropic magnetic characteristics of the SMC core, such arrangement should reproduce similar magnetic properties of the actual TPMLG. The adopted arrangement enables to achieve higher saturation than the actual configuration, since flux lines have to cross narrow stray air-gaps, provided that the SMC modules are assembled as tightly as possible.

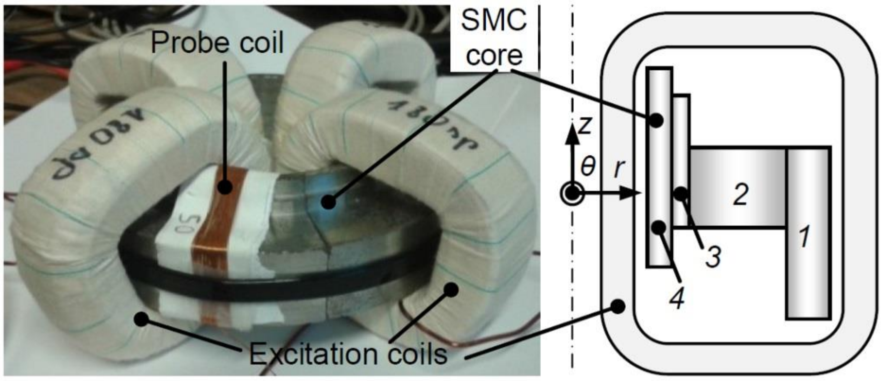

Figure 6.2. *Experimental setup for the magnetic characterization of the SMC core with the sketch of a radial section; 1,…,4: subdivisions of the core section used for the determination of the magnetic parameters.*

6.2 Determination of the permanent magnet parameters

As for the PM characteristics, the spatial flux density distribution along the PM surface is measured, the mover being extracted from the stator. The flux density is measured by a gaussmeter with a regular sampling step Δ = 2 mm, enabling to define the coercivity and the magnetization profile to be implemented in the FE model.

Three different magnetization spatial distributions are considered (dashed lines of Figure 6.3), compatible with measures and datasheet from PM manufacturer:

- *type 1*: a pure radial scheme, being $H_{C,1}$ the PM coercivity;
- *type 2*: an equivalent quasi Halbach scheme, being $H_{C,3}$ the PM coercivity and $\alpha_{z,r}$ the ratio between the axial and the radial magnetization amplitudes (light blue line);
- *type 3*: a pure radial scheme with a 3rd harmonic injection, being $H_{C,2}$ α_r^I and α_r^{III} the fundamental and 3rd harmonic coefficients, respectively.

The parameters $H_{C,1}$, $H_{C,2}, H_{C,3}$, α_r^I, α_r^{III} and $\alpha_{z,r}$ are determined by minimizing the deviation between measured and simulated data, the latter obtained by corresponding 2D rz FEA. In Figure 6.3, the flux density profiles with $H_{C,1} = -380\,kA/m$ for the *type 1*, $H_{C,2} = -342\,kA/m, \alpha_{z,r} = 0.2$ for the *type 2* and $H_{C,3} = -380\,kA/m$, $\alpha_r^I = 0.9$, $\alpha_r^{III} = 0.3$ for the *type 3* are compared. The FEA results show that the flux density profile is not adequately reproduced by a pure radial magnetization. Even if the presence of asymmetries between the lateral and middle pole is fairly reproduced by a *type 1* pattern, only the magnetization *type 2* satisfactorily accounts for the spikes in the middle pole region, and is more consistent with the PM segmentation and the actual magnetizer assembly. An appreciable reduction of the magnetic coercivity with respect to the declared design value (-400 *kA/m*) is evidenced for both the cases, and a consequent TPMLG performance derating is therefore to be expected.

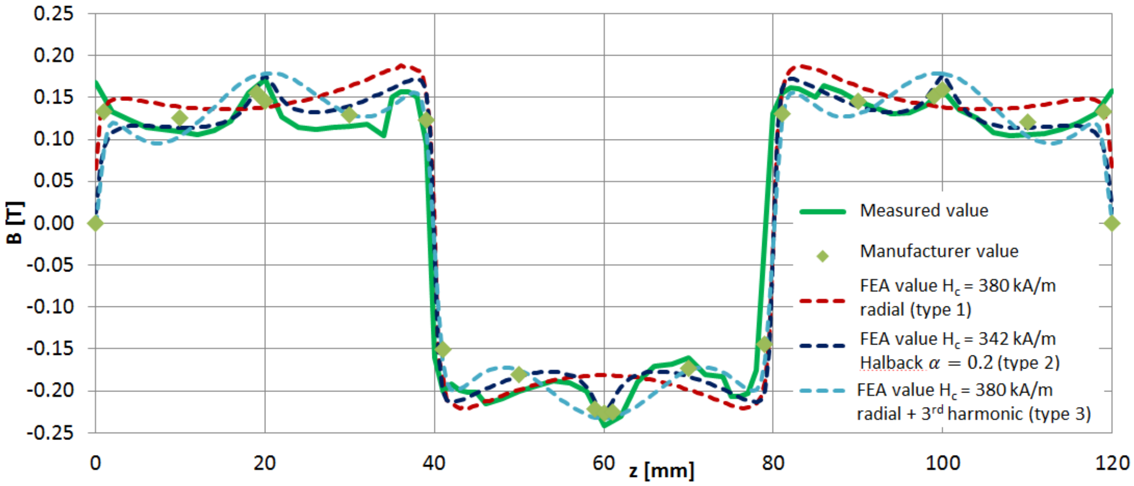

Figure 6.3. *Comparison between flux density data related to manufacturer sheet, laboratory measurements and FE simulations.*

6.3 Determination of SMC magnetization curve

In order to reproduce the material magnetization curve $B(H)$, a general analytical representation is considered. Among the different proposed formulations, the following function for the relative permeability $\mu_r(B)$ is selected [223]:

$$\mu_r(B) = \begin{cases} \mu_{lin} & \text{for } B < B_0 \\ \dfrac{1}{C_1\, e^{C_2(B-B_0)^2} + \dfrac{1}{\mu_{lin}} - C_1} & \text{for } B > B_0 \end{cases} \tag{6.1}$$

with μ_{lin} relative permeability of the linear unsaturated characteristic, B_0 [T] flux density value delimits the linear region and C_1, C_2 [T^{-2}] coefficients representing the μ_r decrease. The function appropriateness is evidenced by the very good agreement, even for high saturation, between the input material data and the interpolation obtained by the best-fit coefficients in (6.1) (Figure 6.4).

The coefficients C_1 and C_2 related to the prototype B(H) curve are determined evaluating the core magnetic flux as function of the excitation m.m.f. To such purpose, the excitation coils are supplied at low frequency (f = 30 Hz, sinusoidal voltage waveform) and the instantaneous values of the current supply and the induced e.m.f. on a probe coil (N_p = 50 turns), tightly coupled to the core, are recorded. Then, the flux linkage is straightforwardly determinated by integrating the probe coil per turn e.m.f., no correction for winding leakage fluxes and heating being required.

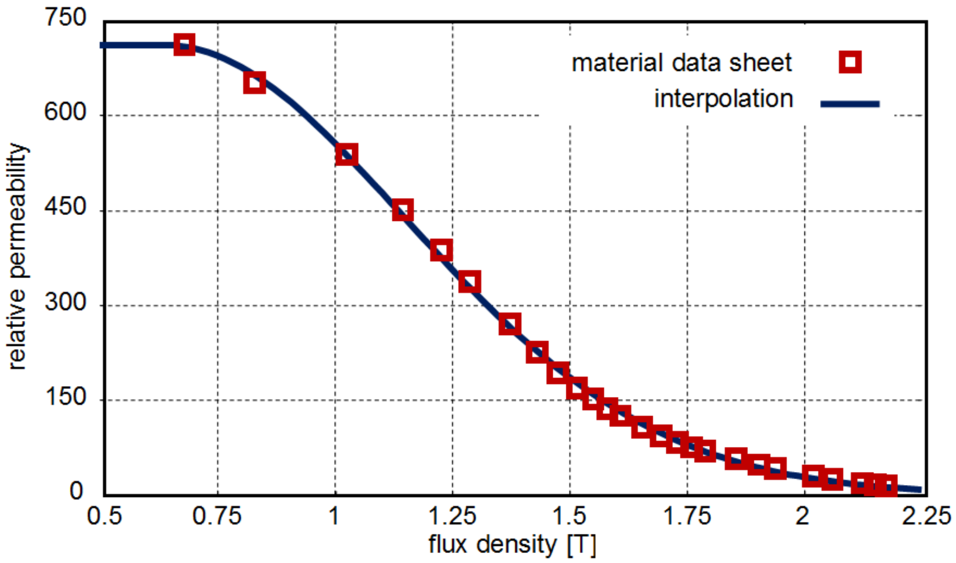

Figure 6.4. *Interpolation of the Somaloy® 700 3P relative permeability as a function of the flux density B ($B_0 = 0.64\,T$; $C_1 = 1.6\ 10^{-3}$ and $C_2 = 1.69\,T^{-2}$).*

The current peak value $\hat{I}_j^*$ in the excitation coils related to the j-th test ($j = 1 \div N_t' = 10$ with N_t' test number, * superscript identifies measured quantities) goes from 0.31 A to 8.05 A, the latter one corresponding to a remarkably high saturation. Figure 6.5 shows the dependence of the probe coil per turn flux linkage on the supply current. The material hysteresis loops centred on the magnetization characteristic $\hat{\phi}^*(\hat{I}_j^*)$, clearly recognizable in the figure, are obtained by the Fourier interpolations of both current and flux time samples. Such characteristic is related to the mean value of the flux density inside the whole core section; nevertheless, it takes by no means into account the non-uniform flux density distribution in the section itself due to the dependence of H on r.

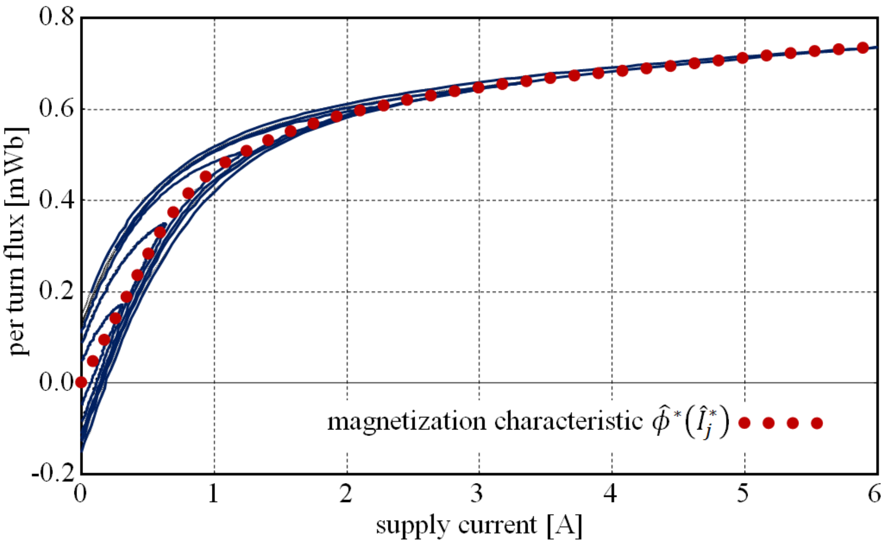

Figure 6.5. *Probe coil per turn flux linkage as a function of the supply current for different maximum current values ($\hat{I}_j^*$ = 0.31, 0.64, 1.23, 2.25, 3.34, 6.27 A).*

Therefore, an iterative procedure is set up, based on the determination of the core flux contributions of N_s = 4 subdivisions of the stator cross section (Figure 6.2) a uniform flux density being assumed in each zone, by virtue of its limited radial extent. This assumption is confirmed by a preliminary 3D magnetostatic FEA, using the maximum current supply (I = 5 A). The corresponding flux density map is shown in Figure 6.6. In particular the analytical prediction of the flux density mean value for each region is only 2.5% lower than the FE simulation, enabling a reasonable evaluation of the actual permeability values.

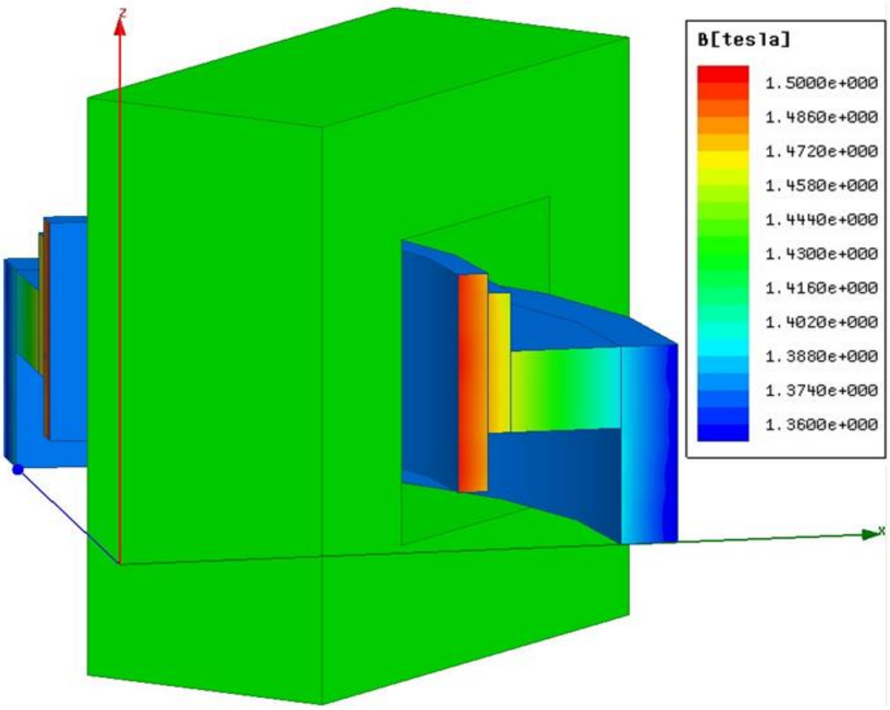

Figure 6.6. *Flux density map corresponding to* $I^* = 5$ *A*

Known the excitation m.m.f. and given the coefficients C_1 and C_2, the corresponding permeability values and the core fluxes in each region, can be calculated analytically. Based on such considerations, an iterative process varies C_1 and C_2 to minimize the deviations between the measured data and the analytical evaluations.

A detailed flow diagram of the procedure is represented in Figure 6.7. The following calculation steps can be identified:

a) with reference to j-th experimental test, the maximum instantaneous value of the magnetic field $\hat{H}_{j,k}$ in the k-th region ($k = 1, \dots, N_s$) is determined as:

$$\hat{H}_{j,k} = \frac{N_e N_t \, \hat{I}_j^*}{2\pi \, \bar{R}_k} \tag{6.2}$$

with $\bar{R}_k$ mean radius of the k-th region;

b) given a set of the $\left\{C_1^{(h)}, C_2^{(h)}\right\}$ coefficients (h: iteration index), the relative permeability $\mu_{r,j,k}^{(h)}$ in the k-th region can be determined by (1);

c) the corresponding magnetic reluctance $\Re_{j,k}^{(h)}$ and flux peak value $\hat{\phi}_{j,k}^{(h)}$ can be obtained by the expressions:

$$\Re_{j,k}^{(h)} = \frac{2\pi}{\mu_0\, \mu_{r,j,k}^{(h)}\, w_k \ln \frac{R_{e,k}}{R_{i,k}}} \tag{6.3}$$

$$\hat{\phi}_{j,k}^{(h)} = \frac{N_e N_t\, \hat{I}_j^*}{\Re_{j,k}^{(h)}} \tag{6.4}$$

with w_k, $R_{e,k}$ and $R_{i,k}$ axial width, outer and inner radius of the k-th region, respectively;

d) the j-th total flux linkage $\hat{\phi}_j^{(h)}$ is then obtained by summing the flux contribution of each k-th core region;

e) by repeating the steps a) to d), the sum of the square flux relative deviations $\sigma^{(h)}$ with respect to the experimental values is calculated; if the variation of $\sigma^{(h)}$ with respect to the previous step value $\sigma^{(h-1)}$ is lower than a predefined threshold ε, the iteration is stopped, otherwise a new set $\left\{C_1^{(h)}, C_2^{(h)}\right\}$ is imposed by the minimization algorithm.

Table 6.1 reports the main coefficients related to the SMC magnetic properties corresponding to the datasheets (model A) and to the elaboration of the flux-current measurements according to the flow diagram of Figure 6.7, assuming uniform bulk properties (model B) or including the influence of parasitic air-gaps between the core modules (model C). Such condition is simulated by introducing a constant magnetic reluctance $\Re_{gp}$, to account for the difference between the datasheet and the experimental m.m.fs for a given flux value in the linear region.

Table 6.1. *SMC magnetic parameter comparison between manufacturer data sheet values (model A) and experimental data (model B and C).*

Source of elaboration (*model*)	B_0 $[T]$	μ_{Lin}	$c_1 \cdot 10^{-3}$	c_2 $[T^{-2}]$
Data sheet (model A)	0.64	711	1.60	1.69
Experimental data (model B)	0.64	400	3.32	2.64
Experimental data (model C)	0.64	711	3.50	2.58

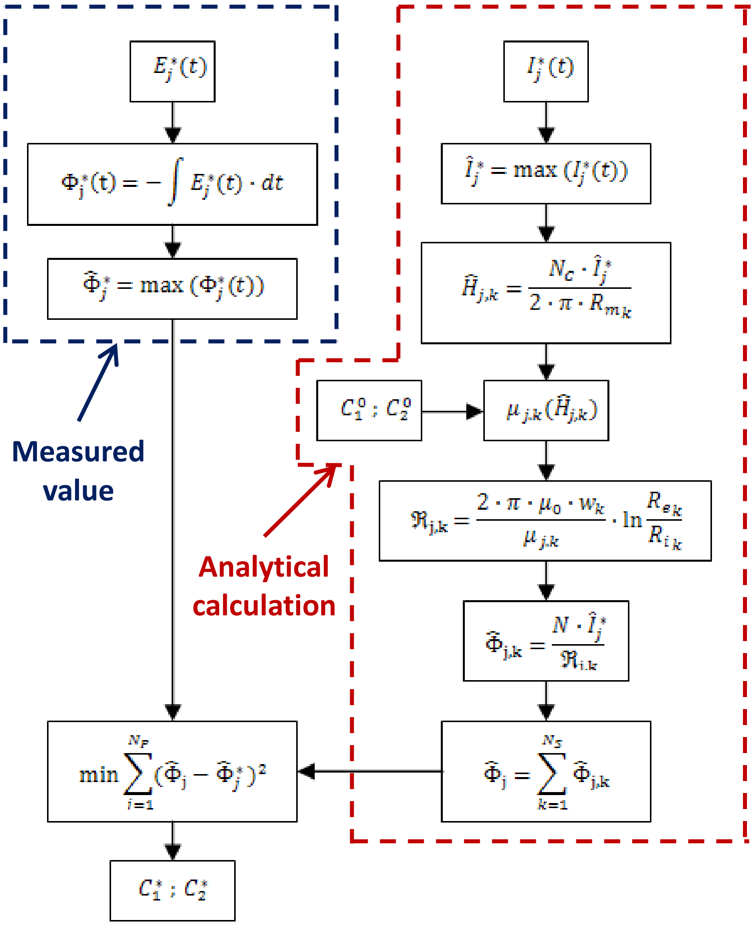

Figure 6.7. *Flow diagram of the procedure to evaluate the SMC magnetization parameters* C_1 *and* C_2.

In order to obtain the same datasheet $\mu_{lin} = 711$, a reluctance value $\Re_{gp} = 489600\ \mathrm{H}^{-1}$ has to be assumed, equivalent to an air-gap width $g_p = 0.337\ \mathrm{mm}$, consistent with the core assembly allowance. However, Figure 6.8 evidences a remarkably higher saturation for $B > 1\ \mathrm{T}$ with respect to datasheets, whatever the model adopted. For instance, at the design working point of the stator core ($B_{max} \cong 1\ \mathrm{T}$), the permeability is about 1/3 (from 326 to 110).

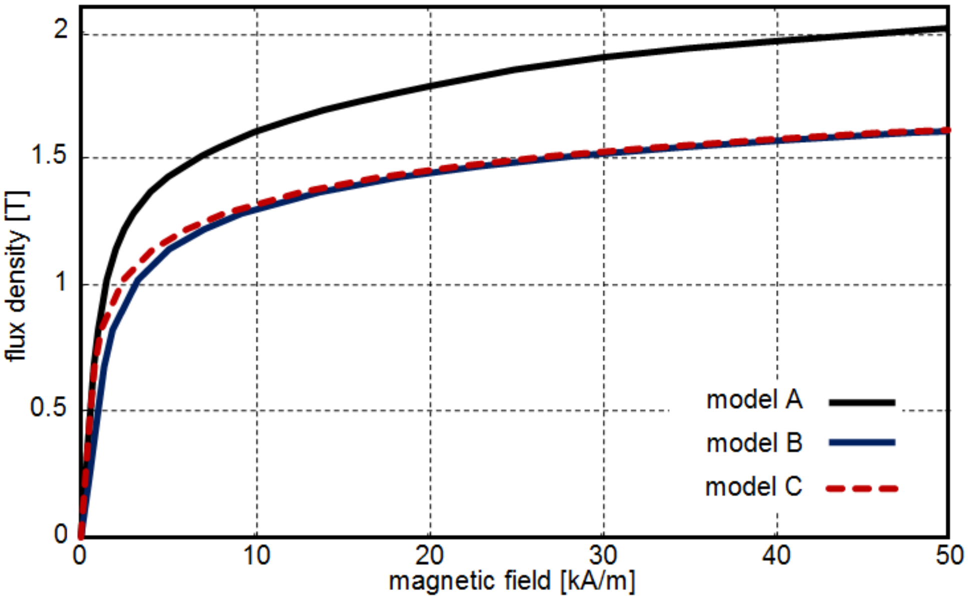

Figure 6.8. *Comparison between the magnetization functions obtained from the SMC datasheet (model A) and the measurement elaboration (models B and C).*

Both models A and B are checked by 3D FEAs, agreeing with measurements. Taking advantage of symmetry conditions, the FEA can be restricted to only one-quarter model (Figure 6.9).

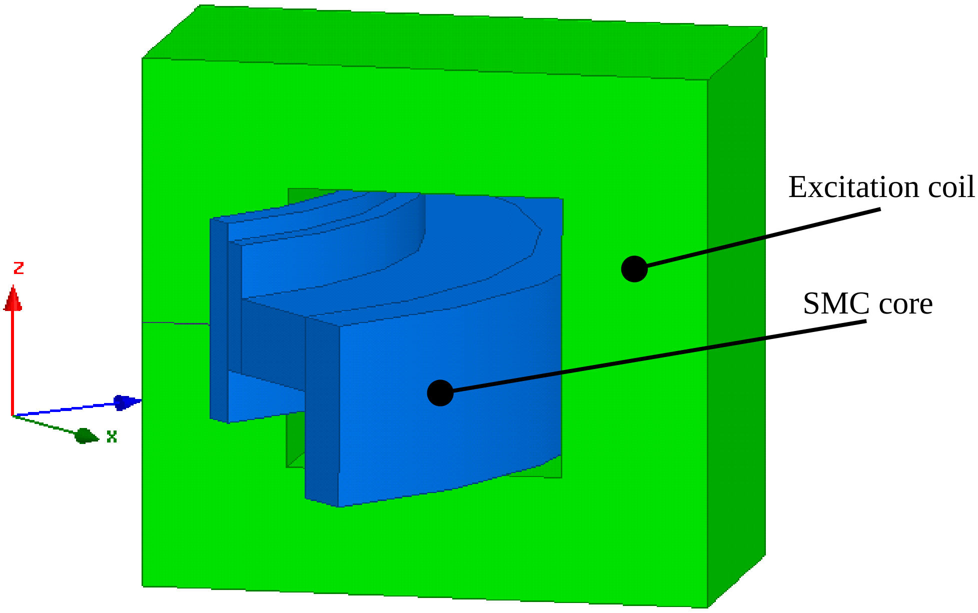

Figure 6.9. *One fourth of 3D FEA geometric model for the calculation of the magnetic flux.*

Figure 6.10 shows the magnetic flux as a function of the total excitation ampere-turns. In particular, it evidences a very good concordance between the FEA applying model *B* (FEA-B) and the measurement elaboration. With respect to the results related to datasheets (FEA-A), flux values are lower by about −20% for ampere-turns higher than 2 kA.

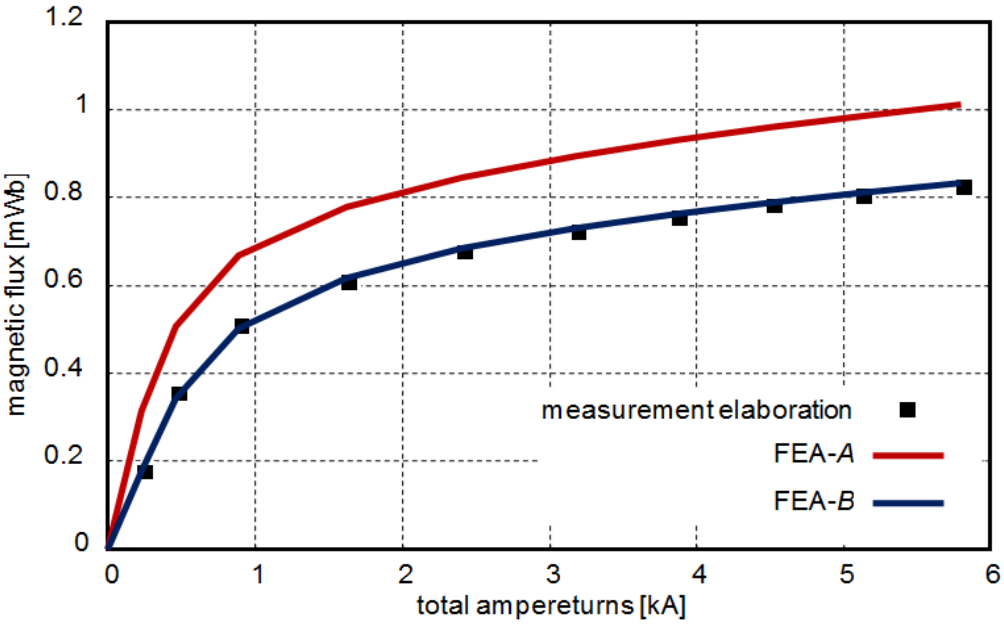

Figure 6.10. *SMC magnetic flux as a function of total coil ampere-turns, obtained by measurement and FEA data elaboration.*

6.4 Determination of SMC core loss coefficients

Due to the high remanence of the adopted NdFeB PMs, an appropriate utilization of the SMC material calls for a careful evaluation of the core losses. Despite of the limited operating frequency, saturation effects and distorted flux density waveform can appreciably affect the TLPMG electromagnetic efficiency. Furthermore, in this particular case, the prototype machining process could exalt possible eddy current generation especially on the stator module surfaces, due to the deterioration of the powder insulation coating [224].

Because of the test bench excitation symmetry, only the dependence on time of flux density circumferential component B_θ must be determined. Thus the average value of the core loss density p_{fe} [W/m^3] can be calculated by the sum of the hysteresis p_h, the eddy current p_{ec} and the excess loss p_{ex} terms, according to the formulation [224]:

$$p_{fe} = p_h + p_{ec} + p_{ex} = k_h\, f\, \hat{B}_\theta^2 + \frac{1}{T}\int_0^T \left(\frac{k_{ec}}{2\pi^2} \left| \frac{dB_\theta}{dt} \right|^2 + \frac{k_{ex}}{8.76} \left| \frac{dB_\theta}{dt} \right|^{\frac{3}{4}} \right) dt \qquad (6.5)$$

where $f = 1/T$ is the fundamental frequency, $\hat{B}_\theta$ is the peak value of B_θ, k_h, k_{ec} and k_{ex} are the hysteresis, eddy current and excess loss coefficients, respectively.

The total core losses P_{fe} are finally obtained by integrating the average core loss density on the volume V_k of each k-th stator subdivision:

$$P_{fe} = P_h + P_{ec} + P_{ex} = \sum_{k=1}^{N_s} \int_{V_k} p_{fe,k}\, dV = \sum_{k=1}^{N_s} 2\pi\, w_k \int_{R_k^i}^{R_k^o} r_k\, p_{fe,k}\, dr \qquad (6.6)$$

where w_k is the width of the k-th zone, R_k^i and R_k^o are the inner and outer radius of k-th zone respectively, r_k is the radius coordinate referred to k-th zone. It is worth pointing out the equation (6.6) is numerically evaluated, elaborating the flux density values sampled on a uniform grid.

Likewise for C_1 and C_2, the coefficients k_h, k_{ec} and k_{ex} are determined by minimizing the deviation between the data obtained by the elaboration of the measurements on the prototype and the results of the above described analytical formulation.

The procedure is based on the elaboration of data related to measurements with different frequencies f_j^* and current peak values $\hat{I}_j^*$ (with $j = 1, \dots, N_t''$, with $N_t'' = 21$ test index). Let v_j^* and i_j^* the corresponding recorded instantaneous values of supply voltage and current and R_e the excitation winding resistance, the total core losses $P_{fe,j}^*$ derived from measurements are determined as the difference between the input power $P_{in,j}^*$ and copper loss power $P_{cu,j}^*$:

$$P_{fe,j}^* = P_{in,j}^* - P_{cu,j}^* = \frac{1}{T_j^*} \int_0^{T_j^*} \left(v_j^*\, i_j^* - R_e\, {i_j^*}^2\right) dt \qquad (6.7)$$

where $T_j^* = 1/f_j^*$ is the period.

The frequency ranges from 20 Hz to 200 Hz, the latter value to the maximum allowable for the supply equipment. Because of voltage limitations, the maximum supply current has to be decreased for the highest frequency values, thus limiting to some extent the saturation conditions. Actually, some smoothing and regularization procedure has to be applied, to mitigate the influence of error sources (influence of temperature on R_e, disturbances, sample discretization, etc.). Corresponding flux linkage peak values $\hat{\Psi}_j^*$ are evaluated by integrating the e.m.f.:

$$\hat{\Psi}_j^* = \max \int \left(v_j^* - R_e\, i_j^*\right) dt \qquad (6.8)$$

The values $P_{fe,j}^*/f_j^*$ of the core energy loss per cycle are then fitted by a function of frequency and flux linkage peak value given by $k_1 \hat{\Psi}^n + k_2 \hat{\Psi}^m f^p$. The first term, related to hysteresis losses, can be extrapolated from energy losses for $f \rightarrow 0$, and hysteresis losses can be estimated by the function:

$$\tilde{P}_h(\hat{\Psi}, f) = k_1 \hat{\Psi}^n f \tag{6.9}$$

Then, the residual losses $\tilde{P}_{res,j}$ are obtained, including the excess and the eddy current loss contributions:

$$\tilde{P}_{res,j} = \tilde{P}_{ec,j} + \tilde{P}_{ex,j} = P^*_{fe,j} - \tilde{P}_h(\hat{\Psi}^*_j, f^*_j) = P^*_{fe,j} - \tilde{P}_{h,j} \tag{6.10}$$

The core loss model (i.e., k_h, k_{ec} and k_{ex} coefficients) is determined by a fitting procedure, aiming to match the values obtained according to $\tilde{P}_{h,j}$ and $\tilde{P}_{res,j}$, respectively.

The main calculations can be summarized as follows:

a) the instantaneous magnetic field in the m-th sampling point of the core section ($m = 1, \dots, n_s$ with $n_s = 51$ number of sample points in the core section) and related to the j-th experimental test, is determined as (r_m: sample radius):

$$H_{j,m} = \frac{n_e N_e \cdot i^*_j}{2 \cdot \pi \cdot r_m} \tag{6.11}$$

b) the corresponding flux density tangential component $B_{\theta,j,m}(H_{j,m})$ is obtained by the magnetization curve; the Fourier analysis (13 odd harmonics are considered) of the instantaneous values yields the maximum value $\hat{B}_{\theta,j,m}$ and the time derivative function $B'_{\theta,j,m}$;

c) the total core losses are obtained integrating the core loss densities by equation (6.6);

d) by repeating the steps a to c for all N''_t tests, the sum of the relative square flux deviations $\sigma^{(h)}_{loss}$ with respect to the experimental values is calculated (h: iteration index); if the variation of $\sigma^{(h)}_{loss}$ with respect to the value $\sigma^{(h-1)}_{loss}$ at the previous (h-1)-th step is lower than a predefined threshold ε, the iteration is stopped, otherwise the core loss coefficients are updated and the process is repeated.

The flow diagram of the procedure utilized to determine the core loss coefficients is reported in Figure 6.11.

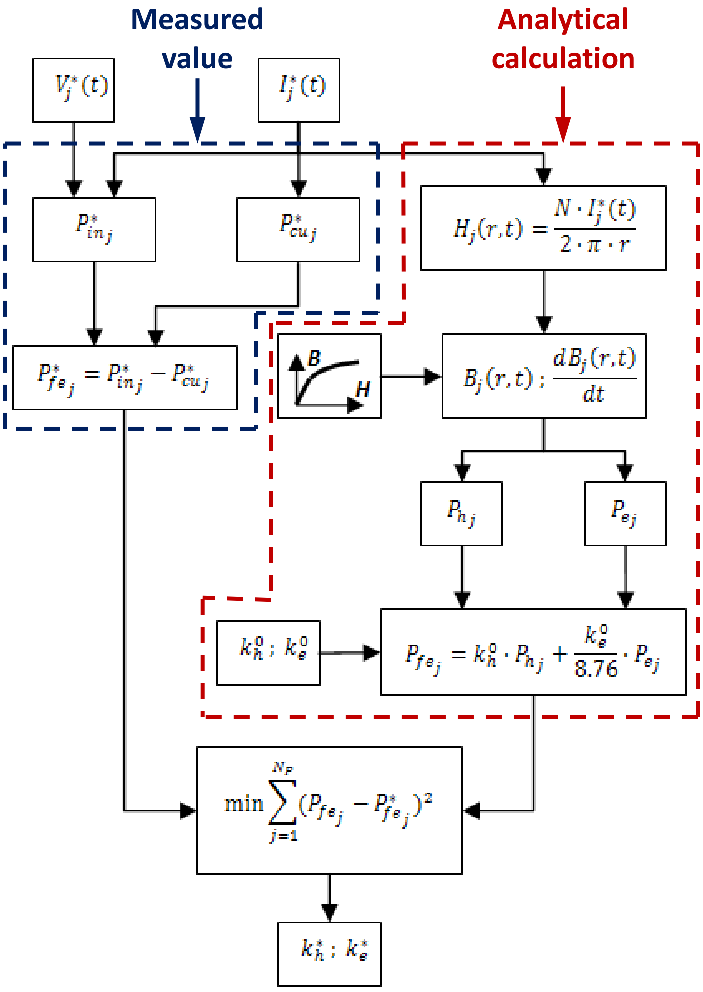

Figure 6.11. *Flow diagram of the procedure to evaluate the SMC core loss coefficients.*

As for the core loss model, Table 6.2 reports the coefficients derived from material datasheet elaboration and the application of the procedure described in Figure 6.11, applied to the measured losses. A good correspondence is obtained between the hysteresis coefficients k_h (about 12% difference). On the contrary, in the datasheet elaboration, the excess losses are prevalent [9], while the residual losses evaluated by experimental elaboration depend on $\cong f^2$, suggesting to adopt $k_{ex} = 0$.

Table 6.2. *Core loss coefficients comparison between data sheet and experimental values.*

Source of elaboration	$k_h \left[\frac{Ws}{T^2 m^3}\right]$	$k_{ec} \left[\frac{W}{T^2 s^{\frac{1}{2}} m^3}\right]$	$k_{ex} \left[\frac{W}{T^{\frac{3}{2}} s^{\frac{2}{3}} m^3}\right]$
Datasheet	615	0.14	9.64
Experimental data	688	12.2	-

Such result confirms the possible core loss increase due to the machining process. The hysteresis and residual core losses obtained from the measurement elaboration and evaluated by the coefficients k_h and k_{ec} related to datasheet elaboration are compared in Figure 6.12: a satisfying agreement is attained in the low and medium frequency range, whatever the flux value. On the other side, the discrepancy is appreciable for the highest frequency value (150 Hz), which can however regard minor flux density harmonic contributions with respect to the TPMLG rated frequency.

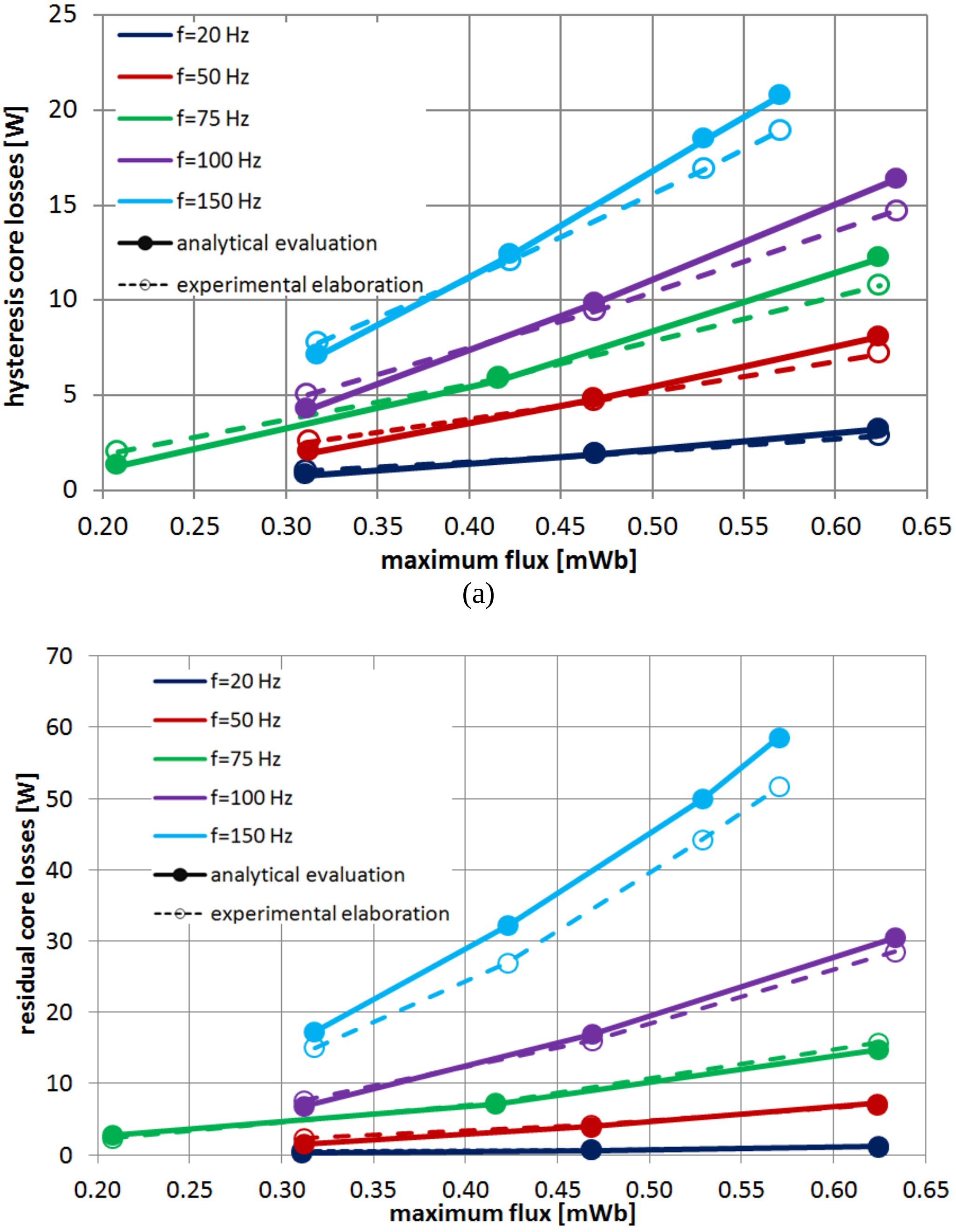

(a)

(b)

Figure 6.12. *Hysteresis losses* (a) *and residual losses* (b) *vs flux peak value* $\hat{\psi}_m$ *and frequency f by measurement elaboration and by analytical evaluation.*

From Figure 6.12 it's worth noticing the relevant values of the eddy current losses for the experimental elaboration which become even higher than the hysteresis losses as frequency $f \geq 75\,\text{Hz}$, whatever the flux value. Such effect is not recognizable in the measurement elaboration data, where the ratio P_{ex}/P_h is always lower than 25% even at high frequency values. Even if core machining could have introduced a significant loss increase with respect to the SMC pressure molding process adopted for mass production, as a precautionary approach, the calculated core loss model is adopted to evaluate the TPMLG performances.

Furthermore, a sample transient 3D FEA related to the condition $\{f, I\} = \{100\,\text{Hz}, 0.67\,\text{A}\}$is executed to evaluate the core losses by the code built-in routine. The FEA adopting the same coefficients as for experimental elaboration yields $P_{c,FEA} = 10.6\,\text{W}$, 10.2% lower than the measured value ($P_c^* = 11.8\,\text{W}$). Analytical approach for experimental elaboration provides $P_{c,an} = 11.0\,\text{W}$ (-6.8% than measurement, +3.8% than FEA). Even in this case, the accuracy of the procedure can be therefore considered satisfactory.

6.5 Evaluation of the actual TPMLG performances

Because of the appreciable mismatch between design and experimental PM and SMC magnetic properties, an update of the analysis of the TPMLG prototype performances is required. To such purpose, the material magnetic models related to the datasheet and calculated parameters are considered.

Carbon steel magnetic properties are assigned to the mover shaft, suitably downgraded to take into account eight lightening holes ($\emptyset = 12\,\text{mm}$). For the model related to datasheet elaborations, a PM radial magnetization is assumed with coercivity $H_c = -400\,\text{kA}$, while *type 3* magnetization (quasi Halbach scheme with $H_{c,3} = -342\,\text{kA/m}$ and $\alpha_{z,r} = 0.2$) is assumed for experimental model.

In order to compare the results of the experimental model with the results explained in the previous chapter (in which the electromagnetic properties has been provided by the manufacturer datasheets), the same working conditions have been considered:

- simple harmonic motion: $v(t) = \hat{V}\cos(\omega t)$;
- sinusoidal load current: $i_G(t) = \sqrt{2}\, I_G\, \cos(\omega t)$.

The instantaneous voltage and power (related to both datasheet and experimental models) are shown in Figure 6.13: in spite of the sinusoidal dependence of flux linkage on s, no-load voltage e_{G0} is non-sinusoidal due to the speed variation; voltage e_G at load is even more distorted, due to the armature reaction. The high third to fundamental harmonic amplitude ratio for no-load voltage ($\cong 21\%$ and $\cong 24\%$ for datasheet and experimental model, respectively) confirms this configuration is more suitable for a pulsed rather than sinusoidal current supply [212].

The heavy second harmonic component of output power p_G (greater than mean value) is inherent in single-phase operation, and likely could require some suitable storage device to interface with the electrical network. Correspondingly, high input shaft thrust oscillations result, to be taken into account in the engine design.

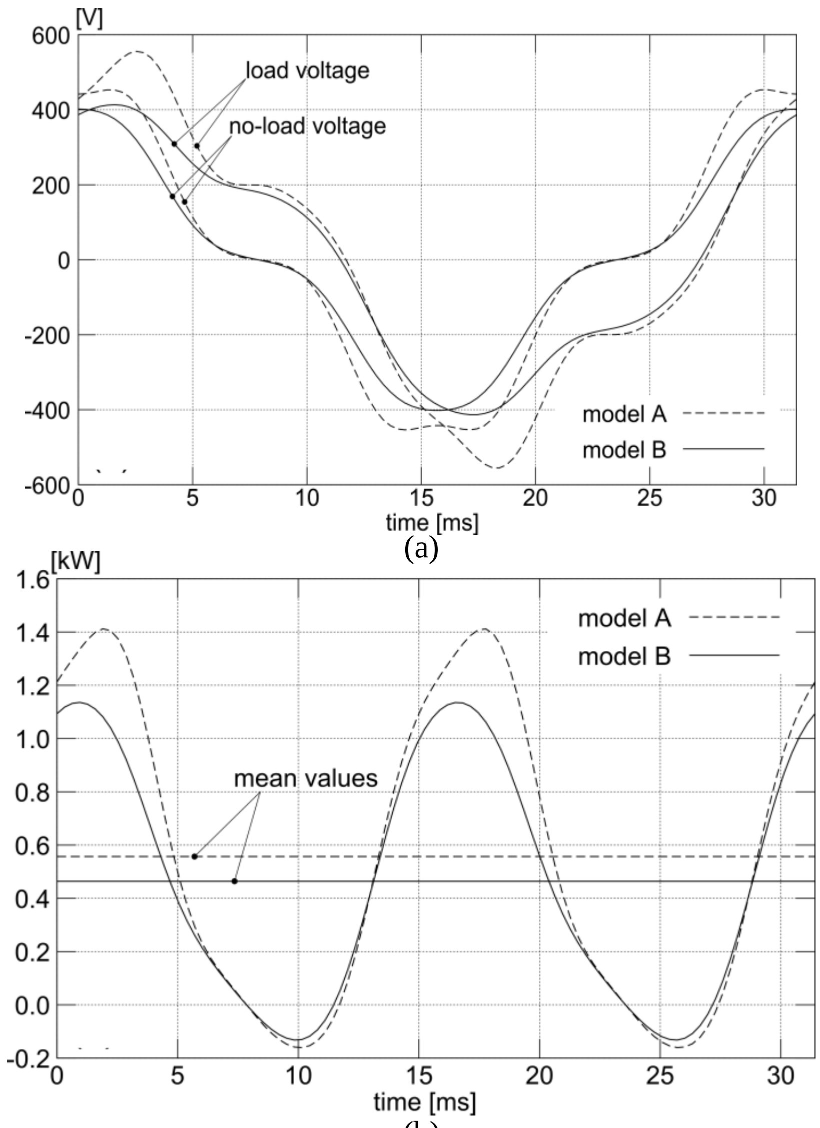

(a)

(b)

Figure 6.13. *Simulated TPMLG instantaneous quantities of voltage and power calculated by the datasheet and experimental models. (a): no-load* e_{G0} *and load voltage* e_G*; (b): output power* p_G *with corresponding mean value*.

Table 6.3 shows the remarkable influence on the electromagnetic quantities of the mismatch between the datasheet and the measured magnetic properties. In particular, both no-load voltage E_{G0} and mean output power decrease P_G (−17.6% and −16.7%, respectively), while stator core losses remarkably increase (+21.4%) due to higher core loss coefficients. Nevertheless, the detriment of efficiency is not so dramatic (about 1.7%).

Furthermore, both cogging force peak $\hat{F}_{z0}$ value and winding inductance mean value $\langle L_G \rangle$ remarkably decrease, enhancing dynamic performance and power factor, respectively.

Table 6.3. *Comparison of TPMLG performances and output parameters for datasheet and experimental models.*

Model	E_{G0} **[V]**	$\hat{F}_{z0}$ **[N]**	$\langle L_G \rangle$ **[H]**	P_G **[W]**	P_h **[W]**	P_{res} **[W]**
Datasheet	293	48.4	0.405	557	10.6	1.1
Experimental data	242	25.6	0.330	464	8.1	6.1

6.6 Conclusion

In this chapter, an analytical technique to estimate the electromagnetic parameters of a TPMLG by suitable experimental tests is developed. Measurement with variable supply voltage frequency and amplitude are elaborated to define the SMC magnetic properties, resulting in a remarkable mismatch with respect to datasheet, likely due to the heavy impact of the manufacturing processes. In detail, an analytical procedure to characterize the magnetization curve (*BH* curve) and the core losses of the SMC material utilized in stator core. The determination of the magnetization curve is based on the minimization of the flux linkage obtained by measurement and by analytical way. The procedure to estimate the core losses is based on the estimation of the core loss coefficients due to hysteresis, eddy current and excess losses. The characterization of core loss coefficients is deduced from minimization between the core losses evaluated by measurement and by analytical way.

The procedure’s effectiveness is nevertheless confirmed by the agreement of FEA results with measurements.

The actual PM magnetization pattern is identified by measurement as well. The flux density on the PMs surface of the removed mover was measured by means of a gauss-meter. The measured values are then compared with the results obtained from FEAs for

3 different possible magnetization profiles. It was found that the magnetization profile that fit the measured values in the best way is the Halbach magnetization profile.

The characterization of the TPMLG parameters enabling to analyse the main performances of the machine with the updated material characteristics: a power output decrease results, anyway not invalidating the initial design as to the application effectiveness.

Chapter 7

Dynamic model of Stirling Free-piston cogeneration system

7.1 Introduction

Linear generators find application in cogeneration systems powered by free-piston engines. Such kinds of systems present several advantages, such as the reduction of moving parts that means an increasing of reliability, a reduction of maintenance and then an improving in terms of efficiency.

The Stirling engine represents one of the most promising solution as regard the free-piston engine since it allows to achieve very high efficiency (theoretically the Carnot efficiency).

One of the most favourable features for their application is the possibility to integrate the LG mover with the machine member driven by energy source, with no additional mechanical couplings. As a result of the simplification of the kinematic system, both dynamic response and conversion efficiency are improved.

Particularly, the linear generator analysed and optimised in the previous chapters, cause of its low power ratings, it is designed to fit in a small domestic cogeneration system. In this case, the Stirling engine utilizes the waste heater of a boiler, which would otherwise be lost, to move a linear generator for electric energy production. Therefore, the Stirling engine converts the thermal energy obtained from the gas combustion process into mechanical energy that, in turn, is converted in electrical energy by linear generator. The linear generator is connected to the grid by means of an electric converter that allows the power exchange with the grid. It can be integrated with an energy storage system, such as a batteries or ultracapacitors bank, to store the surplus of electric energy that is not required to the load. The scheme of a free-piston cogeneration system is reported in Figure 7.1 where is also shown the major component of the system.

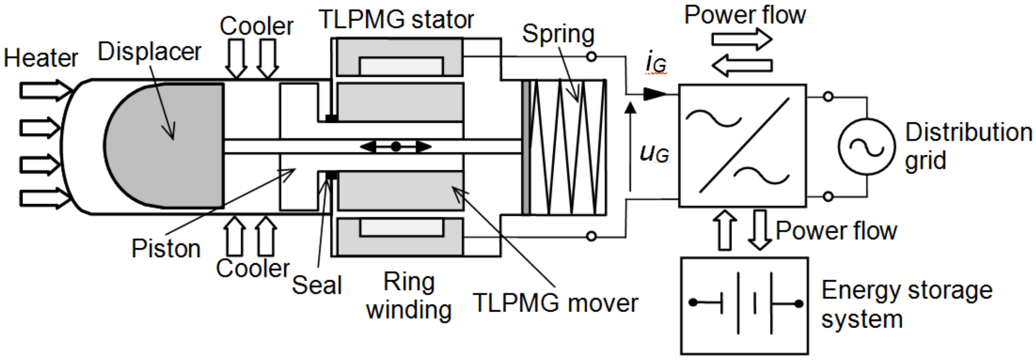

Figure 7.1. *Scheme of a free-piston energy converter integrating a Stirling engine and a single phase TLPMG.*

The operation of the whole co-generation system can be simulated only by developing a dynamic model of the power conversion devices (Stirling engine, linear generator and static converter) taking into account the electromechanical interaction among each other. To the purpose a Matlab Simulink® code is set-up aiming to the solution of both the mechanical and the electrical equations.

In particular, such code allows analysing the cogeneration system for the different load condition, as well as for different heat supply. Moreover, it allows finding the optimum solution in term of mechanical oscillating frequency ω_m [rad/s]. In fact, on one hand, is advisable to work at high frequency in order to obtain high e.m.f. and then high converted power values, but, on the other hand, this means to have a large spring constant k [N/m], in order to comply with the resonance condition:

$$\omega_m = \sqrt{\frac{k}{m}} \tag{7.1}$$

where m [kg] is the mass of the moving part.

Furthermore, at high speed, the thermal exchange between the heat exchangers and the working fluid considerably worsens.

It has been shown [225] that, due to the low-pass-filter effect of the mechanical mass-spring-damper subsystem, the piston velocity v [m/s] and the mover displacement x [m] according to the expressions:

$$x = \frac{x_M}{2}\sin(\omega_m\, t) \tag{7.2}$$

$$v = \int x\, dt = v_M \cos(\omega_m\, t) \tag{7.3}$$

where x_M and $v_M = \omega_m\, x_M/2$ are the maximum stroke and the maximum speed that can be achieved by the linear generator.

Another important issue that should take into account is the non-ideality of Stirling cycle, since the relatively high speed value. In this condition, the Stirling cycle deviates considerably from the ideal one, because of the non-ideality of energy transformations, which can be reproduced by adiabatic rather than isothermal curves in the pressure-volume (pV) diagram (Figure 7.2).

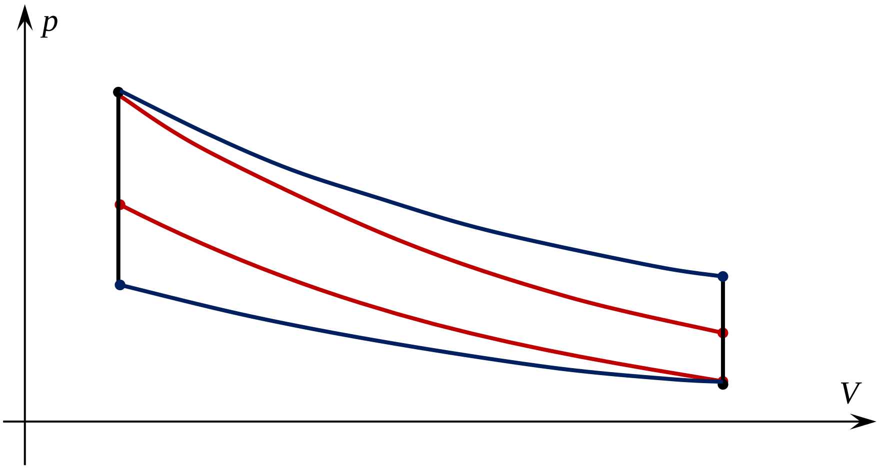

Figure 7.2. *pV diagram of Stirling cycle: isothermal transformations (blue lines) and adiabatic transformations (red lines).*

The above mentioned phenomenon is due to the extreme rapidity in which the fluid evolves inside the cylinder, which does not allow at working fluid to exchange heat with heater and cooler. For such reason, the temperature of working fluid cannot keep unvaried. This phenomenon involves a remarkably efficiency reduction that can be achieved the 50% of the ideal Carnot efficiency.

The simplest way to control the cogeneration system consists in controlling the reaction force of linear generator. Such condition is obtained by adjusting the load resistance in order to control the load current and then the linear generator force. The dynamic model is therefore convenient also to set up the control strategy in order to optimize the energy yield.

The model of the Stirling engine is developed starting from the ideal gas equation, and then it was elaborated, taking into account the non-ideality. For such purpose a real spatial thermal profile of the heat exchangers (heater and the cooler) was considered.

As for the model of the linear generator, it was developed by elaborating suitable FEAs, where the force and the flux linkage were calculated for different position and current values, storing the values in suitable lookup tables.

To connect the output of linear generator to the grid an electric converter arranged by a rectifier and an inverter has been considered. The output frequency of linear generator depends on the spring constant and the moving mass, as shown in equation (7.1). However, this value can vary in the neighbourhood of the mechanical resonant frequency in function of the electric load. In any case, generally, the mechanical resonant frequency can be lower than the grid one, requiring controlled interface converters to adapt both frequency and voltage to the grid values. The converter action is simulated by a variable resistive load which value is adjusted according to the signal elaborated by a PI regulator. Therefore it is possible to correct the position error with respect to the reference value established by resonant condition changing the LG current and then the thrust. The real position value can be provided by simply elaborating an output voltage measurement. In fact, measuring the output voltage and subtracting the internal voltage drop of the linear generator, is possible to achieve the speed value, and finally the mover position by integrating the speed estimation.

7.2 Dynamic model of cogeneration system

In a dynamic point of view, the resulting motion of the Stirling engine piston (Figure 7.3) is described by the Newton's second law:

$$\begin{cases} F_r = m\dfrac{d^2x}{d^2t} = F_{St}(x) - F_{lg}(x,i) - F_s - F_f \\ F_s = k_s\, x \\ F_f = b\, v \end{cases} \tag{7.4}$$

where: F_r is the resultant force; F_{St} is the force provided by free-piston engine, function of the mover position; F_{lg} is the linear generator electromagnetic force, function of the mover position and of the load current ; F_s is the force provided by the spring, with k_s [N/m] constant of the spring; F_f is the frictional force due to the working fluid viscosity and bearing friction, with b fluid friction coefficient $[N\ s/m]$.

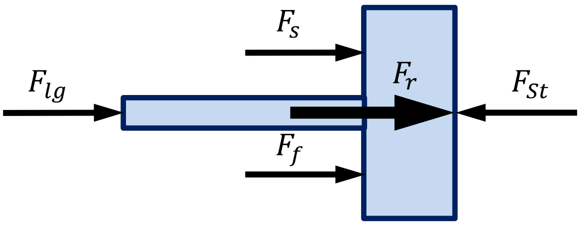

Figure 7.3. *Force balance on the Stirling engine piston.*

Equation (7.4) denotes the system nonlinearity therefore requiring a numerical solution. To the purpose, a Matlab Simulink code is developed schematically reported in Figure 7.4.

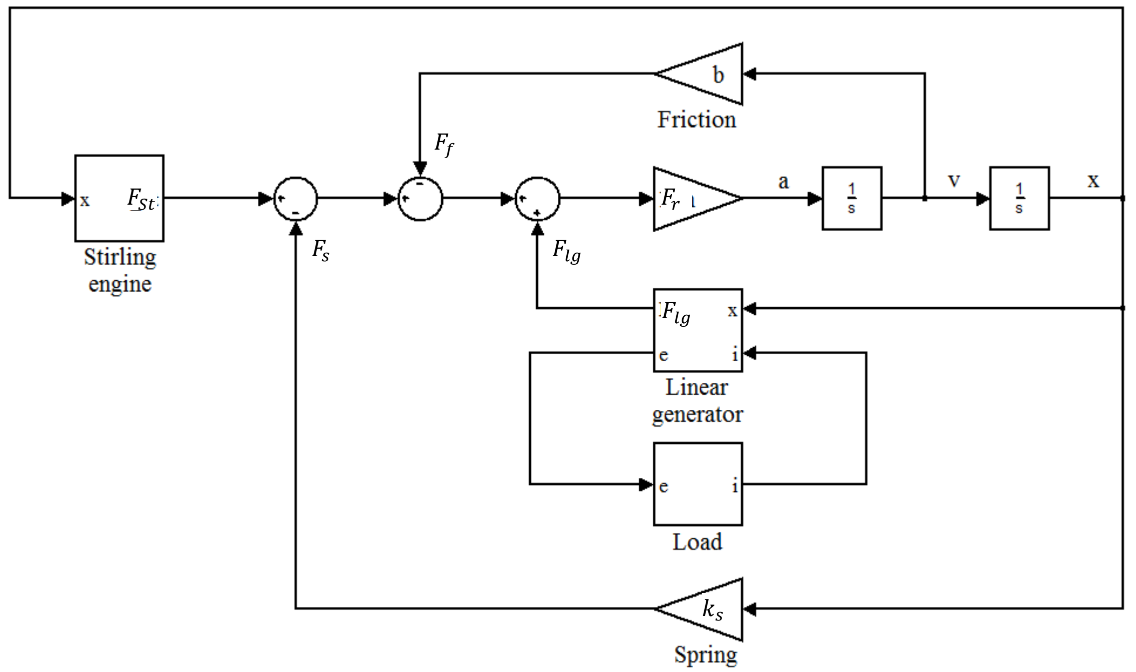

Figure 7.4. *Scheme of the dynamic model implemented with Matlab Simulink®.*

The model integrates the mechanical and the electrical systems. The mechanical system reproduces the force balance expressed by Equation (7.4). The electric model implements the voltage equation including the LG parameters and the equivalent load which simulates the converter action. In particular, the TPMLG represents the electromagnetic coupling between the mechanical and the electrical system, namely it converts the input mechanical power into the output electrical power at net losses. For TPMLG the following equations can be applied:

- for the electrical system (Faraday-Neumann-Lenz):

  $$e_{G0} = -\frac{d\varphi|_{I=0}}{dt} = -\frac{\partial\varphi|_{I=0}}{\partial x}\frac{\partial x}{\partial t} = -\frac{\partial\varphi|_{I=0}}{\partial x} v = k_e(x)\, v \qquad (7.5)$$

  where the flux linkage φ is only due to PMs magnetization and $k_e(x)$ is defined as the back-emf coefficient of the TPMLG, is dependent on the displacement of the permanent magnet.

- For the mechanical system:

  $$F_{lg} = \frac{P_G}{v} = \frac{e_G\, i_G}{v} = k_m(x) i + F_{lg0} \qquad (7.6)$$

  where $k_m(x)$ is defined as the thrust force coefficient of TPMLG, it is dependent on the mover displacement as well and F_{lg0} is the cogging force.

The coefficient $k_c(x) = k_e(x) = k_m(x)$ is the electromagnetic coupling coefficient of TPMLG.

In order to simplify the model it is convenient to report all the quantities in the same system. If we compare the differential equation of a mass-spring-damper mechanical system (Figure 7.5a):

$$F(t) = m\,a + b\,v + k\,x = m\frac{dx}{dt} + b\,v + k\int v(t)\,dt \tag{7.7}$$

with the differential equation of a series RLC electric circuit (Figure 7.5b):

$$u(t) = L\frac{di(t)}{dt} + R\,i(t) + \frac{1}{C}\int i(t)\,dt \tag{7.8}$$

the relationship between the two systems results as following:

$$m \Leftrightarrow L$$

$$b \Leftrightarrow R$$

$$\frac{1}{k} \Leftrightarrow \mathrm{C}$$

$$F(t) \Leftrightarrow u(t)$$

$$v(t) \Leftrightarrow i(t)$$

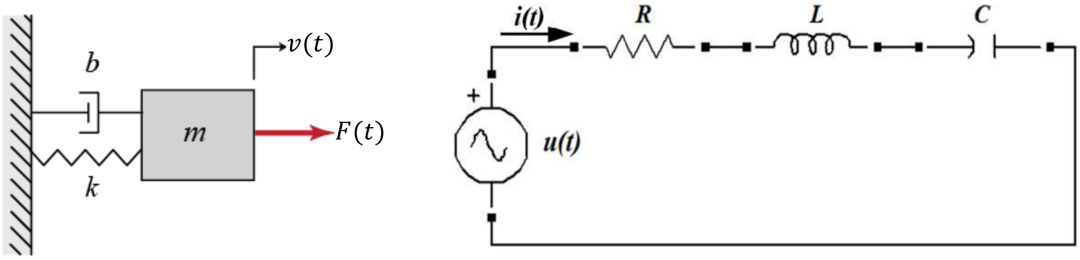

(a) (b)

Figure 7.5. *Mass-spring-damper mechanical system* (a) *and equivalent RLC series electric circuit* (b).

This analogy allows converting the mechanical elements into equivalent electrical elements and in this way a pure-electric system is obtained (Figure 7.6).

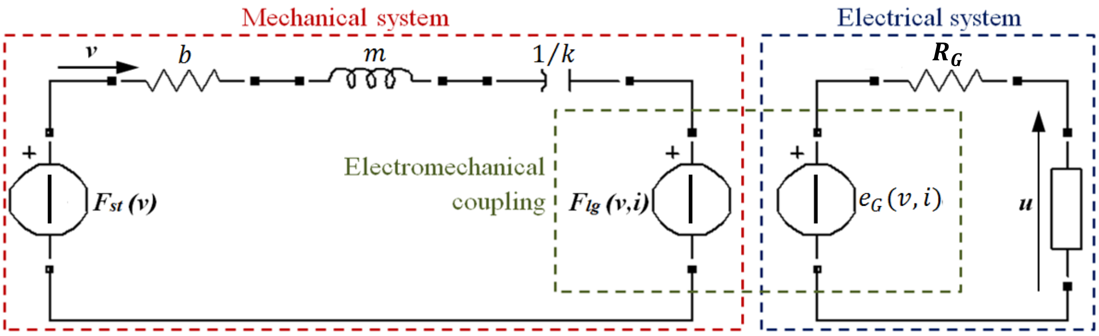

Figure 7.6. *Electric circuit utilized for the dynamic study of the system. The mechanical elements are converted into equivalent electrical elements.*

7.3 Stirling engine model

There is an increasing interest in the use of Stirling engine based cogeneration systems for residential and commercial cogeneration because of their prospect for high efficiency, good performance at partial load, fuel flexibility, low emission level, low vibration and noise level.

The model of a Stirling engine results quite troublesome to develop since there are many causes to take into account. Particularly, the main challenge is to describe the heat exchange between the working fluid and the heater/cooler, since it depends on the configuration (geometry, materials, etc.) of heat exchangers (geometry, materials, etc.). To such purpose, firstly an ideal model (assuming ideal gas) was developed. Then, the model was improved by taking into account the non-ideal phenomena, such as dead volumes, non-isothermal expansion and compression, thermal and mechanical losses and imperfect regeneration. These non-ideal phenomena result in efficiency decay with respect to the ideal case, and strongly affect the engine operating condition.

- ***Ideal model***

In the case of ideal gas (viz. ideal Stirling engine), the instantaneous value of the force $F_{St}(t)$ [N] provided by the Stirling engine can be obtained by rearranging the ideal-gas equation $p_g\, V_p = m_g\, R\, T_g$, where p_g is the pressure of the gas [Pa], $V_p(t) = x_p(t)\, S_p$ is the piston volume [m^3], m_g is the gas mass [g], $R = 0.287$ is the universal gas constant $\left[{}^{J}/_{g\,K}\right]$ and $T_g(t)$ is the gas temperature [K], respectively:

$$F_{St}(t) = p_g(t)\, S_p = \frac{m_g\, R\, T_g(t)}{V_p(t)} S_p = \frac{m_g\, R\, T_g(t)}{x_p(t)} \tag{7.9}$$

where S_p is the piston surface [m^2] and $x_p(t) = x(t) + x_{0,p}$ is the piston position, with $x_{0,p}$ the mean oscillating position of the piston.

During the isothermal expansion, the piston speed is positive and the gas temperature is maintained at the heater temperature value (T_h). Whereas, during the isothermal compression, the piston speed result negative and the gas temperature is maintained at the cooler temperature (T_c). Then, the equation (7.9) can be arranged as:

$$F_{St}(t) = \begin{cases} \dfrac{m_g\, R\, T_h}{x_p(t)} & for\ isothermal\ expansion\ (v > 0, T_g(t) = T_h) \\ \dfrac{m_g\, R\, T_c}{x_p(t)} & for\ isothermal\ compression\ (v < 0, T_g(t) = T_c) \end{cases} \tag{7.10}$$

The Stirling engine force can be expressed by a general formulation:

$$F_{St}(t) = \frac{m_g\, R\, \bar{T}_g + m_g\, R\, \frac{\Delta T_g}{2}\, \mathrm{sign}(v_p(t))}{x_p(t)} \tag{7.11}$$

where $\bar{T}_g = (T_h + T_c)/2$ is the mean temperature of the working fluid [K] and $\Delta T_g = T_h - T_c$ is the temperature gap of the working fluid [K].

By defining $\bar{K} = m_g\, R\, \bar{T}_g$ and $\Delta K = m_g\, R\, \frac{\Delta T_g}{2}$, the equation (7.11) can be rearranged as:

$$F_{St}(t) = \frac{\bar{K} + \Delta K\, \mathrm{sign}(v_p(t))}{x_p(t)} \tag{7.12}$$

Another important issue to investigate in order to describe the operating process of the system is mean position of the spring $x_{0,s}$ [m]. In fact, the mean position of the spring affects the mean position of the piston and consequently the dynamic of the system. For such purpose some energetic considerations were carried out.

The potential energy provided by the spring E_s [J] during a complete cycle is given by the difference between the maximum stored energy that corresponding to the maximum compression condition ($x_s = x_M/2 - x_{0,s}$), and the minimum stored energy, that corresponding to the minimum compression condition ($x_s = -x_M/2 - x_{0,s}$):

$$E_s = \frac{1}{2}k\, \left[\left(x_{0,p} + \frac{x_M}{2} - x_{0,s}\right)^2 - \left(x_{0,p} - \frac{x_M}{2} - x_{0,s}\right)^2\right] = k\, x_M\, \left(x_{0,p} - x_{0,s}\right) \tag{7.13}$$

with x_M the stroke length [m] (Figure 7.7).

The work provided by the Stirling engine during the compression phase, is given by the area under the lower isothermal ($T_g = T_c$) curve of the of the pV diagram. This area can be evaluated by analytical way by means of the integral:

$$E_{St} = \int_{-\frac{x_M}{2}}^{\frac{x_M}{2}} F_{St}\, dx = (\bar{K} - \Delta K) \ln\left(\frac{x_{0,p} + \frac{x_M}{2}}{x_{0,p} - \frac{x_M}{2}}\right) \tag{7.14}$$

The energy stored by the spring should be equals to the energy of Stirling engine during the compression phase. Therefore, by equating (7.13) and (7.14), it results:

$$x_{0,s} = x_{0,p} - \frac{\bar{K} - \Delta K}{k\, x_M}\, \ln\left(\frac{x_{0,p} + \frac{x_M}{2}}{x_{0,p} - \frac{x_M}{2}}\right) \tag{7.15}$$

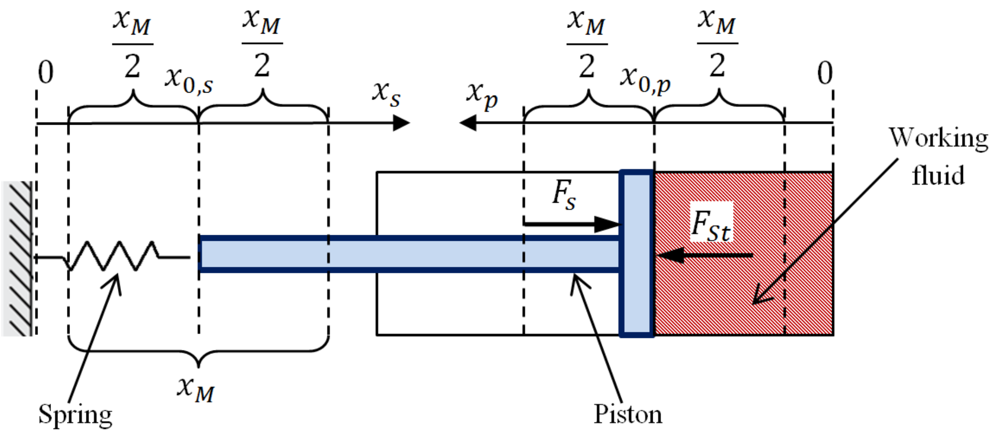

Figure 7.7. *Spring and the piston position reference.*

- ***Simplified model***

The ideal model does not take into account the non-ideal phenomena that adversely affect the TPMLG efficiency. Such phenomena can be summarized as:

- *dead volumes*: dead volumes are defined as the total void volume in a Stirling engine. In general, the dead volume refers to the volume of working fluid contained in the total dead space in the engine, including the regenerator and transfer port. It is evidenced that a real Stirling engine must have some unavoidable dead volume. In normal Stirling engine design practice, the total dead volume is approximately 58% of the total volume [228].

  Dead volumes alter the efficiency, in fact the output work as well as the adsorbed heat is proportional to:

$$\ln \frac{V_{max} + V_{dead}}{V_{min} + V_{dead}} \tag{7.16}$$

- *non isothermal expansion and compression*: due to high working frequency of the machine that does not allow at working fluid a heat exchange at constant temperature;
- *thermal losses*: due to conduction, convection and radiation losses;
- *mechanical losses*: due to friction between the operating parts of the system;
- *imperfect regeneration*: due to finite thermal capacitance of the regenerator and the not null thermal capacitance of the working fluid.

For such purpose equation (7.12) does not describe in the correct way the operation of the system. However, equation (7.12) can be generalized by:

$$F_{St}(t) = \frac{K(t)}{x_p(t)} \tag{7.17}$$

where $K(t)$ is a suitable non-linear function given by:

$$K(t) = \int \big(G_h(x)(K_h - K(t)) + G_c(x)(K_c - K(t))\big)\, dt \tag{7.18}$$

with $G_h(x)$ and $G_c(x)$ functions that represent the spatial profile of the heater and cooler heat exchange, respectively. A typical spatial profile of $G_h(x)$ and $G_c(x)$ is reported in Figure 7.8. $K_h = m_g\, R\, T_h$ and $K_c = m_g\, R\, T_c$ are two coefficients proportional to heater T_h and cooler T_c temperature, respectively.

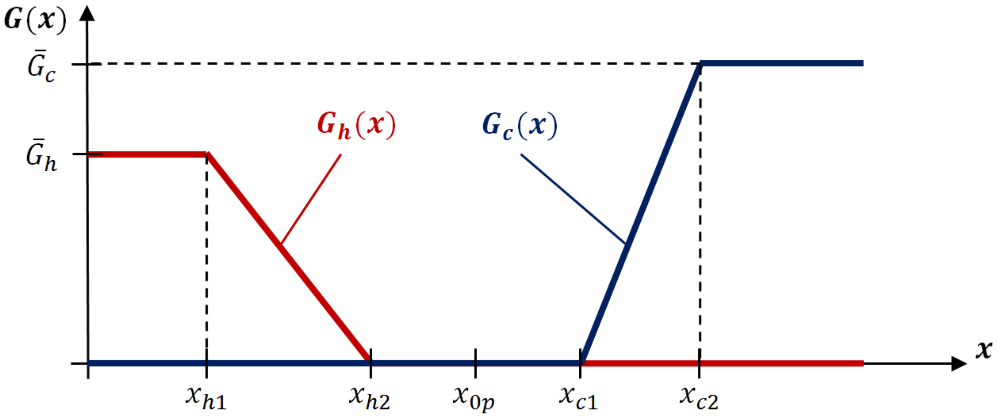

Figure 7.8. *Typical spatial profile of the heater $G_h(x)$ and cooler $G_c(x)$ heat exchange functions.*

Function $G_h(x)$ and $G_c(x)$ can be expressed analytically as:

$$G_h(x) = \begin{cases} \bar{G}_h & for\ x < x_{h1} \\ \bar{G}_h \dfrac{x - x_{h2}}{x_{h1} - x_{h2}} & for\ x_{h1} \leq x \leq x_{h2} \\ 0 & for\ x > x_{h2} \end{cases} \tag{7.19}$$

$$G_c(x) = \begin{cases} 0 & for\ x < x_{c1} \\ \bar{G}_c \dfrac{x - x_{c1}}{x_{c2} - x_{c1}} & for\ x_{c1} \leq x \leq x_{c2} \\ \bar{G}_c & for\ x > x_{c2} \end{cases} \tag{7.20}$$

Figure 7.9 reports the simulation comparison of the an ideal and a practical Stirling cycle. It’s worth pointing out that the area of the real Stirling cycle results lower than the ideal one. This is due to the working fluid temperature that is not able to achieve the heater and the cooler temperature. This results in an output power decreasing ($P_{G,real} \cong$ 1200 W) with respect to the ideal case ($P_{G,ideal} \cong$ 1750 W).

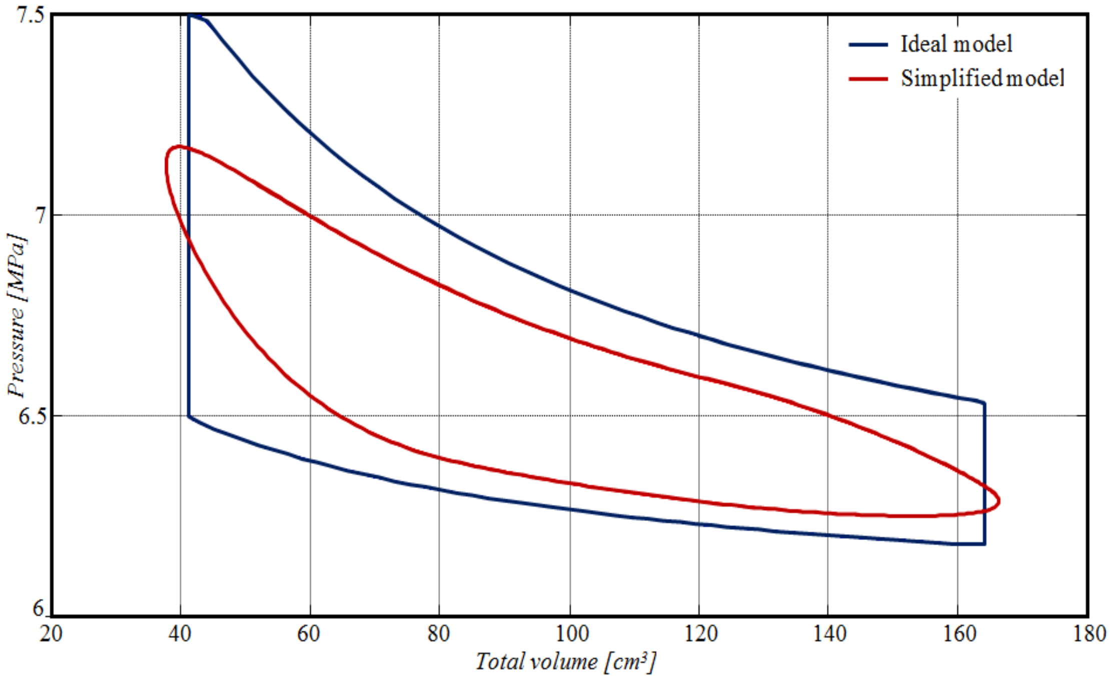

Figure 7.9. *Comparison between ideal and real Stirling engine ($f = 30\ Hz, T_h = 600\ °C, T_c = 25\ °C, \bar{G}_h = 150, \bar{G}_c = 200$).*

In order to validate the proposed model, the experimental results of a free-piston engine proposed in the literature are chosen as reference [226]. They are related to the model of the RE-1000 studied by the NASA during the 80's, having the characteristics reported in Table 7.1.

Table 7.1. *Most important characteristics of RE-1000.*

Output power [W]	955	Overall efficiency [%]	23.7
Swept volume [cm^3]	74.9	Operating frequency [Hz]	30.1
Piston stroke [cm]	4	Mean pressure [MPa]	7.034
Working fluid	Helium	Total mass of fluid [kg]	$4 \cdot 10^{-4}$
Heater temperature T_h [°C]	600	Cooler temperature T_c [°C]	25
Piston weight [kg]	0.25	Piston diameter [mm]	35

By comparison between Figure 7.9 and Figure 7.10, it can be observed the good agreement between the manufacturer data and the values obtained by means of mathematical model can be therefore considered satisfactory.

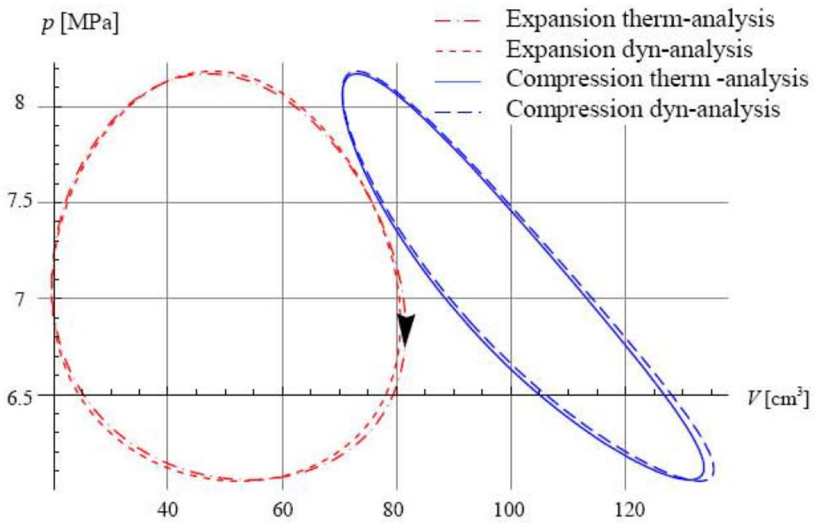

Figure 7.10. *Clapeyron diagrams for compression and expansion spaces* [227].

7.4 TPMLG model

The model of linear generator is based on two lookup tables obtained by means of a suitable sequence of FEAs. Through FEAs, the thrust force F_{lg} [N] and the flux linkage φ [Wb] for different values of supply current i [A] and mover position x [m] were carried out, thus lookup tables $F_{lg}(i,x)$ and $\varphi(i,x)$ are developed.

The e.mf. e_G [V] provided by linear generator to the load is given by:

$$e_G = -N_c \frac{d\varphi}{dt} \tag{7.21}$$

And then the load current i [A] is given by:

$$i = \frac{e}{R_{lg} + R_{eq}} \tag{7.22}$$

where R_{lg} is the internal resistance of linear generator [Ω] and $R_{eq} = \frac{v}{i}$ (with v the output voltage [V]) is the equivalent resistance of the load [Ω], which value is controlled adjusting the parameters of the electronic converter.

The scheme of the liner generator implemented in the Simulink code of the linear generator is reported in Figure 7.11.

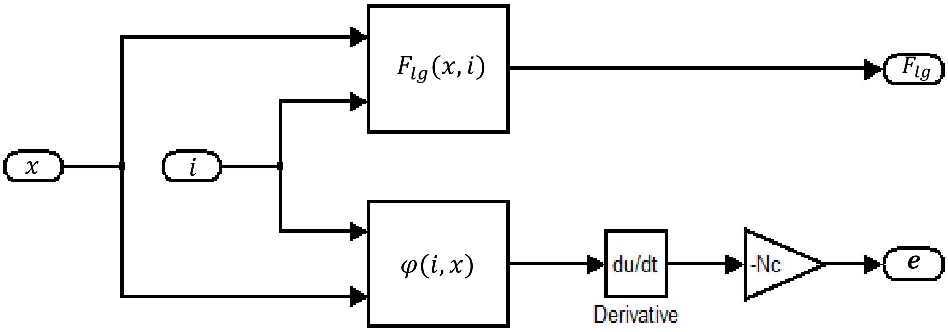

Figure 7.11. *Linear generator model.*

7.5 Electronic power converter model

The supply voltage of linear generator is usually at low frequency (a typical value is around at 30 Hz) since the mechanical constraint (mover mass and spring constant) limits the dynamic performances of the system. Moreover, the amplitude of the output voltage is related to the speed, which can vary during the operation of the machine. For such reason, an electronic converter is needed to connect the linear generator to the grid or to the electric load regulating the frequency and the amplitude of the output voltage. Such device generally consists of an AC/DC converter (i.e. a buck/boost or a simple rectifier) and an inverter.

A convenient control strategy of electronic converter is achieved by keeping the output current in phase with respect to the output voltage in order to maximize the highest converted power.

7.6 Control system

A cogeneration system produces simultaneously electricity and useful heat. Thanks to multi-fuel operation of the Stirling engine, the primary energy source can be derived from different heat sources such as fossil fuels or green fuels (biomass, geothermal and thermodynamic solar). Some renewable energy sources presents discontinuous and often unpredictable energy yield, since they are related to the climatic conditions. In addition, also the electric and the heat loads may present large variations especially in case of weaken. In particular, a sudden variation of the heating temperature in the Stirling engine system (due to fuel injection or heat load of the heater temperature involves a variation of the force provided by Stirling engine that, in turns, induces a variation of the speed of the system. In case of electric load variations, the TPMLG force may be affected altering the system speed. For example, if the load is sudden disconnected, the output current and then the reaction force of linear generator drops instantly.

For such reason, a control system has to be developed, in order to maintain the speed within the design limits. In fact, if the speed exceeds the maximum value means that the mover stroke would be greater than the mechanical constraints on the mover position.

The control the input fuel, where possible, is generally not convenient, since the thermal dynamics results too slow due to the high thermal capacitance of the heater. The most convenient solution is represented by the control of the load current, in order to comply with the reference speed profile.

The control of the load current is based on the load compensation, namely to adjust the load resistance by means of a fictitious resistance. The fictitious resistance is varied by changing the parameter of the electric converter in order to the linear generator supply to the load the required current. The electric converter works as a variable resistance and adjusts the resistance to the required value. In the case the output power of linear generator is greater than the power required to the actual load, the excess power may be provided to a storage system.

The scheme of the current control is reported in the Figure 7.12.

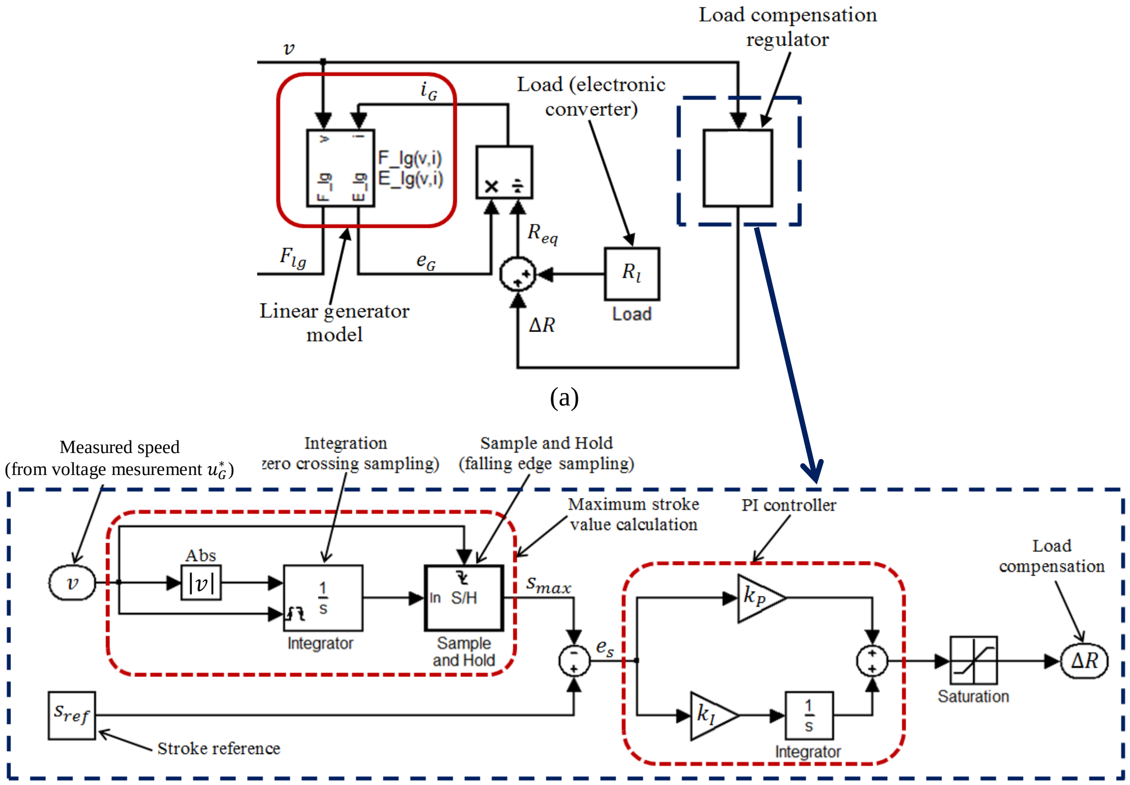

(a)

(b)

Figure 7.12. *Model of current control based on load compensation: current control* (a) *and detail of load compensation* (b).

The fictitious resistance of the load compensation is regulated by a PI controller from the error e_s between the reference value s_{ref} of the maximum stroke s_{max} and the measured value. The maximum value of the stroke is obtained from the following procedure:

- calculation of the absolute value ($|v|$);
- integrating by synchronization with the zero crossing, in order to achieve the profile of the stroke;
- sampling on the maximum value (sample on falling edge of the speed).

It's worth pointing out that the speed v can be obtained by a simple voltage and current measurement. The speed can be obtained from the following procedure:

$$e_G = u_G^* - R_G\, i_G^* \tag{7.23}$$

$$v = \frac{e_G}{k_e(x)} \tag{7.24}$$

where u_G^* [V] and i_G^* [A] are the measured output voltage and current values, respectively.

The advantage of this technique is that no mechanical measurement is required (seemingly sensor-less control with consequent improvement of the system reliability and maintenance and costs reduction).

The parameters of the PI controller are chosen in order to achieve a prompt dynamic response without an excessive overshoot. The saturation block after the PI controller limits the load compensation so that the load current does not excess the rated value due to thermal constraints.

7.7 Dynamic analysis

The Stirling engine considered in the proposed model is the RE-1000, since it fits the requirements of the cogeneration system and it is consistent with linear generator sizing. The most important features of the RE-1000 engine are reported in Table 7.1.

The dynamic model is utilized to analyse the electromechanical performances of the free-piston cogeneration system. In the free-piston arrangements, develop a model of the whole system is very important as, unlike to crank-shaft based arrangement, the working condition is heavily affected by the working point of the system. Since free-piston arrangements are not equipped of gearbox, the speed of the system is the same for all the parts that compose the system. For such reason, it is very important to determine the best solution from a speed point of view. The speed of the system is strongly linked to the mechanical resonant frequency ω_m.

From a performance point of view, the mechanical resonant frequency should be as large as possible, since the no load e.m.f. e_G is proportional to the speed v, as shown by (7.5). On the other hand, a high mechanical resonant frequency means having a high value of the spring constant and then a large spring that, inevitably, increase the size and the costs of the system. Furthermore, increasing the working fluid speed, it has not been able to achieve the temperature of the heater and cooler (no isothermal transformations). The real cycle of the Stirling engine deviates significantly from the ideal one, and thus results in an efficiency decreasing.

Figure 7.13 reports the simulated (real) Stirling cycle for different mechanical resonant frequency.

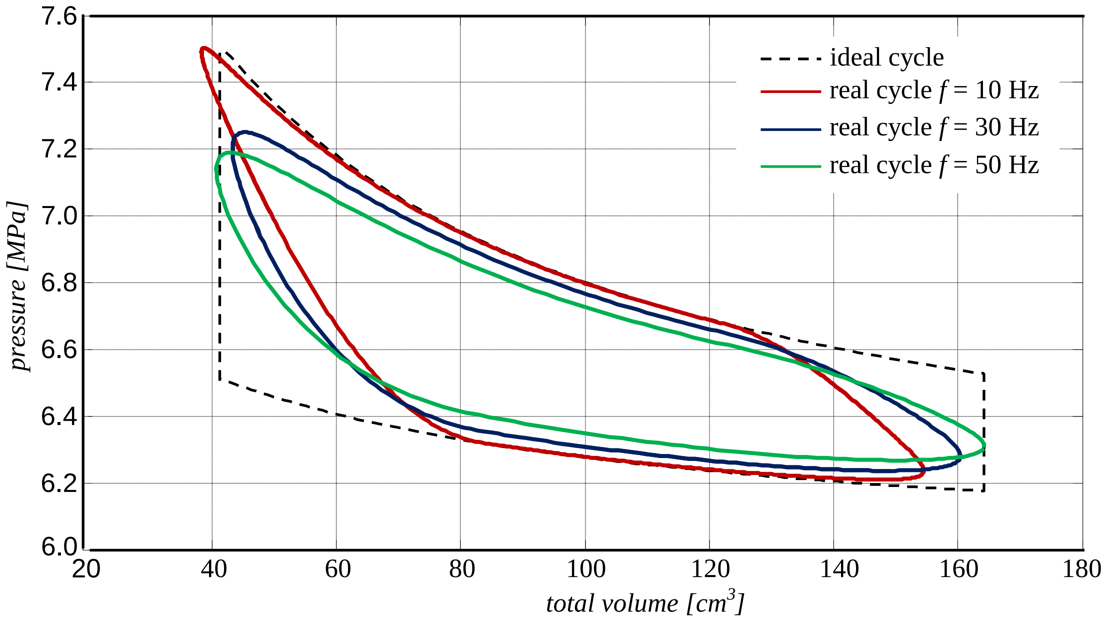

Figure 7.13. *Comparison of simulated (real) Stirling cycles for different mechanical resonant frequency.*

Therefore, the speed of the system can be regulated by changing the constant value of the spring. It is possible only by an adjustable gas spring, for example by means of pressure regulation. It is clear that such kind of technique cannot be employed as control strategy, since it would require a compressor that would involve an increasing of losses, costs and dimensions. In any case, it has not been able to fulfil the dynamic requirements of the system, such as the constraint regarding the maximum stroke of the mover, as it is not fast enough.

The other parameter that affects the dynamic system is the friction due to the viscosity of the working fluid. It is represented by the frictional coefficient b and it is proportional to the speed. The friction can be characterised as an electrical load and particularly it behaves as a resistor. It is worth to point out that increasing the speed of the system the friction losses increase as well.

Another important issue to investigate is the heater and cooler temperature. From equation (7.12), it can be noted that the mean temperature affects the main value of the thrust force, whereas amplitude of the force is proportional to the temperature rise between the heat exchanger (heater and cooler). It is therefore convenient to have a temperature rise the largest possible.

The temperature of the heater depends on heater behaviour. When the heat is provided by fuel (it can be green fuel such as biomass or biogas or even traditional fossil fuel), the temperature depends on the amount of injected fuel. In the cogeneration system it depends on the thermal consumption as well. If the heat is provided by a thermodynamic solar panel, the temperature is linked with solar radiation. Whereas, the cooler temperature depends on the temperature of the exchanger fluid, generally water.

Of course such approach cannot be adopted to prompt speed regulations because the large time constants characterizing the thermal phenomena.

As previously mentioned, the linear generator model is based on two lookup tables, $F_{lg}(i,x)$ and $\varphi(i,x)$, obtained by suitable FEAs where the experimental values of the magnetic material characteristics are used.

The thrust force F_{lg} and the flux linkage φ were evaluated for current i and for position x (Table 7.2), resulting in 1681 different conditions and as many simulations. The current and position limits were chosen in order to take into account any working condition. Particularly, the maximum current value is about 3 times the rated value. This allows, for brief periods, to supply the load with higher current values with respect to the nominal one, in order to improve the dynamic performances of the system.

Table 7.2. *Initial, final and step values of the current and the position utilized to build the lookup tables.*

Quantity	Initial value	Final value	Step value
Current [A]	$-\sqrt{2}\,4$	$\sqrt{2}\,4$	$\sqrt{2}\,0.2$
Position [mm]	-20	20	1

The thrust force and flux linkage profiles, utilised in the lookup tables, evaluated for different position and output current values are reported in Figure 7.14.

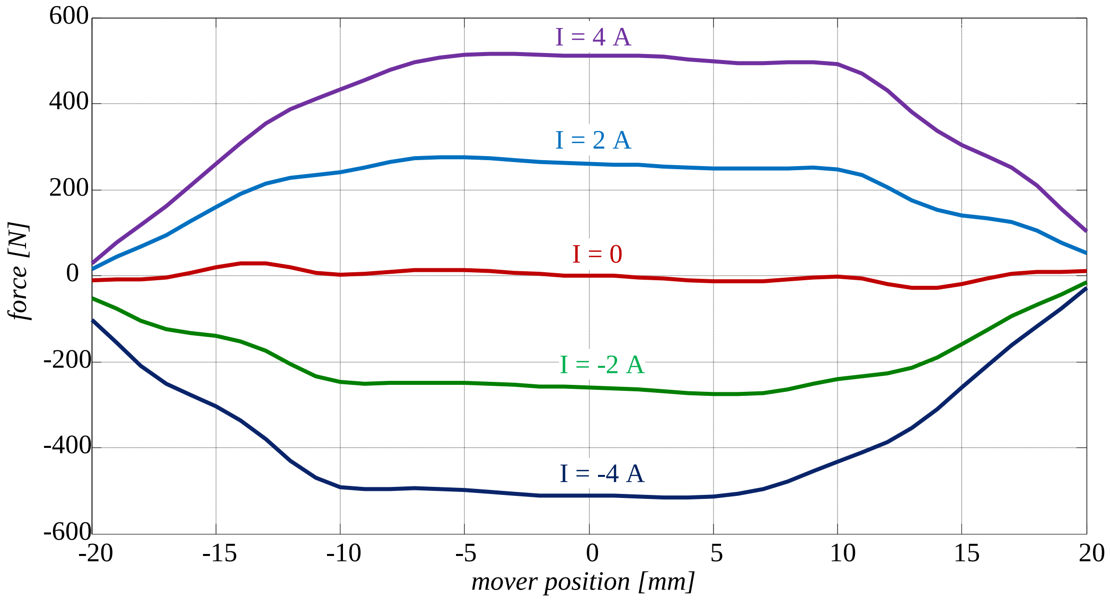

(a)

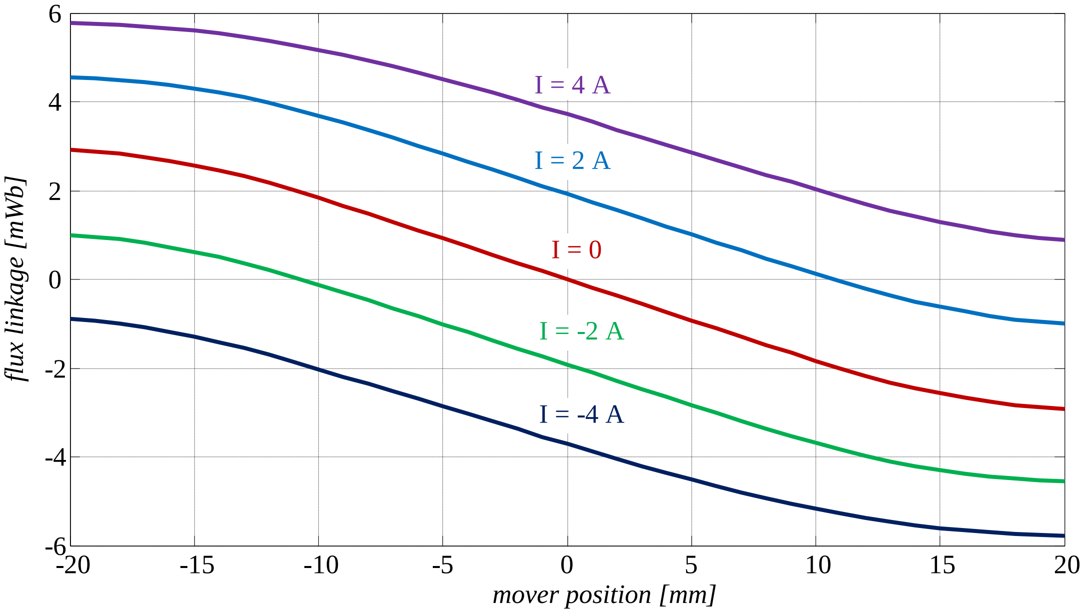

(b)

Figure 7.14. *Interpolated FEAs of the force* (a) *and the flux linkage* (b) *as function of current supply and mover position values*.

From Figure 7.14*a* it can be noted that the cogging force can be neglected with respect to the load force. From Figure 7.14*b* can be noted the ferromagnetic cores results rather saturated when the current supply achieve the maximum value, the saturation effect involves a reduction of the flux linkage of ≅ 25.2%. It worth pointing out that the effect due to current supply is more pronounced than the effect due to PMs, involving a demagnetizing effect.

Another important issue that should be investigated is the control strategy of the cogeneration system. Particularly, the aim of the control system is firstly to regulate the speed of the co-generator in order to maximize the converted power, and then to constrain the mover position within the mechanical limits.

Rearranging the equation (7.7) results:

$$v = \frac{\int F_r \, dt}{m} = \frac{\int \left(F_{St} - F_{lg} - F_s - F_f \right) dt}{m} \tag{7.25}$$

whereby, the unique quantities that can be varied in order to control the speed of the system are:

- the Stirling engine force F_{St}: it proportional to the heater and cooler temperatures gap ΔT_g;
- the linear generator force F_{lg} : it is proportional to the output current i;
- the spring force F_s: it is proportional to the spring constant k, that affects the mechanical resonant frequency ω_m as well.

Some numerical analyses were carried out in order to check the effectiveness of the control system. To such purpose an instantaneous variation of the heater temperature was considered. The thermal dynamics was neglected in order to focus the attention only on the mechanical and electrical systems that have a faster dynamic than thermal system. To the purpose, it is assumed the application of two step variations to the heater temperature. In particular, after 5 and 10 seconds two steps of $\Delta T_h = \pm 200$ °C with respect to the steady state temperature $\bar{T}_h = 600$ °C, then after 15 seconds the temperature is reset to the initial value $\bar{T}_h = 600$; such condition can, for example, refers to a sudden variation of the solar irradiation in the case of solar thermal panel. The reference value of the maximum stroke was chosen in order to take into account any overshooting due to PI controller. Thus, a safety coefficient was considered in order to prevent that the mover position exceeds the limit due to mechanical constraint, thus s_{ref} =34.8 mm.

The instantaneous values of the heater temperature T_h, the equivalent load resistance R_{eq}, the maximum output current i and the mover position x are reported in Figure 7.15.

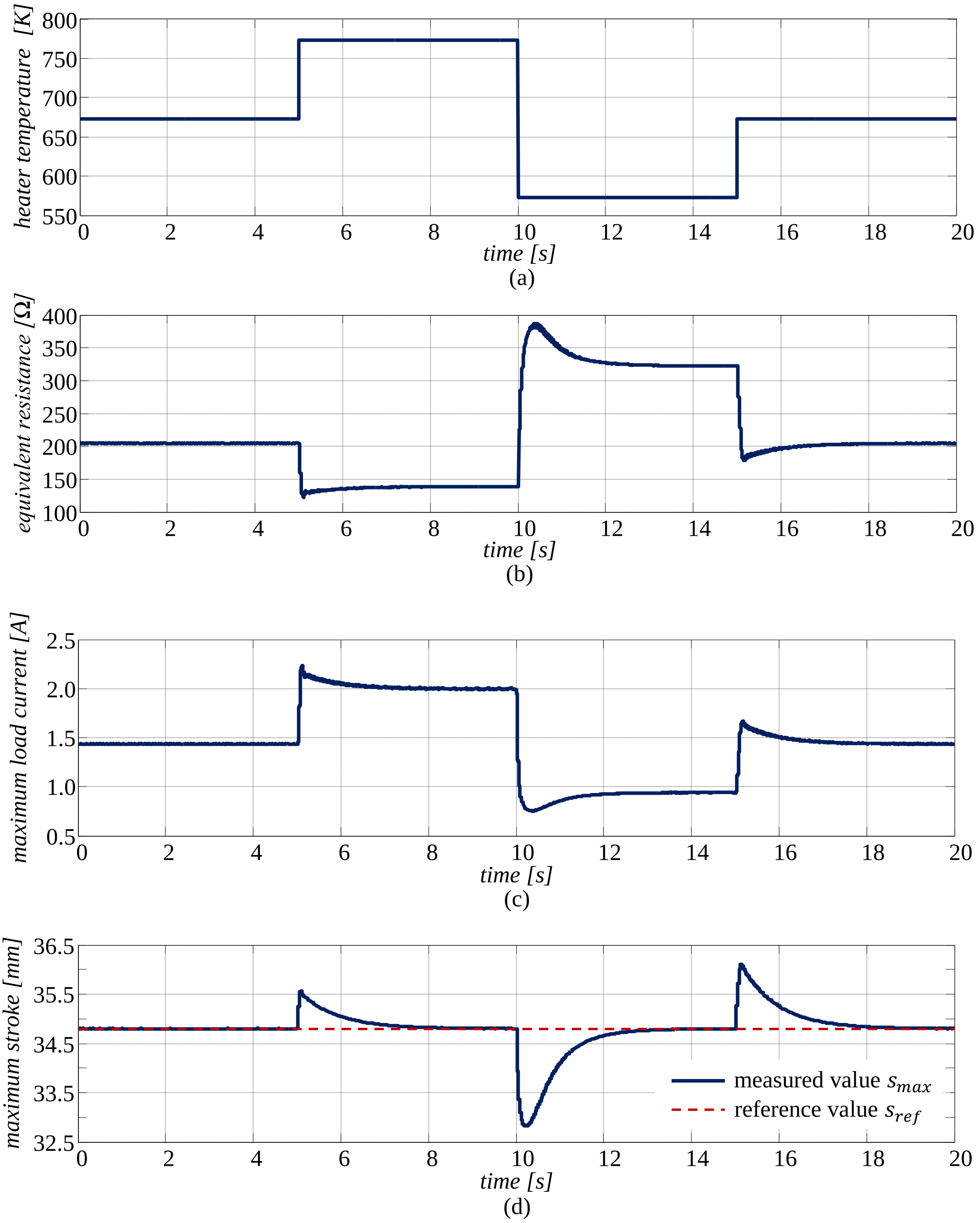

Figure 7.15. *Instantaneous values of the heater temperature* T_h (a), *equivalent load resistance* R_{eq} (b), *maximum value of the output current* i (c) *and maximum mover position* x (d).

As can be noted from the Figure 7.15, the control compensates satisfactorily the variations of maximum mover stroke. The maximum stroke value remains always within the mechanical constraints.

From Figure 7.15 is also possible note that an increasing of the heater temperature involves an increasing of the Stirling engine force that in turn tends to increase the speed and maximum mover stroke. This involves an increasing of the position error e_s, so the PI controller decrease the compensation resistance ($\Delta R < 0$), thus the current and consequently the linear generator reaction force increase. As results, the linear generator force increases the speed and consequently the maximum stroke value decrease. In the case the heater temperature decreases, the process is the same but with the signs reversed.

The instantaneous values of load current and the speed are reported in Figure 7.16.

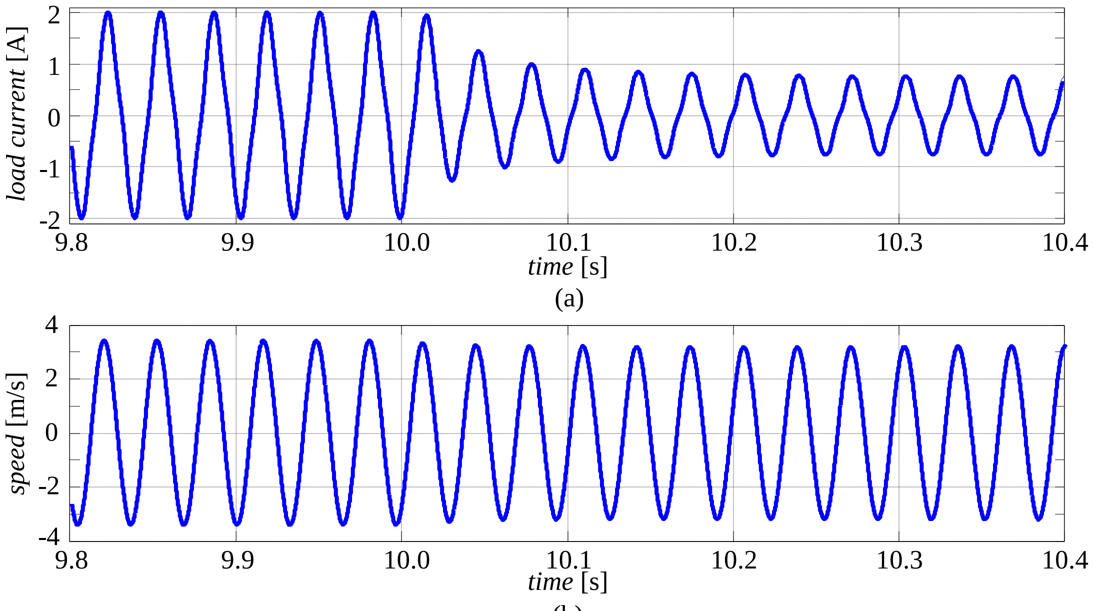

(a)

(b)

Figure 7.16. *Instantaneous values of the load current* (a) *and the speed* (b).

7.8 Conclusion

In this chapter the dynamic model of a free-piston cogeneration system was developed. The dynamic model allows analysing and tuning the parameters of the cogeneration system. Since in the FPEC the alternating motion is obtained through the interaction between the piston force and a spring reaction, it is important to tune the system operation at the mechanical resonance frequency. In this condition, the best performance can be obtained in terms of output power and efficiency.

The dynamic operation is studied by the development of a numerical code in Matlab/Simulink environment, integrating the Stirling engine, the linear generator and the electronic power converter. The analytical model of the Stirling engine was firstly developed assuming ideal gas and ideal Stirling cycle and then elaborated to introduce the non-ideality due to non-conservative phenomena. The model parameters are chosen with reference to an existent Stirling engine, the RE-1000, developed by NASA in

1986. The output quantities calculated by means of analytical model are in agreement with the quantities provided by the datasheet of RE-1000.

The linear generator model is based on two lookup tables obtained by means a sequence of FEAs, using the magnetic parameters derived from the measurement elaborations on a scale prototype.

The electronic converter model is developed by simulating an equivalent load connected to the LG terminals. Such approach is adopted mainly to set up a convenient control strategy to be applied for the speed regulation. In particular, the control system is based on the load current adjustment in order to vary the linear generator reaction force. The control is also necessary to keep the mover position within the limit due to mechanical constraints for any working condition.

The results show a good dynamic response and accuracy, even in the presence of a rapid variation of the heater temperature. This situation, used especially to test the model, may be linked to variations in the quantity of fuel or solar radiation which can occur in typical applications of free-piston Stirling engine.

Chapter 8

Conclusions and future work

In this thesis a micro-cogeneration system, consisting of a free-piston Stirling engine (FPSE) and a tubular permanent magnet linear generator (TPMLG), was investigated. Particularly, the following issues have been addressed:

- development of a semi-analytical model (HFEA), based on simplified FEA, that allows to analyse and optimize the TPMLG in terms of magnetization profile and supply current strategy;
- development of a technique to estimate the electromagnetic parameters of the TPMLG by the elaboration of suitable experimental tests, in order to predict the actual performance of the machine;
- development of a dynamic model of the whole cogeneration system, in order to study and to predict the output performance with different thermal, mechanical and electrical conditions.

Firstly, a brief description with the state-of-the-art, the history, the applications, the configurations and the working principle of Stirling engines were illustrated. As regards the linear generators, their different typologies as well as their possible structures and the working principle were presented.

Different hard ferromagnetic materials utilised as permanent magnets, such as NdFeB, SmCo, Alnico and ceramic were compared, highlighting strengths and weaknesses. The soft magnetic composites (SMC) materials, utilised in the ferromagnetic stator and mover cores, were described.

From the preliminary literature review, it was found that a single-phase, tubular, permanent magnet linear generator (TPMLG) represents the best choice from the technical-economic point of view.

Particularly, the tubular configuration allows achieving a higher power density and the axial component of the force is eliminated. As regards the magnetization profile, the Halbach magnetization results in the more appropriate for such kind of applications.

The most important advantages of Halbach magnetization are the reduction of the harmonic content in the emf and the reduction of the mover saturation. This feature allows reducing the mover thickness, involving a mover mass reduction and thus a greater performance from the dynamic point of view.

The SMC materials utilized to build the stator core allow achieving complicated geometry profile and a core losses reduction, thanks to their lower eddy current loss with respect to the traditional laminated machines.

An innovative calculation procedure, called HFEA, based on simplified FEAs was described and developed. An iterative procedure to define suitable current sheets on the mover surface was developed in order to take into account the mover yoke saturation, generally not negligible in such kinds of applications. From such analysis the flux density and the flux linkage can be reconstructed by superposing the effects of the different magnetization harmonic order, the effect of the coil current and the effect of the mover sheet current. By means of such quantities the force, the *emf*, the core losses and thus the machine efficiency were estimated.

After the preliminary elaborations, any magnetization pattern can be analysed and therefore HFEA can be effectively adopted for parametric analyses and design optimization.

The HFEA procedure enables a considerable time saving with respect to direct FEAs, since it operates on fixed geometric configurations with predefined sinusoidal magnetization patterns. It is particularly convenient to improve the TPMLG performance by comparing different magnetization schemes and supply strategies and can apply to parametric variations and optimization analyses as well. Its effectiveness is confirmed by the good agreement with the corresponding direct FEA results even with heavy mover saturation.

The example of application shows that, assuming a simple harmonic motion, the best performances as for output power and efficiency are obtained by Halbach-type magnetization and non-sinusoidal current-controlled supply. The procedure enabled also to investigate on the convenience of adoption of high permeable SMC material for the cores.

An analytical technique to estimate the electromagnetic parameters of a TPMLG by suitable experimental tests was developed. Measurements with variable supply voltage frequency and amplitude are elaborated to define the SMC stator core magnetic properties, resulting in a remarkable mismatch with respect to the datasheets, likely due to the heavy impact of the manufacturing processes and stray air-gaps between the modules. The procedure effectiveness is nevertheless confirmed by the agreement of FEA results with measurements. The actual PM magnetization pattern is identified by measurement as well, enabling to analyse the TPMLG main performances with the updated material characteristics: an output power decrease is appreciated, anyway not invalidating the initial design as to the application effectiveness.

A dynamic model of the cogeneration system was developed. Such a model allows analysing the whole cogeneration system, including the Stirling engine, the TPMLG and the electronic converter. The model of the Stirling engine reproduces the effect on the Stirling cycle of the spatial profile of the heater and cooler temperatures. The model of the linear generator is obtained from lookup tables provided from suitable FEAs, representing dependence of both the flux linkage and the thrust on the mover position and on the coil current.

Due to the low-pass-filter effect of the mechanical mass-spring-damper subsystem, the piston velocity and the displacement of the compressor vary essentially sinusoidally with time, and higher order harmonics can be neglected.

As regards the further works, a simplified dynamic model, which considers only the fundamental component of the forces provided by Stirling and linear generator, should be developed. This kind of model allows to study the system with lower time consumption and to optimize the system in order to achieve the highest power conversion. Furthermore, a dynamic experimental setup should be arranged in order to check the effectiveness of the dynamic model.

References

[1] DG for Energy and Transport (2009). "EU energy and transport in figures" - Luxembourg: Office for the Official Publications of the European communities.

[2] REMODECE Project Members (2008). "Report with the results of the surveys based on questionnaires for all countries in REMODECE - Residential Monitoring to Decrease Energy Use and Carbon Emissions in Europe (IEEA Program Funded Project)".

[3] European Environmental Agency (2001). Chapter "Households" in "Indicator Fact Sheet Signals 2001" - European Environmental Agency.

[4] Almeida, A. and Fonseca, P. "Residential monitoring to Decrease Energy use and Carbon Emissions in Europe" in European Council for an Energy Efficient Economy, ECEEE Conference 2007 Summer Study. 2007. Côte d´Azur, France.

[5] "Presidency Conclusions - Council of the European Union 8/9 March 2007" - European Parliament and European Council - Doc No. 7224/1/07 REV 1.

[6] The World Bank (2010). "Part II-7Accelerating innovation and technology diffusion" in "World Development Report 2010" - The International Bank for Reconstruction and Development / The World Bank. Washington, USA.

[7] "Directive 2009/28/EC of the European Parliament and of the Council of 23 April 2009 on the promotion of the use of energy from renewable sources" - European Parliament and European Council.

[8] Macchi, E., Campanari, S. and Silva, P. La Microcogenerazione a gas naturale, ed. Polipress. Vol. Scienza e tecnologia per l'energetica. 2005, Milano: Polipress.

[9] Josephson, M. "*Edison; a biography"*. 1959, New York, USA: McGraw-Hill.

[10] Eurostat. "Eurostat Web Portal". Main Database - Environment and Energy.

[11] Lai, S.M. and Hui, C.W. "Feasibility and flexibility for a trigeneration system" Energy, 2009. 34: pgs. 1693-1704.

[12] Carvalho, M., Serra, L.M. and Lozano, M.A. "Geographic evaluation of trigeneration systems in the tertiary sector. Effect of climatic and electricity supply conditions" Energy, 2010. 36(4): pgs. 1931-1939.

[13] Borg, S. P. "Micro-trigeneration for energy-efficient residential buildings in southern Europe" Ph.D. Thesis, University of Strathclyde, Department of Mechanical & Aerospace Engineering, 2012.

[14] Wu, D.W. and Wang, R.Z. "Combined cooling, heating and power: A review" Progress in Energy and Combustion Science 2006. 32: pgs. 459-495.

[15] W. Beale, "Power Piston Actuated Displacer Piston Driving Means for Free-Piston Stirling Cycle Type Engine", U.S. Patent No. 3,937,018, February 10, 1976.

[16] Neill W. Lane, "Commercialization Status of Free-piston Stirling Machines", 12th International Stirling Engine Conference, Durham (UK), September 2005

[17] W. Beale, G. Chen, "Small Stirling Free-Piston Engines for Cogeneratio", Sunpower Inc., Athens (Ohio), June 1992.

[18] S. A. Zulkifli, M. N. Karsiti and A. R. A. Aziz, "Starting of a Free-Piston Linear Engine-Generator by Mechanical Resonance and Rectangular Current Commutation", IEEE Vehicle Power and Propulsion Conference (VPPC), September 3-5, 2008, Harbin, China.

[19] J. Wang, D. Howe, "A linear permanent magnet generator for a free-piston energy converter", Conference on Electric Machines and Drives, 2005 IEEE International, 15-15 May 2005, San Antonio, TX.

[20] Key World Energy Statistics

[21] International Energy Statistics, www.eia.gov.

[22] A. D. Minassians, "Stirling Engines for Low-Temperature Solar-Thermal-Electric Power Generation", Pd.D. Thesis, Electrical Engineering and Computer Sciences, University of California at Berkeley, 2007.

[23] Parabolic Dish Stirling Module Development and Test Results.

[24] Introduction to Dish Stirling Technology – ennex developments, Solar South Africa, 21 June 2011, http://www.ennex.co.za/downloads/Dish Stirling Solar South Africa Conference 21 June 2011.pdf

[25] W. T. Welford, Roland Winston, "High Collection Nonimaging Optics", ACADEMIC PRESS, INC.

[26] M. Gräf, P. Treffinger, S. Pohl, F. Rinderknecht: "Investigation of a high efficient Free-piston Linear Generator with variable Stroke and variable Compression Ratio", 2007, WEVA Journal Volume l.

[27] F. Rinderknecht, "A Highly Efficient Energy Converter for a Hybrid Vehicle Concept – Focused on the Linear Generator of the Next Generation", 2013 Eighth International Conference and Exhibition on Ecological Vehicles and Renewable Energies (EVER), 2013.

[28] Thorpe, T.W., "An Overview of Wave Energy Technologies" Report AEAT-3615, Office of Science and Technology, AEA Technology, 1999.

[29] "2004 Survey of Energy", World Energy Council, London (UK), 2004.

[30] EV ANS, D.V.: "A theory for Wave-Power absorption by oscillating bodies", Journal of Fluid Mechanics, 77, 1976, ppl-23

[31] Mueller, MA, et al., "Low Speed Linear Electric Generators for Renewable Energy Applications", Proceeding of the Conference on Linear Drives in Industrial Apllications (LDIA 2003), Birmingan (UK), pp. 121- 124, 2003.

[32] L. Szabo, C. Oprea, J. Viorel, K. A. Biro "Novel Permanent Magnet Tubular Linear Generator for Wave Energy Converters", Electric Machines & Drives Conference, 2007. IEMDC '07. IEEE International (Volume:2), 3-5 May 2007, Antalya.

[33] Yokobori, K., "Survey of Energy Resources," 19th edition, World Energy Council, Tokyo (Japan), 2002.

[34] Danielsson, O., Thorburn, K., Eriksson, and M., Leijon, M., "Permanent magnet fixation concepts for linear generator," Proceedings of the 5th European Wave Energy Conference, Cork (Ireland), pp. 117-124, 2003.

[35] Mueller, M.A. et al., "Dynamic Modelling of a Linear Vernier Hybrid Permanent Magnet Machine Coupled to a Wave Energy Emulator Test Rig," Conference Record of the International Conference on Electrical Machines (ICEM '2004), Cracow (Poland), on CD: 495.pdf, 2004.

[36] Brooking, P.R.M., "Power conversion in a low speed reciprocating electrical generator," Conference Record of the International Conference on Electrical Machines (ICEMA'2002), Brugge (Belgium), on CD: 452.pdf, 2002.

[37] Baker, N.J., "Linear Generators for Direct Drive Marine Renewable Energy Converters," Ph.D. Thesis, School of Engineering, University of Durham (UK), 2003.

[38] C. A. Oprea, C. S. Martis, F. N. Jurca, D. Fodorean, L. Szabó, "Permanent Magnet Linear Generator for Renewable Energy Applications: Tubular vs. Four-Sided Structures", International Conference on Clean Electrical Power (ICCEP) 2011, 14-16 June 2011, Ischia (Italy).

[39] P. Frangois, I. Garcia Burrel, H. Ben Ahmed, L. Prevond, B. Multon, "3D Analytical Model for a Tubular Linear Induction Generator in a Stirling cogeneration system", Electric Machines & Drives Conference, IEMDC '07, IEEE International, 2007.

[40] S. Hor, A. Tabesh, A. Zamani, "Analytical Model of an Improved Linear Generator for Seawave Energy Harvesting", Conference on Renewable Power Generation (RPG 2011), IET, 6-8 Sept. 2011, Edinburgh (Scotland).

[41] T. T. Dang, P. François, L. Prévond, H. B. Ahmed, "Theoretical and experimental results of Tubular Linear Induction Generator for Stirling Cogenerator System", Conference on Electrical Machines (ICEM), 2010 XIX International, 6-8 Sept. 2010, Rome (Italy).

[42] Van Arsdell BH. Stirling engines. In: Zumerchik J, editor. Macmillan encyclopedia of energy, vol. 3. Macmillan Reference USA; 2001. p. 1090–95.

[43] Senft JR. Ringbom Stirling engines. New York: Oxford University Press, 1993.

[44] Walker G. Stirling engines. Oxford: Clarendon Press, 1980.

[45] Walpita SH. Development of the solar receiver for a small Stirling engine. In: Special study project report no. ET-83-1. Bangkok: Asian Institute of Technology; 1983.

[46] West CD. A historical perspective on Stirling engine performance. In: Proceedings of the 23rd Intersociety Energy Conversion Engineering Conference, Paper 889004. Denver: American Society of Mechanical Engineers; 1988.

[47] Trayser DA, Eibling JA. A 50-Watts portable generator employing a solar-powered Stirling engine. Sol Energy 1967;11:153–9.

[48] Gupta RK, Deshpande AM, Brave KM. Development of 1 kW solar powered reciprocating engine for rural applications. In: International Solar Energy Congress, New Delhi. 1978. p. 2016–20.

[49] Spencer LC. A comprehensive review of small solar-powered heat engines: Part I.I. Research since 1950—“Conventional” engines up to 100 kW. Sol Energy 1989;43:197–210.

[50] Pearce JM, Al Zahawi BA, Auckland DW, Starr F. Electricity generation in the home: evaluation of single-house domestic combined heat and power. IEE Proc-A 1996;143:345–50.

[51] Prodesser E. Electricity production in rural villages with biomass Stirling engine. Renew Energy 1999;16:1049–52.

[52] Dixit DK, Ghodke SV. Renewable energy powered Stirling engines—a viable energy alternative. In: Sayigh AAM, editor. Renewable energy technology and the environment. Proceedings of the Second World Renewable Energy Congress, vol. 2. 1992. p. 934–8.

[53] Markman MA, Shmatok YI, Krasovkii VG. Experimental investigation of a low-power Stirling engine. Geliotekhnika 1983;19:19–24.

[54] Orunov B, Trukhov VS, Tursunbaev IA. Calculation of the parameters of a symmetrical rhombic drive for a single-cylinder Stirling engine. Geliotekhnika 1983;19:29–33. 152 B. Kongtragool, S. Wongwises / Renewable and Sustainable Energy Reviews 7 (2003) 131–154

[55] Abdalla S, Yacoub SH. Feasibility prediction of potable water production using waste heat from refuse incinerator hooked up at Stirling cycling machine. Desalination 1987;64:491–500.

[56] Nakajima N, Ogawa K, Fujimasa I. Study on micro-engines: miniaturizing Stirling engines for actuators. Sensor Actuator 1989;20:75–82.

[57] Aramtummaphon D. A study of the feasibility of using heat energy from producer gas for running Stirling engine by steam as working Fluid. Master thesis, King Mongkut’s University of technology Thonburi; 1996.

[58] Hirata K, Iwamoto S, Toda F, Hamaguchi K. Performance evaluation for a 100 W Stirling engine. In: Proceedings of Eighth International Stirling Engine Conference. 1997. p. 19–28.

[59] Costea M, Feidt M. The effect of the overall heat transfer coefficient variation on the optimal distribution of the heat transfer surface conductance or area in a Stirling engine. Energy Convers Manage 1998;39:1753–63.

[60] Wu F, Chen L, Wu C, Sun F. Optimum performance of irreversible Stirling engine with imperfect regeneration. Energ Convers Manage 1998;39:727–32.

[61] Wu F, Chen L, Sun F, Wu C, Zhu Y. Performance and optimization criteria for forward and reverse quantum Stirling cycles. Energ Convers Manage 1998;39:733–9.

[62] Wu F, Chen L, Sun F, Wu C. Finite-time exergoeconomic performance bound for a quantum Stirling engine. Int J Eng Sci 2000;38:239–47.

[63] Gu Z, Sato H, Feng X. Using supercritical heat recovery process in Stirling engines for high thermal efficiency. Appl Therm Eng 2001;21:1621–30.

[64] Winkler W, Lorenz H. Design studies of mobile applications with SOFC-heat engine modules. J Power Sources 2002;106:338–43.

[65] Hsu ST, Lin FY, Chiou JS. Heat-transfer aspects of Stirling power generation using incinerator waste energy. Renew Energ 2003;28:59–69.

[66] Ptrescu S, Costea M, Harman C, Florea T. Application of the direct method to irreversible Stirling cycles with finite speed. Int J Energ Res 2002;26:589–609.

[67] Rizzo JG. The Stirling engine manual. Somerset: Camden miniature steam services, 1997.

[68] Jordan RC, Ibele WE. Mechanical energy from solar energy. In: Proceedings of the World Symposium on Applied Solar Energy, Phoenix. 1955. p. 81–101.

[69] Spencer LC. A comprehensive review of small solar-powered heat engines: Part I. A history of solar-powered devices up to 1950. Sol Energy 1989;43:191–6.

[70] Ericsson J. Sun power; the solar engine. Contributions to the Centennial Exhibition, Philadelphia: John Ericsson, 1870. p. 571–77.

[71] Daniels F. Direct use of the sun’s energy. New Haven: Yale University Press, 1964.

[72] Meinel AB, Meinel MP. Applied solar energy: an introduction. Reading, MA: Addison-Wesley, 1976.

[73] Reader GT, Hooper C. Stirling engines. London: Cambridge University Press, 1983.

[74] Ghai ML. Small solar power plants. In: Daneils F, Duffie JA, editors. Solar energy research. London: Thames and Hudson; 1955. p. 81–4 [Section 4].

[75] Dunn PD. Solar powered pumps. Joint Conference: University of Reading and U. K. I.S.E.S.: Solar Energy in Agriculture; 1976. p. 55–7.

[76] Meijer RJ. STM4-120 Stirling engine for solar application. Abs. I.S.E.S, Solar World Congress, Hamburg; 1987. p. 2, 13, 16.

[77] Jordan RC. Conversion of solar to mechanical energy. In: Zarem AM, Erway DD, editors. Introduction to the utilization of solar energy. New York: McGraw-Hill; 1963. p. 125–52.

[78] Utz JA, Braun RA. Design and initial tests of a Stirling engine for solar energy applications. MS thesis, Mechanical Engineering Department, University of Wisconsin; 1960.

[79] Finkelstein T. Internally focussing solar power systems. American Society of Mechanical Engineers, Paper 61-WA-297. Annual Meeting; 1961.

[80] Gurtler RW. Optically driven solar engine. U.S. Patent; 1979. p. 4, 173, 123.

[81] Walker G, Kentfield J, Johnson E, Fauvel R, Srinivasen V. Coal-fired Stirling engines for railway locomotive and stationary applications. Proc Inst Mech Eng 1983;197:46.

[82] Hull PG, Hunt AJ. A reciprocating solar-heated engine utilizing direct absorption by small particles. J Sol Eng Trans ASME 1984;106:29–34.

[83] Holland MB. The Stirling engine—power plant of the future? Charter Mech Eng 1979;April:60–3.

[84] Pons RL, Fox RJ. A solar/Stirling total energy system. In: Sharing the Sun, Solar Technology in the 1970s Conference, Winnipeg. 1976. p. 77–91.

[85] Brown CT, Mackie PE, Neale DH. Advanced component research in the solar thermal program. In: Proceedings of the Solar World Congress, Perth. 1983. p. 1421–5.

[86] Marriott AT. Solar electric power from parabolic dishes. In: Proceedings of the Solar World Congress, Perth. 1983. p. 1438–43.

[87] Selcuk MK, Bowyer JM. Dish Stirling module performance analysis as evaluated from tests ofvarious TBC concentrator/USAB engine configurations as the parabolic dish test site. Ext. Abst. Intersol ’85, Montreal; 1985. p. 313.

[88] McGlaun MA. The LaJet energy large scale innovative solar concentrator study of wind loading effects. Abs., I.S.E.S. Solar World Congress, Hamburg; 1987. p. 2, 18, 15.

[89] Schlaich J. Solar power plants with a membrane concave mirror-50 kW. Abs., I.S.E.S. Solar World Congress, Hamburg; 1987. p. 2, 18, 16.

[90] Al-Rebaian A, Hansen J. 50 kW Solar concentrators with stirling generators—results of the first six mounts of operation in Saudi Arabia. Abs., I.S.E.S. Solar World Congress, Hamburg; 1987. p. 2, 13, 15.

[91] Leibowitz L, Hanseth E. Solar thermal technology-outlook the 80’s. Mech Eng 1982;104:30–5.

[92] Ahmed A, Al-Agami M, Al-Garni M. Solar powered Stirling engine with a single membrane dish concentrator. In: Proceedings of the First World Renewable Energy Congress, Energy and the Environment, Reading, UK, September 23–28, vol. 2. 1990. p. 1202–7.

[93] Childs WD, Dabiri AE, Al-Hinai HA, Abdullah HA. VARI-RO solar-powered desalting technology. Desalination 1999;125:155–66.

[94] Audy Ch, Fischer M, Messerschmid EW. Nonsteady behaviour of solar dynamic power systems with Stirling cycle for space stations. Aerosp Sci Technol 1999;1:49–58.

[95] Washom B. Parabolic dish Stirling module development and test results. In: Proceedings of the IECEC, Paper No. 849516, San Francisco. 1984.

[96] Stine WB, Diver RP. A compendium of solar dish/Stirling technology. Sandia National Laboratories, Albuquerque, Report SAND93-7026 UC-236; 1994.

[97] West CD. Principles and applications of Stirling engines. New York: Van Nostrand Reinhold, 1986.

[98] Droher J, Squier S. Performance of the Vanguard solar dish-Stirling module. Electric Power Research Institute, Palo Alto, Report AP-4608; 1986.

[99] Lopez CW, Stone KW. Design and performance of the Southern California Edison Stirling dish. In: Proceedings of the 1992 ASME-JSES-KSES International Solar Energy Conference, Maui. 1992.

[100] Lopez CW, Stone KW. Design and performance of the Southern California Edison Stirling dish. Sandia National Laboratories, Albuquerque, Report SAND93-7098; 1993.

[101] Stone KW, Drubka RE. Impact of Stirling engine operational requirements on dish-Stirling system life cycle costs. In: Proceedings of the 1994 ASME Solar Energy Conference, San Francisco. 1994.

[102] Stone KW, Lopez CW, McAlister R. Economic performance of the SCE Stirling dish. In: Proceedings of the IECEC, Atlanta. 1993.

[103] Bean JR, Diver RB. The CPG 5-kWe dish/Stirling development program. In: Proceedings of the IECEC, San Diego, Paper No. 929181. 1992. 154 B. Kongtragool, S. Wongwises / Renewable and Sustainable Energy Reviews 7 (2003) 131–154

[104] Gallup DR, Mancini TR, Christensen J, Beninga K. The utility scale joint-venture program. In: Proceedings of the IECEC, Monterey, AIAA-94-3945-CP. 1994.

[105] Beninga K, Davenport R, Sellars J, Smith D, Johansson S. Performance results for the SAIC/STM prototype dish/Stirling systems. In: Proceedings of the 1997 ASME International Solar Energy Conference, Washington. 1997.

[106] Diver R, Andraka CE, Rawlinson KS, Goldberg V, Thomas G. The advanced dish development system project. In: Proceedings of the Solar Forum 2001, Technical paper. 2001.

[107] Davenport R, Mayette J, Forristall RE. The salt river project sundish/Stirling system. In: Proceedings of the ASME Solar Forum 2001, Washington. 2001.

[108] Davenport RL, Butler BL, Taylor R, Forristall R, Johansson S, Ulrich J et al. Operation of second generation dish/Stirling power systems. In: Proceedings of the ASES 2002 Solar Conference, Reno. 2002.

[109] Umarov GY, Orunov BB, Klyuchevskii YE, Tursunbaev IA, Trukhov VS. Thermodynamic analysis and choice of optimal parameters of dynamic converter for solar energy plant. Geliotekhnika 1976;12:31–4.

[110] Umarov GY, Trukhov VS, Tursunbaev IA, Orunov BB. A method for optimizing heat exchangers of a Stirling engine. Geliotekhnika 1976;12(6):18–23.

[111] Howell JR, Bannerot RB. Optimum solar collector operation for maximizing cycle work output. Sol Energy 1977;19:149–53.

[112] Eldighidy SM, Taha IS, Darwish MA. Optimum conditions for maximum solar energy absorbed by flat plate collector augmented by plane reflector. In: Proceedings of the Energy Symposium (ISATED), Montreux, Swiss. 1979. p. 28–32.

[113] Eldighidy SM. Optimum outlet temperature of solar collector for maximum work output for an Otto air-standard cycle with ideal regeneration. Sol Energy 1993;51:175–82.

[114] Gordon JM. On optimized solar-driven heat engines. Sol Energy 1988;40:457–61.

[115] Altfeld K, Leiner W, Feebig M, “Second law optimization of flat-plate air heaters. Part I: the concept of net exergy flow and the modelling of solar air heaters”, Sol Energy 1988;41:127–32.

[116] Altfeld K, Leiner W, Feebig M, “Second law optimization of flat-plate air heaters. Part II: results of optimization and analysis of sensibility to variations of operating conditions”, Sol Energy 1988;41:127–32.

[117] Costea M, Petrescu S, Harman C, “The effect of irreversibilities on solar Stirling engine cycle performance”, Energ Convers Manage 1999;40:1723–31.

[118] Chen YT, Chong KK, Bligh TP, Chen LC, Yunus J, Kannan KS et al, “Non-imaging, focusing heliostat”, Sol Energy 2001;71:155–64.

[119] Haneman D, “Theory and principles of low-temperature hot air engines fuelled by solar energy”, Report Prepared for U.S. Atomic Energy Comm. Contract W-7405-Eng-48; 1975.

[120] Spencer LC, “A comprehensive review of small solar-powered heat engines: Part III”, Research since 1950-“unconventional” engines up to 100 kW. Sol Energy 1989;43:211–25.

[121] White EW, “Solar heat engines”, U.S. Patent; 1983. p. 4, 414, 814.

[122] O’Hare R, “Convection powered solar engine”, U.S. Patent; 1984. p. 4, 453, 382.

[123] Senft JR, “An ultra-low temperature differential Stirling engine”, In: Proceedings of the Fifth International Stirling Engine Conference, Paper ISEC 91032, Dubrovnik, May. 1991.

[124] Stine WB. Stirling engines. In: Kreith F, editor. The CRC handbook of mechanical engineers. Boca Raton: CRC Press; 1998. p. 8-7–8-6.

[125] C.D. West, “Principles and applications of Stirling engines”, Van Nostrand Reinhold, 1986.

[126] J.R. Senft, “Ringbom stirling engines”, Oxford University Press, 1993.

[127] B. Kongtragool, S. Wongwises, “Investigation on power output of the gamma-configuration low temperature differential Stirling engines”, Renewable Energy, 30 (2005):465-476.

[128] J.I. Prieto, J. Fano, C. González, M.A. González, R. Diaz, “Preliminary design of the kinematic Stirling engine using dynamic similarity and quasi-static simulation”, Proceedings of the Institution of Mechanical Engineers, Part C: Journal of Mechanical Engineering Science, 211 (1997):229-238.

[129] J.I. Prieto, A.B. Stefanovskiy, “Dimensional analysis of leakage and mechanical power losses of kinematic Stirling engines”, Proceedings of the Institution of Mechanical Engineers, Part C: Journal of Mechanical Engineering Science, 217 (2003):917-934.

[130] J.I. Prieto, M.A. González, C. González, J. Fano, “A new equation representing the performance of kinematic Stirling engines”, Proceedings of the Institution of Mechanical Engineers, Part C: Journal of Mechanical Engineering Science, 214 (2000):449-464.

[131] J. Prieto, D. Garcia, “Comparison between Kolin’s cube law for power and other criteria for preliminary design of kinematic Stirling engines”, Proceeding of 12th international Stirling engine conference, Durham UK, 2005, pp. 389-397.

[132] W.R. Martini, “Stirling Engine Design Manual”, Arch, 1978.

[133] N.C.L. Chen, F.P. Griffin, “A review of Stilring engine mathematical models”, Report No ORNL/CON 135, OAK Ridge National Laboratory, Tennessee, 1983.

[134] K. Mahkamov, “Stirling Engine Based Micro-Energy Systems”, In: R. Beith, I.P. Burdon, M. Knowles (Eds.). Micro-Energy Systems. John Wiley & Sons, 2004, pp. 101-144.

[135] G. Walker, “Stirling engines”, Clarendon Press, 1980.

[136] G. Walker, J.R. Senft, “Free Piston Stirling Engines”, Springer, 1985.

[137] F. Toda, S. Iwamoto, K. Nagajima, “Development of Low-Temperature Difference Stirling engine- Behaviour of the mechanism effectiveness for the performance prediction method”, Proceeding of 13th international Stirling engine conference, Tokyo, 2007, pp. 49-51.

[138] I. Urieli, D.M. Berchowitz, “Stirling cycle engine analysis”, A. Hilger, 1984.

[139] M. Abbas, N. Said, B. Boumeddane, “Thermal analysis of Stirling engine solar driven”, Revue des Energies Renouvelables, 11 (2008):503 - 514.

[140] J.M. Strauss, R.T. Dobson, “Evaluation of a second order simulation for Sterling engine design and optimisation”, Journal of Energy in Southern Africa, 21 (2010):17-29.

[141] I. Urieli, “Stirling cycle machine analysis”, Available at http://www.ent.ohiou.edu/ urieli/stirling/me422.html (accessed on 17 November 2008)

[142] F.J.G. Granados, M.A.S. Perez, V. Ruiz-Hernandez, “Thermal Model of the EuroDish Solar Stirling Engine”, Journal of Solar Energy Engineering, 130 (2008):011014-011018.

[143] F. Nepveu, A. Ferriere, F. Bataille, “Thermal model of a dish/Stirling systems”, Solar Energy, 83 (2009):81-89.

[144] W. Reinalter, S. Ulmer, P. Heller, T. Rauch, J.-M. Gineste, A. Ferriere, F. Nepveu, “Detailed performance analysis of the 10 kW CNRS-PROMES dish/stirling system”, Proceedings of the 13th SolarPACES International Symposium, Seville Spain, 2006.

[145] N. Parlak, A. Wagner, M. Elsner, H.S. Soyhan, “Thermodynamic analysis of a gamma type Stirling engine in non-ideal adiabatic conditions”, Renewable Energy, 34 (2009):266-273.

[146] I. Tlili, Y. Timoumi, S.B. Nasrallah, “Analysis and design consideration of mean temperature differential Stirling engine for solar application”, Renewable Energy, 33 (2008):1911-1921.

[147] Y. Timoumi, I. Tlili, S. Ben Nasrallah, “Design and performance optimization of GPU-3 Stirling engines”, Energy, 33 (2008):1100-1114.

[148] S. Schulz, F. Schwendig, “A General Simulation Model for Stirling Cycles”, Journal of Engineering for Gas Turbines and Power, 118 (1996):1-7.

[149] K.K. Makhkamov, D.B. Ingham, “Analysis of the Working Process and Mechanical Losses in a Stirling Engine for a Solar Power Unit”, Journal of Solar Energy Engineering, 121 (1999):121-127.

[150] Ö. Ercan Ataer, H. Karabulut, “Thermodynamic analysis of the V-type Stirling-cycle refrigerator”, International Journal of Refrigeration, 28 (2005):183-189.

[151] H. Karabulut, H.S. Yücesu, C. Çinar. Nodal, “Analysis of a Stirling engine with concentric piston and displacer”, Renewable Energy, 31 (2006):2188-2197.

[152] S.K. Andersen, H. Carlsen, P.G. Thomsen, “Preliminary results from simulations of temperature oscillations in Stirling engine regenerator matrices” Energy, 31 (2006):1371-1383.

[153] N. Martaj, L. Grosu, P. Rochelle, “Thermodynamic Study of a Low Temperature Difference Stirling Engine at Steady State Operation”, International Journal of Thermodynamics, 10 (2007):165-176.

[154] A. Robson, T. Grassie, J. Kubie, “Modelling of a low-temperature differential Stirling engine”, Proceedings of the Institution of Mechanical Engineers, Part C: Journal of Mechanical Engineering Science, 221 (2007):927-943.

[155] R.W. Dyson, S.D. Wilson, R.C. Tew, “Review of Computational Stirling Analysis Methods”, Proceedings of 2nd International Energy Conversion Engineering Conference, Paper No AIAA20045582, Providence RI, (2004) 1-21.

[156] S.K. Andersen, “Numerical Simulation of Cyclic Thermodynamic Processes”, PhD Thesis (2006). Department of Mechanical Engineering, Technical University of Denmark.

[157] R.C. Tew, R.W. Dyson, S.D. Wilson, R. Demko, “Overview 2004 of NASA-Stirling Convertor CFD Model Development and Regenerator R&D Efforts”, Report No NASA/TM-2004-213404, NASA, 2004.

[158] S.K. Andersen, H. Carlsen, P.G. Thomsen, “Control volume based modelling in one space dimension of oscillating, compressible flow in reciprocating machines”, Simulation Modelling Practice and Theory, 14 (2006):1073-1086.

[159] K. Mahkamov, “An Axisymmetric Computational Fluid Dynamics Approach to the Analysis of the Working Process of a Solar Stirling Engine”, Journal of Solar Energy Engineering, 128 (2006):45-53.

[160] M.B. Ibrahim, R.C. Tew, Z. Zhang, D. Gedeon, T. Simon, “CFD modeling of free-piston Stirling engines”, Report No NASA/TM-2001-211132, NASA, 2001.

[161] K. Mahkamov, D. Djumanov, “Three- Dimensional CFD Modelling of a Stirling Engine”, Proceeding of 11th International Stirling Engine Conference, Rome, Italy, 2003, pp. 96-107.

[162] R. Tan, K. Mahkamov, D. Djumanov, “Experimental and numerical investigations on a small physical Model of a solar Stirling engine”, Proceeding of 12th International Stirling Engine Conference, Durham, UK, 2005, pp. 74-85.

[163] K. Mahkamov, “Design Improvements to a Biomass Stirling Engine Using Mathematical Analysis and 3D CFD Modeling”, Journal of Energy Resources Technology, 128 (2006):203-215.

[164] K. Mahkamov, E. EiD, “Technical feasibility study of a concept of a medium temperature Stirling engine solar power unit”, Proceeding of 14th International Stirling Engine Conference (on CD only), Groningen, The Netherlands, 2009.

[165] R.W. Dyson, S.D. Wilson, R.C. Tew, R. Demko, “Fast whole-engine Stirling analysis”, Report No NASA/TM—2005-213960, NASA, 2005.

[166] D.A. Blank, C. Wu, “Power optimization of an extra-terrestrial, solar-radiant stirling heat engine”, Energy, 20 (1995):523-530.

[167] L.B. Erbay, H. Yavuz, “Analysis of the stirling heat engine at maximum power conditions”, Energy, 22 (1997):645-650.

[168] M. Costea, S. Petrescu, C. Harman, “The effect of irreversibilities on solar Stirling engine cycle performance”, Energy Conversion and Management, 40 (1999):1723-1731.

[169] S.T. Hsu, F.Y. Lin, J.S. Chiou, “Heat-transfer aspects of Stirling power generation using incinerator waste energy”, Renewable Energy, 28 (2003):59-69.

[170] Y.C. Hsieh, T.C. Hsu, J.S. Chiou, “Integration of a free-piston Stirling engine and a moving grate incinerator”, Renewable Energy, 33 (2008):48-54.

[171] N. Martaj, L. Grosu, P. Rochelle, "Exergetical analysis and design optimisation of the Stirling engine", International Journal of Exergy, 3 (2006):45-67.

[172] P.C.T. de Boer, "Optimal regenerator performance in Stirling engines", International Journal of Energy Research, 33 (2009):813-832.

[173] L. Yaqi, H. Yaling, W. Weiwei, "Optimization of solar-powered Stirling heat engine with finite-time thermodynamics", Renewable Energy, 36 (2011):421-427.

[174] J.R. Senft, "Optimum Stirling engine geometry", International Journal of Energy Research, 26 (2002):1087-1101.

[175] B. Cullen, J. McGovern, "Development of a theoretical decoupled Stirling cycle engine", Simulation Modelling Practice and Theory, 19 (2011):1227-1234.

[176] F. Formosa, G. Despesse, "Analytical model for Stirling cycle machine design", Energy Conversion and Management, 51 (2010):1855-1863.

[177] A. Altman. SNAPpro: Stirling numerical analysis program (2004). Available at http://home.comcast.net/snapburner/SNAPpro (accessed on 13 March 2009).

[178] B. Orunov, V.T. Krykov, A.P. Korobkov, K. Mahkamov, D. Djumanov, "The first stage of the development of a small Stirling tri-generation power unit", Proceeding of 12th international Stirling engine conference, Durham, UK, 2005, pp. 416-423.

[179] J. Zarinchang, A. Yarmahmoudi, "Optimization of Thermal Components in a Stirling Engine", WSEA Transactions on Heat and Mass Transfer, 4(2009):1-10.

[180] P. Rochelle., "LTD Stirling engine simulation and optimization using Finite dimension thermodynamics", Proceeding of 12th international Stirling engine conference, Durham, UK, 2005, pp. 358-366.

[181] S. Abdullah, B.F. Yousif, K. Sopian, "Design consideration of low temperature differential double-acting Stirling engine for solar application", Renewable Energy, 30 (2005):1923-1941.

[182] P. C. Sen, "Principles of Electrical Machines and Power Electronics" J Whiley & sons inc. ISBN 0-471-02295-0, p292, 1997.

[183] M. J. Balchin, J. F. Eastham and P. C. Coles, "Effects of pole flux distribution in a homopolar linear synchronous machine", Journal of Applied Physics 75 (10): pp 6987-6989 Part 2B May 1994.

[184] A. Cosic, C. Sadarangani, J. Timmerman, "Design and Manufacturing of a Linear Transverse Flux Permanent Magnet Machines", Industry Applications Society Annual Meeting (IAS 08), Edmonton (Alta), 5-9 Oct. 2008, pp 1-5.

[185] M. Husband, "Developing the transverse flux motor TFM", One day seminar, 'New topologies for electrical machines', UK Magnetics Society, Leicester, September 2002.

[186] E. Spooner and & L. Ha Ydock, “Vernier Hybrid Machines”', to be published, lEE Proceedings Part B, Electric Power Applications.

[187] B. C. Mecrow and A. G. Jack, “'A new high torque density permanent magnet machine configuration”, Proc. of the Int. Elec. Machines Conf., Cambridge Mass. USA, Sept 1990

[188] M. R. Harris and B. C. Mecrow, “Variable Reluctance Permanent.Magnet Motors for High Specific Output”, 'Proc. lEE International Conference ID Electrical Machines and Drives, Oxford, UK, 1993

[189] Iw Abuchi, N, W. A. Ka, T. Kume, T. Kabashima & N. Nagaska, “A novel High-Torque Reluctance Motor with Rare Earth Magnet”, IEEE Trans on Ind. App.,. Vol. 30, No.3, June 1994, pp609-613

[190] M. R. Harris, G. H. Pajooman and S. M. Abu Sharkh, “The problem of power factor in the VRPM Transverse Flux Machines”, Int. Conf. On Electrical Machines and Drives, Cambridge 1997, lEE publication 444, ISBN 0 85296 6962

[191] M.A. Mueller, N.J. Backer, P.R.M. Brooking and J. Xiang, “Low speed linear electrical generators for reversible energy applications”, Record of LDIA-2003, Birmingham, U.K., pp. 29-32.

[192] W. Cawthorne, P. Famouri and N. Clark, “Integrated design of linear alternator/engine system for auxiliary unit”, Record of IEEE-IEMDC, 2001.

[193] Boldea and S. A. Nasar, “Linear electric actuators and generators,” IEEE Trans. Energy Convers., vol. 14, no. 3, pp. 712–717, Sept. 1999.

[194] Yacine Amara, Jiabin Wang and David Howe, “Analytical prediction of eddy current loss in modular tubular permanent-magnet machines,” IEEE Trans. Energy Convers., vol. 20, no. 4, pp. 761–770, Dec. 2005.

[195] Mats Leijon, Hans Bernhoff, Olov Agren, Jan Isberg, Jan Sundberg, Marcus Berg, Karl Erik Karlson and Arne Wolfbrandt, “Multiphysics simulation of wave energy to electric energy conversion by permanent magnet linear generator,” IEEE Trans. Energy Convers., vol. 20, no. 1, pp. 219–224, Mar. 2005.

[196] H. Polinder, M.E.C. Damen and F. Garder, “Linear PM generator for wave energy conversion in the AWS,” IEEE Trans. Energy Convers., vol. 19, no. 3, pp. 583–589, Sept. 2004.

[197] H. Polinder, Barrie C. Mecrow, Alan G. Jack, Phililip G. Dickinson and Markus A. Mueller, “Conventional and TFPM linear generators for direct drive wave energy conversion,” IEEE Trans. Energy Convers., vol. 20, no. 2, pp. 260–267, Jun. 2005.

[198] J. Wang, W. Wang, G.W. Jewell, and D. Dowe, “Design and experimental characterization of a linear reciprocating generator”, Electric Power Applications, IEE Proceedings, Volume: 145, pp. 509 – 518, Nov. 1998.

[199] J. Wang and D. Dowe, “A Linear Permanent Magnet Generator for a Free-Piston Energy Converter”, Conference on Electric Machines and Drives, 2005 IEEE International, pp. 1521 – 1528, 15-15 May 2005.

[200] J. Faiz, M.E. Salari, Gh. Shahgholian, “Reduction of Cogging Force in Linear Permanent-Magnet Generators”, IEEE Transaction on magnetic, vol. 46, No. 1, January 2010.

[201] V. Delli Colli, P. Cancelliere, F. Marignetti, R. Di Stefano, “A Tubular-Generator Drive For Eave Energy Conversion”, IEEE Transactions on Industrial Electronics, pp. 1152 – 1159, June 2006.

[202] M. Trapanese, “Analytical model of an improved linear generator for sea wave energy harvesting”, IEEE Transactions on Magnetics, Dec. 2008.

[203] P. Francois, Ecole Normale Cachan, I.G. Burrel, H. Ben Ahmed, L. Prevond, “3D Analytical Model for a Tubular Linear Induction Generator in a Stirling cogeneration system”, IEEE International Electric Machines & Drives Conference (IEMDC), pp. 392 – 397, 3-5 May 2007.

[204] S.Y. Kim, J. Huth, and J.G. Wood, “Performance Characterization of Sunpower Free-Piston Stirling Engines”, 3rd Int. Energy Conversion Engineering Conf., 15-18 August 2005, San Francisco (USA).

[205] Saiful A. Zulkifli, Mohd N. Karsiti and A. Rashid A. Aziz, “Starting of a Free-Piston Linear Engine-Generator by Mechanical Resonance and Rectangular Current Commutation”, IEEE Vehicle Power and Propulsion Conference (VPPC), September 3-5, 2008, Harbin (China).

[206] J. Wang, M. West, D. Howe, H. Z. De La Parra, “Design and Experimental Verification of a Linear Permanent Magnet Generator for a Free-Piston Energy Converter”, IEEE Transaction on Energy Cconversion, vol. 22, no. 2, June 2007, pp. 299-306.

[207] J. Wang and D. Howe, “Magnetic field distribution of quasi-Halbach magnetized cylinder for tubular permanent magnet machines,” in Proc. 4th Int. Symp. Linear Drives Ind. Appl., Birmingham, U.K., Sep. 8–10, 2003, pp. 481–484.

[208] Y. Amara, J. Wang and D. Howe, “Eddy current loss in tubular modular permanent magnet machines”, Proceedings of International Conference on Electrical Machines (ICEM 2004), Cracow, Poland, Paper ID 193, 2004.

[209] J. Wang, G.W. Jewell, and D. Howe, “A General Framework for the Analysis and Design of Tubular Linear Permanent Magnet Machines”, IEEE Trans. on Magn., vol. 35, no. 3, May 1999, pp.1986-2000.

[210] X. Chen, Z.Q. Zhu, and D. Howe, “Modeling and Analysis of a Tubular Oscillating Permanent-Magnet Actuator”, IEEE Trans. on Industry Appl., vol. 45, no. 6, Nov./Dec. 2009, pp.1961-1970.

[211] N. Bianchi, A. Canova, G. Gruosso, M. Repetto, and F. Tonel, “Analytical and finite element design optimisation of a tubular linear IPM motor”, COMPEL, Vol. 20 ,no. 3, 2001, pp. 777-795.

[212] M. Andriollo, L. Dall’Ora, A. Tortella, “Magnetization space harmonic analysis of TLPMGs allowing for magnetic saturation”, Proceedings of International Symposium on Power Electronics, Electrical Drives, Automation and Motion SPEEDAM 2012 pp. 501-506, ISBN: 9781467313001, Sorrento (Italy), 20-22 June 2012.

[213] D. Lin, P. Zhou, W. N. Fu, Z. Badics, and Z. J. Cendes, “Dynamic Core Loss Model for Soft Ferromagnetic and Power Ferrite Materials in Transient Finite Element Analysis”, IEEE Trans. on Magnetics., vol. 40, no. 2, March 2004, pp.1318-1321.

[214] M. Andriollo, L. Dall'Ora, G. Martinelli, A. Tortella “Performance comparison of saturated tubular linear permanent magnet generators by simplified FEAs”, Proceedings of the International Conference on Renewable Energy Research and Applications (ICRERA), 2012 pp. 1-6, Nagasaky (Japan), 11-14 Nov. 2012.

[215] GKN Sinter Metals GmbH, SMC Material Data Sheet.

[216] Hoeganaes Corp., Insulated Powder Composites: Characteristics And Electromagnetic Application Guidelines, 2010.

[217] Höganäs, Somaloy® Prototyping Material Datasheet, http://www.hoganas.com/Documents/Somaloy Broschyrer och Wear Resist/SMC/Somaloy Prototyping Material March 2011.pdf

[218] J. Wang and D. Howe, “Influence of soft magnet materials on the design and performance of tubular permanent magnet machines”, IEEE Trans. on Magnetics, vol. 41, no. 10, Oct. 2005, pp. 4057–4059.

[219] L. Hultman, and Z. Ye, “Soft Magnetic Composites-Properties and Applications” World Congress on Powder Metallurgy & Particulate Materials, PM2TEC 2002, 18 June 2002, Orlando, USA.

[220] M. Andriollo, L. Dall'Ora, A. Tortella, “Electromagnetic parameter characterization of a short-stroke linear PM generator for renewable energy application”, International Conference on Clean Electrical Power (ICCEP), 11-13 June 2013, Alghero, Italy p. 383-390.

[221] J. Brauer, “Simple equations for the magnetization and reluctivity curves of steel”, IEEE Trans. on Magnetics, vol. 11, no. 1, 1975, pp.81.

[222] O. Andersson and P. Hofecker, “Advances in Soft Magnetic Composites – Materials and Applications”, in Int. Conf. on Powder Metallurgy & Particulate Materials PowderMet 2009, 19-22 July 2009, Las Vegas, 2009.

[223] D. Lin, P. Zhou, W. N. Fu, Z. Badics, and Z. J. Cendes, “Dynamic Core Loss Model for Soft Ferromagnetic and Power Ferrite Materials in Transient Finite Element Analysis”, IEEE Trans. on Magnetics., vol. 40, no. 2, March 2004, pp.1318-1321.

[224] J. Wang, T. Ibrahim, and D. Howe, “Prediction and Measurement of Iron Loss in a Short-Stroke, Single-Phase, Tubular Permanent Magnet Machine”, IEEE Trans. on Magnetics, vol. 46, no. 6, June 2010, pp.1315-1318.

[225] J. Wang, Z. Lin, and D. Howe, “Characteristics of linear compressors under current source excitation,” Proc. Inst. Mech. Eng. A, J. Power Energy, vol. 221, no. 7, pp. 1057–1065, 2007.

[226] Martini WR. Stirling engine design manual, report no. NASA CR-135382. In: M.J. Collie, editor. Stirling engine design and feasibility for automotive use. New Jersey: Noyes data corp.; 1979.

[227] J. G. Schreiber, S. M. Geng and G. V. Lorenz, “RE-1000 Free-Piston Stirling Engine Sensitivity Test Results”, NASA TM-88846 (1986).